



UNIVERSIDAD AUTÓNOMA DE
MADRID



DEPARTAMENTO DE FÍSICO-QUÍMICA APLICADA

**PHOTOCATALYSIS IN CONSTRUCTION:
METHODOLOGIES FOR DETERMINATION OF ACTIVE
SPECIES**

**FOTOCATÁLISIS EN CONSTRUCCIÓN:
ESTABLECIMIENTO DE METODOLOGÍAS PARA LA
DETERMINACIÓN DE ESPECIES ACTIVAS**

Tesis Doctoral

Eva María Jiménez Relinque

2017

DIRECTOR

Marta María Castellote Armero

Instituto de Ciencias de la Construcción “Eduardo Torroja”
Departamento de Seguridad y Durabilidad de Estructuras
Madrid, España

SUPERVISOR UNIVERSIDAD

Pilar Herrasti Gonzalez

Universidad Autónoma de Madrid
Departamento de Físico-química Aplicada

REVISORES EXTERNOS

Maria Pia Pedferri

Politecnico di Milano

Dipartimento di Chimica, Materiali ed Ingegneria Chimica "G. Natta"

Luis Fernandez Luco

Universidad de Buenos Aires
Departamento de Ingeniería

La tesis doctoral cuya memoria se presenta ha sido financiada mediante una beca predoctoral en el Consejo Superior de Investigación Científica (CSIC) desde el 1 de octubre del 2012 hasta el 1 de octubre del 2016 con cargo al proyecto “Fotocatálisis en construcción: establecimiento de la metodología para la cuantificación de especies activas”: JAEPREDOC-CP 2012_00062.

Acknowledges – Agradecimientos

Escribir esta nota de agradecimiento es el toque final de este trabajo de tesis. Ha sido un periodo de intenso aprendizaje para mí, no solo en el ámbito científico, sino también a nivel personal, en el que han participado numerosas personas a las que me gustaría agradecerles en este apartado.

En primer lugar quería agradecerle a mi directora de tesis, Marta Castellote, por su excelente dirección y por su confianza en mí. Sus conocimientos en el campo de la investigación y su motivación han sido imprescindibles para llevar a cabo este trabajo.

I would also like to express my gratitude to Professor Andrew Mills for giving me the opportunity to work in his group during my stay at Queens University in Belfast, where I had the opportunity to learn and finish part of this work.

My colleagues in Belfast, Nathan Wells, C. O'Rourke, Dan Hawthorne, Ysufu Dilidaer, Luke Burns and David Hazafy, to welcome me as one of your group and make me feel at home. I cannot forget other Belfast friends who took care of me during my stay as Marta, Isabel, Daniel, Darius, Federico, Laura, Kike, Albert, Ana, Eunice and Fabio.

Todo este trabajo hubiera sido más difícil sin la ayuda de compañeros de Instituto "Eduardo Torroja" como Luis, Miriam, Fran Rubiano, Alicia, Fernando Martin-Consuegra, a los compañeros de servicios generales, los "chicos de mantenimiento", y por su puesto a todos los miembros de mi grupo de investigación ISCMA. Agradecer de forma especial a grandes compañeros y amigos como Maria Grande, Francisco Rozas, Isaias, Filipe, Maria Sapiña y Sara por su paciencia, ánimo y por acompañarme en los momentos de crisis y de felicidad. Como siempre os digo, ¡qué haría yo sin vosotros!

También a mis amigas de siempre, Carol, Pili, Laura ("mi sueca"), Cecilia, y en especial a Bego y Eva, mis mejores amigas, y sus dos preciosidades que vienen de camino. A mis compañeras de piso, Laura y Cris (¡te vamos a echar de menos!), por esas charlas y risas al llegar del trabajo que tanto me han ayudado.

Por último a mi familia, "mis gaditanos", de los que me siento orgullosa por encima de todo. A mi padre por sus consejos, dedicación y apoyo incondicional. A mi madre por mostrarme siempre su cariño y comprensión. Y a mi hermano por protegerme siempre que lo he necesitado y del que me siento muy orgullosa.

Muchas gracias a todos!

Eva María Jiménez

Madrid, 10 de Mayo 2017

Abstract

In big cities with dense population, the concentration of pollutants in the air is still quite too high, **and air quality problems** persist. A significant proportion of Europe's population lives in areas, especially cities, where exceedances of air quality standards occur, which has been proved to be very pernicious for human health. On the other hand, polluted environment causes **soiling and gradual deterioration of construction infrastructure and monuments** (sculptures, buildings, pavements, roads, bridges, etc.). A proper maintenance to preserve aesthetics and, more importantly, the structural integrity of urban architecture (residential buildings, institutions, monuments, historic heritage, etc.) entails enormous regular budget expenditures.

To address these problems that greatly affect society, in recent years the use of **photocatalytic construction materials** has emerged as a new technology to remediate the contamination of urban atmosphere and maintain the esthetics and functionality of the build patrimony. Pavements and building vertical surfaces provide optimal substrates for the application of photocatalytic solutions given the large surface area exposed and the relatively flat configuration that facilitate the exposure of the photocatalyst to sunlight.

The growing interest of this technology and the good results generally obtained at the laboratory have encouraged many producers of construction materials to develop and market their own photocatalytic products. In this sense, a large variety of type of products whose range of efficiencies is quite broad is available currently, such as paints, tiles, glass, plastics, cementitious materials, etc. Among these materials, cementitious substrates (e.g. cement paste or mortar and concrete) have become one of the most widely TiO₂-modified materials used in construction field.

Although photocatalytic construction materials show good prospects, some aspects such as improving the stability and the photoactive performance of the materials have not been fully addressed and are of important for its large-scale application. In addition, although some standards have been developed to assess the photocatalytic activity, **an ideal method is still not available** and some crucial drawbacks must be solved: (i) The currently used methods are related to the ability to remove specific contaminants (mainly NO_x and Rhodamine B); (ii) differ in many experimental parameters which are relevant to the results, which makes it hard to compare experimental results between tests performed at different conditions; (iii) require expensive equipment and/or are very time consuming; (iv) are not able to be applied on site; and (v) some of them are dependent on the colour of the sample, not being suitable for coloured samples.

Then, it is clear that there is an important gap in the assessment of the photocatalytic behaviour of TiO₂ construction materials, not literature references were found about any method able to give the **global potential** of a material **as a photocatalyst**.

Provided the photocatalytic mechanism is determined by the energy states of charge carriers (photo-generated e^- and h^+) and the reactive oxygen species (ROS, e.g. OH^\bullet , $O_2^{\bullet-}$, H_2O_2 , etc.) formed in the photocatalytic process, it seems that the ideal method should be based in the measurement of these species. However, they present some characteristics that make very difficult its direct detection, such as a very short lifetime and high reactivity; and the expensive analytical equipment and long analysis time required if using the currently available methods.

In this context, this research deals with the **developed of new procedures for assessing the photocatalytic activity of TiO_2 construction materials based on the detection of active species formed during the photo-activation process**, and to contribute, as far as possible, to solve the drawbacks of current standards. Clearly, it would be desirable that the newly developed method/s were able to probe, easy, rapid and cheaply, the wide available range of photocatalytic materials, especially the cement-based materials due to their extensive range of applications in the construction field.

To undertake this global objective, several steps have been followed:

- Selection of probes and active species to be measured for evaluation of the photo-activity.
- Development of the specific methods applicable to a wide range of construction materials with different photocatalytic activities and intrinsic properties.
- Validation of the developed methods as compared with the standard methods used to assess the photocatalytic efficiency.

In the development of the methods, a first step using a **plain photocatalyst** has been carried out in order to study the main features of the methods and to assess their meaning and real possibilities with simpler materials. Then a **wide variety of construction materials** with different photocatalytic activities and intrinsic properties have been used in the development and optimization of the methods.

As a conclusion, **new methods for evaluating the photocatalytic activity of TiO_2 construction materials based on the detection of the active species formed during the photo-activation process has been developed**. Specifically, the **Terephthalic acid (TA) fluorescence (FL) probe method, the Resazurin (Rz) and nitrobluetetrazolium (NBT) ink methods**. The TA-FL probe method allows **quantifying the photocatalytic OH^\bullet formed in the bulk solution, while the ink method detects free and shallowly trapped electrons**, which the ones susceptible to participate in the redox reactions.

Validation of the developed methods towards the current standards has allowed pointing out the importance of having methods that allow the comparison between different samples independently of a specific contaminant, and to demonstrate and justify the differences obtained, even in the ranking of materials, when using different contaminants to measure the photocatalytic efficiency.

In addition, the potential to “simple-to-use”, the short timescale involved, the clear visible changes (for ink tests) and inexpensive measurements give the developed tests significant advantages over conventional photoactivity tests. Beside this, RZ –NBT ink test allows assessing the activity of photocatalytic construction materials using just a portable spectrophotometer or digital camera to record the change in colour, making it ideal for testing these materials “in situ”—a capability which is currently not available using the conventional tests.

Resumen

En las grandes ciudades con una densa población, la concentración de contaminantes en el aire es todavía demasiado alta y los **problemas de calidad del aire** persisten. Una proporción significativa de la población europea vive en zonas, especialmente en ciudades, donde se producen excedencias en las normas de calidad del aire, lo que ha derivado en grandes problemas para la salud humana. Por otro lado, el medio ambiente contaminado provoca **suciedad y deterioro gradual en infraestructuras y monumentos**. Un mantenimiento adecuado para preservar la estética y, lo que es más importante, la integridad estructural de la arquitectura urbana (edificios residenciales, instituciones, monumentos, patrimonio histórico, etc.) implica enormes gastos del presupuesto ordinario.

Para abordar estos problemas que afectan en gran medida a la sociedad, en los últimos años, el uso de **materiales de construcción fotocatalíticos** ha surgido como una nueva tecnología para remediar la contaminación de la atmósfera urbana y mantener la estética y funcionalidad de las infraestructuras y patrimonio de la construcción. Los pavimentos y las superficies verticales de las infraestructuras proporcionan sustratos óptimos para la aplicación de soluciones fotocatalíticas dada la gran superficie expuesta y la configuración relativamente plana que facilitan la exposición del fotocatalizador a la luz solar.

El creciente interés de esta tecnología y los buenos resultados generalmente obtenidos en el laboratorio han alentado a muchos productores de materiales de construcción a desarrollar y comercializar sus propios productos fotocatalíticos. En este sentido, actualmente se dispone de una gran variedad de tipos de productos cuya gama de eficiencias es bastante amplia, tales como pinturas, baldosas, vidrio, plásticos, materiales cementosos, etc. Entre estos materiales, los sustratos cementicios (por ejemplo, pasta de cemento o mortero y hormigón) se han convertido en uno de los materiales más ampliamente utilizados en fotocatalisis el campo de la construcción.

Aunque los materiales de construcción fotocatalíticos muestran buenas perspectivas, algunos aspectos tales como la mejora de la estabilidad y el rendimiento fotoactivo de los materiales no se han abordado completamente y son importantes para su aplicación a gran escala. Además, aunque se han desarrollado algunas normas estandarizadas para evaluar la actividad fotocatalítica, **todavía no se dispone de un método ideal** y deben resolverse algunos inconvenientes cruciales. Como por ejemplo: (i) los métodos actualmente utilizados están relacionados con la capacidad de eliminar contaminantes específicos (principalmente NO_x y Rodamina B); (ii) difieren en muchos parámetros experimentales que son relevantes para los resultados, lo que hace difícil comparar los resultados experimentales entre los ensayos realizados en diferentes condiciones; (iii) requieren equipos costosos y/o consumen mucho tiempo; (iv) no pueden aplicarse “in – situ”; and (v) algunos de ellos dependen del color de la muestra, no siendo adecuados para muestras coloreadas.

Por tanto, hasta el momento está claro que hay una brecha importante en la evaluación del comportamiento fotocatalítico de los materiales de construcción TiO_2 , además, no se encontraron referencias bibliográficas sobre ningún método capaz de dar el **potencial global de un material como fotocatalizador**.

Teniendo en cuenta que el mecanismo fotocatalítico esté determinado por los estados de energía de los portadores de carga (e^- y h^+ foto-generados) y las especies reactivas de oxígeno (ROS, por ejemplo OH^\bullet , $\text{O}_2^{\bullet-}$, H_2O_2 , etc.) formados en el proceso fotocatalítico, Parece que el método ideal debe basarse en la medición de estas especies. Sin embargo, estas presentan algunas características que dificultan su detección directa, tales como una vida útil muy corta y alta reactividad; Y el costoso equipo analítico y el largo tiempo de análisis requerido si se utilizan los métodos actualmente disponibles.

En este contexto, este trabajo trata de desarrollar nuevos procedimientos para evaluar la actividad fotocatalítica de materiales de construcción de TiO_2 basados en la detección de especies activas formadas durante el proceso de fotoactivación y contribuir, en la medida de lo posible, a resolver los inconvenientes de las normativas actuales. Claramente, sería deseable que el método o los métodos recién desarrollados pudieran sondear, fácil, rápido y barato, la amplia gama disponible de materiales fotocatalíticos, especialmente los materiales a base de cemento debido a su amplia gama de aplicaciones en el campo de la construcción.

Para llevar a cabo este objetivo global, se han seguido varios pasos:

- Selección de sondas y especies activas a medir para la evaluación de la fotoactividad.
- Desarrollo de los métodos específicos aplicables a una amplia gama de materiales de construcción con diferentes actividades fotocatalíticas y propiedades intrínsecas.
- Validación de los métodos desarrollados en comparación con los métodos estandarizados utilizados para evaluar la eficiencia fotocatalítica.

En el desarrollo de los métodos, se ha llevado a cabo una primera etapa utilizando diferentes **fotocatalizadores puros** para estudiar las principales características de los métodos y evaluar su significado y posibilidades reales con materiales más simples. A continuación se ha utilizado una amplia variedad de **materiales de construcción** con diferentes actividades fotocatalíticas y propiedades intrínsecas para el desarrollo y optimización de los métodos.

Como conclusión, se han desarrollado **nuevos métodos para evaluar la actividad fotocatalítica de materiales de construcción TiO₂ basados en la detección de las especies activas formadas durante el proceso de foto-activación.** Específicamente, el método de la sonda de fluorescencia de **Ácido Tereftálico (TA -FL), los métodos de tinta Resazurin (Rz) y Nitroazul de tetrazolium (NBT).** El método de la sonda TA-FL permite **cuantificar la producción de OH• en la solución a granel,** mientras que el método de la tinta detecta **electrones atrapados libremente y superficialmente,** los cuales son susceptibles de participar en las reacciones redox.

La validación de los métodos desarrollados con respecto a las normas actuales ha permitido señalar la importancia de contar con métodos que permitan la comparación entre diferentes muestras independientemente de un contaminante específico y demostrar y justificar las diferencias obtenidas incluso en la clasificación de materiales cuando se utilizan diferentes contaminantes para medir la eficiencia fotocatalítica.

Además, el potencial de "simple de usar", la corta escala de tiempo implicada, los claros cambios visibles (para pruebas de tinta) y el tipo de medición de bajo coste dan a las pruebas desarrolladas ventajas significativas sobre las pruebas de fotoactividad convencionales. Además de esto, la prueba de tinta RZ-NBT permite evaluar la actividad de los materiales de construcción fotocatalíticos usando sólo un espectrofotómetro portátil o una cámara digital para registrar el cambio de color, lo que los hace ideal para probar estos materiales "in situ"-una capacidad que actualmente no está disponible utilizando las pruebas convencionales.

Table of Contents

CHAPTER 1.....	1
INTRODUCTION	1
1.1 GENERAL CONCEPTS OF SEMICONDUCTOR PHOTOCATALYSIS.....	2
1.2 BASIC PRINCIPLES OF SEMICONDUCTOR PHOTOCATALYSIS	3
1.2.1 <i>TiO₂ semiconductor photocatalysis.....</i>	<i>4</i>
1.2.2 <i>TiO₂ the lattice and electronic structure.....</i>	<i>5</i>
1.2.3 <i>Mechanism aspects of heterogeneous photocatalysis on TiO₂.....</i>	<i>6</i>
1.2.3.1 Generation of Reactive Oxygen Species (ROS)	7
1.3 TiO ₂ PHOTOCATALYSIS IN CONSTRUCTION MATERIALS	9
1.3.1 <i>Properties and applications of TiO₂ construction materials</i>	<i>10</i>
1.3.1.1 Depollution Effect	10
1.3.1.2 Self-cleaning Effect	11
1.3.1.3 Self-disinfecting Effect.....	11
1.3.1.4 Antifogging [40].....	12
1.3.1.5 Cooling Effect [40]	13
1.3.2 <i>TiO₂ photocatalytic cement-based materials</i>	<i>14</i>
1.3.3 <i>Research development and practical applications of photocatalytic cement based materials: self-cleaning and air purification applications.....</i>	<i>15</i>
1.3.4 <i>Problems and limitations in real-life applications of photocatalytic construction materials</i>	<i>19</i>
1.4 STANDARDS METHOD FOR EVALUATION OF PHOTOCATALYTIC ACTIVITY	21
1.4.1 <i>ISO 22197 - Test methods for air-purification performance of semiconductor photocatalytic materials</i>	<i>22</i>
1.4.2 <i>JIS 1703-2:2007 Methylene blue decomposition</i>	<i>23</i>
1.4.3 <i>UNI 11259:2008 – Photocatalytic activity determination of hydraulic binder -Rhodamine method.....</i>	<i>24</i>
1.4.4 <i>ISO 27448:2009: Test methods for self-cleaning performance of semiconductor photocatalytic materials – measurement of water contact angle.....</i>	<i>25</i>
1.4.5 <i>Problems and limitations of current standards.....</i>	<i>26</i>
1.5 METHODS FOR EVALUATION OF PHOTOCATALYTIC ACTIVITY BASED ON THE DETECTION OF PHOTO-GENERATED CHARGE CARRIERS AND REACTIVE OXYGEN SPECIES (ROS).....	29
1.5.1 <i>Electron Paramagnetic Resonance (EPR) or Electron Spin Resonance (ESR).....</i>	<i>31</i>
1.5.2 <i>Fluorescence spectroscopy</i>	<i>33</i>
1.5.3 <i>Absorbance ultraviolet-visible spectrometry</i>	<i>36</i>
1.5.4 <i>Chemiluminescence (CL).....</i>	<i>39</i>
1.5.5 <i>Electrochemical techniques</i>	<i>41</i>
1.5.6 <i>Other techniques</i>	<i>42</i>
CHAPTER 2.....	46
OBJECTIVES OF PHD'S WORK	46
CHAPTER 3.....	48
EXPERIMENTAL PART.....	48
3.1 PRELIMINARY SELECTIONS	50
3.1.1 <i>Selection of probes to detect active species</i>	<i>50</i>
3.1.2 <i>Selection of construction materials.....</i>	<i>53</i>
3.1.3 <i>Selection of standard methods for determination of photocatalytic activity</i>	<i>59</i>
3.2 CHARACTERIZATION OF MATERIALS	60
3.2.1. <i>Elemental composition - X-ray powder diffraction (XRD)</i>	<i>61</i>

3.2.2	<i>Elemental composition - X-ray fluorescence (XRF)</i>	63
3.2.3	<i>Surface area and Porosity analysis- Physical gas adsorption and Mercury intrusion porosimetry</i>	63
3.2.4	<i>Optical properties -UV-Vis diffuse reflectance</i>	64
3.2.5	<i>Valence band position - X-Ray Photoelectron Spectroscopy, XPS</i>	67
3.3	DEVELOPMENT OF THE METHODS FOR CONSTRUCTION MATERIALS	69
3.3.1	<i>Calibration of the probes</i>	69
3.3.2	<i>Optimal probe concentration</i>	72
3.3.3	<i>Selectivity of the optimal probe concentration</i>	72
3.3.4	<i>Preliminary tests: Study on plain TiO₂ photocatalysts</i>	73
3.3.4.1	<i>Hydroxyl radical (OH•) quantification on irradiated photocatalyst using terephthalic (TA)</i>	73
3.3.4.2	<i>Electron (e-) quantification on irradiated photocatalyst using Resazurin (Rz) probe</i>	74
3.3.4.3	<i>Photocatalytic degradation of Rhodamine B</i>	74
3.3.4.4	<i>Irradiation setup</i>	75
3.3.5	<i>Development of the method on construction materials</i>	76
3.3.5.1	<i>METHOD 1 Hydroxyl radical quantification using terephthalic acid (TA) fluorescence (FL) probe method</i>	76
3.3.5.2	<i>METHOD 2: Electron (e-) reductive measurement using Rz and NBT ink method</i>	77
3.3.5.3	<i>Irradiation setup</i>	79
3.4	VALIDATION OF DEVELOPMENT METHODS	80
3.4.1	<i>Photocatalytic oxidation of gaseous NO to nitric acid (ISO 22197-1:2007 and UNI 11247:2010)</i>	80
3.4.2	<i>Rhodamine (RhB) discoloration (UNI 11259:2008)</i>	84
CHAPTER 4		89
RESULTS AND DISCUSSION		89
4.1	SELECTION OF PROBES	90
4.2	OPTIMIZATION OF SELECTED PROBES	93
4.2.1	<i>Calibration of probes</i>	94
4.2.2	<i>Optimal probe concentration</i>	94
4.2.3	<i>Selectivity analysis</i>	95
4.3	PRELIMINARY STUDY: APPLICATION OF SELECTED PROBES ON PLAIN TiO ₂ PHOTOCATALYST NANOPARTICLES IN AQUEOUS DISSOLUTION	97
4.3.1	<i>TiO₂ photocatalyst characterization</i>	97
4.3.2	<i>Quantitative formation rate of OH• on irradiated TiO₂ photocatalyst using terephthalic acid probe (TA)</i>	101
4.3.3	<i>Formation rate of e- on irradiated TiO₂ photocatalyst using Resazurin ink</i>	102
4.3.4	<i>Rhodamine B discolouration test</i>	104
4.4	DEVELOPMENT OF METHODS ON CONSTRUCTION MATERIALS	109
4.4.1	<i>Characterization of construction materials</i>	109
4.4.1.1	<i>Composition -XRD and FRX</i>	109
4.4.1.2	<i>BET Surface area and porosity- physical gas absorption and mercury intrusion porosimetry (MIP)</i>	114
4.4.1.3	<i>Optical properties - UV-Vis diffuse reflectance (DRS)</i>	117
4.4.2	<i>METHOD 1: Hydroxyl radical quantification using terephthalic acid fluorescence probe method (TA-FL)</i>	123
4.4.3	<i>METHOD 2: Electron (e-) rate measurement using Rz and NBT ink method</i>	126
4.4.3.1	<i>Optimization of procedure: analysis of interferences of O₂•- or O₂ in the reduction yield of inks by electron</i>	126
4.4.3.2	<i>e- reduction rate in photocatalytic construction materials</i>	128
4.4.3.3	<i>Monitoring of the e- reduction rate using the inks</i>	130
4.4.3.4	<i>Determination of efficiency parameter: Half-life of the ink decomposition</i>	137
4.5	VALIDATION OF THE METHODS	140

4.5.1 Photocatalytic activity results using photocatalytic oxidation of gaseous NO to nitric acid (ISO 22197:1-2007 and UNI 11247:2010) and Rhodamine (RhB) discoloration (UNI 11259:2008)	140
4.5.2 Comparative between methods: TA-FL method, reductive ink tests, photo-oxidation of gaseous NO to nitric acid (ISO 22197:1-2010 and UNI11247:2010) and RhB discoloration (UNI 11259:2008)	142
4.5.2.1 NOx degradation vs RhB discoloration	142
4.5.2.2 TA-FL vs reductive inks	144
4.5.2.3 NOx degradation vs TA-FL and reductive inks	145
4.5.2.4 RhB discoloration vs TA-FL and reductive inks	155
CONCLUSIONS - CONCLUSIONES	168
SCIENTIFIC PRODUCTION AND DISSEMINATION	173
PUBLISHED ARTICLES ON SPECIALIST JOURNAL OR BOOKS	174
<i>SCI journals</i>	174
<i>Collective publications</i>	175
COMMUNICATIONS AT CONGRESS, SEMINAR OR COURSES	176
<i>Seminar or courses</i>	176
<i>Congress</i>	176
PATENTS	180
APPENDIX	182
APPENDIX A EFFECT OF PHYSICOCHEMICAL AND OPTICAL PROPERTIES OF THE MATERIALS ON PHOTOCATALYTIC PERFORMANCE PARAMETERS	183
A.1 <i>Physical parameters</i>	183
A.2 <i>Optical properties</i>	184
APPENDIX B EFFECT OF IRON OXIDE BASED PIGMENT ON PHOTOCATALYTIC PERFORMANCE PARAMETERS	187
B.1 <i>Iron oxide based pigment characterization-XRF and XRD</i>	187
B.2 <i>Effect of iron oxide based on photocatalytic parameters</i>	188
APPENDIX C COLLECTION AND ADJUSTMENT OF DATA OVER IRRADIATION TIME FOR RZ AND NBT INKS ON THE ALL MATERIALS TESTED	196
C.1 <i>Rz ink – Absorbance and CIELAB colour</i>	196
C.2 <i>NBT ink – Absorbance and CIELAB colour</i>	198
C.3 <i>Rz ink – RGB from images</i>	203
C.4 <i>NBT ink – RGB from images</i>	205
APPENDIX D PHOTOCATALYTIC ACTIVITY RESULTS USING PHOTOCATALYTIC OXIDATION OF GASEOUS NO TO NITRIC ACID (ISO 22197:1-2007 AND UNI 11247:2010)...	210
APPENDIX E ABSORBANCE SPECTRA VARIATION OF RHB DYE TESTED UNDER PLAIN TiO₂ PHOTOCATALYSTS.....	213
REFERENCES	215

Figure Captions

- Figure 1. 1** Diagram of energy bands in solid (a) insulator, (b) semiconductor, and (c) conductor. VB: valence band; CB: conduction band; Eg: band gap.....3
- Figure 1. 2** Schematic illustration of the basic principles of semiconductor photocatalysis.(I) absorption of radiation of energy higher or equal to the band gap, (Eg) of the semiconductor, thereby generating an electron–hole pair; (IIa) migration of photogenerated conduction band electrons, e⁻, to the surface and reaction with an adsorbed electron acceptor, A; (IIb) migration of photogenerated valence band holes, h⁺, to the surface and reaction with an adsorbed electron donor, D; (III) e⁻-h⁺ recombination.....4
- Figure 1. 3** Crystal structures of the two forms of titanium dioxide - (A) Rutile unit cell, (B) Anatase unit cell[8].5
- Figure 1. 4** Schematic diagram of reduction potential of photo-excited conduction band electron and the oxidation potential of the valence band hole at the surface of TiO₂ anatase along with the main redox equilibria for O₂ and H₂O.....6
- Figure 1. 5** TiO₂ photocatalytic reaction scheme for the generation of reactive oxygen species.8
- Figure 1. 6** Illustration of depollution effect on photocatalytic building materials.10
- Figure 1. 7** Illustration of self-cleaning effect on photocatalytic building materials.....11
- Figure 1. 8** Combined images of SEM (grey scale) and carbon mapping (red scale) measured by EDS for both pollen allergen extracts (PAE) and four different configuration (I PAE onto SEM support; II PAE + UV; PAE onto photocatalyst (dark conditions); PAE onto photocatalyst + UV).....12
- Figure 1. 9** Anti-fogging effect of automobile side-view mirror: conventional mirror (left) and TiO₂-coated mirror (right)[40].12
- Figure 1. 10 Energy-saving system using solar light and stored rainwater[40].13
- Figure 1. 11** PICADA project, Guerville, France (www.picada-project.com).....16
- Figure 1. 12** Images of two platforms from Life –Photoscaling project (a) Centro de Automática y Robótica CSIC-UPM, Campo Real way, Km 0,2, 28500 Arganda del Rey(Madrid) and (b) Intitute Eduardo Torroja, CSIC. Serrano Galvache street, 4, 28033 (Madrid).....17
- Figure 1. 13** (a) Photocatalytic sprays on sidewalk tiles, (b) draining bituminous pavements percolated with photocatalytic slurry, (c) photocatalytic tiles to pavement sidewalks, and (d) photocatalytic tiles to pavement roadways.18
- Figure 1. 14** Image of prestige construction made with photocatalytic cement (a) church Dives in Miserocordia and (b) church Riberas de Loiola (<http://www.fym.es>)19
- Figure 1. 15** Schematic illustration of the test equipment for the air purification ISO standards. (1) UV light, (2) glass cover, (3) tested sample, (4) standard gas – test pollutants, (5) air source, (6) humidifier, (7) mass flow controllers, (8) pollutant gas analyzer [60].22
- Figure 1. 16** Schematic illustration of the set up using for the methylene blue standard. (1) UV light source, (2) glass cover, (3) testing cylinder, (4) testing area and (5) sample under test.[60]24
- Figure 1. 17** Three different surface tensions effecting the drop shape [62]......25
- Figure 1. 18** Molecular structure of dihydrocompounds most commonly used as fluorescent probes[75].34
- Figure 1. 19** Structure of HPF and APF with ROS.34
- Figure 1. 20** Structure of fluorescence probes used for quantification of OH• formed during the photocatalytic process.35
- Figure 1. 21** Reaction mechanism considered to determine OH• using DMSO.....36
- Figure 1. 22** Structure and reaction with superoxide radical of tetrazolium salts, Nitroblue tetrazolium (NBT) and 2,3-Bis(2-methoxy-4-nitro-5-sulfophenyl)-2H-tetrazolium-5- carboxanilide (XTT)[78]......38
- Figure 1. 23** Proposed reaction scheme of the photocatalyst ink identifying the major underlying reactions. SC is the underlying semiconductor and D/D⁻ and SED/SED_{ox} are the

oxidised/reduced forms of the indicator dye and sacrificial electron donor, respectively, encapsulated in the polymer film printed or coated onto the semiconductor[112].	38
Figure 1. 24 Structures of Resazurin (blue, left) and its reduced form Resorufin (pink, right)[112].	39
Figure 1. 25 Chemiluminescence reaction of luminol[78].	40
Figure 3. 1 Experimental design and methodology of this research.	50
Figure 3. 2 Aspects to considered for selection probe/test methods to detect the generated photocatalytic active species.	51
Figure 3. 3 (a) Image of the aspect of the three emulsions before application and (b) Image of emulsions coating process onto the prepared base mortars.	53
Figure 3. 4 Lab-made samples (#L1 and #L2) preparation following the procedure described on UNE-EN-196-1 and UNE-EN-197-1 standards.	54
Figure 3. 5 Imagen of some lab-made coloured mortar mixtures (a) #L6, (b) #L8, (c) #L7 and (d) #L11.	55
Figure 3. 6 Diffuse and specular reflection of incident light on surface [157].	65
Figure 3. 7 Schematic diagram of UV-Vis spectrophotometer and image of accessory “integrating sphere”.	66
Figure 3. 8 Image of UV-Vis spectrophotometer Shimatzu UV-2600.	67
Figure 3. 9 Photo-electron generation from XPS technique[159].	68
Figure 3. 10 Reaction for detecting OH• in solution with terephthalic acid (TA) to form 2 hydroxylterephthalic (TAOH).	70
Figure 3. 11 Fluorescence spectrophotometer (Perkin –Elmer, LS-55).	70
Figure 3. 12 Diagram to show the structure of the redox dye Resazurin (Rz) and its reduced forms. The reduction of Rz is 4e- in two steps.	70
Figure 3. 13 Diagram to show the structure of the redox dye, Nitrobluetetrazolium (NBT), and its reduced form (formazan). The reduction of NBT is a 2e- process in one step.	71
Figure 3. 14 Reactor and illumination system setup.	75
Figure 3. 15 Light spectra of the Actinic BL 15W/10 SLV lamp used to supply UV radiation (data obtained using a fiber optic UV/VIS/NIR spectrophotometer-AvaSpec ULS3648-USB2-UA-25).	75
Figure 3. 16 (a) UV/VIS/NIR spectrophotometer (AvaSpec ULS3648-USB2-UA-25) and (b) AvaLight-DH-CAL.	76
Figure 3. 17 Diagram and image of experimental setup of OH• quantification method.	77
Figure 3. 18 (a) air compressor, (b) air-brush, and (c) example of spray-coated process with Rz, the left of the samples was coated with NBT (pale yellow).	78
Figure 3. 19 Three-dimensional CIELAB system represented by the three colour coordinates L* a* and b*.	78
Figure 3. 20 (a) Spectrophotometer used for reflectance UV-vis measurements, (b) portable spectrophotometer used for CIELab color measurements, and (c) Mobile phone used for make digital images.	79
Figure 3. 21 Experimental set-up for the NOx tests.	81
Figure 3. 22 (a) Illumination system ⁽¹⁾ , transparent window of reactor ⁽²⁾ and sample ⁽³⁾ for the NOx remediation tests, (b) NOx analyzer ⁽⁴⁾ and control system for the mass flow controllers ⁽⁵⁾ , and (c) NOx circuit ⁽⁶⁾ and mass flow controllers ⁽⁷⁾ .	81
Figure 3. 23 Imagens of the chamber with MP control –MP CLIM used in RhB tests.	85
Figure 3. 24 Image of 365 nm LEDs illumination system used in RhB tests.	86
Figure 3. 25 Schematic diagram of this PhD’s project.	88
Figure 4. 1 Fluorescence calibration curves in function of probes concentration. (a) Fluorescein (FC), (b) Rhodamina WT (RhWT), (c) Yellow alizarin (YA), (d) Phenolphthalein (PH), (e) Rhodamine B (RhB), and (f) terephthalic acid (TA).	91
Figure 4. 2 Variation of probe concentration(C/Co) in function of the addition of H ₂ O ₂ of (a) TA and (b)FC.	92
Figure 4. 3 Absorbance curve in function of Rz probe concentration.	94

Figure 4. 4 (a) Irradiation time dependence of the TAOH concentration in function of TA probe concentration (0.2-3.5 mM) and (b) Formation rate of TAOH calculated from the corresponding slope of TAOH concentration on irradiation time in function of [TA].	95
Figure 4. 5 Effect of various scavengers on percentage of TAOH formation rate at the selected concentration of TA (2mM).	96
Figure 4. 6 Decay in relative absorbance at 560 and 259 nm of Rz and NBT probes under ambient conditions (O ₂ atmosphere and N ₂ atmosphere)	97
Figure 4. 7 XRD patterns of TiO ₂ samples calcined at different temperatures	98
Figure 4. 8 (a) absorption spectra obtained via DRS of TiO ₂ calcinated powder samples, the absorbance was plotted as the Kubelka–Munk function (FR) (b) Tauc plot of (FRhν) ^{1/2} vs the energy (eV) of the incident photon. Extrapolating the tangent of the band edge curve to the energy axis obtains the indirect bandgap energy (values included in Table 4.1).	100
Figure 4. 9 Fluorescence spectra at various irradiation periods that are obtained from supernatant liquid of the irradiated TiO ₂ -500 suspension containing 2mM of TA probe.	101
Figure 4. 10 (a) Time dependence of FL intensity of TiO ₂ samples (average of two measurements) and (b) Formation rate of OH• (μmol/min) calculated from the corresponding slope of FL intensity on irradiation time (Figure 4.10 (a)) by comparing the FL intensity obtained to that of the calibration curve, FL (a.u.)=143.66·[TAOH](μM), using a trapping factor of 35%.	102
Figure 4. 11 Variation of the absorbance (Abs ₆₀₀) due to irradiation time of all TiO ₂ samples suspensions using Rz probe (a) with glycerol and (b) without glycerol, and (c) formation rate of e-(R _e). The percentages of surface e-recombination were also included using the Eq. 4.2.	103
Figure 4. 12 Image of Rz with glycerol probe degradation in function of irradiation time of samples TiO ₂ -700°C (measures each 2 minutes, final time 14 minutes).	104
Figure 4. 13 (a) RhB photo-degradation and (b) pseudo first order kinetic rate constant (K _{RhB}) for RhB degradation in the presence of TiO ₂ samples (average of two measurements).	104
Figure 4. 14 Kinetic constant of degradation of RhB versus (a) Crystallite size, (b) BET area and (c) percentages of each phase (anatase or rutile).	105
Figure 4. 15 Dependences of rate constant for RhB decomposition (K _{RhB}) on the rate of OH• formation (R _{OH•}) of TiO ₂ samples (geometric symbols: square: anatase, circle: anatase-rutile mixed, and triangle: rutile)	106
Figure 4. 16 Rate of degradation of RhB versus formation of electrons, as detected by the probes both (a) with, and (b) without glycerol. (geometric symbols: square: anatase, circle: anatase-rutile mixed, and triangle:rutile)	107
Figure 4. 17 Rate of degradation of RhB versus the percentage of e- recombination (geometric symbols: square: anatase, circle: anatase-rutile mixed, and triangle:rutile)	107
Figure 4. 18 Production rate of OH• (R _{OH•} , μmol/min), free and shallowly trapped electrons (R _e , μmol/min), e- surface recombination (%) and RhB photo-degradation (K _{RhB} , min ⁻¹) in function of the temperature of calcination, BET surface area, anatase/rutile percentage content and anatase crystallite size.	109
Figure 4. 19 XRD of hardened cement-based samples. The right-hand side images are a detail of the XRD spectra at the left in order to identify the crystal phases of TiO ₂ . (× Quartz, = Calcite, □ Dolomite, A Anatase and R Rutile).	110
Figure 4. 20 XRD spectra of (a) cement-based support of emulsion coating samples. and (b) emulsion coating dispersed on glass support. (× Quartz, = Calcite and A Anatase).	111
Figure 4. 21 XRD of lab-made cement based samples. The right-hand side images are a detail of the XRD spectra at the left in order to identify the crystal phases of TiO ₂ . (× Quartz, = Calcite, • Portandite and A Anatase).	112
Figure 4. 22 XRD of lab-coloured mortar samples. Right-hand images are a detail of the XRD spectra in order to visualize the crystallite phase of TiO ₂ (× Quartz, = Calcite, □ Dolomite and A Anatase).	113
Figure 4. 23 Cumulative and incremental pore size distribution of commercial hardened cement-based samples.	115

Figure 4. 24 Cumulative and incremental pore size distribution of cement-based support of commercial emulsions.....	115
Figure 4. 25 Cumulative and incremental pore size distribution of lab-made cement-based samples.	115
Figure 4. 26 Cumulative and incremental pore size distribution of coloured lab-made mortar samples.	116
Figure 4. 27 Absorbance spectra in Kubelka Munk units of commercial hardened cement-based samples (a-b). Plot of Tauc's relation versus photoenergy from DRS measurement (c-d). The inset diagram is the example of sample #C1 and sample #C7 apparent photoabsorption edge energy estimation (PE_{app}).	118
Figure 4. 28 (a) Absorbance spectra in Kubelka Munk units of commercial emulsion coating onto Portland cement –based support and (b) Plot of Tauc's relation versus photoenergy from DRS measurement.	118
Figure 4. 29 (a) Absorbance spectra in Kubelka Munk units of lab-made cement-based samples and (b) Plot of Tauc's relation versus photoenergy from DRS measurement.....	119
Figure 4. 30 (a) Absorbance spectra in Kubelka Munk units of lab-made coloured mortar samples, (b) Plot of Tauc's relation versus photoenergy from DRS measurement, (c) detail of visible range of Figure (a), and (d) detail of visible range of Figure (c).	119
Figure 4. 31 Determination of Urbach energy of photocatalytic commercial cement-based materials	121
Figure 4. 32 Determination of Urbach energy of TiO_2 photocatalytic commercial emulsions.....	121
Figure 4. 33 Determination of Urbach energy of TiO_2 lab-cement based samples and lab-coloured mortars	122
Figure 4. 34 Typical change of fluorescence intensity of TA on irradiated photocatalytic samples (examples of #L5).	123
Figure 4. 35 (a) Time dependence of the fluorescence intensity at 425 nm on commercial cement-based samples and (b) production rate of $OH\cdot$ calculated from the corresponding slope of fluorescence intensity on irradiation time of figure (a) using a trapping factor of 35%.	124
Figure 4. 36 (a) Time dependence of the fluorescence intensity at 425 nm on commercial emulsions samples and (b) production rate of $OH\cdot$ calculated from the corresponding slope of fluorescence intensity on irradiation time of figure (a) using a trapping factor of 35%.....	124
Figure 4. 37 (a) Time dependence of the fluorescence intensity at 425 nm on lab-made cement-based samples and (b) production rate of $OH\cdot$ calculated from the corresponding slope of fluorescence intensity on irradiation time of figure (a) using a trapping factor of 35%.....	125
Figure 4. 38 (a) Time dependence of the fluorescence intensity at 425 nm on lab-made cement-based samples and (b) production rate of $OH\cdot$ calculated from the corresponding slope of fluorescence intensity on irradiation time of figure (a) using a trapping factor of 35%.....	125
Figure 4. 39 Spectral profiles for the photocatalyzed reduction of RZ and NBT inks under N_2 atmosphere and air-free conditions by a replicate specimen of sample #C7 upon irradiation at $5 W/m^2$	127
Figure 4. 40 Decay in relative absorbance at 608 nm and 560 nm of RZ and formazan from NBT of data presented in Figure 4.39.	128
Figure 4. 41 Conversion of absorbance spectra and color of RZ upon contact with the emulsion coating samples (#E1, #E2 and #E3) and lab-made non-carbonated mortar samples (#L1 and #L2) in dark conditions – ‘reactive’ samples. Sample #C6 (non-photocatalytic) also included as reference spectra and color of RZ without any change.....	130
Figure 4. 42 Plot of the change in absorbance Kubelka–Munk units and change of color coordinate of CieLab system in function of irradiation time (a) ΔAbs_{608} and ΔLab_{at} and (b) ΔAbs_{560} and ΔLab_{bt} as a function of irradiation time. The inset graphs are the plot of ΔAbs_t vs ΔRGB_t , showing the linear relationship for both inks.	131
Figure 4. 43 Plot of variation of absorbance and colour measurement of all selected samples for (a) RZ - ΔAbs_{608t} vs ΔLAB_{at} , and (b) NBT- ΔAbs_{560t} vs ΔLAB_{bt}	132

Figure 4. 44 Change in the diffuse reflectance spectrum of the (a) Rz and (b) NBT ink on non-photocatalytic sample #C6, irradiated with UV irradiance at 5 W/m ²	133
Figure 4. 45 Plots of the variation of the normalized RGB component in function of irradiation time from digital photographs (a) ΔRGB_{Rt} for Rz and (b) ΔRGB_{Bt} for NBT.	134
Figure 4. 46 Plot of (a) ΔAbs_{608t} vs ΔRG_{Rt} – Rz and (b) ΔAbs_{560t} vs ΔRG_{Bt} – NBT of all selected samples.....	135
Figure 4. 47 Example of photograph of the colour change of the Rz and NBT inks on sample#C7 upon irradiation at 5 W/m ²	136
Figure 4. 48 (a) Mean half-life time ($t_{1/2}$ mean) obtained from the $t_{1/2}$ obtained of the three techniques to monitor the photocatalytic reduction of Rz and NBT inks (change of absorbance in Kubelka–Munk units from diffuse reflectance monitoring, change in color coordinate of CIELab form hand-spectrophotometer and change in color component of RGB from digital mobile camera images), and (b) Linear relationship between the $t_{1/2}$ mean obtained for Rz ink vs NBT ink.....	139
Figure 4. 49 Photocatalytic removal rate (%) of gaseous NO to nitric acid using the test conditions defined on the standard: (a) ISO 221917-1:2010 and (b) UNI 11247:2010 at 10 W/m ² and (c) UNI 11247:2010 at 20 W/m ²	141
Figure 4. 50 Percentage of RhB degradation (UNI 11259:2008) of selected samples.....	142
Figure 4. 51 Comparison between the photoactivity results determined by NOx (ISO 22197-1:2010) and RhB degradation upon irradiation at (a) 4 hours and (b) 26 hours.	143
Figure 4. 52 Plot of OH• production rate ($\mu\text{mol}/\text{min cm}^2 \times 10^{-4}$) vs time taken for Rz (a) and NBT (b) to lose half its color ($t_{1/2}$) on photocatalytic samples. $t_{1/2}$ mean is the average value of data collected by absorbance and color (RGB and CIELAB) measurements for both inks.....	144
Figure 4. 53 Plot of OH• production rate ($\mu\text{mol}/\text{min cm}^2 \times 10^{-4}$) of photocatalytic samples vs NOx degradation (%). $t_{1/2}$ mean is the average value of data collected by absorbance and color (RGB and CIELAB) measurements for both inks.	146
Figure 4. 54 Plot of time taken for Rz and NBT to lose half its color ($t_{1/2}$) on photocatalytic samples vs NOx degradation (%). $t_{1/2}$ mean is the average value of data collected by absorbance and color (RGB and CIELAB) measurements for both inks.....	147
Figure 4. 55 NOx removal (UNI 11249:2010) vs production rate of OH• on $\mu\text{mol}/\text{min} \cdot \text{cm}^2$ units...148	148
Figure 4. 56 Percentage of degradation of RhB with respect to control test without scavenger.	149
Figure 4. 57 XPS Valence Band (VB) spectra of selected samples. The values presented in the figure indicated the maximum energies associated with the BV and band tails. The band tail energies were shown using parentheses.	151
Figure 4. 58 Schematic illustration of approximate position of conduction band (CB), valence band (VB) and band tail of VB of selected samples.	152
Figure 4. 59 Pourbaix diagram for nitrogen species together with the equilibrium lines corresponding to OH•/OH ⁻ and •O ₂ ⁻ /O ₂	153
Figure 4. 60 Schematic illustration of reaction mechanism proposed based on the detection of OH• and NOx removal.	154
Figure 4. 61 Schematic diagram of relationship between methods.....	155
Figure 4. 62 Plot of OH• production rate from TA-FL measurements and time taken for Rz and NBT to lose half its color ($t_{1/2}$) on photocatalytic samples under an irradiance vs percentage of RhB discoloration at 4 hours (a, c and d) and 26 hours (b, e and f). RhB test performed using the procedure defining on UNI 11259: 2008 standards. $t_{1/2}$ mean is the mean value of data collected by absorbance and color (RGB and CIELAB) measurements for both inks.	156
Figure 4. 63 Probable mechanism for the photocatalytic degradation of RhB dye (Taken from [205]).	157
Figure 4. 64 Configuration of mainly degraded RhB molecules on N-de-ethylation process. ¹ 554 nm RhB, ² 539 nm (N,N,N'-Triethylrhodamine), ³ 522 nm (N,N'-Diethylrhodamine), ⁴ 510 nm (N-Ethylrhodamine) and ⁵ 498 nm (Rhodamine)[207].	158

Figure 4. 65 Examples of temporal absorbance spectral changes of RhB dye by #C7 and #C2 samples.	159
Figure 4. 66 RhB degradation of all analyzed samples in function of irradiation time.....	159
Figure 4. 67 Variation of UV–Vis absorbance spectra of the (a) R _Z and (b) RhB probe deposited onto a sample of replicated specimen of sample #C7 (#C7E) as a function of irradiation time at 3.75 W/m ² (b) Plot of the relative Abs ₆₁₀ vs. irradiation time of (c) R _Z and (d) RhB onto replicated specimens of sample #C7 at different irradiation intensity (0-3.75 W/m ²).....	162
Figure 4. 68 Chronological series of images recorded for the replicated specimens of sample #C7 at different irradiation intensity.....	163
Figure 4. 69 (a) R _{Rz} and R _{RhB} vs. irradiance intensity (W/m ²) and (b) Relationship between R _{Rz} and R _{RhB} . The numbers in parenthesis indicated the values of irradiance intensity used (W/m ²)....	164

Table Captions

Table 1.1 Primary events in heterogeneous photocatalysis and the characteristic times for TiO ₂ semiconductor. e_{CB}^- is the conduction band electron, h_{VB}^+ is the valence band hole, A is an electron acceptor, D is an electron donor, Δ and $h\nu$ represent the heat and light respectively.....	7
Table 1. 2 Overview of International, European and National standard related with photocatalysis process.....	21
Table 1. 3 General sample pre-conditioning step conditions of various standards	27
Table 1. 4 Air purification ISO standard test conditions*.....	27
Table 1. 5 Comparative between NO _x air purification standards: ISO 22197-1:2007 and UNI 11247:2010.....	28
Table 1. 6 Main features of the probes used in the determination of reactive oxygen species(ROS) ...	43
Table 3. 1 Fluorescence excitation and emission wavelength of probes.....	52
Table 3. 2 Nomenclature and main characteristics of different commercial tested samples.....	56
Table 3. 3 Analytical methods used for the characterization of all materials used.	60
Table 3. 4 Main measurement conditions used on XRD characterization of samples.	62
Table 3. 5 Techniques for pour size measurements and the range of pore sizes able to be measured. .	63
Table 3. 6 Main measurement conditions used on UV-vis characterization.	67
Table 3. 7 Characteristics of the mass flow controllers used to adjust and control the flow rate of gases	80
Table 3. 8 Summary of experimental conditions used on NO _x oxidation test.	83
Table 3. 9 Summary of the main performed photocatalytic proposed and standardized tests on selected construction materials and irradiance conditions used.....	87
Table 4. 1 Summary of physicochemical and optical properties of TiO ₂ samples. A: anatase; R: rutile.	100
Table 4. 2 TiO ₂ phases detected by XRD analysis of selected construction samples.	114
Table 4. 3 Summary data of characterization parameters by MIP and physical gas absorption measurements	116
Table 4. 4 Summary of optical parameter calculated of tested samples.....	122
Table 4. 5 Summary of parameters used to assess the photocatalytic conversion of dyes over the irradiation time.	137
Table 4. 6 Elapsed time required for the Rz and NBT to lose half its original concentration/colour ($t_{1/2}$) for their reduction on photocatalytic cement-based samples. $t_{1/2}$ were obtained from: ^a change of absorbance in Kubelka–Munk units (from diffuse reflectance monitoring), ^b change in color of LAB cielab components (form hand-spectrophotometer), and ^c change in color component of RGB (from digital mobile camera images).	138
Table 4. 7 Calculation of the probable position of VB and CB of TiO ₂ samples.....	151
Table 4. 8 Identification of samples and results of analysis of Rz and RhB degradation on photocatalytic replicated samples (#C7A-#C7E).	162
Table 4. 9 Summary of the main differences between photocatalytic performed test.....	166

Nomenclature

Abbreviations, symbols and chemicals	Definition
#C	Commercial samples
#E	Emulsion samples
#L	Lab-made samples
ΔAbs_{506t}	Variation of absorbance in function of the time at 506 nm
ΔAbs_{608t}	Variation of absorbance in function of the time at 608 nm
ΔLAB_{at}	Variation of coordinate a*of CIELAB system in function of the time
ΔLAB_{bt}	Variation of coordinate b*of CIELAB system in function of the time
$\Delta n\text{RGB}_{bt}$	Variation of component blue of RGB colour system in function of the time
$\Delta n\text{RGB}_{Rt}$	Variation of component red of RGB colour system in function of the time
BL (Fluorescence light)	Black light
BLB(Fluorescence light)	Black light blue
CB	Conduction band
CEN	European Committee for standardization
CIELAB	LAB colour space (L* luminosity describing the brightness from black to white where 0 is black and 100 white, a* the colour tone from green (negative value) to red (positive value) and b* from blue (negative value) to yellow (positive value))
DRS	diffuse reflectance
e⁻	electron
E_b	Binding energy eV
E_g	Band gap (eV)
e⁻-h⁺	Electron-hole pair
EPR	Electron Paramagnetic Resonance
ESR	Electron Spin Resonance
Eu	Urbach energy (eV)
F(R)	Kubelka-Munk function
FC	Fluorescein
FID	flame ionization detector
FL	Fluorescence spectrophotometry
FWHM	Full width at half of peak maximum
GC	Gas chromatography
GFRC	Glass Fiber Reinforced Cement
h⁺	Positive charge (hole)
H₂O	Water
H₂O₂	Hydrogen peroxide
H₂O_{ads}	Adsorbed water (on TiO ₂ surface)
HOMO	Highest occupied molecular orbital
HRf	dihydro-resofurin

hν	Photonic energy
IR	Infrared
ISO	International Organization for Standardization
K_{RhB}	RhB photo-degradation rate
LC	Chemiluminescence spectrophotometry
LUMO	Lowest unoccupied molecular orbital
MB	Methylene blue
MIP	Mercury intrusion porosimetry
NaOH	Sodium hydroxide
NBT	Nitroblue tetrazolium
NIR	Near infrared
NO	Nitric oxide
NO₂	Nitrogen dioxide
NO₂⁻	Nitrite ion
NO₃⁻	Nitrate ion
NO_x	Nitrogen dioxides (NO and NO ₂)
O₂^{•-}	Superoxide radical
OH•	Hydroxyl radical
P25	A commercial TiO ₂ photocatalytic (75 % anatase/25 % rutile)
PE_{app}	Apparent photoabsorption edge (eV)
pH	Potential of Hydrogen
PH	Phenolphthalein
PhCM	Photocatalytic coloured mortars
R_e	Formation rate of e ⁻
Rf	Resorufin
RGB	Red, Green, Blue component colour system
RH	Relative humidity (%)
RhB	Rhodamine B
RhWT	Rhodamine WT
R_{OH•}	Formation rate of OH•
ROS	Reactive oxygen species
Rz	Resazurin
SHE	Standard hydrogen electrode (eV)
TA	Terephthalic acid
TAOH	hydroxyterephthalic
TiO₂	Titanium dioxide
TiO₂(e⁻)	negative charge on irradiated titanium
TiO₂(h⁺)	Positive charge on irradiated titanium dioxide
UV	Ultraviolet light
VB	Valence band
Vis	Visible light
VOCs	Volatile organic compounds
Vp	Pore volume
XPS	X-ray photoelectron spectroscopy
XRD	X-ray diffraction
YA	Yellow Alizarin
λ	wavelength (nm)

CHAPTER 1

Introduction

1.1 General concepts of semiconductor photocatalysis

i) Catalysis and photocatalysis

Catalysis, is the process by which the speed of a chemical reaction is increased by the participation of a substance called a catalyst, which is not consumed throughout the process (which does not imply that it cannot be Inhibited, deactivated or destroyed by secondary processes), being clearly differentiated from a reagent. When the activation of the catalyst involves the absorption of light by the latter, then we speak of photocatalysis, and the catalyst is commonly called "photocatalyst".

Photocatalysis encompasses a set of chemical reactions of oxidation-reduction (redox) occurring on the surface of semiconductor materials when they are irradiated with light of suitable wavelength (λ). These reactions occur between very reactive species generated in the semiconductor (as a consequence of the absorption of the light) and the species adsorbed on its surface. On the other hand, in this process frequently develops a type of photocatalysis called "heterogeneous", since reagents and photocatalyst are in different phase.

ii) Semiconductors[1]

Semiconductors are particularly useful as photocatalysts because of a favorable combination of electronic structure, light absorption properties, charge transport characteristics and excited-state lifetimes. A semiconductor is defined as a nonconductive substance in its undoped ground state because an energy gap, the *band gap*, exists between the top of the filled valence band and the bottom of the vacant conduction band. Thus, electron transport between these bands must occur only with appreciable energy change. In semiconductor photocatalysis, excitation of an electron from the valence band to the conduction band is accomplished by absorption of a photon of energy equal to or higher than the band gap energy of the semiconductor. The photocatalytic properties of a semiconductor are explained based on its electronic structure as detailed below.

The electronic characteristics of conductors, semiconductors, and insulators can be described according to the *band theory*. Because of the very large number of atoms that interact in a solid material, the corresponding energy levels are so closely spaced that they form bands. Each band has a different energy, and the electrons fill these bands from the lowest energy to the highest, similar to the way that electrons occupy the orbitals in a single atom. The highest energy filled band, which is analogous to the highest occupied molecular orbital (HOMO) in a molecule, is called the valence band (VB). The next higher band, which is analogous to the lowest unoccupied molecular orbital (LUMO) in a molecule, is called the conduction band (CB). The VB and the CB are separated by an energy gap, the band gap (E_g).

The filling of bands in a solid and the size of the band gap determine if a material is a conductor, a semiconductor, or an insulator (Figure 1.1). In general, for electrons to flow in a solid under the application of an electric field, they must be in a partially filled band or have access to a nearby empty band. In an electrical insulator, there is no possibility for electron flow, because the valence band is completely filled with electrons, and the conduction band is too far away in energy to be accessed by these electrons. In conductors like metals the valence band overlaps the conduction band. Thus, the electrons can access empty areas within the valence band and move freely across all atoms that make up the solid. Finally a semiconductor is a special case in which the band gap is small enough (generally less than 4 eV) that it can be bridged by either heat or light, because these stimuli promote electrons from the valence band to the conduction band.

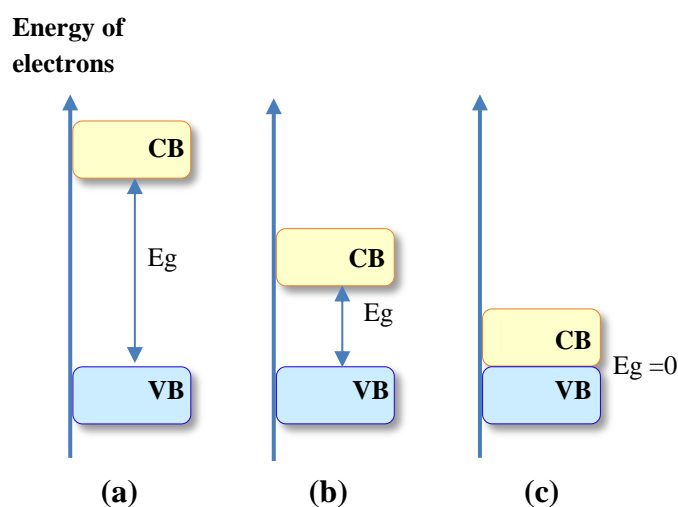


Figure 1. 1 Diagram of energy bands in solid (a) insulator, (b) semiconductor, and (c) conductor. VB: valence band; CB: conduction band; E_g : band gap.

1.2 Basic principles of semiconductor photocatalysis

The basic principles of semiconductor photocatalysis, as summarised by the schematic in Figure 1.2, have been reported by numerous studies [2-5]. When a semiconductor absorbs a photon of energy equal to or higher than its bandgap ($h\nu \geq E_g$), an electron is promoted from its valence band to its conduction band, within a femtosecond timescale[6]. The photonic excitation leaves behind an exciton with an empty valence band hole and a filled conduction band (electron-hole pair, e^-h^+) (Process I in Figure 1.2). The separated e^- and h^+ charge carriers can follow different pathways, some photogenerated electron and hole reach the surface of semiconductor by diffusion (designated “Free charge carriers”) and react with an adsorbed electron acceptor (A) (process IIa), usually molecular oxygen. In turn, a donor species (D) can be oxidized by the valence band hole (process IIb), generally H_2O or OH^- . These charge transfer processes are dependent on the position of the valence and the conduction band edges respectively and also on the redox potential of the adsorbed species[3]. For a desired electron transfer reaction to occur, the potential of

the electron acceptor species should be located more positive than the conduction band of the semiconductor, whereas the potential of the electron donor species should be located more negative than the valence band of the semiconductor.

Electron–hole recombination can occur either in the semiconductor bulk or at the surface resulting in the release of heat or light (Δ or $h\nu$) (process III) and is detrimental for the photocatalytic activity because it competes with hole-donor and electron-acceptor electron-transfer reactions [3].

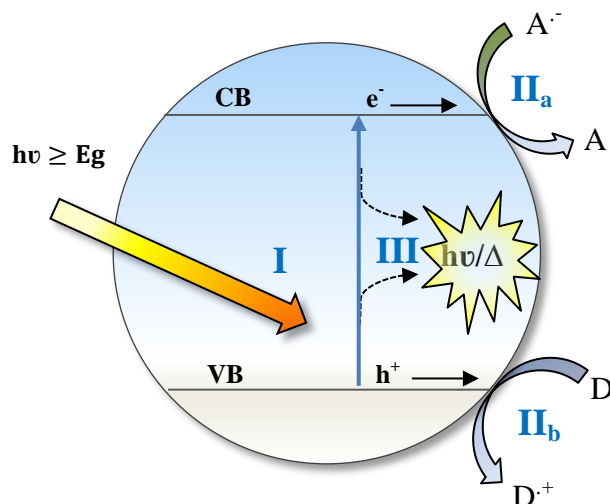


Figure 1. 2 Schematic illustration of the basic principles of semiconductor photocatalysis. (I) absorption of radiation of energy higher or equal to the band gap, (E_g) of the semiconductor, thereby generating an electron–hole pair; (IIa) migration of photogenerated conduction band electrons, e^- , to the surface and reaction with an adsorbed electron acceptor, A; (IIb) migration of photogenerated valence band holes, h^+ , to the surface and reaction with an adsorbed electron donor, D; (III) e^- - h^+ recombination.

1.2.1 TiO₂ semiconductor photocatalysis

Although there are many semiconducting materials in this world, only a few are very effective as semiconductor photocatalysts. Ideally, a semiconductor photocatalyst should be chemically and biologically inert, photocatalytically active, easy to produce and use, activated by sunlight and cheap[7]. In fact, not surprisingly, no semiconductor fits this list of ideals, although one semiconductor, titanium dioxide, TiO₂, comes close. Thus, titanium dioxide displays all the desired features of an ideal semiconductor photocatalyst, with the exception that it does not absorb visible light. Titanium dioxide has a large bandgap, $E_g \approx 3.2\text{--}3.0$ eV, and, therefore, is only a UV light absorber and, as a consequence, is limited to absorbing a small fraction, ca. 5%, of the solar spectrum. Despite this substantial limitation, its positive features far outweigh this one negative, and so titanium dioxide has become the semiconducting material to use in the field of

semiconductor photochemistry. Its dominant position extends not only to basic research but, more importantly with respect to this overview, to commercial applications.

1.2.2 TiO₂ the lattice and electronic structure

TiO₂ exists mainly in three crystallographic phases: anatase, rutile and brookite. Unit cell structures of the rutile and anatase TiO₂ can be described in terms of chains of TiO₆ octahedra, where each Ti⁴⁺ ion is surrounded by an octahedron of six O²⁻ ions (Figure 1.3).

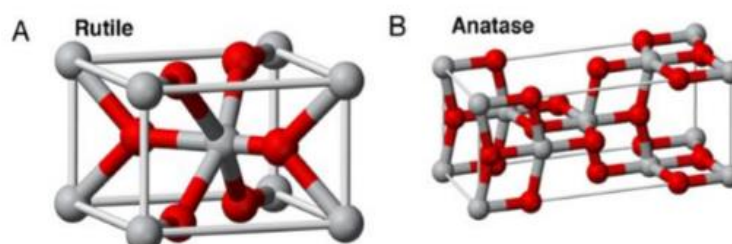


Figure 1.3 Crystal structures of the two forms of titanium dioxide - (A) Rutile unit cell, (B) Anatase unit cell[8].

The two crystal structures differ in the distortion of each octahedron and by the assembly pattern of the octahedra chains. In anatase the Ti-Ti distances is larger and each octahedron is in contact with eight neighbours, whereas in rutile the Ti-O distances is larger than anatase and each octahedron is in contact with ten neighbour octahedrons. Deviations between the two forms of TiO₂ lattice structures cause differences in mass densities and electronic band structures[9].

These structures have different stability. Rutile is the most stable phase for particles above 35 nm in size, anatase is the most stable phase for nanoparticles below 11 nm, and brookite is the most stable in the 11-35 nm range nanoparticles[10]

Anatase and rutile are the two phases which can be used for practical applications in photocatalysis due to their high photoactivity and higher stability compared to brookite. Although anatase is generally considered to be the single most photoactive phase [11], the synergistic mixtures of anatase and rutile have been often reported to possess even higher photo-activity. The difference in band structure between anatase and rutile (E_g, rutile ~3.0 eV and E_g, anatase ~3.2 eV) and band edge energy position can to some extent explain the difference in photo-activity.

As previously mentioned, the band energy positions, i.e. the oxidation potential of the valence band and the reduction potential of the conduction band, are crucial for the photocatalytic properties of the semiconductor. The band gap energy position effect on photocatalytic mechanism is well described on the example with anatase TiO_2 at pH 7 and the redox equilibria for O_2 and H_2O (Figure 1.4). The oxidation potential for the photo-generated hole is $+2.53\text{V}$ vs. SHE, which is theoretically powerful enough to oxidize water and hydroxide ions to produce hydroxyl radicals ($\text{OH}\cdot$). The reduction potential for the conduction band electrons is -0.52V vs. SHE is sufficient to reduce O_2 [12].

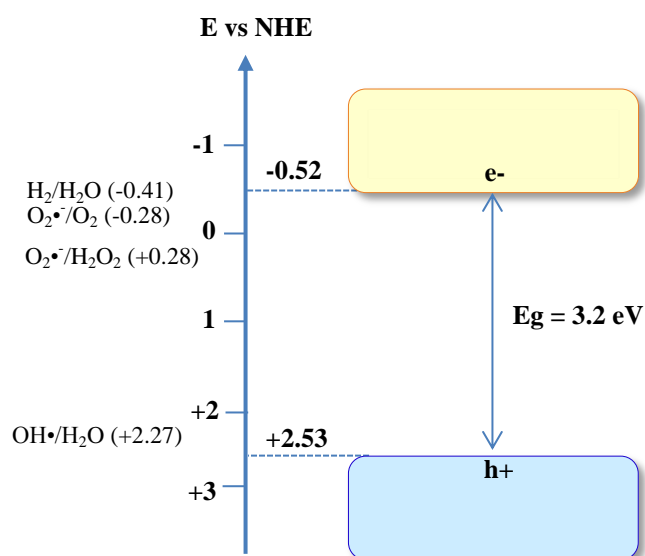


Figure 1. 4 Schematic diagram of reduction potential of photo-excited conduction band electron and the oxidation potential of the valence band hole at the surface of TiO_2 anatase along with the main redox equilibria for O_2 and H_2O .

1.2.3 Mechanism aspects of heterogeneous photocatalysis on TiO_2

The primary photocatalytic events and the characteristic time intervals for the photo-reactions occurring on TiO_2 semiconductor are summarized in Table 1.1

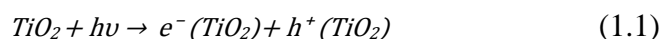
Table 1.1 Primary events in heterogeneous photocatalysis and the characteristic times for TiO₂ semiconductor. e_{CB}^- is the conduction band electron, h_{VB}^+ is the valence band hole, A is an electron acceptor, D is an electron donor, Δ and $h\nu$ represent the heat and light respectively.

Electronic step	Primary process reaction	Time
Charge carriers generation	$TiO_2 \xrightarrow{h\nu \geq E_g} e_{CB}^- + h_{VB}^+$	10^{-15} s
Hole charge carrier trapping	$h_{VB}^+ + D \rightarrow D^+$	10^{-7} s
Electron charge trapping	$e_{CB}^- + A \rightarrow A^-$	10^{-3} s
Charge carrier recombination	$e_{CB}^- + h_{VB}^+ \rightarrow \Delta \text{ or } h\nu$	10^{-8} - 10^{-7} s

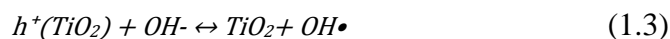
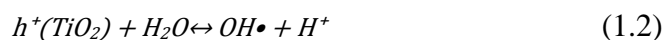
Generally, the electron donor (D) and the electron acceptor (A) are related to water/OH- and oxygen respectively, generating ROS (reactive oxygen species) able to promote further redox reactions.

1.2.3.1 Generation of Reactive Oxygen Species (ROS)

The photocatalysis mechanism to produce reactive oxygen species (ROS) start from the generation of electron-hole pairs after irradiation (Eq.1.1).



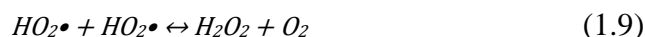
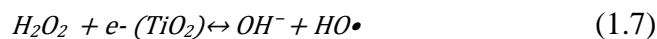
The generated valence band positive holes react with water molecules or hydroxyl group adsorbed on titanium dioxide particles generating hydroxyl groups (Eq.1.2 and Eq.1.3).



The electrons of the conduction band, with strong reducing potential, react with oxygen to produce superoxide radicals (1.4).



From this point, these free radicals may react with the pollutant molecules converting them into other compounds or may create other oxidative species (Eq.1.5-1.9).



The proposed photocatalytic reaction schemes for the generation of ROS were summarized in Figure 1.5.

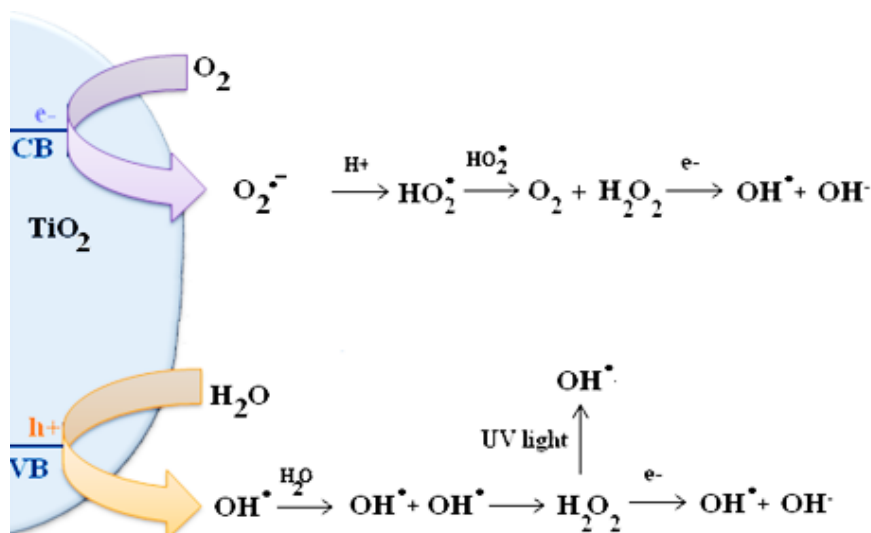


Figure 1. 5 TiO₂ photocatalytic reaction scheme for the generation of reactive oxygen species.

Most reports on photocatalytic systems focus on either the oxidation step (as in oxidative photocatalysis, OP) or, much less often, the reduction step (reductive photocatalysis, RP), although both are just one part of an overall two-part photocatalysed redox reaction.

Concerning OP reactions, it is generally assumed that the oxidation of chemical compounds occurs via indirect transition mechanism with the intervention of hydroxyl radicals (OH[•]) [13-15]. However, several recent studies have support the idea that oxidation may occur directly via the photogenerated holes [16, 17]. The hydroxyl radical is a very powerful oxidant with a redox potential of +2.80 V vs. SHE at pH 7, while the photo-generated valence band hole in TiO₂ anatase has a redox potential of +2.53 V vs. SHE at pH 7[12, 18]. Even though hole-oxidation and hydroxyl radical mediated reaction pathways are different process, both leaving to a distribution of photo-oxidation product very similar, making it difficult to distinguish between them.

Concerning RP on TiO₂ photocatalytic reaction, the reduction reactions are less studied than oxidative reactions by h⁺/OH•, except for the photoreduction of molecular oxygen to O₂•- [19, 20] because in some cases it is considered that this reductive process may determine the efficiency of the overall photocatalytic reactions [21]. In the case of direct reduction of other chemical compounds via the photogenerated electron has been studied individual cases such as the photo-reduction of water[22] and CO₂ with water[23]. The photo-generated conduction band electron in TiO₂ anatase has a redox potential of -0.52V vs. SHE at pH 7[12].

Information about both OP and RP is essential as not every reactant will necessarily be sensitive to all possible pathways, and not in all photocatalytic samples the same reaction mechanisms will be present.

1.3 TiO₂ photocatalysis in construction materials

Application of photocatalysis to construction materials began from the early 1990s[5]. In this field, the main properties related to the nature of photoactive TiO₂ catalyst:

- i. Self-cleaning effect and depollution effect due to redox reactions promoted by sunlight (or in general, weak UV light) on the photocatalyst surface [4];
- ii. Photo-induced hydrophilicity [24] of the catalyst surface, which may produce cooling and antifogging properties. Superhydrophilicity also enhances the self-cleaning effect (inorganics causing dirt and stains on surfaces can be easily removed due to rainwater soaking between the adsorbed substance and the TiO₂ surface).

The main reasons why TiO₂ is, so far, the most used photocatalyst for such applications are:

- i. Its brilliant white colour, hence very suitable to obtain white materials;
- ii. High photocatalytic efficiency;
- iii. TiO₂ is very cheap compared to another semiconductor photocatalysts;
- iv. Chemical stable and compatible with traditional construction materials[5].

The versatile functions of TiO₂ significantly promote its application in building envelope (paints, tiles, glass, plastics, and panels), interior furnishing (paints, tiles, wall paper, window blinds and finishing coatings), and road construction (paints, concrete pavements, soundproof walls, tunnel walls, road-blocks)[5].

1.3.1 Properties and applications of TiO₂ construction materials

1.3.1.1 Depollution Effect

TiO₂ photocatalytic process is considered as an efficient technique for photo-degradation of environmentally relevant outdoor and indoor air pollutants, derived from several sources such as industrial plants, heating systems, road traffic, cigarette smoke, household product [25, 26].

TiO₂ can decompose many kinds of air pollutants: volatile organic compounds (VOCs) such as benzene, aldehydes and toluene; and variety of inorganic compounds, such as NO_x (nitrogen oxides), SO_x and NH₃, at relative low concentrations. VOCs and NO_x are major causes of concern on outdoor air quality [27-29]. Indoor air pollutants mainly include also NO_x, VOCs and particulates. Indoor air presents high concentration of organic chemicals (most of which highly volatile) due to ordinary human activities. These chemical (alcohol, aldehydes aromatic compounds, etc.) are common ingredient in a wide series of household products such as detergent, perfums, and deodorants.

The presence of NO_x in the atmosphere has many damaging effects on human health and environment. In atmospheric chemistry NO_x refers to the sum of nitric oxide, NO, and nitrogen dioxide, NO₂. NO is considered a primary pollutant[30] because mainly introduced in the atmosphere directly from a source (high temperature combustions in transport and industrial activities). NO₂, is considered as a secondary pollutant because mainly formed in the atmosphere by interaction of a primary pollutant (NO) with O₂ (or O₃) and/or sunlight. Compared with all other technologies, TiO₂ as a photocatalyst provides the great advantage to decrease NO_x levels in the atmosphere since it only requires UV exposure, atmospheric oxygen and water[3, 31].

The depollution effect on photocatalytic building materials for NO_x and VOCs are illustrated on Figure 1.6

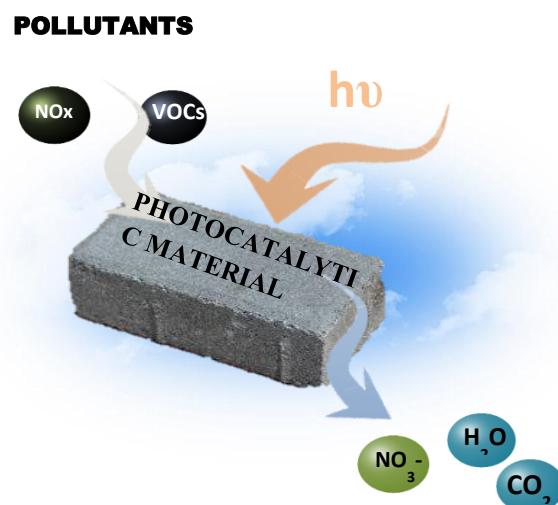


Figure 1. 6 Illustration of depollution effect on photocatalytic building materials.

1.3.1.2 Self-cleaning Effect

As previous mentioned, the simultaneity of superhydrophilicity and photocatalysis redox reaction is very important to obtain self-cleaning surface, which is a consequence of photocatalytic degradation of deposits accumulating on the surface and subsequent washing away of reaction products by water in contact with the hydroxylated surface layer[12] (see Figure 1.7).

In the built environment, it is a common phenomenon that the aesthetic and lustre of the surface of ordinary buildings are gradually lost in time due to aging of the material. The building surface could be soiled by greasy and sticky deposits, which results in a strong adherence of ambient dusts. As a result, dirt built up on the surface alters the visual appearance and the reflectance properties, which influences also heat gain on account of a higher heat absorption in darker materials. Without constant and proper maintenance, it is difficult to restore the buildings aesthetic properties[32].

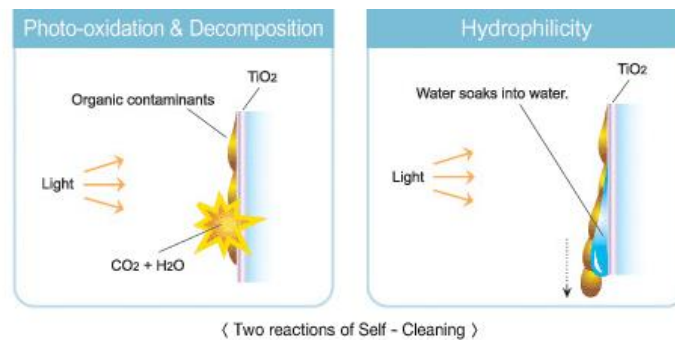


Figure 1. 7 Illustration of self-cleaning effect on photocatalytic building materials.

1.3.1.3 Self-disinfecting Effect

The photocatalytic properties of TiO₂ can also be used for destruction of wide spectrum of microorganisms including viruses, fungi, pollen and many species of bacteria which cause the triggering of undesired chemical and aesthetical changes, and control of the biological growth depositing on surfaces[33, 34]. The light induced bactericidal activity of TiO₂ is often referred to as photosterilization, and is an effective way to decrease bacteria counts to negligible levels. [35]. Our recent exploratory studies [36, 37] have shown that photocatalysis can also reduce the number of pollen particles in aqueous solutions and on mortars specimens. Furthermore, the amount of allergen proteins of *Cupressus arizonica* and *Platanus hybrid* decreases after photocatalytic treatment and enzymatic activity was completely inhibited [38] (Figure 1.8). Applying TiO₂ building materials to indoor furnishing, mainly in microbiologically sensitive environments, such as medical facilities and food industries, where biological contamination must be prevented, have been proved to be an effective way for sterilization[39]

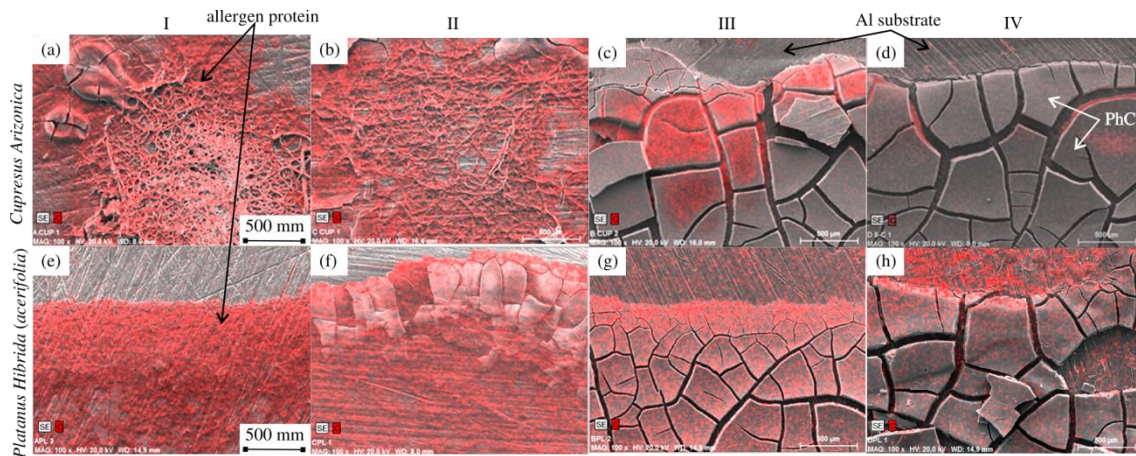


Figure 1. 8 Combined images of SEM (grey scale) and carbon mapping (red scale) measured by EDS for both pollen allergen extracts (PAE) and four different configuration (I PAE onto SEM support; II PAE + UV; PAE onto photocatalyst (dark conditions); PAE onto photocatalyst + UV).

1.3.1.4 Antifogging [40]

Antifogging surface can be related to the superhydrophilic effect. Fogging of the surfaces occurs when humid air condenses, with the formation of many small water droplets, which scatter light. On a superhydrophilic surface, no water droplets are formed. Instead, a uniform film of water can form on the surface, and this film does not scatter light. Since fogging only forms on surfaces with contact angles higher than 20° , photocatalytic antifogging materials the contact angle of the water will be changed down to nearly 0° during the irradiation. Anti-fogging glass is a typical anti-fogging photocatalytic construction material, and is usually used in mirrors in bathroom and driving mirrors of automobiles (Figure 1.9).

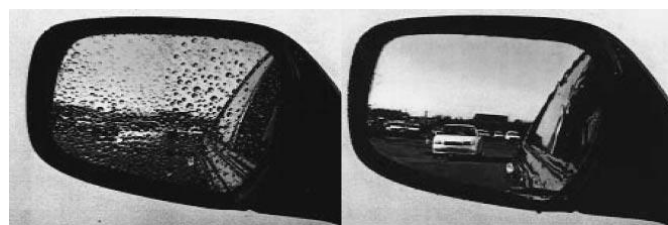


Figure 1. 9 Anti-fogging effect of automobile side-view mirror: conventional mirror (left) and TiO_2 -coated mirror (right)[40].

1.3.1.5 Cooling Effect [40]

Surface wettability of TiO_2 increase under UV exposure related to the decrease in water contact angle; thus TiO_2 as a superhydrophilic material that allows water to spread completely on the surface rather than forming droplets. This phenomenon could increase the amount of heat consumed as a consequence of liquid-vapour phase transition, thus dissipating heat coming from sunlight, and absorbed by the building. It was suggested that sprinkling water onto the surfaces of buildings [12] with a TiO_2 photocatalyst may be used as a novel building cooling method, with the intent to decrease the urban heat island problem for major cities, which occurs when built-up areas are warmer than the surrounding environment, and to reduce the electricity consumption by air conditioners in summer[40, 41] (Figure 1.10).

Under UV exposure, the surface of the photoactive material becomes highly hydrophilic, thus it minimizes the amount of sprinkling water required to form a water film. Continuously supplied small quantities of water, with a layer thickness of approximately 0.1 mm, can cover the whole building surface, and then while evaporates it subtracts heat from the surface. Thus, the building and surrounding can be cooled by the heat consumption that accompanies water evaporation. Moreover, natural rainwater can be collected and stored in specially designed reservoirs for this purpose so that the cost of the water can be reduced. The water film also helps in maintaining the building surface clean by the self-cleaning effect.

The cooling of the building surfaces is expected to result in the reduction of electricity consumption by 10% to several tens of percentage. Therefore, photocatalytic materials could contribute to the development of energy saving technologies.

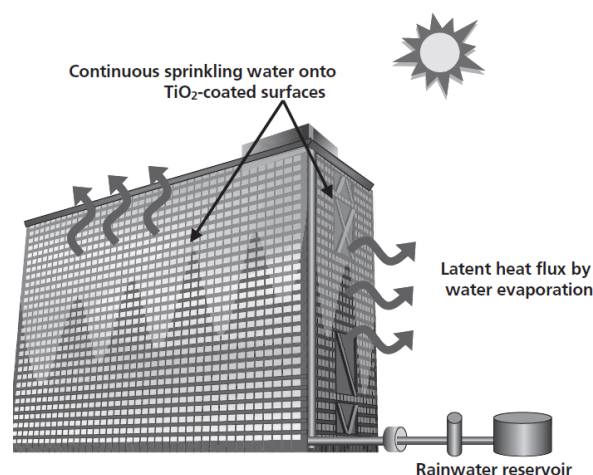


Figure 1. 10 Energy-saving system using solar light and stored rainwater[40].

1.3.2 TiO₂ photocatalytic cement-based materials

Cementitious materials (e.g. cement paste or mortar and concrete) has become the most widely TiO₂-modified material used in construction field due to:

- i. the nature of matrix represented by cement paste (e.g. strong binding properties and their porous structure in hardened state) is suitable for adding TiO₂ particles[17];
- ii. the wide usage of these materials in the traditional construction field.

In particular, for cementitious materials, the main properties related to the nature of photoactive TiO₂ catalyst are the self-cleaning capability and air purification potential.

For these reasons, attention of this chapter hereon will be main focused on cement-based materials containing TiO₂ and their use on the photocatalytic applications (self-cleaning and air purification).

There are two possible ways to attribute photocatalytic properties to cementitious building materials: TiO₂ can be added to the mixture proportion of cement-based materials or applied as a surface coating. Many works pay attention to the use of TiO₂ as a surface coating to exploit the whole quantity of TiO₂ employed, as only the surface layers can be activated by UV light[42]. If TiO₂ is added in mass in the mix proportion of concrete, only the small percentage of it contained in the outer layers exposed to the external environment will exert photoactivity, and this approach ends up in wasting potentially active material. Although the best photo-efficiency and the highest exploitation of the photoactive admixture are exhibited by a mortar containing TiO₂ as surface covering [43], there are severe durability problems on the surface layer, in particular the removal of the photoactive component due to wind (erosion), rain (leakage) and in general all environmental agents. On the other hand, bulk admixtures exhibit greatest stability, since erosive phenomena only have the effect of exposing fresh photocatalyst surface. TiO₂ addition to finishing layers of mortar or plaster can be a good compromise to avoid durability problems on surface coatings and excessive usage of photoactive material in bulk admixtures[44].

The applications of these materials concern horizontal and vertical structures such as:

- i. Ready-mix materials: wall, columns, beams and pavements.
- ii. Precast materials: panel, columns, road barriers, sound-adsorbing panels, paving block, slabs, tiles, GFRC (Glass Fiber Reinforced Cement).
- iii. Pre-mix coatings: paints (thickness 0.3-0.4 mm), skim coat and fine coatings (1-3 mm), and renderings (8-15 mm).

1.3.3 Research development and practical applications of photocatalytic cement based materials: self-cleaning and air purification applications

Several research studies have confirmed the self-cleaning and air remediation effectiveness of photocatalytic cement based materials.

Nitrogen oxides (NO_x) and volatile organic compounds (VOCs) have been chosen by most studies as representative airborne pollutants due to their potential health risks and ability to generate photochemical smog. The NO removal paving blocks made by waste materials and TiO₂ were evaluated by [5]. They found that an optimum mix design which incorporated recycled glass, sand, cement and 10 % TiO₂ achieved 4.01 mg h⁻¹ m⁻² NO removal.

Strini et al.[45] carried out photo-degradation of selected VOCs (benzene, toluene, ethylbenzene and o-xylene, i.e. BTEX) in gas phase at ppb concentrations on the surface of photocatalytic cementitious materials. They observed that the photocatalytic activity of pure TiO₂ sample was three to ten times greater than the cementitious sample that was prepared with the incorporation of 3% catalyst. The decomposition rate of BTEX was linearly dependent on the concentration of the reactant and the intensity of the irradiation. However, the catalytic activity was not linearly dependent on the TiO₂ content in the samples probably because the formation of highly agglomerated catalyst clusters in the cementitious paste was influenced by the different viscosities of the paste.

Chen et al. (2011) [46] evaluated colour changes of rhodamine B dye on various mortar mixtures with TiO₂ added to the cement matrix using the CIE L*a*b* system with a spectrometer. The dye faded at a rate that was independent of the content of TiO₂, indicating that the photocatalytic material was effective in discoloring the dye under UV irradiation through its self-cleaning ability. Diamanti et al. (2008) [44] measured colour changes of fiber-reinforced mortars with varying amounts of anatase in both powder and suspension forms. The samples, which were white at the beginning of the test, were monitored using a spectrophotometer. A change in colour occurred for almost all samples that were exposed outside. A yellowing effect was exhibited by samples with higher photocatalytic activity.

Our group evaluated the effect of addition of photocatalyst on the characteristics of TiO₂ modified mortars and the influence of type of binder, surface roughness and microstructure, on their photoactivity for self-cleaning of organic dyes (rhodamine B and methylene blue) and NO_x degradation. Mortars with four different types of cements and three levels of roughness were prepared. From the results, it was found that the available active surface is a parameter more influential than surface roughness for assessing photocatalytic efficiency. Concerning the composition of the mixes, the classification according to photocatalytic efficiency was the same for both NO_x and self-cleaning, being, in decreasing order: Portland cement (quite similar to calcium aluminate cement for NO_x), fly ash and slag mortars. The difference has been explained on the basis of

oxidation-reduction potentials and photoabsorption energy of the different constituents of cementitious matrix[17].

The series of laboratory tests presented above served as a scientific basis to support a number of real world applications and pilot tests executed throughout Europe over the past ten years.

In this sense, the European Project PICADA project (Photocatalytic Innovative Coverings Applications for De-pollution assessment, Figure 1. 1111) is indeed a pioneer example, which is intended to verify the benefits provided by the use of TiO_2 -based photocatalytic cementitious materials in a car park and photocatalytic vertical walls in a simulated street canyon. The self-cleaning effect has been proved by degradation of Rhodamine B, a red organic dye, by colorimetric measurements. The experimental results showed that the samples recovered about 65% of their initial coloration in less than a day of exposure to artificial sunlight [47]. Experimental evidence also showed that abatement of hazardous gas pollutants like NO_x (in climatic conditions typical of South of Europe) can reach and, in some optimal conditions of light exposure, wind circulation, initial pollutants concentration depending on traffic conditions, etc., breakthrough the threshold of 60%.

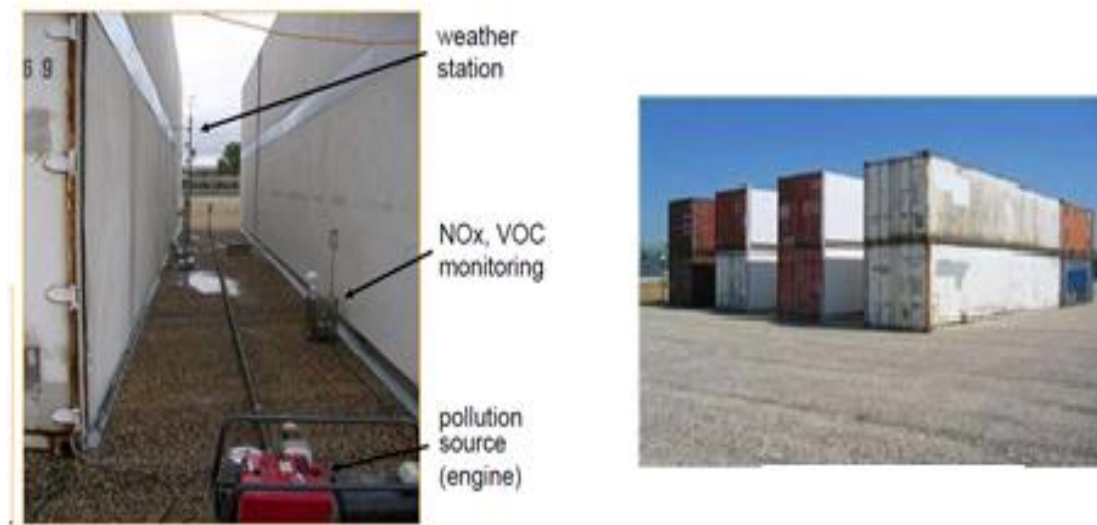


Figure 1. 11 PICADA project, Guerville, France (www.picada-project.com).

In recent years, various LIFE project related with the application of photocatalytic on construction materials has been performed in Madrid (Spain).

- i. Life Minox-street (2013): monitoring and modelling NO_x removal efficiency of photocatalytic materials.
- ii. Life-Equinox (2013): Application in asphalt pavements for removing nitrogen oxides

iii. Life-Photoscaling (2014): Sustainability of photocatalytic technologies on urban pavements: From laboratory tests to in field compliance criteria-

This last project, whose coordinator from CSIC is our research group, aimed to demonstrate the validity of photocatalytic technology in urban agglomerations by establishing instruments enabling scaling-up from laboratory measurements to application in cities, by developing a decision-support tool and by assessing the sustainability of different solutions in different environments to encourage the widespread use of this technology. To do this, two demonstration platforms (same materials, different emplacements) on an intermediate pilot plant technical scale with different photocatalytic materials' types were performed (emulsion coating, cementitious slurries, hardened cement-based samples and ceramic tiles) (Figure 1.12)

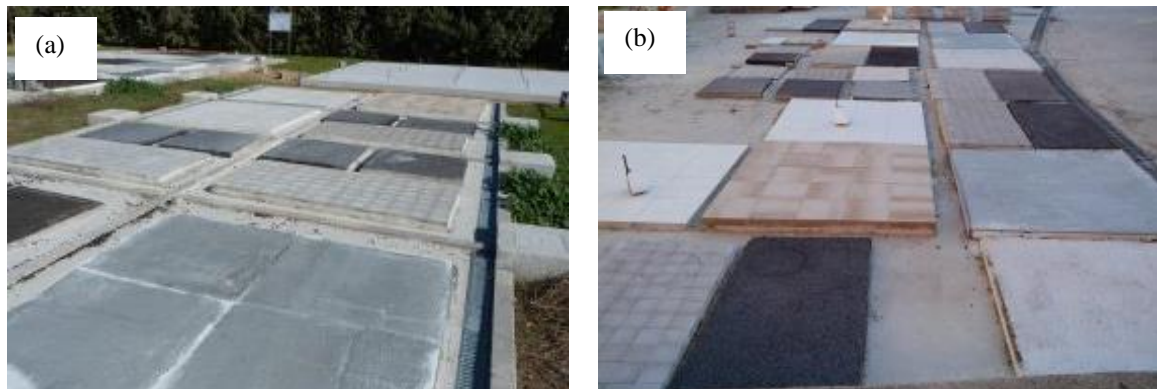


Figure 1. 12 Images of two platforms from Life –Photoscaling project (a) Centro de Automática y Robótica CSIC-UPM, Campo Real way, Km 0,2, 28500 Arganda del Rey(Madrid) and (b) Intitute Eduardo Torroja, CSIC. Serrano Galvache street, 4, 28033 (Madrid)

Other projects in real-life applications have been, for example, In Bergamo, Italy, a street in the city centre was re-paved by the photocatalytic concrete paving blocks (total area of about 12000 m²). NO_x concentration was measured by chemiluminescence analysers simultaneously on two sites: the area where photocatalytic blocks were present and the extension of the road paved with normal bituminous concrete used as a reference. The air monitoring campaign showed an average NO_x abatement of 45% in day time (from 9 am to 5 pm) [48]. In Antwerp, Belgium, 10000 m² photocatalytic pavement blocks have been used to execute a new parking lane. Measurements on the site indicated a 20% drop of NO_x concentration due to the presence of the photocatalytic materials[49]. For instance, the implementation of ordinary TiO₂ in concrete over a total area of about 7000 m² of the roads in Milan, ITALY, contributed to a reduction by 60 % the NO_x concentration in the air in one single year [50]. In Madrid, Spain, different pavement area has been modified with various photocatalytic materials' types (Figure 1.13).



Figure 1. 13 (a) Photocatalytic sprays on sidewalk tiles, (b) draining bituminous pavements percolated with photocatalytic slurry, (c) photocatalytic tiles to pavement sidewalks, and (d) photocatalytic tiles to pavement roadways.

Laboratory results about self-cleaning effect of photocatalytic cementitious surfaces have been also proved to be achieved in real world applications. In the church Dives in Misericordia in Rome, over a total monitoring period of six years, only a lightly difference between the external and internal values of the lightness was observed. The art city hall in Chambéry (France), which the primary colour almost remained constant for approximately 5 years in different positions of the facade (West/ North/East/South) [51]. As an example of building in Spain where photocatalytic building materials have been used, we can highlight the Riberas de Loiola church in Donostia-San Sebastián, whose façade is covered with this type of material Figure 1.14.

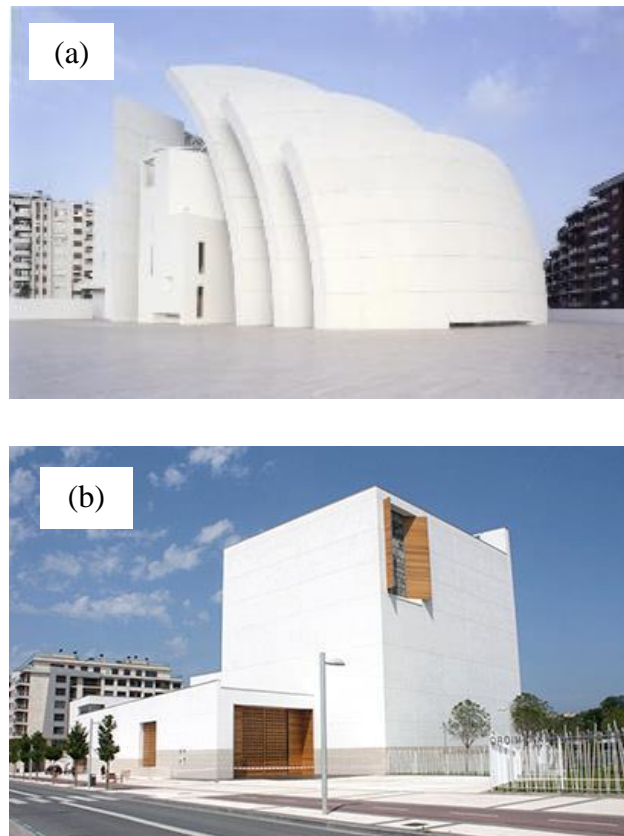


Figure 1. 14 Image of prestige construction made with photocatalytic cement (a) church Dives in Misericordia and (b) church Riberas de Loiola (<http://www.fym.es>)

1.3.4 Problems and limitations in real-life applications of photocatalytic construction materials

Although the self-cleaning and depollution effects of photocatalytic construction materials are evident, there are still three main unresolved obstructions when these materials are used in real-life applications.

- i. Although the prices can vary in a more or less wide range according to market price and formulation of the material, today, the low economic profitability of the TiO_2 based photocatalytic materials is the main limitation for their extensive use. However, this cost evaluation is still very difficult to determine because it should take into consideration many parameters such as the manufacture, application and maintenance costs in the long term. Not forgetting that the advantages of the application of these materials such as improving environmental conditions cannot be qualified in economic terms.

- ii. The photocatalyst is able to degrade only pollutants which are absorbed on their surface. In widely open spaces, the pollutant removal efficiency may be low as only a small fraction of the pollutants can be trapped. For this reason the applicability of photocatalytic construction materials in outdoor environments is restricted to confined spaces and street canyons where, due to low pollutants dispersion and poor ventilation, the degradation of hazardous substances is significant[52].
- iii. Problem and limitation of current standard for evaluation of photocatalytic activity (*more detail on section 1.4.5 Problem and limitation of current standard*).

Other limitations can derive from the nature of the cementitious materials:

- i. The conventional properties of cement-based materials would be changed by the addition of TiO_2 . For example, the strength, sensitivity and ageing process of TiO_2 -containing mortar might be directly affected by TiO_2 additives [17, 53-57]. In some cases contradictory results, mainly regarding influence in porosity and resulting mechanical strength. However it is important to note that this effect depend of the characteristics of photocatalyst addition (e.g. amount, microstructure, mixed procedure).
- ii. Additionally, the use of organic admixture for concrete and other cementitious materials must be minimized to avoid possible reduction of the photocatalytic activity. Rachel et al. showed that the presence of ionic species, which could contribute to charge recombination in the activated photocatalyst, are the reasons for the catalytic activity loss[58]. In a study of our research group has been prove that the photocatalytic performance depend of the cementitious matrix composition, and the reason has been explained on the basis of oxidation-reduction potentials and photoabsorption energy of these different constituents[17].
- iii. Moreover, photocatalytic activity may be lost by physicochemical change in the cement surface followed by carbonation[53]. The photocatalytic effect may also be limited due to the physical anchoring of the dirt in large pores of cement-based materials. TiO_2 deactivation may be caused by deposition of surface species, intermediates, by-products or pollutants which are difficult to decompose[59]. It has been reported that the accumulation of contaminants on nano- TiO_2 coated paving blocks in Hong Kong caused significant inactivation after 4 months [5]. This could imply that periodic servicing and washing the surfaces might be necessary to maintain the air pollution remediation properties.

1.4 Standards method for evaluation of photocatalytic activity

National and international organizations have developed different standards to assess the photo-activity of photocatalytic materials. Japan and Italy are currently the most active national publishers of standards. The European committee, CEN TC 386-Photocatalysis and the International Standards Organization (ISO) are the worldwide biggest publishers of standards. Table 1.2 shows an overview of the different international and national standards published. The standards try to cover the applications mentioned in *Section 1.3.1*.

The following sections (1.4.1 -1.4.5) includes a short description of the most important standards applied to photocatalytic construction materials to assess the purification and self-cleaning properties, that as previously mentioned are the most common applications on these materials.

Table 1. 2 Overview of International, European and National standard related with photocatalysis process.

Application defined in section 1.4.1	Principles of test method	National standard	European standard	International standard
Air purification	Nitric oxide removal	JIS R 1701-1:2010		
		UNI 11247:2010		
		UNI 11848:2013		
		XP B 44-011: 2009		
		UNE-ISO 22197-1:2012		ISO 22197-1:2007
		BS-ISO 22197-1:2011		
		CEN/TS 16980-1:2016		
		UNE 12197-1:2013		
	VOC removal	UNI 11238-1:2007		
		UNI 11238-2:2007		
		XP B 44-013		
	Acetaldehyde removal	JIS R 1701-2:2008		ISO 22197-2:2011
Toluene removal	JIS R 1701-3:2007		ISO 22197-3:2011	
Formaldehyde removal	JIS R 1701-4:2008		ISO22197-4: 2013	
Metyl mercaptane	JIS R 1701-5:2008			
Self-cleaning	Water contact angle change	JIS R 1703-1:2007		ISO 27448:2009
	Methylene blue decomposition	JIS R 1703-2:2007		ISO10678:2010
	Rhodamine b degradation	UNI11259:2008		
Disinfecting effect	Antibacterial activity	JIS R 10702:2006		ISO27447:2009
	Antifungal activity	JIS R 1705:2008		
-	Light source for test under UV irradiation	JIS R 1709:2007		

1.4.1 ISO 22197 - Test methods for air-purification performance of semiconductor photocatalytic materials

Three methods for photocatalytic air purification have been published. They differ mainly in the pollutant, whose removal is studied: nitric oxide (ISO 22197-1: 2007), acetaldehyde (ISO 22197-2: 2011), toluene (ISO 22197-3: 2011) and formaldehyde (ISO 22197-4: 2013).

All the three air-purification test methods have the same equipment system that shown in Figure 1.15. The illumination source is the UVA light which is applied on a sample ($50 \times 100 \times 5$ mm) in a quartz or borosilicate glass. The pollutant is in the mixture with air. The inlet and outlet gas streams are regularly analysed to evaluate any change. The material of reactor must be inert to UV light and pollutant. Stainless steel is the most suitable material to be used. At the beginning the test gas flows into the photo-reactor without any illumination (ca. 30 min before turning on the light). After starting the experiment (detected by turning on the light), the pollutant concentration in time is detected. Every air-purification standard differs in the concentration of test pollutant, overall gas stream flow rate, sample run test time and system for analysis[60].

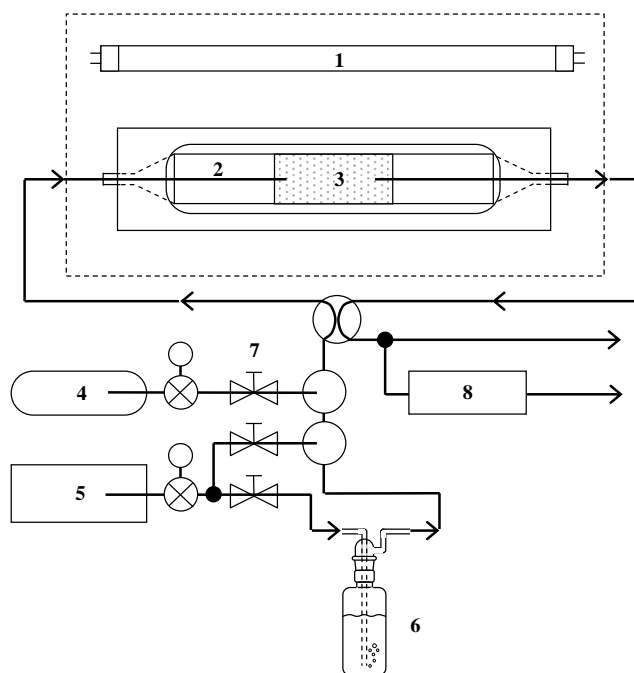


Figure 1. 15 Schematic illustration of the test equipment for the air purification ISO standards. (1) UV light, (2) glass cover, (3) tested sample, (4) standard gas – test pollutants, (5) air source, (6) humidifier, (7) mass flow controllers, (8) pollutant gas analyzer [60].

1.4.2 JIS 1703-2:2007 Methylene blue decomposition

This method represents a simple evaluation for new photocatalytic materials. It is based on assessment of photocatalytic bleaching rate of an indicator ink – Methylene Blue (MB).

The photoreaction system for standard measurement is illustrated in Figure 1.16, and contains a sample (typically 10 cm plate) with photocatalytic layer and the cylinder fixed on the sample (3-4.7 cm diameter). The sample must be exposed to UVA light before starting the standard assessment. At “conditioning step”, 35 ml of MB solution ($2 \cdot 10^{-5}$ M) is poured into the created vessel and left for 12 hours in the dark. After that, the concentration of MB in the solution must be higher than 10^{-5} M. If not, the conditioning step must be done again until it meets the requirements. Then another 35 ml of MB solution is placed into the vessel and the UV transparent glass cover is put over it. After that the irradiation of the system by UVA light ($1 \text{ mW} \cdot \text{cm}^{-2}$) begins and the solution is stirred every 20 min. The change of absorbance as a function of time is measured by spectrophotometer directly or by sampling (absorbance detection at 665 nm). The irradiation process lasts 3 hours or less – in the case of faster decolorizing of the MB solution. The reaction temperature is recommended to be 23 ± 2 °C. The blank experiment in the dark conditions is performed as well. Then the photonic efficiency of the active sample is calculated according to following equation (Eq. 1.9):

$$\xi_{MB} = \frac{100 \times r(MB^+)}{I_{UV}} \quad (\text{Eq. 1.9})$$

Where $r(MB^+)$ represents the rate of MB bleaching ($\text{molecules} \cdot \text{cm}^{-2} / \text{s}$), I_{UV} is irradiance ($\text{number of photons} \cdot \text{cm}^{-2} \cdot \text{s}^{-1}$).

If the photonic efficiency is bigger than 0.1%, the experiment should be done once again with the irradiance source $0.25 \text{ mW} \cdot \text{cm}^{-2}$. The benefit of using this method is surely its simple and easy performance. The standard is given for low photoactivity samples $\xi < 0.1\%$. Higher photonic efficiency is not suitable for the evaluation according to this standard, and is probably caused by mass transfer effects which are not assumed in this method. It is suggested that MB would be more suitable for water purification standards rather than for photocatalytic evaluation of self-cleaning films[60, 61].

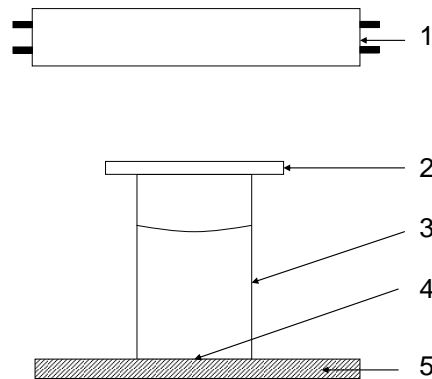


Figure 1. 16 Schematic illustration of the set up using for the methylene blue standard. (1) UV light source, (2) glass cover, (3) testing cylinder, (4) testing area and (5) sample under test.[60]

1.4.3 UNI 11259:2008 – Photocatalytic activity determination of hydraulic binder -Rhodamine method

The method consists of measuring the self-cleaning capacity of hydraulic binders with clear cement base through a colorimetric method: the color evolution, with a colorimeter, is evaluated with the passage of time (4 and 26 hours) of samples of cement mortar whose surface has been treated with rhodamine B (RhB). The dye is deposited on the surface of the samples in a known concentration. The test allows evaluate if, through the discoloration of the rhodamine, the cement sample can be considered photocatalytic. The material tested is considered photocatalytic with respect to rhodamine if the percentages of color decrease are greater than 20% and 50% at 4 and 26 hours respectively. The color evaluation was monitored using a spectrophotometer via CIEL*a*b* color analysis of the coordinate a* due to the red colour of RhB.

The experimental setup consists of the sample and the UV lamp, and the test is carried out at $20^{\circ} \pm 2^{\circ}\text{C}$; H.R. $70 \pm 10\%$. Before proceeding with the test, the specimen is placed in a dark environment (at $20^{\circ}\pm 1^{\circ}\text{C}$ and RH $60 \pm 10\%$) for at least 24 h, the first measurement of the parameter a (0h), just before exposure of the probe to the lamp. Measurements are then taken after 4 and 26 hours of exposure.

It is important to note that is the only one method designed to apply on hydraulic binder samples, such as cement-based materials. However, as requires the accurate measurement of the colour of the indicator film, it is only appropriate for clear samples.

1.4.4 ISO 27448:2009: Test methods for self-cleaning performance of semiconductor photocatalytic materials – measurement of water contact angle

This method is known as the one based on photoinduced superhydrophilic effect. It uses an oleic acid and determines its degradation by changing of water droplet contact angle during illumination (the wettability is increased). The contact angle is measured until it reaches the value of 5° – then the test is suggested to be finished [60].

Firstly, each sample (10 cm^2) is pre-treated by UV illumination. Secondly, the oleic acid is placed on the sample – either manually or by dipping. When the manual way is chosen, the sample must be weighted and the $200 \text{ }\mu\text{l}$ of organic compound is placed in the centre of the sample so the created surface is homogenous (usually done by non-woven cloth). The weight of oleic acid on the sample should be $2 \pm 2 \text{ mg}$. In the case of dipping, the sample is placed in the solution of oleic acid and then pulled out at the rate 60 cm/min . Finally, the sample is dried at $70 \text{ }^\circ\text{C}$ for 15 min . No specification about the mass of oleic acid on the sample is given. Next step is the contact angle measurement – each sample is tested at 5 different places before and during UV irradiation (for manual coated samples: 2 mW/cm^2 , for dipped ones 1 mW/cm^2). It is recommended to carry out the experiment 5 times with 5 samples prepared in the same way. According to the ISO standard, the initial and final values of contact angle should be recorded as well as the irradiation time [60].

Contact angle is defined as the angle between the surface plane and the tangent of the drop. The contact angle measurement provides a good way in prediction how the material is going to behave when deposited on the support. As seen in the Figure 1.17, it is not only the property of adsorbed material, support material and surrounding environment are important as well. All these 3 parameters, each characterized by the value of surface tension, decide whether the adsorbent is spreading over the surface or not.

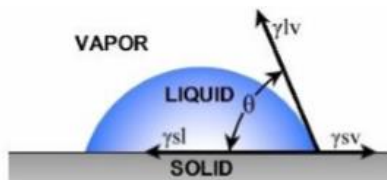


Figure 1. 17 Three different surface tensions effecting the drop shape [62].

If consider a drop on the solid surface, Young's equation describes the effect of the forces acting on the drop – by the relation between surface tensions and the contact angle (Eq.1.10).

$$Y_{SV} = Y_{SL} + Y_{LV} \times \cos\theta \quad (1.10)$$

The value of contact angle indicates whether the liquid drop is spreading on the support or not. If the contact angle is greater than 90° , the surface is non-wetting. In opposite case – the contact angle is smaller than 90° , the liquid is spreading on the surface meaning the surface is wetting. The smaller the angle, the better the wetting ability. If the contact angle is close to zero (complete wetting) the surface is called *superhydrophilic*.

The Young's equation considers the surface to be an ideal plane without any roughness. Actually this kind of surface is hard to find. We can often observe two different contact angles values for the same system. This phenomenon is characterized by the term “hysteresis”. Then it is possible to distinguish between the apparent contact angle and the true one. The relation between them depends on the value of surface roughness[62, 63] (Eq. 1.11).

$$\cos\theta = R_{rough} \cos\theta_{true} \quad (1.11)$$

The surface roughness is the ratio between actual surface area and the apparent surface area and is equal (ideal case) or greater than 1. In the case of wetting surfaces, the apparent contact angle is smaller than the true one[62, 63].

1.4.5 Problems and limitations of current standards

In spite of successful application of TiO_2 photocatalysis in construction materials, an ideal method to determinate the photocatalytic activity is still not available. The current ISO and planned CEN tests have three crucial drawbacks[60]:

- i. are not rapid;
- ii. require relatively expensive equipment, that in most cases, it require a reasonable degree of technical support for operation and maintenance;
- iii. are not suited for use in situ.

Furthermore, the fact that the pre-conditioning protocols and experimental conditions stated in the published standards differs in many aspects makes it very difficult to compare experimental results [64, 65] and to be able to predict the behaviour of a system in real conditions. It has been experimentally verified that the experimental conditions influence the resulting photocatalytic activity [65]. In addition to this, the diversity in methods for data analysis and expression of the test results increment these difficulties. The further Tables 1.3, 1.4 and 1.5 illustrating examples of the large differences which exist in the pre-conditioning protocol, experimental conditions and data analysis of published standards.

Table 1.3 General sample pre-conditioning step conditions of various standards

Principles of test method	Standard	Pretreatment	Duration (hours)
Methylene blue decomposition	JIS R1703-2:2007	Washed with purified water, and dry in the test chamber at $> 1 \text{ mW cm}^{-2}$	≥ 24
	ISO 10678:2010		
RhB discolouration	UNI 11259: 2008	dark conditions, $20^{\circ}\pm 1$, RH 60 ± 10	≥ 24
Nitric oxide removal	ISO 22197-1:2007	$\geq 1 \text{ mW cm}^{-2}$ and immerse the test piece in deionized water, remove it, and air-dry at room temperature	≥ 5 (UVA) and ≥ 2 (water)
	UNE-ISO 22197-1:2012		
Acetaldehyde removal	JIS R1703-2:2008	$\geq 1.5 \text{ mW cm}^{-2}$	16-24
	ISO 22197-2:2011		
Toluene removal	JIS R1703-3:2007	$\geq 1.5 \text{ mW cm}^{-2}$	16-24
	ISO 22197-3:2011		
Water contact angle change	JIS R 1703-1:2007	2 mW cm^{-2}	24
	ISO 27448:2009		
Antibacterial activity	JIS R 10702:2006	none	none
	ISO 27447:2009		

Table 1.4 Air purification ISO standard test conditions*.

Parameter	Nitric Oxide	Acetaldehyde	Toluene
Concentration, [X]/ppmv	1.0	5.0	1.0
Flow rate, $f/(\text{dm}^3 \text{ min}^{-1})$	3.0	1.0	0.5
Test time, t / h	5	3	3
Total pollutant load / mmol	40.2	40.2	4.02
Analytical method	Chemiluminescence: NO, NO ₂	Acetaldehyde: GC-FID	Toluene: GC-FID
	Ion chromatography: NO ₃ ⁻	CO ₂ : IR	

* Common standard conditions include: (1) photoreactor; (2) irradiance (1.0 mW cm^{-2}); (3) light source: BL or BLB; (4) temperature: 25°C and (5) relative humidity: 50%

Table 1. 5 Comparative between NO_x air purification standards: ISO 22197-1:2007 and UNI 11247:2010.

Standardization body/publication	ISO	UNI
Standard	22197-1:2007	11247: 2010
Irradiance source	Fluorescence light BL or BLB; Xenon with filter letting pass (300-400 nm)	Hg vapour $\lambda < 400$ nm: $\lambda < 350$ less than 10%
Irradiance intensity (w/m ²)	10	20
Temperature (°c)	25	27
Relative humidity (%)	50	0
Ga flow (l/min)	3	1,5
Initial concentration NO (PPM)	1	0
Initial concentration NO ₂ (PPM)	0	0,15
Flow regime	Laminar	mixed
Size sample (cm ²)	49	64
Pretreatment	≥ 1 mW/cm ² (5 hours) and immerse the test piece in deionised water , remove it(2 hours), and air-dry at room temperature	3 days at 25±5°C and 60±10 % RH

On the other hand, the standard methods are designed to get a result of photocatalytic activity related to a specific contaminant. Only *ISO 27448:2009 – measurement of water contact angle* is designed to get a result regardless of a specific contaminant [64], although currently its reaction mechanism is still controversial [66, 67]. The problem stems from the assumption, that photocatalytic materials have the same degradation performance for all contaminants. Different studies show that a particular test method may favor one material and disadvantage another [65, 68]. Even, some studies indicated that it is advisable to make several different tests to assess the photoactivity of a material [69], however as previously mentioned as a drawback (ii), the standards require relatively expensive equipment and technical support. Besides this, it is important to note that the standard methods are focused solely on the oxidative process and none considered the reductive photocatalysis.

In the case of cementitious test pieces, that has become the most widely TiO₂-modified material used in the construction field, as previously explained in section 1.3.2, the current standards may not always be feasible for its use due to not considering some properties of cementitious materials that make it special, mainly their alkalinity and porous structure, thereby making that the test conditions are not appropriate for the evaluation of these materials. For example, all four ISO air purification tests described above (ISO-22197:1-4) are not good for assessing the activities of porous materials due to high flow rates [70]. For the *Acetaldehyde test system: ISO 22197-2*, the standard notes that ‘the measurement of CO₂ may not always be feasible for cement-based test pieces due to a high ability to

adsorb and react with any CO₂ generated, as might be expected for alkaline samples; In the case of *ISO 27448:2009 – measurement of water contact angle*, due to measurement characteristics, this method cannot be used for evaluation of rough surfaces, porous surfaces or highly hydrophobic materials[71].

As special case, the *Rhodamine method - UNI 11259:2008* (section 1.4.3) is the only method specified designed to measure the photocatalytic activity of cement based materials (“hydraulic binders”). However, in this case, the big disadvantage is the unequal distribution of dye film [11] and even in some cases, due to the colour of the sample; the colorimetric test is not feasible. Beside this, the colour evolution is slow (test time 26h) and little visual due to during the irradiation only decrease the intensity of colour. The higher limitation of this method is the dye-photosensitization under visible light that may results on higher degradation rate, which is not related with the photocatalytic activity of the materials[72].

1.5 Methods for evaluation of photocatalytic activity based on the detection of photo-generated charge carriers and reactive oxygen species (ROS)

Considering the previous described limitations of current standards, recently, several other techniques have been proposed to evaluate the effectiveness of photocatalytic properties of semiconductor; even some are more often used than the conventional standards as they are easier and faster. Some of them, with a quantitative approach are based on the measurement of active species generated during the photocatalytic process (charge carriers and ROS). This new concept of measure, provides information additional for understand the photocatalytic mechanism, which make it more attractive for testing such materials.

However, these species presents some characteristics that make its direct detection difficult, such as a very short lifetime (e.g. 10^{-10} s for OH•)[73] and high reactivity. As a result, a wide variety of indirect methods through the use of spectroscopic probes has been proposed. Some important aspects to consider when selecting an analytical method to determine ROS include: (i) sensitivity; (ii) selectivity and specificity towards the analyte of interest; (iii) measurements with sufficient fast time resolution; and (iv) stability of the probe and its reaction products. Other considerations that must be taken into account are related to the availability, robustness and cost of instrumentation and probe molecules. Moreover, the choice of operating conditions is essential to avoid the reaction of ROS with themselves or prevent further reaction of the product.

The main techniques used with this purpose are indirect spectroscopic probes methods that can be summarized in the following categories: (i) Electron Spin Resonance (ESR), where the spin-trap agent reacts with the unpaired electron of the free radical; (ii) UV/Vis

absorption spectroscopy, based on either the absorbance loss of the probe or the increasing absorbance of the product; (iii) chemiluminescence, based on the reaction of a chemiluminogenic probe with active species to yield a chemiluminescent product that irradiates light without being externally excited (iv) fluorescence, where the reaction between the probe and the active specie leads to the formation of products showing strong fluorescence when they are excited at a specific wavelength;(v) electrochemical analysis based on cyclic voltammetry (CV), chronoamperometry (CA) and electrochemical detection (ED).

There are some papers gathering information about the main probes used with the aim to qualitatively/quantitatively determine the presence of ROS. Bartdoz et. al [80] discussed the properties of the spectroscopic probes most commonly used for ROS detection in cellular systems, highlighting their limitations. Among spectroscopic techniques, the use of fluorescence methodologies to detect ROS generated in biological and physiological media have been reviewed by Gomes et al.[74] and Soh [75]. On the other hand, Lu et al.[76] evaluated the current state and the limitations of different chemiluminescence systems used in the identification of ROS in biological systems, pointing out the necessity of future research to find specific chemiluminescent probes for ROS quantification. It can be noticed that the above mentioned works are focused on the analysis of ROS mainly in biological media which is quite different from photocatalytic systems. For instance, Murphy et al. [77] has published a general overview about ESR characterization of solid surface, in which TiO_2 has been included from the viewpoint of the physical characterization of nanoparticles. Fernandez-Castro et al. [78] provides an overview of the determination methods of ROS in the application of advanced oxidation process (AOPS) that includes the category "photocatalytic systems". Wang et al. [79] performed a mini review of the main detection of active species, including charge carries and reactive oxygen species, by ESR during photocatalytic events. It is important to note that the most of works have been applied with the purpose of study of the determination methods of ROS, and less frequently of charge carriers.

With the aim to facilitate the comprehension of the potential of each technology for the qualitative/quantitative determination of the active species, a division into sections depending on the technique categories has been made. Tables 1.6, with the selected most critical developments and scientifically interesting spectroscopies techniques for the determination of active species in TiO_2 photocatalysis, were included with the following information: compounds used as probe; the analytical features that include the analytical techniques used for active specie determination with specification of the measured product, analysis pH if a specific value is required; and finally, the analysis of the strengths and weaknesses of reported methods, which also includes the influence of interferences.

1.5.1 Electron Paramagnetic Resonance (EPR) or Electron Spin Resonance (ESR)

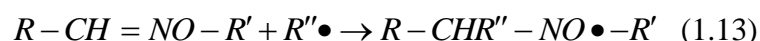
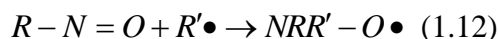
EPR is the only spectroscopy technique that specifically and directly "saw" the unseen spins[80] and therefore allows the detection of the presence of any system paramagnetic (ions, free radicals, free electrons, etc.).

This technique consists in subjecting a paramagnetic material to electromagnetic radiation. This radiation causes an excitation in the electrons, which absorbs this radiation, making its momentum align in the direction of the field. This allows the electron to pass from one spin to another, from $+1/2$ to $-1/2$, or *viceversa*. The transition from one spin to another is the basic concept of EPR. If the electron changes its spin, it is due to the absorption or emission of energy. This energy is quantified and monitored which allows determining the amount of species ROS or unpaired electrons that are the material to be analyzed.

Despite the interesting possibilities of this technique, as discussed above, these species (ROS and charge carriers) are generally unstable species, which practically prevents their direct measurements. This limitation is produced especially in aqueous solutions and at room temperature[80].

The most extensively known method to compensate this problem is the introduction into the system under investigation a specific compound (scavenging or trapping agents) that reacts with the radicals forming a more stable compound (spin-adducts), which then can be detected by EPR. EPR spin-trapping is capable of overcoming most of these limitations and currently represents the most efficient technique for detection of various radical species (e.g. EPR detection of the superoxide radical with DEPMPO is 40 times more sensitive than spectrophotometric analysis with cytochrome c [81]).

The most commonly used spin trap compounds are those having the bonds: C = C, C = N, N = N, C = O or N = O. However, due to the importance of providing directly or indirectly information about the nature of the trapped radical, R•, the vast majority of spin traps are based on two structures: Nitro compounds (Eq.13) and nitrones (Eq.14). Both types of compounds have as a common characteristic that the addition reaction with a radical leads to the formation of a nitroxide radical.



A wide variety of spin-traps are now available which can simultaneously trap different free radicals and trace them to their origin. DMPO (Table 1.6) is, perhaps, the spin trap and one of the probes most used for the quantitative determination of the $\bullet\text{OH}$ generated in different photocatalytic system [82, 83]. Although high sensitivity was observed using DMPO as molecular probe, its non-selectivity is an important drawback that has to be considered because DMPO may react with $\text{O}_2^{\bullet-}$, $^1\text{O}_2$ and $\text{ROO}\bullet$. Therefore, it is difficult to distinguish between hydroxyl radicals and superoxide if they are generated simultaneously in one system. An addition of the quenching effect of superoxide dismutase (SOD) on superoxide or that of DMSO on hydroxyl radicals can provide additional confirmation to distinguish between these free radicals[84]

In addition, Hirakawa et al. [13] argued that $\text{OH}\bullet$ spin trapping by DMPO in TiO_2 irradiated system was not reliable since DMPO agent can simultaneously react with both trapped holes. Some investigations are devoted to the ESR study of the hole trapped centers in TiO_2 nanomaterials upon low temperature irradiation [85-87]. However, there is no consensus on the exact nature of this paramagnetic species. The aforementioned controversy on trapped holes assignments mainly results from the fact that holes are localized in TiO_2 surface region, which are greatly susceptible to surface treatment and modification[87]. Therefore, the interpretations of the observed ESR signals of photoproducted holes are still less clear now. In 1993, Micic [86] et al. reported their ESR signals reassignment of the trapped holes in the anatase and rutile. They prepared TiO_2 catalysts using isotopically exchanged water- D_2O and ^{17}O enriched water H_2^{17}O to identify the photogenerated surface centers.

Among the spin traps, DMPO and BMPO are used most often for detecting superoxide anions. Harbour and Hair [88] have detected the superoxide generated from photoexcited CdS dispersions using DMPO as a spin trap. Zhao et al. [53] have shown that use of the spin trap BMPO has advantages over DMPO as a spin trap for superoxide.

Howe and Gratzel [89] firstly identified the electron centers generated from irradiation colloidal TiO_2 by ESR measurement at low temperature. The trapped electron tends to localize in the d orbital of a cation and can be detected in the form of Ti^{3+} . Recently, a number of papers have appeared concerning the electron transfer in mixed phase (anatase-rutile) titania materials, such as well-known Degussa P25 [90-92].

Regardless of the difficulties discussed above, mainly about the selectivity of the probe, the main drawback of this technique is that it requires a very expensive spectrometer which is not usually of laboratory but is almost an equipment of "great facilities".

1.5.2 Fluorescence spectroscopy

Fluorescence spectrometry (also called fluorimetry or spectrofluorimetry) is an electromagnetic spectroscopy technique in which molecules are excited by absorption of a beam of light, usually light ultraviolet. The species that have been excited then relax to the fundamental state, releasing excess energy in the form of photons, usually visible light (though not necessarily). The equipment employed is basically a HPLC or a spectrophotometer, both coupled with a fluorescence detector. The main advantage of fluorescence is its high sensitivity and wide range of linear concentration, both characteristics superior to that of absorption spectroscopy. In addition to its simplicity in data collection, and a high spatial resolution in microscopic image [74]. The disadvantage of this technique is mainly because the number of chemical systems exhibit appreciable fluorescence.

Numerous studies have emerged in recent years that rely on the use of dihydro-compounds as fluorescent probes for the specific detection of some ROS species, generally $O_2^{\bullet-}$. However, this issue is highly discussed in some works, among which the study by Nobuaki Soh [75]. According to this author, these dihydro-compounds have two serious disadvantages. One of them is that these compounds are originally highly photosensitive, to a greater or lesser extent, and as a result tend to autoxidize to produce background fluorescence in absence of ROS in fluorescent measurements. As a result, the experimental results obtained with these compounds should be interpreted with caution. Another drawback is that these lack selectivity and are usually thought which react with various types of ROS. Consequently, the selectivity of dihydro-compounds is controversial, although they are suitable for detection of their presence [75]. Figure 1.18 shows the molecular structure of dihydro-compounds most commonly used as fluorescent probes.

Undoubtedly, it is important to mention processes assisted with HPF and APF probes. Setsukinai et al (2003)[93], synthesized these two new probes for the detection of ROS, 2- [6- (4-hydroxy) phenoxy-3Hxanthen-3-en-9-yl] benzoic acid (HPF) and 2- [6- (4-amino-phenoxy-3H-xanthen-3-en-9-yl] benzoic acid (APF). Both compounds are initially weakly fluorescent, while the fluorescein form is highly fluorescent on the reaction with ROS (Figure 1.19). These probes have been extensively applied to the TiO_2 photocatalytic systems [94-96].

Regarding the selectivity of these probes, Price et al. [97] studies the effect of DMSO as solvent. The study specifically states that if the solvent of APF and HPF probes containing 0.1% DMSO suppresses fluorescence by the presence of OH^{\bullet} and only detects 1O_2 . Taking this relationship into account, one can estimate the relative importance of each ROS in the response studied. However, the main advantage of these probes is the very high price. These same authors affirm that the fluorescence detection is superior to EPR and to chemiluminescence by its greater sensitivity and for their convenience from an experimental point of view. This is in line with Gomes et al.[74].

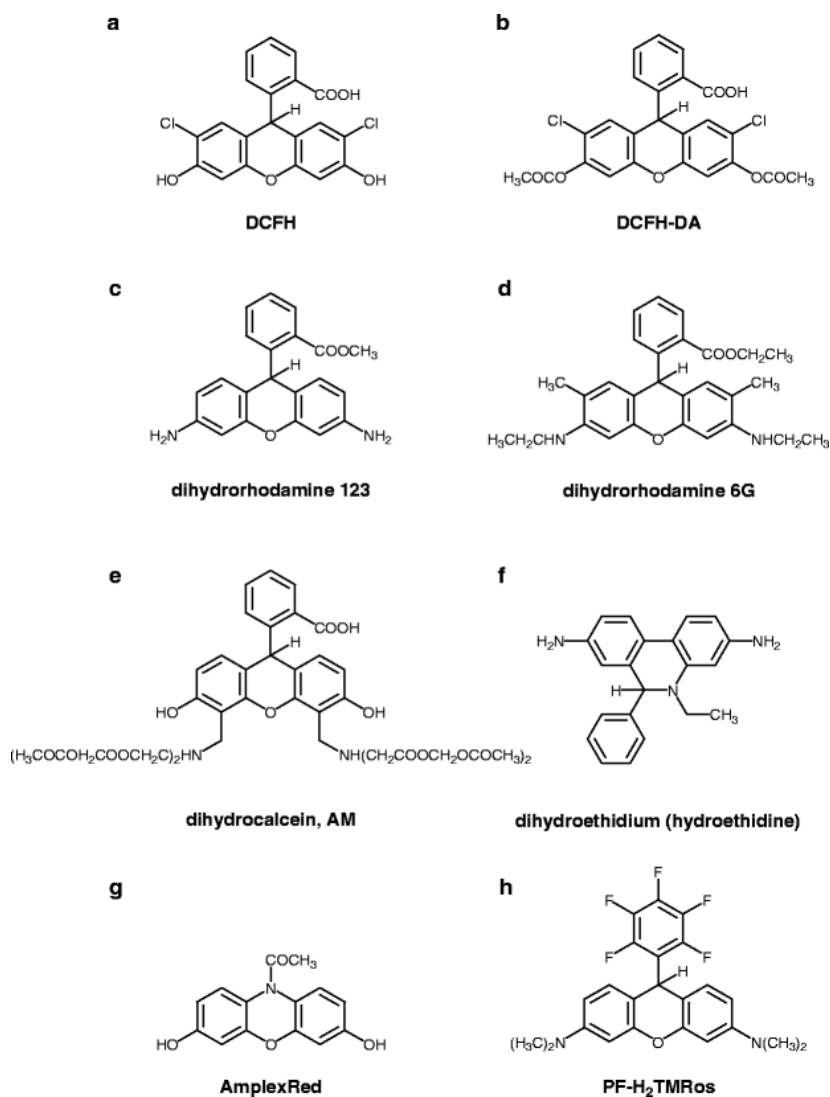


Figure 1. 18 Molecular structure of dihydrocompounds most commonly used as fluorescent probes[75].

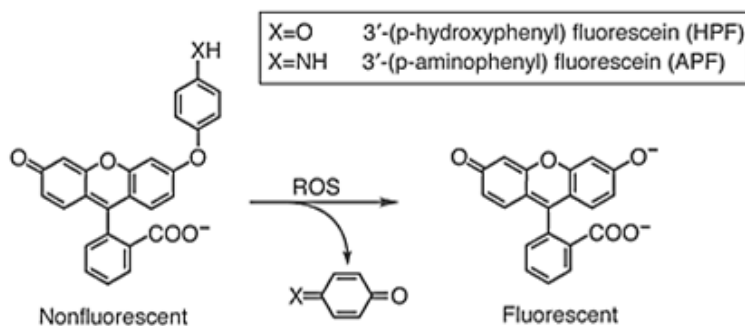


Figure 1. 19 Structure of HPF and APF with ROS.

In recent years, a simple method to quantitative OH• fluorescence probing method consists in the appearance of a fluorescence product after the reaction of the molecular probe with •OH. The excitation of the reaction product at a specified wavelength results in the emission of fluorescence which is then recorded and translated in terms of concentration through a calibration curve. In this sense, compounds such as terephthalic acid (TA, [64, 98, 99], Table 1.6), coumarin [14, 99, 100] (Table 1.6), coumarin-3-carboxylic-acid (3CCA, [100]) have been successfully applied in the quantification of OH• generated in photocatalytic system (Figure 1.20). Some of the main strengths displayed by these methods are simplicity, sensitivity, reproducibility and accuracy. However, some issues must be considered, as is the case of fluorescence pH-dependence, formation of other hydroxylated products in addition to the quantifiable ones. Between them, the most extensively use is TA. 3 CCA present the lowest stability and produce various fluorescent species with different fluorescence intensity [78]. However, the trapping efficiency of OH• formed for coumarin was assumed on the level of about 4.7% [64, 101] , in comparison with a 35% yield of the reaction of TA with OH• [64, 102]

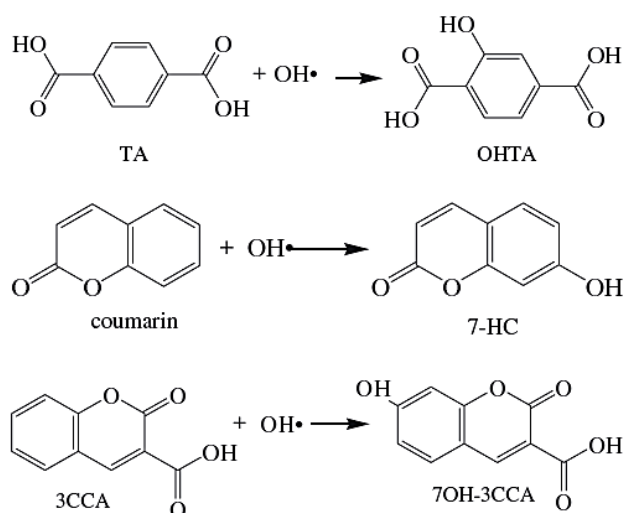


Figure 1. 20 Structure of fluorescence probes used for quantification of OH• formed during the photocatalytic process.

1.5.3 Absorbance ultraviolet-visible spectrometry

Absorbance probing methods consist of tracking either the loss of probe absorbance or the increase of the product absorbance. The equipment used in the works studied is a high performance liquid chromatograph (HPLC) or a spectrophotometer, both coupled with a UV/vis or photodiode array (PDA) detector [78].

This technique involves spectroscopy of photons in the region of ultraviolet-visible radiation. In this region of the electromagnetic spectrum, the molecules are subjected to transitions that can be quantified. This technique is complementary to fluorescence spectrometry, which transitions from the excited state to the basal state, whereas spectrometry of absorption measures transitions from the basal state to the excited state. The use of spectrophotometric collectors is perhaps the most simple; However, their sensitivity is usually lower than others [80].

One of the probes most successfully applied to determine $\text{OH}\cdot$ is dimethyl sulfoxide (DMSO) [103-105] (Table 1.6). The reaction between DMSO and $\text{OH}\cdot$ starts a set of chain reactions leading finally to formaldehyde. Then, a derivatization procedure with 2,4 dinitrophenylhydrazine (DNPH) is carried out according to the EPA method 8315 A[106] to produce the corresponding adduct formaldehyde-2,4-dinitrophenylhydrazine (HCHO-DNPH), which is finally analyzed by HPLC coupled with a UV detector[78]. However, other works showed an underestimation of $\text{OH}\cdot$ generated due to the photocatalytic degradation of formaldehyde, which is the quantification product[104]. Figure 1.21 summarized the reaction process applied to determine $\text{OH}\cdot$ using DMSO.

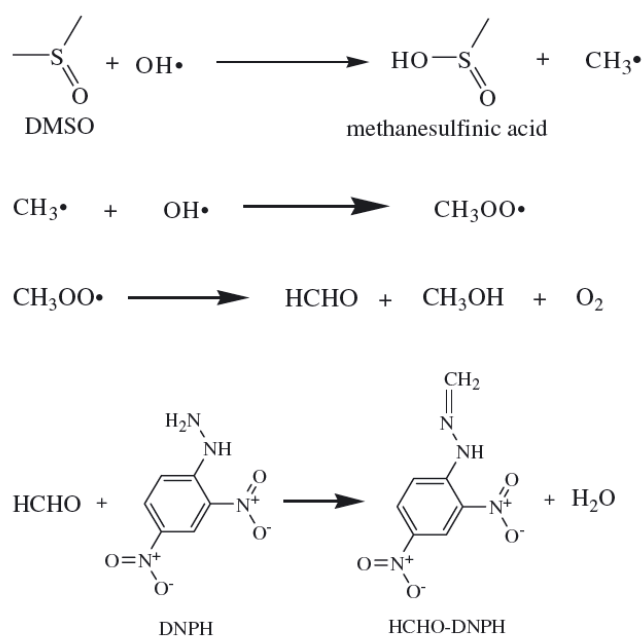


Figure 1. 21 Reaction mechanism considered to determine $\text{OH}\cdot$ using DMSO.

Alternatively, salicylic acid (SA) is an aromatic probe widely used for the determination of $\text{OH}\cdot$. Basically, the quantification method is based on the hydroxylation reaction of SA to yield 2,3-dihydroxybenzoic acid (2,3-dHBA) and 2,5-dihydroxybenzoic acid (2,5-dHBA). Although quantification of the products concentration has been performed either with absorbance, fluorescence and electrochemical detectors, the measurements based on absorbance are the most frequently used[78]. The quantification of $\text{OH}\cdot$ with this method has been successfully achieved in fenton systems, electrochemical methods, process based on ultrasound with or without photocatalyst[78]. According to the data summarized in Table 1.6, the use of SA as molecular probe provides sensitivity, reproducibility and repeatability in the analysis of $\text{OH}\cdot$. Despite these strengths, it is important to select the proper ratio between SA and the quantification products, 2,3-dHBA and 2,5-dHBA because they have similar hydroxylation kinetic constants that can result in the underestimation of $\text{OH}\cdot$. Another limitation that may interfere in this analysis is the formation of reaction products other than the quantification ones. Furthermore, it must be considered that the degradation of SA has been observed under certain operating conditions in photocatalysis systems[107, 108], facts that severely limits its application as molecular probe.

A group of usable compounds as UV/Vis molecular probes includes tetrazolium salts. Among them, Nitroblue tetrazolium (NBT) and 2,3-Bis(2-methoxy-4-nitro-5-sulfophenyl)-2H-tetrazolium-5-carboxanilide (XTT) were used in photocatalytic systems to identify the generation of $\text{O}_2^{\cdot-}$ by absorbance measurements (Figure 1.22, [20, 21, 109, 110], Table 1.6). Although luminol is the most applied one to determine $\text{O}_2^{\cdot-}$, NBT and XTT may have easier application, simpler implementation and better results than luminol due to the fact that analytical quantification techniques are simpler and, above all, these probes are less affected by the presence of interferences such as H_2O_2 , metals and ionic species that may oxidize the probes[78]. Water solubility problems may arise specially using NBT as molecular probe due to the product of the univalent reduction of NBT is the radical Tetrazoylyl, whose dismutation generates a stable and insoluble formazan [80].

However, it is important to note that, Zhao et al.[111] report the enhanced oxidation properties of tetrazolium salts induced by UV-irradiation, and demonstrate that there is real deviation in the photo-induced superoxide anion radical assay based on tetrazolium salts due to reaction with electron under an O_2 atmosphere. It is demonstrated that electrons originating from the photochemical reaction of the graphene oxide solution is the doubtless and dominant reason for XTT reduction under O_2 -free conditions.



Figure 1. 22 Structure and reaction with superoxide radical of tetrazolium salts, Nitroblue tetrazolium (NBT) and 2,3-Bis(2-methoxy-4-nitro-5-sulfophenyl)-2H-tetrazolium-5-carboxanilide (XTT)[78].

In a recent years, a novel method to monitored the photocatalytic reaction of photocatalytic materials was developed by Mills et al.[112, 113]. The typical intelligent ink comprises a redox dye, which can be readily reduced by the conductance band electron in the semiconductor photocatalyst. Its mixture is usually prepared with glycerol (electron donor) for increase the reaction rate due to electron-hole recombination is controlled. The reaction can be summarized as follow (Figure 1.23).

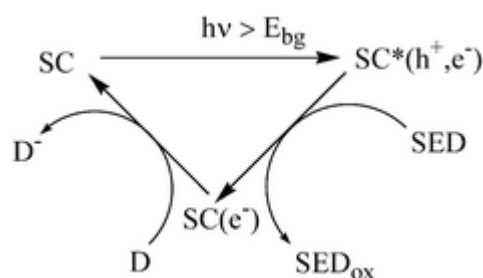


Figure 1. 23 Proposed reaction scheme of the photocatalyst ink identifying the major underlying reactions. SC is the underlying semiconductor and D/D⁺ and SED/SED_{ox} are the oxidised/reduced forms of the indicator dye and sacrificial electron donor, respectively, encapsulated in the polymer film printed or coated onto the semiconductor[112].

The redox dyes that can be designed for photocatalytic activity evaluation are large (2,6-dichloroindophenol (DCIP), acid orange 7, methylene blue, resazurin, resorufin, solvent violet 11, etc., [112-115]. Among the wide variety of inks, resazurin is the most extensively used due to its reduction create forms with different color that can be visually observed due to color change from blue to pink. (Figure 1.24)

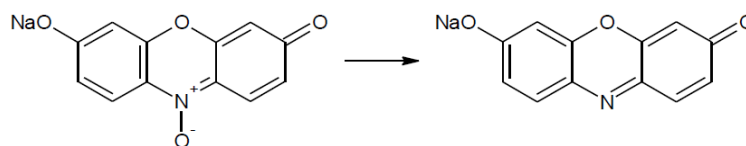


Figure 1. 24 Structures of Resazurin (blue, left) and its reduced form Resorufin (pink, right)[112].

This method is relevant due to the increasing number of researchers that using the reductive reaction of this Rz-based “intelligent” ink formulation to assess the activity of their photocatalytic films [68, 69, 116-118]. The ink test are fast (typically <10 minutes), simple to employ, and inexpensive. The photocatalytic change of colour of inks can be also monitoring just as effectively using a camera and a scanner[119].

1.5.4 Chemiluminescence (CL)

Chemiluminescence (CL) can be defined as the chemical production of light. Thus, certain substances have the property of emitting light when, by absorbing energy from the oxidative reaction of its own molecule, are placed in a state of "Electronic excitation". The emission of light occurs when returning to its "basal" state, with which the absorbed chemical energy will be given in the form of photons (electromagnetic radiation), easily quantifiable. CL probes can improve the signal-to-noise ratio by eliminating the background fluorescence. In addition, the needed concentration of probes is relatively low due to the high detection sensitivity of the technique, which diminishes the possible interferences of secondary reactions. However, the use of CL probes is problematic, in some cases, due to low emission efficiency and specificity[76].

The most used probe for the quantitative determination of O₂^{•-} in photocatalytic systems the luminol-based probes, leading to generation of chemiluminescence (Figure 1.25)[120-123]. However, there are few published works that treat the detection of OH[•] by luminol [124, 125]. Nevertheless, other ROS species including O₂^{•-} and H₂O₂ are generated at the same time, which the differentiation is difficult [76] and the background noise during the luminescence analyses which restrict its use to alkaline pH[78].

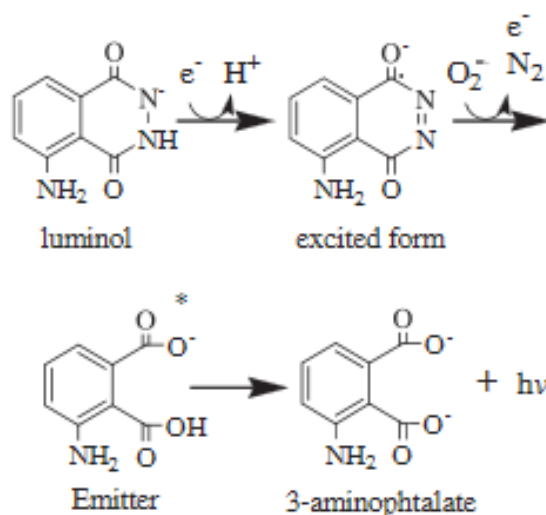
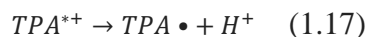
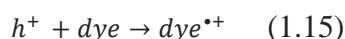
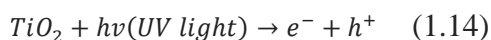


Figure 1. 25 Chemiluminescence reaction of luminol[78].

Other chemiluminescence probe, lucigenin, reacts with $O_2^{\cdot-}$, H_2O_2 and 1O_2 but not with $OH\cdot$ [126, 127]. Other specific detection for the detection of $OH\cdot$ with CL probe is described in [128]. This paper indicates that indoxyl-bglucuronide (IBG) is a probe specific for $OH\cdot$ while it is insensitive to other ROS, such as $O_2^{\cdot-}$, H_2O_2 . Other study, [129], evaluates the luminescent response of probe N, N, N1, N1- [2,6-bis (3-aminomethyl-1-pyrazolyl) -4-hydroxymethylpyridine] Tetrakis (acetate) - Tb^{3+} (BMPTA- Tb^{3+}). These authors determine that the response was significantly higher in the presence of $OH\cdot$, whereas there is almost no BMPTA- Tb^{3+} luminescence responses for additions of 10 equivalents of $O_2^{\cdot-}$, H_2O_2 , 1O_2 and $ONOO^-$. Their results demonstrate that BMPTA- Tb^{3+} is a very specific luminescent probe for the detection of $OH\cdot$.

Other interesting strategy for investigating the photocatalytic oxidation reaction is the use of single-particle chemiluminescence imaging. Tachiwaka et al.[96] proposed an “oxidative–reductive” CL system consist of luminescent dyes, such as $Ru(bpy)_3^{2+}$ (bpy = 2,2'-bipyridine) and its derivatives, in conjunction with tri-*n*-propylamine (TPA) as a sacrificing coreactant. As summarized in reactions (1.14 and 1.19), a number of electrons (e^-) and holes (h^+) are formed in TiO_2 upon UV irradiation. The photo-generated valence band holes (oxidation potential, $E_{ox} = +2.7$ V vs. NHE) oxidize the dyes ($E_{ox} \approx +1.5$ V vs. NHE) and TPA ($E_{ox} = +1.1$ V vs. NHE) to generate the corresponding radical cations, *i.e.*, $dye^{+\cdot}$ and $TPA^{+\cdot}$, respectively. $TPA^{+\cdot}$ produces a TPA radical ($TPA\cdot$) (reduction potential, $E_{red} = -1.5$ V vs. NHE) after being deprotonated prior to annihilation of the radical with the $dye^{+\cdot}$ to produce an excited state dye (dye^*), which then decays to the ground state by emission of a photon in the visible region. The photo-generated electrons in TiO_2 are efficiently scavenged by oxygen molecules dissolved in solution.



1.5.5 Electrochemical techniques

Concerning to processes assisted by electrochemical techniques, there is an interest particular, since they allow a real-time analysis, which makes spatially this technique is interesting for measurements of short-lived species [130]. There are several types of sensors for monitoring $\text{O}_2^{\cdot-}$, for example, the use of superoxide dismutase [131] and cytochrome c [132]. The mechanism for the latter is based on the reduction of cytochrome c by $\text{O}_2^{\cdot-}$ followed by electrooxidation of the redox protein in the gold electrode. Salvador [133] studied the ratio of the steady state photocurrent to the anodic transient rising photocurrent to better characterize the formation of surface bound H_2O_2 and $\text{OH} \cdot$ during basic photoelectrolysis on single crystal n-TiO₂.

Another route of detection by electrochemical methods is based on the mainly in capillary electrophoresis with chronoamperometric or amperometries for the radicals $\text{OH} \cdot$, $\text{O}_2^{\cdot-}$, NO and H_2O_2 [130, 134, 135]. The use of cyclic voltammeteries has also been found to detect electronic transfers between molecules and to evaluate potential oxidation / reduction as well as kinetic and analytical thermodynamic aspects of samples in which radicals are generated[136].

The main advantage of photoelectrocatalysis is its great versatility coupled with simplicity of the reactor in terms of construction and management. However, for the application, the main limitation is to find electrodes with specific characteristics to make the process competitive. The materials that are generally used are: Ti / PbO₂, Ti / SnO₂, Ti / IrO₂, glassy Carbon[137]. Anodic oxidation with diamond anodes doped with boron (BDD) is a new electrode material with many advantages in comparison with the other more well-known materials. This material has shown a high chemical stability and good electrochemical properties. The process of oxidation at the BDD anodes implies the production of $\text{OH} \cdot$ with only one adsorption on its surface, consequently its degradation contaminant is very high [137, 138]. Zigah et al. [139] used the scanning electrochemical microscopy (SECM) for the detection and quantification of adsorbed $\text{OH} \cdot$ generated photoelectrochemically at the surface of a nanostructured TiO₂ substrate electrode.

Special mention should be made of electrochemiluminescence (ECL) processes. This process allows the monitoring of species generated in the electrodes whose electron transfer reactions give rise to excited states that emit light. It is important to highlight the work [123, 140], whose purpose is present a new system sensitive to the measurement of the luminol-O₂ adducts and luminol-H₂O₂. Even so, the practical applications of the luminol system are questioned by a number of factors, especially the very nonspecific ECL (ie, possibly due to the formation of oxygen in the anode in a aqueous solution, followed by chemiluminescence reactions involving the oxygen and the extremely basic conditions (pH > 11) that are necessary to generate a sufficient light emission [141].

1.5.6 Other techniques

Recently, a number of papers have appeared to identify the presence of e- and hole charge carriers by time-resolved spectroscopy. The most extensively used is the transient absorption spectroscopy (TAS). This technique can specifically track the migration of trapped photo-generated charges, to study the direction of hole transfer in the anatase: rutile system [142-144]. Other technique is the time-resolved microwave conductivity (TRMC) that allows the quantitative and qualitative analysis of the separation of loads by measuring the changes in microwave absorption over time [145, 146].

Table 1. 6 Main features of the probes used in the determination of reactive oxygen species(ROS)

Probe	Analytical features	Strengths	Limitations
DMPO	Analysis of DMPO-OH ESR/EPR spectroscopy; LC with positive ion electrospray ionization using a tandem mass spectrometer (LC/ESI-MS/MS)	Quantitative measurement of OH• High sensitivity and reproducibility Good solubility of DMPO Short analysis time EPR analysis is not affected by the photocatalytic suspension Direct photolysis of DMPO was not observed	DMSO, mannitol, Fe(II) and PO ₄ ³⁻ present in solution act as OH• scavengers DMPO may also react with the Photo-generated holes in the catalyst Low DMPO-OH stability: half-life of DMPO-OH is about 20 min. This compound disappears in the presence of Fe(II), PO ₄ ³⁻ and high •OH concentration Non-selective towards •OH. Reactions with con O ₂ ^{•-} , ¹ O ₂ and ROO• may occur
Coumarin	fluorescence spectrophotometry Analysis of 7HC	Quantitative measurement of OH• Good selectivity towards •OH, though it may react with O ₃ Sensitive and fast method Good reproducibility Fluorescence only due to 7HC 7HC is a stable product and it is commercially available The direct photoelectrolysis of coumarin did not occur Coumarin is not oxidized in active anodes, it requires the presence of OH•	Disappearance of 7HC in the presence of O ₂ y O ₂ ^{•-} Different values in the yield of Coumarin-OH• to give 7HC are reported [147-149] Photocatalysis: Slow disappearance of coumarin under UV. Besides, only dissolved •OH reacts with coumarin. At low coumarin concentration, the photocatalysis of 7HC occurs. Coumarin may cause a filter effect absorbing a fraction of the incident light
TA	Analysis of OHTA HPLC-UV/vis (pH 3), HPLC-fluorescence (pH 2.8 or 4.37), fluorescence spectrophotometry (pH 6–11)	Quantitative measurement of OH• Good selectivity towards OH• High sensitivity Rapid and simple technique One quantitative product Fluorescence stability of TAOH lasts 24 h The UV analysis is possible at TAOH concentration higher than 1 mmol L ⁻¹	The reaction TA-OH• is affected by the solution pH The presence of inorganic salts and organics result in •OH scavenging An excess of TA may quench the fluorescence Later oxidation, deprotonation or photolytic reactions are possible Solubility limitations of TA TA reacts only with dissolved OH• Photolytic degradation of OHTA

DMSO	Analysis of HCHO-DNPH HPLC with UV detector (pH 4)	Quantitative measurement of OH• Selectivity DMSO-•OH Good reproducibility Simple and sensitive method, easy to operate One quantitative product High solubility of DMSO and low volatility Commercial availability of DMSO and DNPH Comparison of the •OH formation rates was identical using TA as scavenger[150] Only 0.3–0.5% of the •CH ₃ radicals (precursor of HCHO) are consumed in the production of CH ₄	Inorganic salts and other compounds present in the solution may act as scavengers The derivatization time of HCHO with DMSO requires 30 min Degradation of DMSO and HCHO applying UV/H ₂ O ₂ that implies an underestimation in the quantification of •OH[104]
SA	2,3-dHBA and 2,5-dHBA HPLC-ECD (pH 7.4), HPLC-UV (pH 2), HPLC-PDA or HPLC-fluorescence (pH 5.9), capillary electrophoresis (pH 2.8 or 7.4), UV spectrophotometry	Quantitative measurement of OH• Selectivity SA-•OH Sensitivity, reproducibility and repeatability Stability of the products Solubility of SA in water Good chromatographic separation There is no SA concentration change, when irradiated in the presence of TiO ₂ /SiO ₂ Electrophoresis requires lower sample volume and cheaper instrumentation, shows higher efficiency and higher reproducibility, and is faster than HPLC Results consistent with those obtained with an electrochemical sensor[151]	The presence of DMSO, mannitol or other organics result in the scavenging of •OH The optimum concentration of SA to obtain a high efficiency in the capture of •OH is different based on the advanced oxidation process An excess of SA is recommended, avoiding solubility limitations Importance of the SA/2,5-dHBA ratio because of their similar hydroxylation kinetic constant[151] Production of several products, including catechol and hydroquinone Capillary electrophoresis requires specific pH for the proper separation of reagents and products[152] The mineralization process results in low reliability when electrochemical oxidation or electro-Fenton are applied Photocatalytic degradation Underestimation of OH• values
Luminol	Analysis of the chemiluminescence generated Photon counting system with photomultiplier tube (pH 9–11)	Quantitative measurement of O ₂ •- When photocatalysis is applied, the subsequent addition of luminol prevents its reaction with the photocatalyst	Luminol is not selective. It also reacts with H ₂ O ₂ and other species including trace metals such as Co, Cu, Mn, Cr, Mg, Fe and certain complex of these metals, N ₃ •, CO ₃ •-, SCN-, I-, Br-, Br ₂ • and ClO ₂ Luminol produces background noise during their luminescence analysis and its detection is restricted to alkaline pH

NBT	Analysis of the absorbance of NBT or NBT-formazan UV-vis spectrophotometry	NBT does not react with $\bullet\text{OH}$ or H_2O_2 NBT does not react with TiO_2	Low water solubility of NBT Reaction with electron or $\text{O}_2\bullet^-$ under irradiation?
XTT	Analysis of the absorbance of XTT-formazan UV-vis spectrophotometry	High solubility of XTT in water, especially compared with NBT	Reaction with electron or $\text{O}_2\bullet^-$ under irradiation?

CHAPTER 2

Objectives of PhD's work

As it has been stated in *Chapter 1- Introduction*, most of the experimental tests to evaluate the photocatalytic efficiency of construction materials in published standards and literature:

- are related to the ability to remove specific contaminants;
- differ in many experimental parameters, which makes it difficult to compare experimental results between tests performed at different conditions;
- require expensive equipment and/or are very time consuming;
- are not able to be applied on site;
- some are dependent on the colour of the sample, not being suitable for coloured samples.

Then, it is clear that there is an important gap in the assessment of the photocatalytic behaviour of TiO₂ construction materials, not having found in literature any method able to give the **global potential** of a material **as a photocatalyst**. Thus, this work intends to undertake this aspect, with the global objective of the **development of new methods for evaluating the photocatalytic activity of TiO₂ construction materials based on the detection of the active species formed during the photo-activation process**. From this, the efficiency for a specific contaminant will be deduced from their pathway of degradation through the corresponding redox processes.

This global objective has been undertaken on the basis of the following partial objectives:

- i. **Selection of probes and active species** to be measured for evaluation of the photo-activity.
- ii. **Development of the specific methods** applicable to a wide range of construction materials with different photocatalytic activities and intrinsic properties.
- iii. **Validation of the developed methods** as compared with the standard methods used to assess the photocatalytic efficiency.

CHAPTER 3

Experimental part

The experimental part in this work was developed to achieve the objectives stated in *Chapter 2*. Provided that this work has as aim the developing of new methodologies of measure the activity of photocatalytic construction materials, this part has not been structured under the classical paragraphs. It has been divided into four main steps: (3.1) preliminary selections, (3.2) characterization of materials, (3.3) development of the methods and (3.4) validation (Figure 3.1).

- 3.1) Preliminary selections:** This step includes: (3.1.1) **selection of probes** for evaluation the photo-activity of photocatalytic materials based on the detection of photo-generated carriers (electrons and holes) and reactive oxygen species (ROS), (3.1.2) **selection of the materials** for the photocatalytic activity determination. These were selected with the objective to have a representative range which is currently available on the market and (3.1.3) **selection of standards** to assess the photocatalytic activity. These were chosen to cover the most common applications of photocatalytic construction materials (purification and self-cleaning properties).
- 3.2) Characterization of materials:** This step refers to the methods that were used for the physic-chemical characterization of the materials including both **plain photocatalytic powders** and photocatalytic **construction materials**.
- 3.3) Development of new methods to measure the photocatalytic activity based on the detection of active species during the photocatalytic process on the selected construction materials.** These methods were developed to be applied in a wide range of construction materials with different photocatalytic activities and intrinsic properties.
- 3.4) Validation of methods** that was performed through comparison between the new proposed methods with selected reference standards for determination of photocatalytic activity.

3.1 Preliminary selections	3.1.1 Selection of probes to detect the generated photocatalytic active species 3.1.2 Selection of construction materials 3.1.3 Selection of standards for determination of photocatalytic activity
3.2 Characterization of materials	3.2.1. Characterization of plain TiO ₂ photocatalysts 3.2.2 Characterization of construction materials
3.3 Development of new methods for determination of the photocatalytic activity on construction materials based on the detection of generated active species	3.3.1. Preliminary tests on plain TiO ₂ photocatalysts 3.3.2. Application to construction materials
3.4 Validation of development methods results	3.4.1 Comparative of development methods results with regard to the expected results of previous selected standard methods for determination of photocatalytic activity

Figure 3. 1 Experimental design and methodology of this research.

3.1 Preliminary selections

3.1.1 Selection of probes to detect active species

The selection of probes/test method for detection of generated active species during the photocatalytic activation of TiO₂-based samples was based on three pillars that were analyzed as a whole (Figure 3.2):

- A. ROS or charge carriers' objective for analysis: The aspects considered are the degree of participation and type of reaction (oxidative or reductive) of the active specie on the overall photocatalytic process.
- B. Requirements of the analytical equipment: Some important aspects considered when selecting the analytical method to determine the active species during a photocatalytic process include: (i) sensitivity; (ii) selectivity and specificity towards the analyte of interest; (iii) measurements with sufficient fast time resolution; (iv) other considerations that were considered are related to the availability, robustness and cost of instrumentation. Moreover, the choice of

operating conditions is essential to avoid the reaction of active species with themselves or prevent further reaction of the product;

- C. Probe aspects: The requisites that were considered to select the adequate molecular probe include: (i) the selectivity of the selected probe; (ii) the stability of the probe and the quantifiable reaction product under experimental conditions of the photocatalytic process under study and properties of tested materials. In our case, the stability under UV light irradiation and pH of material tested (e.g. pH high alkaline of cement-based materials) are essential; (iii) the commercial availability of the reagents and products; (iv) the possible formation of several reaction products that makes the quantification tedious and less accurate.

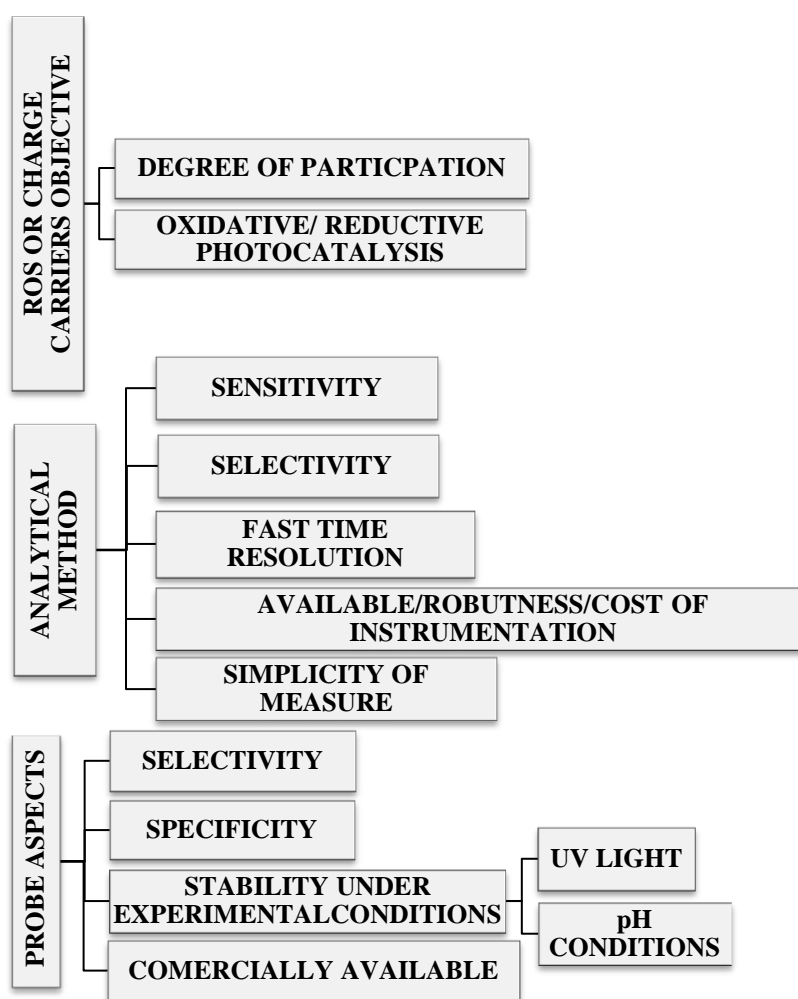


Figure 3. 2 Aspects to considered for selection probe/test methods to detect the generated photocatalytic active species.

Seven probes were pre-selected for the determination of the generated active species during the photocatalytic process on construction materials. These probes can be divided in two groups: (1) oxidative probes: Fluorescein (FC), Phenolphthalein (PH), Rhodamine B (RhB), Yellow Alizarin (YA), Rhodamine WT (RhWT) and TA (Terephthalic acid), and (2) reductive probes: NBT (Nitroblue tetrazolium) and Resazurin (Rz).

All oxidative probes were monitoring in function of their fluorescence characteristic with a Perkin-Elmer LS-55 luminescence spectrometer. TA was prepared by mixing: TA (1 gr, 0.0062 mol) with an aqueous solution of NaOH (62 mL, 0.402 M). Ethanol (70%) was added to obtain 100 mL of the TA solution [71]. In the case of the other probes a stock solutions of known concentration were prepared and from them, successive dilutions were made. This was necessary to generate calibration curves (fluorescence vs. concentration). FL and PH were dissolved in ethanol, 70% and 96% respectively. In the case of RhB, RhWT, MB and YA solutions were prepared in water. The water used to prepare all solutions was purified with a Millipore water system (resistivity 18 M Ω ·cm). A summary of fluorescence wavelength used for each probe were displayed in the Table 3.1.

Table 3. 1 Fluorescence excitation and emission wavelength of probes.

Oxidative probes	Fluorescence wavelength (nm)	
	Excitation	Emission
Rhodamine B	365	564
Fluorescein	350	550
Phenolphthalein	498	523
Yellow Alizarin	335	534
Rhodamine WT	442	619
Terephthalic acid	315	425

In the case of reductive probes different formulations were used. This type of probes was monitoring by absorbance and colour measurements. The details about the composition and the measurement procedure followed in this research are described in the corresponding section of results relative of each probe.

According to the results of this step (*Chapter 4*), two kinds of probes were selected in this research: One oxidative probe: **Terephthalic acid (TA)** and two reductive probes: **Resazurin (Rz)** and **Nitroblue tetrazolium (NBT)** ink probes.

3.1.2 Selection of construction materials

TiO₂ construction samples used in this work were of four different types: (a) commercial hardened cement-based materials, (b) commercial emulsion coatings, (c) lab-made cement-based samples, and (d) lab-made coloured mortars. Table 3.2 gives the details on the formulation of all products tested.

The first and second type (a) and (b) were acquired from different manufacturers with the objective to have a representative range of photocatalytic construction materials, which are currently available on the market, for the two most commonly materials used in this field (cementitious samples and emulsions coating). The commercial coating emulsions (samples #E1, #E2 and #E3, Figure 3.3a) were applied on bases of Portland cement mortar *via* an aerosol spray at an air-pressure feed of 4.5 bar (Figure 3.3b). The mortar bases were coated in stages; spraying vertically from top to bottom in each action before subsequent shifts, in short even steps, across the surface from left to right. The process was repeated several times until the surface was fully covered, creating a layer of 0.0010-0.0015 g/cm². The mortar support was lab-made according to the standard UNE-EN-196-1 and UNE-EN-197-1. The water cement ratio was of 0.5 and the ratio cement: sand (standard siliceous sand) of 1:3. After mixing, the mortars bases were moulded in petri dishes of 90 mm diameter and 16 mm height. The fresh mortars were cured for 28 days at >95%RH and 23±2°C inside the dishes. A Non-photocatalytic commercial hardened cement-based specimen (#C6) was also tested as reference to assess the effect of UV irradiation on probes degradation (photolysis). In one set of experiments, the tests were applied on two replicate emulsions specimens to analyze the repeatability of measurements (samples #E3A-#E3B).

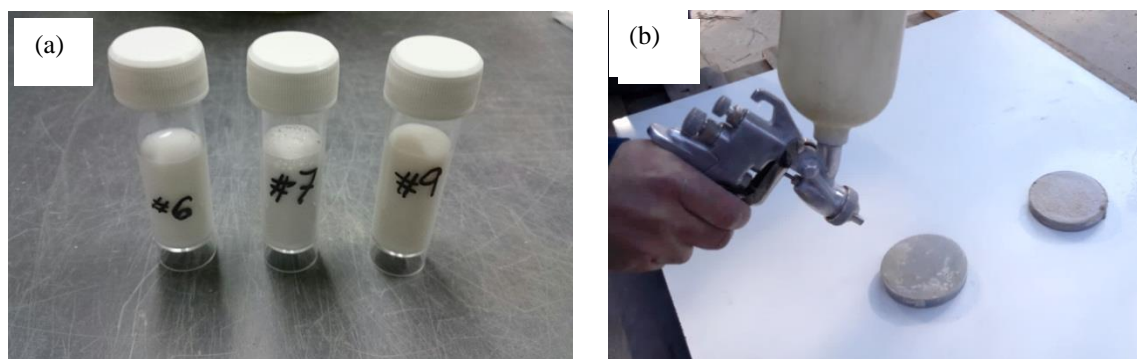


Figure 3. 3 (a) Image of the aspect of the three emulsions before application and (b) Image of emulsions coating process onto the prepared base mortars.

The lab-made cement-based samples, types (c) and (d), were performed following the mixing procedure described on the standards UNE-EN-196-1 and UNE-EN-197-1. Samples #L1 and #L2, were cast using two types of cement (Portland cement I 52.5 R, and Limestone Cement, Cement BLII/A-L 42.5 R). This both lab-made samples included a 2% of TiO_2 (Aeroxide® TiO_2 -P25 from Evonik) of weight of cement. The photocatalysts was pre-mixed together with the water that was used to cast the samples. #L3-#L5 were performed also using the procedure described on the standards UNE-EN-196-1 and UNE-EN-197-1 (Figure 3.4) using three photocatalytic commercial cements (TX active) supplied form FYM Italcementi Group. The water cement ratio was of 0.5 and the ratio cement: sand (standard siliceous sand) of 1:3. The well blended pastes were introduced also into Petri dishes. The moulds with the mortars were vibrated to ensure thorough compaction. These lab-made samples were cured in humid chamber for more than 28 days at $>95\%RH$ and $23\pm 2^\circ\text{C}$ inside the dishes, and were kept in this conditions until the any test will be performed.



Figure 3. 4 Lab-made samples (#L1 and #L2) preparation following the procedure described on UNE-EN-196-1 and UNE-EN-197-1 standards.

The series (d) were lab-made photocatalytic-coloured mortars and were prepared using the procedure and the amount of pigment commonly used in real works (Figure 3.5). Commercial photocatalytic mortar render produced by Grupo Puma S.L. (Spain) was used. This mortar contains TiO₂-based photocatalyst Iactive Tecno 42.5R (FYM Italcementi Group) as cementitious material. Four different types of iron oxide-based pigments were used: red, black, yellow and brown. The samples were prepared as follow: Each dry pigment was mixed uniformly with the dry mortar (15% cement, 84% aggregates and 1% additives). This mix was poured onto the mixer containing the water. Water was adjusted until reaching similar consistency, being necessary the addition of a higher amount of water for photocatalytic mortars. The well blended pastes were introduced into Petri dishes with a diameter of 90 mm and a height 16 mm. The moulds with the mortars were vibrated to ensure thorough compaction. These samples were cured in humid chamber for more than 28 days at >95%RH and 23±2°C inside the dishes, and were kept in this conditions until the any test will be performed. Apart from the coloured photocatalytic samples, ordinary white non-photocatalytic (#L12) and white photocatalytic specimens without pigment (#L6,) were also cast.

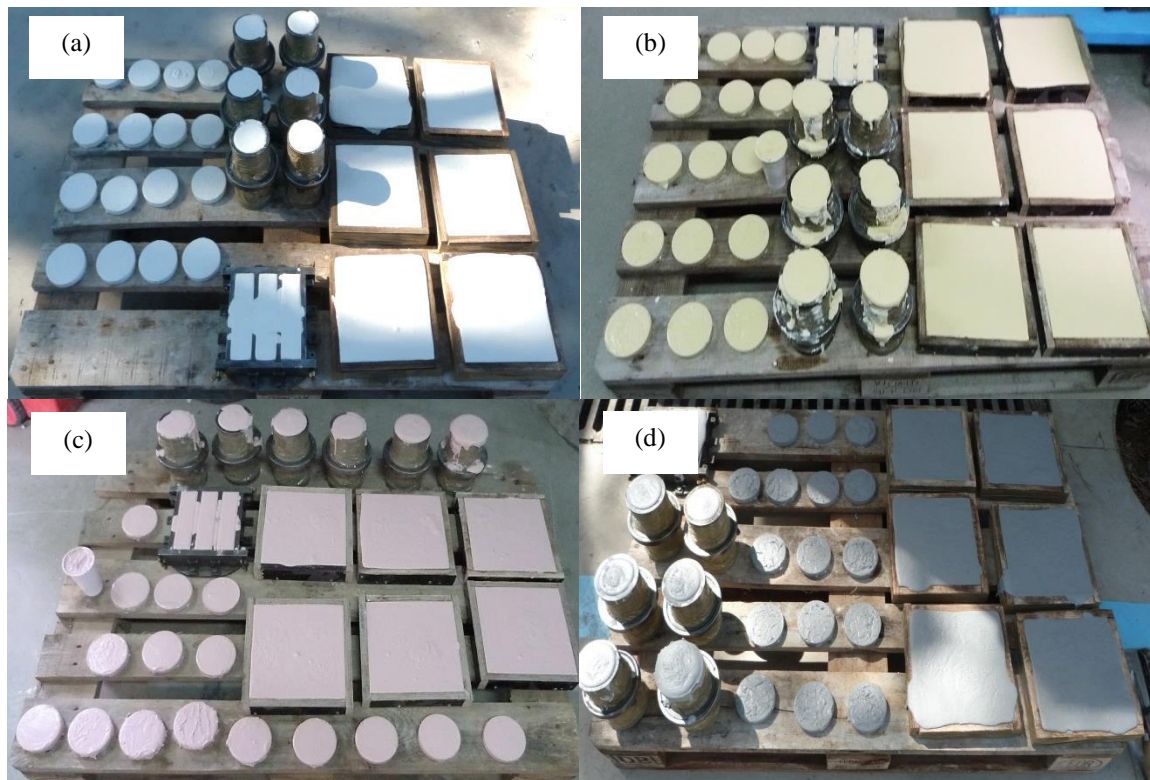
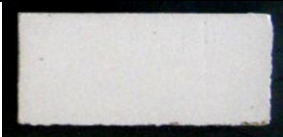
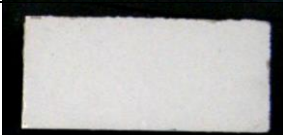
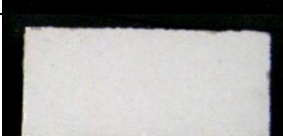
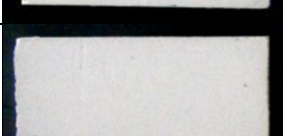
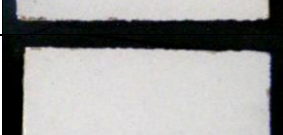
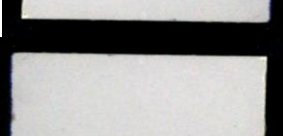

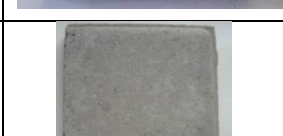









Figure 3. 5 Imagen of some lab-made coloured mortar mixtures (a) #L6, (b) #L8, (c) #L7 and (d) #L11.

Table 3. 2 Nomenclature and main characteristics of different commercial tested samples.




Sample	Formulation details	Colour of samples	Images
(a) Commercial hardened cement-based materials			
#C1	Commercial products purchased in hardened state –non-formulation detail	White	
#C2		White	
#C3		White	
#C4		White	
#C5		White	
#C6 (non-photocatalytic replica of #C5)		White	
#C7		White	
#C8		Grey	
#C9		Grey and white(mottled)	
#C10		White	

Sample	Formulation details	Colour of samples ¹	Images ²
(b) Commercial emulsion coatings onto Portland cement-based support			
#E1	Polymeric emulsion on aqueous base Product aspect: white-transparent Colour after application: grey-beige transparent Crystallite form: anatase pH:8-data provided by the producers in the technical file.	Light grey-beige	
#E2	Non-formulation detail	Light grey-beige	
#E3	Composition: H ₂ O(74-93%), TiO ₂ (5-20%), diethylamine phosphate(1-2%) and diethyl ammonium acetate(0-2%) Product aspect: White pH:7-9 -data provided by the producers in the technical file.	Light grey	





¹ and ² color and images of emulsion samples are referred to the final aspect of emulsions coatings onto Portland based cement support.




Sample	Formulation details	Colour of samples	Images
(c) Lab-made cement-based samples (1/2)			
#L1	W/C:0.5/1 (Cement BLII/A-L 42.5 R) C/S: 1/3 (standard siliceous sand; CEN UNE EN 196-1:1996) TiO ₂ : 2% weight of cement (Aeroxide® TiO ₂ -P25 from Evonik)	White	
#L2	W/C:0.5 /1 (Cement I 52.5 R) C/S: 1/3 (standard siliceous sand; CEN UNE EN 196-1:1996) TiO ₂ : 2% weight of cement (Aeroxide® TiO ₂ -P25 from Evonik)	Grey	

W: Water; C: Cement; S: Sand

Sample	Formulation details	Colour of samples	Images
(c) Lab-made cement-based samples (2/2)			
#L3	Photocatalytic commercial cement W/C:0.5 /1 (Cement I 52.5 N) C/S: 1/3 (standard siliceous sand; CEN UNE EN 196-1:1996)	White	
#L4	Photocatalytic commercial cement W/C:0.5 /1 (Cement II 42.5 R) C/S: 1/3 (standard siliceous sand; CEN UNE EN 196-1:1996)	White	
#L5	Photocatalytic commercial cement W/C:0.5 /1 (Cement I 52.5 N) C/S: 1/3 (standard siliceous sand; CEN UNE EN 196-1:1996)	Grey	

W: Water; C: Cement; S: Sand

Sample	Formulation details	Colour of samples	Images
(d) Lab-made coloured mortars samples (1/2)			
#L6 (Photocatalytic sample without pigment)	W (%): 17.3 pigment proportion: - pigment colour: -	white	
#L7	W (%): 17.5 pigment proportion*:0.04/0.26 pigment colour: Red	Red	
#L8	W (%): 17.4 pigment proportion*:0.05/0.33 pigment colour: Yellow	Yellow	
#L9	W (%): 17.6 pigment proportion*:0.10/0.66 pigment colour: Brown	Brown	

Sample	Formulation details	Colour of samples	Images
(d) Lab-made coloured mortars samples(2/2)			
#L10	W (%): 17.8 pigment proportion*:0.015/0.1 pigment color: Grey	Light grey	
#L11	W (%): 17.6 pigment proportion*:0.03/0.1 pigment color: Grey	Dark grey	
#L12 (Non photocatalytic sample without pigment)	W (%): 16.5 pigment proportion:- pigment color: -	White	

W: Water; C: Cement; S: Sand. * Pigment proportion: % weight of dry mortar /% weight of cement

3.1.3 Selection of standard methods for determination of photocatalytic activity

In order to cover the two main fields of applications of photocatalytic construction materials, i.e. air purification and self-cleaning, two type of standards were considered for the determination of photocatalytic activity of the construction materials.

Air-purification activity was performed using the photocatalytic oxidation of gaseous NO to nitric acid test. In this case, as previous indicated, a wide variety of standards have been published using this contaminant as reference. In this work, two different standards were selected, ISO 22197-1:2007 and UNI 11247:2010, with the objective to get an enable broader comparative analysis. As previously stated, (*Chapter 1*), both standards are very different concerning pre-conditioning protocol, experimental conditions and data analysis.

In the case of activity test based on self-cleaning properties, all samples were characterized using the standard UNI 11259:2008 (Rhodamine, RhB). This standard was selected because it is the only method designed to apply on hydraulic binder samples, such as cement-based materials. In addition, it is the only one that tries to simulate real conditions of the pollutant-deposition, assessing a dried film of the ink on the surface of the material. Beside this, RhB shows low sensibility for UV-light, stability in basic environments and high colorimetric sensibility.

The detail of experimental conditions of both standardized test was described in *Section 3.4- Validation of development methods*.

3.2 Characterization of materials

The physic-chemical and optical properties of materials were characterized. In addition to the construction materials, the oxidative selected probe terephthalic acid (TA) and the reductive RZ ink was applied on TiO₂ plain photocatalysts in order to better understand the behaviour of the both types of probes selected (oxidative and reductive) on photocatalytic system.

Commercial TiO₂ powder was used as supplied (TiO₂ Hombikat UV100; TiO₂-C). Besides that, from this commercial photocatalyst, different mixes anatase/rutile TiO₂ were obtained by the heat treatment at 400-1000 °C. In a typical calcination process, 1.0 g of TiO₂-C powder was transferred into a crucible, followed by calcination at 400–1000°C in a muffle furnace for 4 h (ramp up 40°C/hour). The calcined and untreated TiO₂ powders samples were characterized to evaluate the changes in properties. In this way, the different typical crystalline form anatase, anatase-rutile mixes and rutile were evaluated.

Due to the large differences properties of tested materials, different techniques of characterization and procedures were used. The analytical methods used for the characterization of all materials are summarized in Table 3.3. The specific characteristics of the instruments and the working modalities of each technique employed are described below.

Table 3. 3 Analytical methods used for the characterization of all materials used.

Analytic method	Characterization parameter	Samples
X-ray diffraction (XRD)	Mineralogical composition	<ul style="list-style-type: none"> • Plain photocatalysts • Construction samples • Pigment addition on lab-made coloured mortars.
X-ray fluorescence (XRF)	Elemental composition	<ul style="list-style-type: none"> • Pigment addition on lab-made coloured mortars
Physical gas adsorption	Surface area (BET)	<ul style="list-style-type: none"> • Plain photocatalysts • Construction samples; except the serie lab-coloured mortars (#L6-#L12)
Mercury intrusion Porosimetry	Porosity analysis	<ul style="list-style-type: none"> • Construction samples
UV-vis Diffused reflectance	Optical properties -Light absorption	<ul style="list-style-type: none"> • Plain photocatalysts • Construction samples
X-ray photoelectron spectroscopy (XPS)	Band edge position	<ul style="list-style-type: none"> • Construction samples (#L3-#L5 and #C8-#C10)

3.2.1. Elemental composition - X-ray powder diffraction (XRD)

The X-ray diffraction is a non-destructive technique primarily used for phase identification of a crystalline material and can provide information on unit cell dimensions. In other words, unlike other techniques to obtain the chemical composition, XRD does not give elemental composition but can distinguish different packing ways of the same set of elements.

The following information was revealed and analyzed by XRD:

- Crystallographic structure.
- Crystallite size (grain size).
- Structural information when coupled to lattice refinement such as Rietveld refinement.

X-ray diffractometers consist of three basic elements: X-ray tube, sample holder, and an X-ray detector. X-rays are generated in a cathode ray tube by heating a filament to produce electrons filtered to produce monochromatic radiation, collimated to concentrate, and directed toward the sample. The interaction of the incident rays with the sample produces constructive interference (and a diffracted ray) when conditions satisfy *Bragg's Law* (Eq.3.1).

$$n\lambda = 2d \sin \theta \quad (3.1)$$

where n is called the order of diffraction and is equal to the number of wavelengths in the path difference between rays scattered by adjacent planes, λ is the wavelength of the incident photon, d is the interplanar distance, and θ is the diffraction angle.

This law relates the wavelength of electromagnetic radiation to the diffraction angle and the lattice spacing in a crystalline sample. When electrons have sufficient energy to dislodge inner shell electrons of the target material, these diffracted X-rays are then detected, processed and counted. By scanning the sample through a range of 2θ angles, all possible diffraction directions of the lattice should be attained due to the random orientation of the sample material. Conversion of the diffraction peaks to d -spacings allows identification of the composition. Typically, the identification is achieved by comparison of d -spacing with standard reference patterns.

In this work, this technique is fundamental to characterize the crystalline composition and structure of TiO_2 photocatalysts, and in the case of construction materials, also the mineralogical composition of substrate or matrix. To analyze the elemental composition of construction materials, the analyzed samples are finely ground, homogenized, and average bulk composition is determined. In other cases, which will be specified when it results were present; the samples were characterized on film conditions on inert substrate. The TiO_2 plain powder photocatalysts were analyzed without any treatment before.

For a more quantitative analysis, in the case of plain TiO₂ photocatalysts, the crystal size of TiO₂ crystalline forms (anatase and rutile) was determined according to the *Scherrer's* equation, Eq. 3.2.

$$d = \frac{K\lambda}{\beta \cos\theta} \quad (3.2)$$

where d is the average particle size of the phase under investigation, K is the *Scherrer's* constant (0.89), λ is the x-ray wavelength used (1.5406 Å), β is the width at mean height of the diffraction Peak expressed in radians and θ is the angle in radians of the diffraction peak. The value of the *Scherrer* constant (K) depends on normalized grain size distribution width.

The rutile weight percentage (W_R) of TiO₂ plain photocatalytic samples were also calculated using the diffractograms employing *Spurr's* equation, Eq.3.3[153].

$$W_R = \frac{I_R}{0.884I_A} + I_R \quad (3.3)$$

where I_A and I_R are the diffraction peak intensities of anatase (101) and rutile (110) peaks, which correspond to the peak at $2\theta \sim 25.4$ and 27.5° respectively.

This quantitative characterization of TiO₂ photocatalyst phases did not apply on TiO₂ construction materials due to this type of analysis in complex composite matrices can lead to numerous errors.

The equipment used in this work is a Bruker Advance-D8. Measurement conditions are included in Table 3.4.

Table 3. 4 Main measurement conditions used on XRD characterization of samples.

Voltage	40 Kv
Current	30 mA
Divergence yield	6 mm
Time/step	0.5 s
Step size	0.01973°
Scan time	23' 47''
2theta	5-60°

3.2.2 Elemental composition - X-ray fluorescence (XRF)

X-ray fluorescence is another non-destructive technique that reveals information of the chemical composition of samples. The XRF method depends on fundamental principles that are common to several other instrumental methods involving interactions between electron beams and x-rays with samples, including: X-ray spectroscopy (e.g., SEM-EDS), X-ray diffraction (XRD), and wavelength dispersive spectroscopy (microprobe WDS). The analysis of major and trace elements in geological materials by x-ray fluorescence is made possible by the behaviour of atoms when they interact with radiation. When materials are excited with high-energy, short wavelength radiation (e.g., X-rays), they can become ionized. If the energy of the radiation is sufficient to dislodge a tightly-held inner electron, the atom becomes unstable and an outer electron replaces the missing inner electron. When this happens, energy is released due to the decreased binding energy of the inner electron orbital compared with an outer one. The emitted radiation is of lower energy than the primary incident X-rays and is termed fluorescent radiation. Because of the energy of the emitted photon is characteristic of each type of atom that composes the sample, their intensity being proportional to the present amount of each from them.

In this way, with this type of technique the type and proportion of each element present in the sample can be determined. The analyzed materials are finely ground, homogenized, and average bulk composition is determined. In this work, this technique was applied to characterize the composition of the four different types of iron oxide-based pigments used in lab-made coloured mortars. The equipment used in this work is a Tjjer X-ray S-8 spectrophotometer.

3.2.3 Surface area and Porosity analysis- Physical gas adsorption and Mercury intrusion porosimetry

The porosity analysis was done by to different methods depending on the size of the pores to be measured. Intrusion of a non-wetting liquid was used to determine pores in the micrometre scale down to nanometres, suitable for mortars samples. Gas adsorption was used to analyze pores in the nanoscale adequate for analysis of the porosity of the plain photocatalyst materials and the photocatalyst addition on mortar samples. The techniques, applications and range of pore size measured are given in Table 3.5.

Table 3. 5 Techniques for pour size measurements and the range of pore sizes able to be measured.

Technique	Application	Range of pore size detected
Mercury Intrusion Porosimetry	Mortar support	8 nm – 15 μ m
Physical gas adsorption	Photocatalysts	0.5 nm – 100 nm

A porosity measurement by gas adsorption is a non-destructive method, measuring the quantity of gas adsorbed by increasing the pressure. The isotherms were measured during the increase in pressure and later the release on pressure.

The following information was revealed and analyzed by N₂ gas adsorption porosity measurements:

- Surface area (S_{BET})
- Pore size
- Pore size distribution
- Void structures

The equipment used for the analysis of the N₂ adsorption is an ASAP 2010 from Micromeritics. Prior to analysis the samples are degasified at a temperature of 50°C until reaching a vacuum of 3-4 μm mercury. The amount of sample used is about 0.5 mg.

Adsorption–desorption measurements were conducted on a Micromeritics NOVA2000 apparatus at 77 K using nitrogen as the adsorption gas and the specific surface areas were calculated by the Brunauer–Emmett–Teller (BET) method in the relative pressure range of 0.003 to 0.3. Pore volume and pores-size distribution were calculated according to the Barret-Joyner-Halenda (BJH) method, using data from the adsorption isotherm branch.

The pore size measurement done by mercury intrusion using the instrument Micromeritics AutoPore IV 9500 measuring the external pressure needed to force the liquid into the pores.

The construction materials tested were characterized using cubic samples ca. 1 cm³ of each sample. The TiO₂ plain powder photocatalysts were analyzed without any treatment before (powder structure).

3.2.4 Optical properties -UV-Vis diffuse reflectance

UV-Vis-NIR spectroscopy is one of the most widely used spectroscopic techniques to obtain information about the electronic structure and composition of the samples, also allowing the identification of functional groups. This technique uses electromagnetic radiation from the ultraviolet (200-380 nm), visible (380-700 nm) and near infrared (700 - 1000 nm) regions with which the samples are irradiated. From the relationship between the incident and the resulting radiation after interacting with the sample, the information of interest is obtained.

In the present PhD's work, this technique was used to measure the light absorption characteristics of the TiO₂ construction selected samples. As the samples are solid non-transparent materials, the measurements are not possible using either the optical transmission–reflection or the spectroscopic ellipsometric methods. Thus, the measurement were done using the diffuse reflectance instead that is a more adequate technique [154]. In this type of spectroscopy studies the radiation reflected by solid non-transparent samples, phenomenon from which information about its composition can be obtained, and it also closely related to the colour of the samples. The radiation reflected by a sample can be of two types, specular or diffuse (Figure 3.6). The specular reflectance follows the *Fresnel theory* [155] and is the one that predominates when the material on which the reflection takes place has high values of reflection coefficients for the incident wavelength. Diffuse reflectance occurs in all directions of the surface as a consequence of the absorption and dispersion processes (*Kubelka-Munk theory, K-M theory*[156]), predominating when the materials of the reflecting surface are weakly absorbent at the incident wavelength and when the penetration of the radiation is large in relation to the wavelength. In general, a measure of reflectance contains both reflection components, however, the specular component does not provide information about the composition, so that it is attempted to minimize the maximum by adjusting the position of the detector with respect to the sample, being the diffuse reflectance, the component that provides useful information. In this way, the absorption spectra of the samples are obtained from reflectance data using the *K-M equation* (Eq. 3.4) [156].

$$F(R) = \frac{(1-R)^2}{2R} \quad (3.4)$$

where R is the reflectance obtained values.

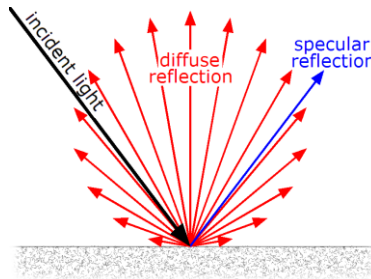


Figure 3. 6 Diffuse and specular reflection of incident light on surface [157].

In the spectrophotometers that carry out this type of measurements, the radiant energy emitted by the source passes through an optical system that connects the source to the monochromator. The monochromator disperses the radiation and transmits it as a narrow band of wavelengths through the exit slit which is optically communicated with the chamber containing the sample to be measured together with a standard. The detector system receives the radiation reflected by the sample and the standard and generates a quotient of the signals that is later transmitted to the computer for analysis and presentation. A special accessory called “*integrating sphere*” was used (Figure 3.7). This accessory provides the ability to collect a quantitative reflectance spectrum from highly scattering or irregularly shaped samples, but acquiring only diffuse light, not the specular signal and so the *K-M* theory can be applied.

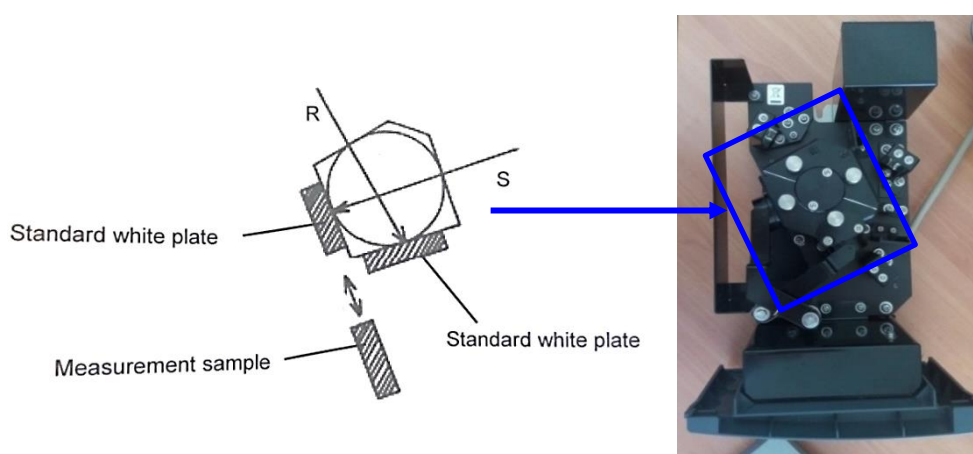


Figure 3. 7 Schematic diagram of UV-Vis spectrophotometer and image of accessory “integrating sphere”.

On the other hand, another application of special interest related to the UV-Vis-NIR spectroscopy is the calculation of the Band Gap value of semiconductors. In the case of the reflectance mode, for the semiconductor materials, the absorbance values un *K-M* units at the different wavelengths can be expressed from the *Tauc’s* equation (Eq. 3.5) [156].

$$FR(h\nu) = (h\nu - E_g)^n \quad (3.5)$$

where E_g represents the Band Gap energy, FR is the absorption values in *K-M* units and n depends on the nature of the electronic transition involved. Specifically, its value is 1/2, 3/2, 2 and 3 for direct, forbidden direct, indirect, and forbidden indirect respectively.

Typically, a *Tauc* plot represents the value of $h\nu$ (eV) on the abscissa axis versus the value $(FRh\nu)^n$ on the ordinate. The resulting curve has a characteristic linear regime whose interruption denotes the start of absorption. Therefore, the extrapolation of the linear region for the abscissa axis ($(FRh\nu)^n = 0$) gives the energy value of the Band Gap (E_g) of the semiconductor. In the case of the E_g calculation, it is important to note that this application is focused to determine the pure semiconductor E_g values. In our case, in the particular case of TiO_2 construction samples used, which are complex mixed matrices, the value in the formula of E_g , will be denoted as “apparent photoabsorption edge” (PE_{app}).

The equipment used in this work is a UV-Vis spectrophotometer Shimadzu UV-2600 (Figure 3.8). Measurement conditions are included in Table 3.6.



Figure 3. 8 Image of UV-Vis spectrophotometer Shimadzu UV-2600.

Table 3. 6 Main measurement conditions used on UV-vis characterization.

Scan speed	fast
Sampling interval	1 nm
Slit width	5
Accumulation time	1 sec

3.2.5 Valence band position - X-Ray Photoelectron Spectroscopy, XPS

The phenomenon used for photoelectron spectroscopy is based on the photoelectric effect outlined by Einstein where the concept of the photon was used to describe the ejection of electrons from a surface when photons impinge upon it (Figure 3.9). For XPS, also known as electron spectroscopy for chemical analysis (ESCA), the photon energies of choice are the fundamental emissions from $\text{Al-}\kappa\alpha$ (1,486.6 eV) or $\text{Mg-}\kappa\alpha$ (1,253.6 eV) cathodes. The XPS technique is highly surface specific due to the short inelastic mean free path (IMFP) of the photoelectrons that are excited from the solid. The energy of the photoelectrons leaving the sample is characteristic of each element.

Each peak area is proportional to the number of atoms being present in the material; the shape of the peak and the binding energy (BE) can be slightly altered by the chemical site of the emitting atom; hence XPS can provide chemical bonding information as well. The fundamental equation that relates the BE of the emitted photoelectron with the measured electron kinetic energy (KE) is given by (Eq. 3.6):

$$BE = hv - KE - \phi \quad (3.6)$$

where hv is the incident photon energy and ϕ is the work function, which has to be well defined for each equipment in order to determine precisely the BE that is usually measured in reference to the material's Fermi level.

The analysis of the XPS spectrum (counts per binding energy) allows us to obtain the surface elemental composition by comparing to standard materials (quantitative) or using XPS databases (semiquantitative). The depth of analysis in XPS is about 1^{-10} nm depending on the incidence energy of the photons, the kinetic energy of the outgoing electrons, and the angle of collection (angle resolved XPS, ARPES). The XPS technique requires ultra-high vacuum conditions (UHV, pressure in a range from 10^{-8} to 10^{-10} mbar), and so the samples have to be evaluated always in dry conditions. The XPS is essentially a non-destructive technique but is very sensitive to surface contamination.

In this work, this technique was applied for the determination of the energy position of the TiO_2 valence band (BV) [158].

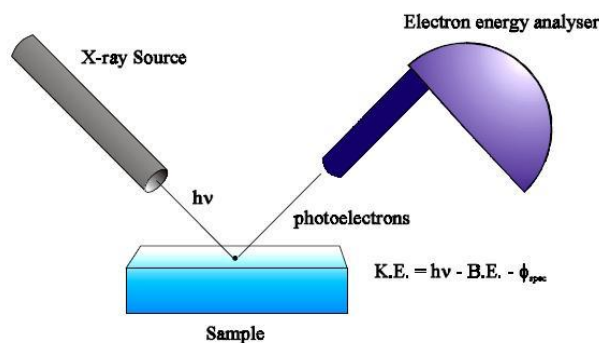


Figure 3. 9 Photo-electron generation from XPS technique[159].

The XPS measurements were performed in an ultrahigh vacuum (UHV) system with a base pressure of $1 \cdot 10^{-8}$ Pa using Mg Ka line (1253.6 eV) of incident X-ray radiation. The angle between the hemispherical analyser and the plane of the sample surface was 60° . The survey spectra were recorded with pass energy of 40 eV and energy step of 0.25 eV. The binding energy (BE) scale was calibrated with respect to the Au 4f at 84 eV.

3.3 Development of the methods for construction materials

This part constitutes the main body of this research and, according to the results in the selection step; it is made of two types of methods:

- Hydroxyl radical (OH•) quantification using terephthalic acid fluorescence probe method.
- Electron (e-) reductive measurement using Rz and NBT ink method.

Prior to the application of the methods both to plain TiO₂ photocatalysts and to construction materials, it has been necessary to make an optimization of the probes for quantification of active species.

1. Calibration of the probes.
2. Optimal probe concentration.
3. Selectivity analysis.

3.3.1 Calibration of the probes

The first optimization step is the probe calibration to quantitatively determine the concentration of photo-generated OH• and e- using terephthalic acid fluorescence probe method and Rz-NBT ink method respectively.

The measurements of the amount of OH• formed at illuminated photocatalytic tested samples were performed by means of the acid terephthalic (TA) fluorescence (FL) probe method [15, 16]. TA readily reacted with the OH• formed on the irradiated photocatalytic samples to produce the highly fluorescent product, 2-hydroxyterephthalic acid (TAOH), gives a peak at the wavelength of about 425 nm by the excitation with the wavelength of 315 nm [99] (Figure 3.10). Fluorescence spectra of solutions were measured with a fluorescence spectrophotometer (Perkin-Elmer, LS-55, Figure 3.11). To do the fluorescence calibration curve, the fluorescence of TAOH standard solutions with various concentrations was measured. Thus, a fluorescence calibration curve was obtained by plotting the FL intensity measured at 425 nm as a function of the concentration of TAOH. Therefore, by comparison of the FL intensity at 425 nm of irradiated photocatalytic system with that of the known concentration of TAOH standard, the amount of produced TAOH can be determined. Thereby, the amount of free OH• formed in photocatalytic construction selected samples was estimated from that of TAOH by adopting the trapping factor of 35%, as commonly assumed in bibliography [102, 150].

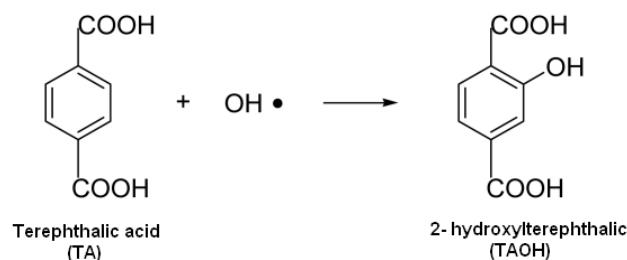


Figure 3. 10 Reaction for detecting OH• in solution with terephthalic acid (TA) to form 2 hydroxyterephthalic (TAOH).



Figure 3. 11 Fluorescence spectrophotometer (Perkin –Elmer, LS-55).

The formation rate of e⁻ at the illuminated photocatalytic tested samples was detected by the UV-Vis absorbance technique using Rz or NBT as a probe molecule. Absorbance spectra of probes were measured with a UV-Vis spectrophotometer (Shimatzu UV-2600, Figure 3.8).

Resazurin (Rz, blue) readily reacted with e⁻ to produce Resorufin (Rf, pink). Rf can be reduced subsequently to its colorless counterpart dihydroresorufin (HRf). Figure 3.12 shows the structure of the redox dye Rz and its reduced forms, resulting of the reaction of the redox dye with the electrons. However, previous studies demonstrated that the reduction of Rz ink by TiO₂ photocatalysis was first order, and the time for Rf to HRf reduction is at least 3.5 times larger than the first reduction step [115]. As such, the rate of degradation of the Rz to Rf can be determined to by assessing the decrease in absorbance at 600 nm at early times, in which the rate of decrease is linear.

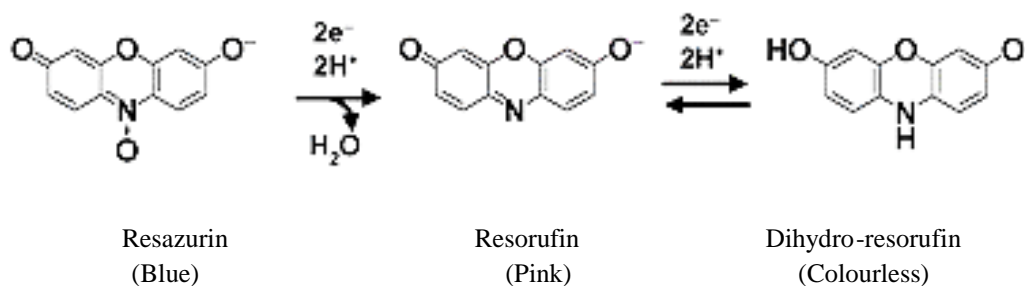


Figure 3. 12 Diagram to show the structure of the redox dye Resazurin (Rz) and its reduced forms. The reduction of Rz is 4e⁻ in two steps.

As previously mentioned, Rz can be specifically reduced by e^- ; therefore, the e^- generated as a result of the photocatalytic reaction can be detected by measurement the decreased intensity of the absorbance of Rz in the solution. To quantitatively determine the concentration of photo-generated e^- , the absorbance of Rz standard compound solutions with various concentrations was measured. Thus, the absorbance calibration curve was obtained by plotting the absorbance intensity measured at 600 nm (which is the maximum value of the spectra) as a function of the concentration of Rz. Therefore, by comparison of the absorbance at 600 nm of irradiated TiO_2 powder solution with that of the known concentration of Rz standard, the amount of e^- generated as a result of the photocatalytic reaction was determined using the reaction of reduction of Rz summarized in Figure 3.12.

In the case of NBT, in one step, reacts with $2e^-$ to produce formazan. Figure 3.13 shows the structure of the redox dye, NBT, and its reduced form (formazan), resulting of the reaction of the redox dye with the electrons. The procedure to make an absorbance calibration curve to quantitatively determine the concentration of photo-generated e^- using the probe NBT will be the same that using the NBT probe. However, in this case NBT, will not be used to quantitative determination of electron. The resultant formazan product is insoluble. Hence, when formazan is produced during photocatalytic reactions in aqueous solutions, it precipitates on the surface of TiO_2 particles, rendering that the decrease the activity by the particles deposition of formazan on the active sites of particles. Therefore, this effect may difficult a suitable quantification of e^- formed on irradiated TiO_2 powder solution.

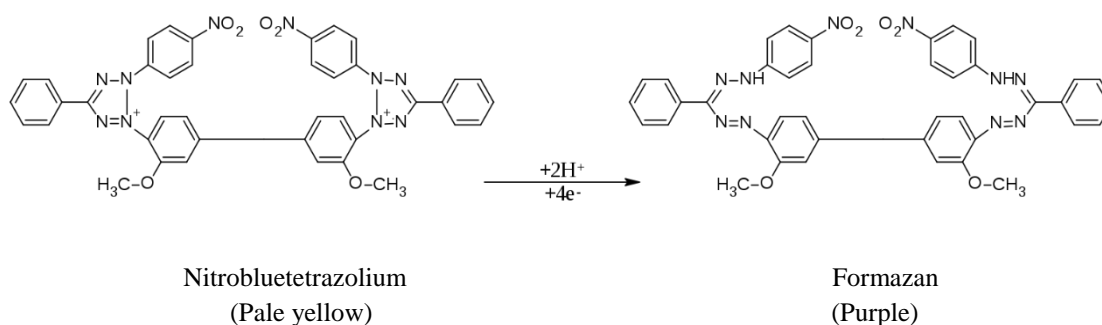


Figure 3. 13 Diagram to show the structure of the redox dye, Nitrobluetetrazolium (NBT), and its reduced form (formazan). The reduction of NBT is a $2e^-$ process in one step.

3.3.2 Optimal probe concentration

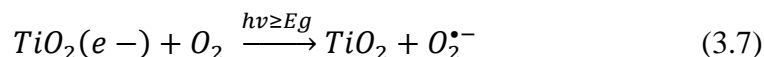
To determine the optimal probe concentration of TA, the product yield was measured as a function of probe concentration. To do so, 150 mg of the photocatalyst (Aeroxide® TiO₂-P25 from Evonik) suspended in 100 ml of aqueous solutions containing TA in the range of 0.5 to 3 mM was used as reference photocatalytic system. The suspensions were kept in dark under magnetic stirring for 5 hours in an aerated Pyrex glass cell until the adsorption–desorption equilibrium was reached. After that, the suspensions were exposed to irradiation under continuous agitation and the product formation yield after different irradiation times was determined measuring the FL spectra of the supernatant liquid after recovering the catalyst by centrifugation.

In the case of reductive probes (Rz and NBT) the concentration of probes used was selected following the previously formulation described in literature [119] with some modifications that will be specifically explained in each corresponding section.

3.3.3 Selectivity of the optimal probe concentration

The selectivity of the optimal probe concentration for OH• was evaluated by adding different scavengers to the TA probe solution. Based on previous research, it is reasonable to consider that the reaction between OH• and TA is unaffected by the presence of other reactive species such as O₂^{•-}, HO₂•, and H₂O [99, 160]. It is also possible for the direct oxidation of TA by photo-generated h⁺ to yield TAOH on the photocatalyst surface. However, the reaction between the photo-generated h⁺ and the probe depend of the concentration and pH of solution. This possibility is ruled out at low concentration of TA probe and the high solution pH, since the amount of terephthalic acid adsorbed on the photocatalysts would be quite small [98, 161]. The selectivity analysis was performed using the same previous photocatalytic reference system (150 mg of the photocatalyst Aeroxide® TiO₂-P25 from Evonik) and experimental procedure used to establish the optimal probe concentration, adding to the TA probe solution the scavengers, DMSO, as OH• scavenger, and EDTA, as h⁺ scavenger, both with a concentration of 1 mM. The amounts of these quenchers were selected based on previous studies [162, 163]. In this way, comparing the product formation yield after different irradiation times of reference system without scavenger and with the yield adding scavengers, it is possible to define the selectivity of probe for the OH•, and the interferences by the presence of other active species.

In the case of reductive probes, Rz and NBT, the specifically reduction by e⁻ only can be affected by the participation of the O₂^{•-} into the reductive yield of inks or interference of O₂ in the experimental conditions via competition for e⁻ of the dissolved O₂ with the ink (Eq.3.7).



In order to clarify the possible interferences in the e- reaction with the inks, 0.0055 g of TiO₂ powder (reference photocatalytic system) was dispersed in 50 mL of RZ-NBT solution. After that, the suspensions were exposed to irradiation under continuous agitation and the absorbance variation of both probes was also monitored under irradiation in a Pyrex glass cell under N₂-conditions (1 L/min) and ambient conditions. Thus, comparing the reduction yield after different irradiation times under N₂-conditions and ambient conditions, it is possible to clarify any potential participation of the O₂^{•-} into the reductive yield of inks or interference of O₂ in the experimental conditions via competition of the dissolved O₂ with the ink (Eq.3.7). The reduction product yield after different irradiation times was determined measuring the absorbance of the supernatant liquid after recovering the catalyst by centrifugation.

3.3.4 Preliminary tests: Study on plain TiO₂ photocatalysts

3.3.4.1 Hydroxyl radical (OH•) quantification on irradiated photocatalyst using terephthalic (TA)

The probe to assess the OH• production rate formed at illuminated photocatalyst/water interface of TiO₂ plain photocatalyst was prepared using terephthalic acid (TA) neutralized NaOH (0.02 M, pH 12.4±0.2). 0.0055 g of TiO₂ powder was suspended in 100 mL of TA (2mM) probe solution in an aerated Pyrex glass cell. Previously, in the optimal probe concentration step, it has been proved that this is the optimal concentration for monitoring the hydroxylation reaction of terephthalic acid proceeds exclusively by OH•.

The suspension was stirred for 15 min in the dark box, and after that, the powder sample was irradiated for 15 min under continuous stirring. Then, the photocatalyst was separated by centrifugation and analyzed by fluorescence. FL intensity of the supernatant solution was measured at 425 nm at different times of irradiation using the excitation with the wavelength of 315 nm. These experiments were performed for each sample irradiated at various periods, that is, 0, 2, 5, 10, 15 and 20 min. By comparison of the obtained fluorescence intensity with the previous performed fluorescence calibration curve, the amount of produced TAOH was determined. The amount of free OH• formed in TiO₂ photocatalyst was estimated from that of TAOH by adopting the trapping factor of 35% [64, 102, 164].

3.3.4.2 *Electron (e⁻) quantification on irradiated photocatalyst using Resazurin (Rz) probe*

Two formulations of Rz ink were used: (i) 3 g of glycerol and 0.04 g of resazurin dye in aqueous solution (1L) following the previously procedure described in literature [119]; and (ii) the same formulation without glycerol. Both Rz probes were tested without incorporation of polymer thickener [119], due to such addition is not necessary for testing photocatalytic powder samples. The ink system with glycerol is known as “intelligent ink” because e^-h^+ recombination is inhibited by the hole scavenger (glycerol), and therefore the photo-generated electrons have more time to take part in reduction processes of the dye.

Experimental procedure was as follows: 0.0055 g of TiO₂ powder was dispersed in 50 mL of Rz solution (with and without glycerol) in a Pyrex glass, at room temperature. The suspensions were kept in the dark under magnetic stirring until the adsorption–desorption equilibrium among the photocatalyst and Rz was reached. After that, the suspensions were exposed to irradiation during 15 minutes with a continuous magnetic stirring. Product reduction yield was determined measuring the supernatant solution after the TiO₂ powder had been removed by centrifugation from aliquots (4mL) of TiO₂/Rz suspension at different irradiation times. The UV-Vis absorption spectra were measured with a Shimadzu UV-2600 spectrophotometer.

3.3.4.3 *Photocatalytic degradation of Rhodamine B*

In order to verify the photocatalytic performance of TiO₂ photocatalyst samples, Rhodamine B (RhB) dye was selected. This organic color dye is often used as a standard target compound in self-cleaning dye tests as it was adopted in the Italian standard (UNI 11259:2008) for determination of the photocatalytic activity of hydraulic binders. Also, the photocatalytic degradation pathway of RhB involves the participation of a wide range of photocatalytic active species [165-167].

The discolouration of RhB aqueous solution was performed under the same conditions as the TA fluorescence and Rz absorbance probe methods. In the RhB aqueous solution of 50 mL with a concentration of 8 ppm, 0.05 g of TiO₂ powders was dispersed. The solution was kept in the dark under stirring to saturate the adsorption of RhB into each sample and then UV irradiation of the solution was started. Concentration of RhB in the solution was determined as a function of irradiation time or in function of absorbance change at the wavelength of 550 nm with a spectrophotometer. Since the plots of logarithm of relative concentration of RhB in the solution $\ln(C/C_0)$ against irradiation time were approximated to be linear, the slope of the linear relation, i.e., rate constant k_{RhB} , was determined on each sample and used as the representative parameter of the photocatalytic activity of the samples.

3.3.4.4 Irradiation setup

The photocatalytic tests using TiO₂ photocatalyst suspension were performed inside the lab made reactor depicted on Figure 3.14. The light source consisted of two fluorescent tubes Philips Actinic BL 15W/10 SLV emitting photons in the wavelength between 350 and 400 nm with an optimum at 360 nm, and four additional thin peaks can be seen at 406, 435, 545 and 576 nm. The light spectrum of lamps was included in Figure 3.15.



Figure 3.14 Reactor and illumination system setup.

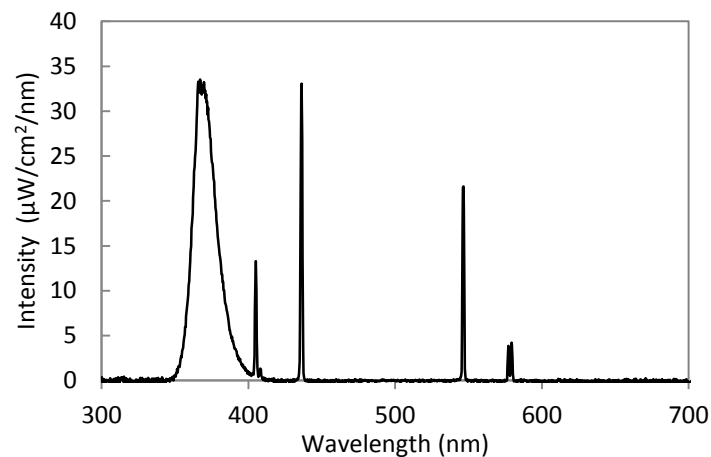


Figure 3.15 Light spectra of the Actinic BL 15W/10 SLV lamp used to supply UV radiation (data obtained using a fiber optic UV/VIS/NIR spectrophotometer-AvaSpec ULS3648-USB2-UA-25).

The light spectral intensity of irradiance source was measured using a fiber optic UV/VIS/NIR spectrophotometer (AvaSpec ULS3648-USB2-UA-25, Figure 3.16a). This spectrophotometer was used with the AvaLight-DH-CAL (200-1099 nm) to calibrate for absolute spectral intensity (Figure 3.16b). It is supplied with a cosine corrector (CC-VIS/NIR) and a combined halogen a deuterium lamps. Two calibration files are included: one for irradiance calibration over the full range (200-1099 nm) and one over the visible

and near infrared range (350-1099 nm). For the first file, both the deuterium and the halogen bulb should be used during calibration. The second file is to be used with only the halogen light. The halogen only spectrum provides a smoother black body calibration spectrum for the longer wavelengths. To measure the average light intensity of experiments, the top window of cosine corrector sensor was placed in a location that corresponded to the center and the same height as the top of TiO₂ liquid suspension. The intensity was let to stabilize 15 minutes before performing the irradiance measurements and the average light intensity at the surface of the reaction solution was about 10 W/m².

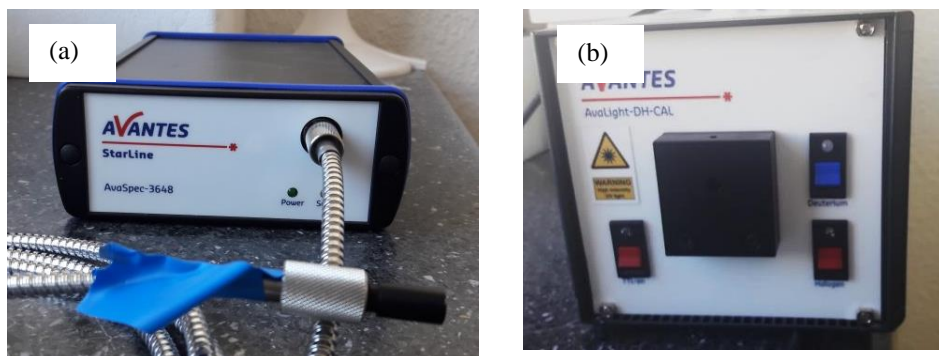


Figure 3. 16 (a) UV/VIS/NIR spectrophotometer (AvaSpec ULS3648-USB2-UA-25) and (b) AvaLight-DH-CAL.

3.3.5 Development of the method on construction materials

3.3.5.1. METHOD 1 Hydroxyl radical quantification using terephthalic acid (TA) fluorescence (FL) probe method

The probe to assess the OH• production rate formed at illuminated TiO₂ construction materials was prepared taking into account the previous defined optimum formulation (TA, 2 mM neutralized NaOH, 0.02 M - pH 12.4±0.2). A test cell (ϕ 67.53 mm × 40 mm) to contain the probe has to be glued to the sample with silicone on the photocatalytic surface of mortars, as depicted in Figure 3.17. 25 ml of TA has to be added into the test cell, which is irradiated under continuous stirring. FL intensity of the solution is measured at 425 nm at different times of irradiation and then is returned to the test cell

To assure that the samples are in the same conditions, they have to be preconditioned for 3 days in a controlled environment at (23±5) °C and (60±10) % relative humidity. A heat control filter is placed on top of test cell in order to avoid any possible evaporation during the irradiation process.

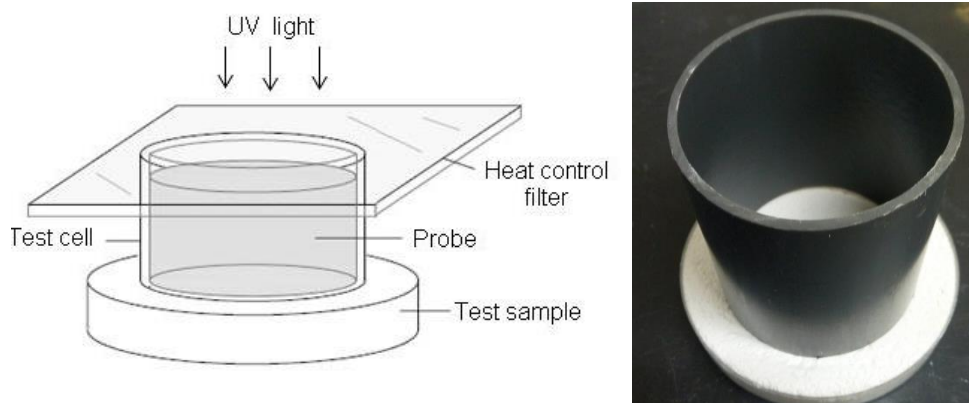


Figure 3.17 Diagram and image of experimental setup of OH• quantification method.

3.3.5.2 METHOD 2: Electron (e^-) reductive measurement using Rz and NBT ink method

3.3.5.2.1 Preparation of inks

Each ink was prepared based on the following generic formulation [112-114, 119] with some modifications. In this work used ultrapure water (25 mL), hydroxypropyl cellulose polymer (HC, 0.5 g), and 2 g glycerol, to which the correspondent dye was added, that is, 0.04g of Resazurin or 0.1g of NBT. The amount of Rz and NBT was adjusted until getting a clearly visible characteristic colour of the ink (pale yellow or blue – NBT or Rz respectively). The HC resin is added to contain the above components, also it favour that the dye kept in the surface and not absorbed through the network of pores. In the reference formulation used hydroxyethyl cellulose polymer; in this study, it was necessary using the polymer HC, in order to obtain a less dense solution suitable for further spray-coating of the samples.

Each solution of ink is left stirring for a minimum of 8 hours with a magnetic stirrer to ensure all the dye is dissolved. The inks are stored in a fridge and used within 2 weeks of its preparation. Before the ink was used, it is stirred at room temperature for 1 hour.

3.3.5.2.2 Coating of the samples with the inks

The samples are spray-coated with the reductive inks at an air-pressure feed of 3.5 bar (Figure 3.18). The ink-coating process has been performed with the air brush typically held at 25 cm away from the samples and passing over the samples for 15 times (spraying left to right and back again), when the characteristic colour of the ink (pale yellow or blue – NBT or Rz respectively) is clearly visible. The ink-coated surface was ca. 8cm². The ink coating then allowed to dry in the dark for 30 min before prior to irradiation.

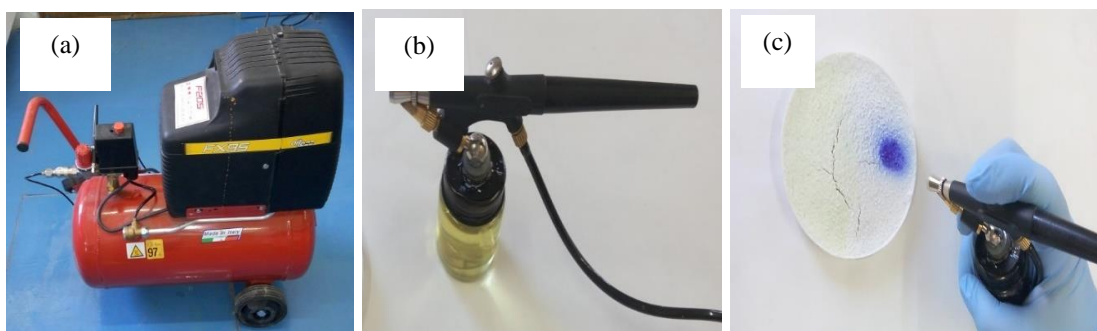


Figure 3. 18 (a) air compressor, (b) air-brush, and (c) example of spray-coated process with Rz, the left of the samples was coated with NBT (pale yellow).

3.3.5.2.3 Monitoring the photocatalytic degradation

The photocatalytic degradation of the inks was monitored using both diffuse reflectance measurements, UV-2600 Shimadzu spectrophotometer, and a portable spectrophotometer with sphere geometry and horizontal alignment, CM-2300d-Konika Minolta. The first spectrophotometer was used to assess the variation of absorbance spectra of the ink film onto the surface during the experiment and the portable spectrophotometer, for the chromatic characterization of the ink films expressed according to CIELAB system (Figure 3.19). In order to assure an adequate surface colour characterization, the measurements were performed on three different point of the ink coloured surface and the mean value was used.

The CIELAB system is based on three colour coordinates named L^* , a^* and b^* forming a three-dimensional space as illustrated in Figure 3.19. L^* describing the brightness from black to white where 0 is black and 100 white, a^* the colour tone from green (negative value) to red (positive value) and b^* from blue (negative value) to yellow (positive value).

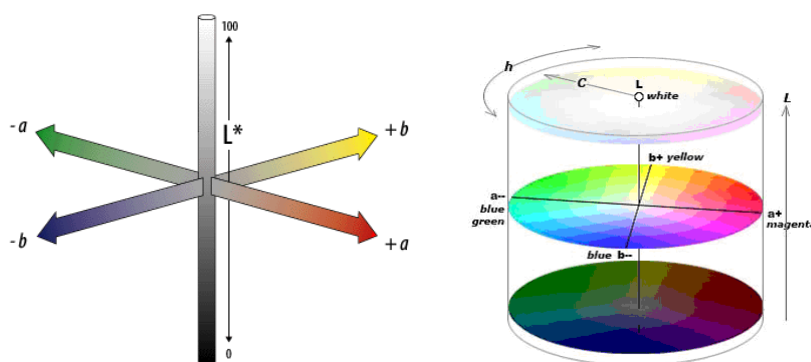


Figure 3. 19 Three-dimensional CIELAB system represented by the three colour coordinates L^* , a^* and b^* .

Beside this, the change of colour of the coating was also recorded as a function of irradiation time by the analysis of digital images obtained just by an ordinary mobile phone camera (Meizu M2 note). Using the digital images obtained, the Red, Green and Blue colors, i.e. RGB, were obtained as a function of irradiation time using the free download software ImageJ. Figure 3.20 illustrates the main instrumentation used here to carry out the ink tests of the photocatalytic samples.



Figure 3. 20 (a) Spectrophotometer used for reflectance UV-vis measurements, (b) portable spectrophotometer used for CIELab color measurements, and (c) Mobile phone used for make digital images.

Monitoring of inks during the photocatalytic degradation on the construction samples were performed in ambient conditions. Additionally, using a replicated specimen of sample #C8, the absorbance variation of both probes was also monitored under irradiation inside a reactor flushed with nitrogen (1 L/min, 20 %RH and 23 ± 2 °C). The reactor and the gas installation used was the same used than in the photocatalytic oxidation of gaseous NO to nitric acid. The UV-Vis spectra were recorded using the 2600 Shimadzu spectrophotometer. Thus, comparing the reduction yield after different irradiation times under N_2 -conditions and ambient conditions, it is possible to clarify, as previous explained in *Section 3.3.1.3*, any potential participation of the $O_2^{\bullet -}$ into the reductive yield of inks or interference of O_2 in these experimental conditions via competition of the dissolved O_2 with the ink (Eq.3.7).

3.3.5.3 Irradiation setup

The illumination of developed methods on construction materials (*Method 1 (Hydroxyl radical quantification using terephthalic acid fluorescence probe method* and *Method 2 (Electron (e^-) yield measurement using Rz and NBT inks)*) were performed inside the lab-made reactor depicted on Figure 3.14 under ambient conditions of temperature and humidity. The light source used are the same that used on previous experiment using TiO_2 plain photocatalyst, consisted of two fluorescent tubes Philips Actinic BL 15W/10 SLV. The light spectrum of lamps was included in Figure 3.15.

The irradiance on the construction sample tested surface was adjusted varying the distance between the light source and the sample. For accurate intensity measurements, the sensor was placed having its top window in the same height as the sample surface and in a location corresponding to the centre of the sample surface. The intensity was let to stabilize 15 minutes before performing the irradiance measurements. The selected construction materials were irradiated at 5 ± 0.25 and 10 ± 0.25 W/m². A summary of experimental irradiation conditions used in each test on selected construction materials is presented in Table 3.9.

3.4 Validation of development methods

In order to confirm that the development analytical tests based on the detection of active species are suitable for monitoring the photocatalytic activity of construction materials, the results from proposed methods were validated through the comparison with the results of previous selected standardized methods for determination of photocatalytic activity (Photocatalytic oxidation of gaseous NO to nitric acid and Rhodamine (RhB) discoloration). The procedure details used of these standardized tests are described in the following sections.

3.4.1 Photocatalytic oxidation of gaseous NO to nitric acid (ISO 22197-1:2007 and UNI 11247:2010)

The NO_x oxidation tests consist of the continuous monitoring of the NO and NO₂ concentration during the gas phase heterogeneous photocatalytic oxidation of NO in air by the tested samples. The gas composition for the oxidation tests was generated by two gas bottles containing NO 4.6 ppmvol, balanced with N₂, relative uncertainty: $\pm 5\%$, and pure dry air Alphagaz 1, O₂ 20% balanced with N₂, purity above 99.999%. The bottle of NO contains a small amount of NO₂ (<7%). The flow of each gas was controlled by two mass flow controllers, keeping the flow rate stable and at desired quantity. The ISO standard uses an initial concentration of NO of 1000 ± 50 ppb and a flow rate of 3L/min, while the UNI standard 400 ± 50 ppb of NO and a flow rate of 1.5 L/min. The mass flow controllers were supervised and managed by Brooks Microprocessor Control & Read Out Unit Model 0154. The maximum flow rate, valve seat and o-ring material and type of gas controlled by each mass flow controller are specified in Table 3.7.

Table 3. 7 Characteristics of the mass flow controllers used to adjust and control the flow rate of gases

Controller	Gas	Maximum flow (l/min)	Valve seat material	O-ring material
1	Dry Air	10	Viton	Viton
2	NO + N ₂	1	Kalrez	PTFE/Kalrez

An overview of the experimental setup is illustrated in Figure 3.21, indicating the connections between the different equipment and valves used to control the flow pattern in the system. Figure 3.22 included some pictures of the principal parts used in this work.

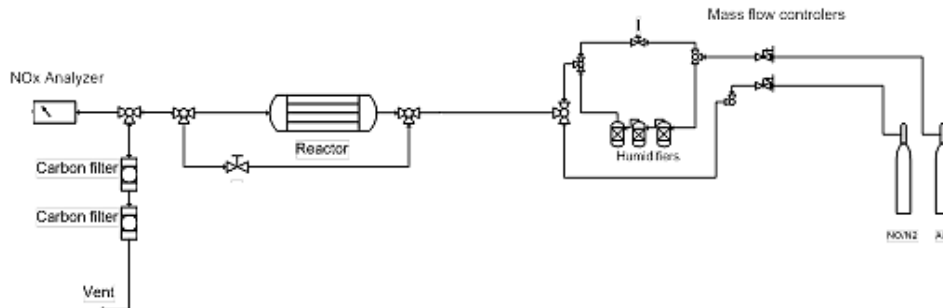


Figure 3. 21 Experimental set-up for the NO_x tests.

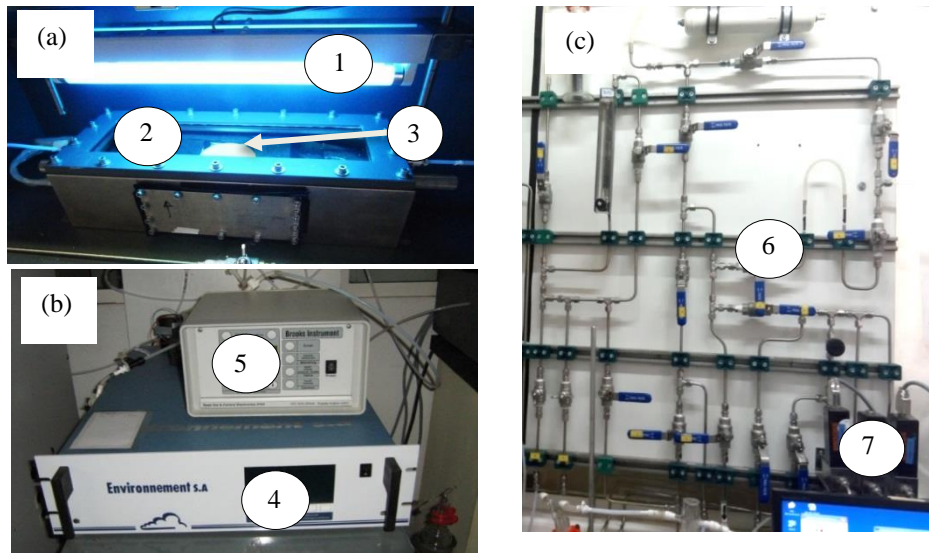


Figure 3. 22 (a) Illumination system⁽¹⁾, transparent window of reactor⁽²⁾ and sample⁽³⁾ for the NO_x remediation tests, (b) NO_x analyzer⁽⁴⁾ and control system for the mass flow controllers⁽⁵⁾, and (c) NO_x circuit⁽⁶⁾ and mass flow controllers⁽⁷⁾.

ISO tests require a controlled humidity of 50%. The test gas humidification was achieved by dividing the air stream in two flows, where one of them was humidified by passing through 3 water flasks connected in series containing deionised water, and the other was passing in a tube connected to valve “I”, without humidification and thereafter the two flows were connected to form only one flow. In this way, the desired humidity was set by adjusting using the valve “I” (see Figure 3.21), that can be gradually closed or opened and hereby step wise regulate the flow that was not humidified and altering the humidity. In the case of UNI standard, it was not necessary the use of humidifiers, and only used the degree of humidity of the feed flow that is approximately $20 \pm 2\%$.

The temperature for both tests was regulated by the ambient temperature in the laboratory ($25\pm 2^\circ\text{C}$). Both parameters were controlled during the test using humidity and temperature logger with digital display measuring each 10 seconds contained in a chamber after the reactor exit.

The reactor used was made of stainless steel and the interior of the reactor in contact with the airflow was made of soda lime glass. The reactor window was made of Pyrex glass permitting the transmittance of UVA. The light source was located outside the reactor vertically above the reactor window to avoid its influence on the gas flow.

The irradiance setup used on NO_x air purification standard tests was the same that used on the proposed developed methods (two fluorescent tubes Philips Actinic BL 15W/10 SLV, see spectra on Figure 3.15).

The irradiation intensities used in all samples were $10\pm 0.25\text{ W/m}^2$ and $20\pm 0.25\text{ W/m}^2$ according to the stipulated conditions on the ISO and UNI standard respectively. In one set of experiments, the UNI tests were performed using $10\pm 0.25\text{ W/m}^2$ with the objective to get a compressive comparison with another's terephthalic acid fluorescence probe (TA-FL) method results using the same experimental irradiance conditions. The intensity of the irradiance was adjusted by altering the distance between the light source and the sample. The intensity was measured placing the top window of the UVA sensor (UV/Vis/NIR spectrophotometer AvaSpec ULS3648-USB2-UA-25) in the same height as the sample surface and placing the reactor window in top of the sensor window. The light source was switched on to stabilize 15 minutes before performing the irradiance measurements. The location of the measurements was in the middle of the fluorescent tube length and just below the middle of the tubes being the same position of the sample when present.

The exit gas stream let to vent was passing through two carbon filters adsorbing the nitrous oxides before being emitted to the atmosphere. The tubes for the gas flow, valves and connections were made of stainless steel for avoid any alteration of NO_x composition.

A summary of the experimental conditions used on photocatalytic oxidation of gaseous NO to nitric acid test and the samples analysed was included in Table 3.8.

Table 3. 8 Summary of experimental conditions used on NO_x oxidation test.

Type of material defined in Section 3.1.2*		Standard procedure**	Initial concentration (ppb)	Flow rate (l/min)	Irradiation time	Irradiation intensity (W/m ²)
(a)	#C1-#C7	ISO	1000±50	3	5 h	10
	#C8-#C10	UNI	400±50	1.5	30 min	10
(b)		ISO	1000±50	3	5 h	10
(c)	#L1-#L2	ISO	1000±50	3	5 h	10
	#L3-#L5	UNI	400±50	1.5	30 min	10
(d)	#L6-#L12	UNI	400±50	1.5	30 min	20
*(a) commercial hardened cement-based materials, (b) commercial emulsion coatings, (c) lab-made cement-based samples, and (d) lab-made coloured mortars. Table 3.2 provided the details on formulation of all products tested. ** ISO: ISO 22197-1:2007 and UNI: UNI 11247:2010.						

In each ISO 22197-1:2007 test, first the NO/air test gas supply was adjusted to establish the required concentration of the test gas (outside reactor). Once established the concentration of supply air/NO gas, the gas stream was introduced into the reactor, and run over the sample in the dark for a period of ca. 30 min until the concentration was stable. Subsequently, the sample localized inside the reactor was irradiated for 5 hours. After that, the photoirradiation was stopped, switch on the zero-calibration gas under the same flow conditions (3 L/min) and was recorded the NO_x volume fraction for 30 min (desorption).

In the UNI set of experiments, the procedure was the following: (1) stabilization of the concentration in dark outside the reactor, (2) the gas stream was introduced into the reactor, and run over the sample in the dark for a period of ca. 30 min until the concentration was stable, (3) photocatalytic degradation (light on, 30 minutes) and (4) return to the original value (light off inside the reactor).

NO_x concentration of the gas was measured using a chemiluminescence analyser (AC-32 M, Environment S.A., Figure 3.22b). The calculation of the amount of NO_x removal during the irradiation by the test sample was calculated as stipulated in the both standards used, ISO 22197-1:2007 (Eq. 3.8-3.10) and UNI 11249:2010 (Eq.3.11)

$$n_{NO} (\mu mol) = \left(\frac{f}{22.4}\right) \cdot (\phi NO_o - \phi NO) dt \quad (3.8)$$

$$n_{NO_2} (\mu mol) = \left(\frac{f}{22.4}\right) \cdot \int (\phi NO_2 - \phi NO_{2,o}) dt \quad (3.9)$$

$$X_{NO_x} (\%) = 100 \cdot \frac{(\phi NO_{x,0} \cdot t_{irr} - \int \phi NO_x dt)}{\phi NO_{x,0} \cdot t_{irr}} \cdot \frac{W_{irr,teoric}}{W_{irr}} \cdot \frac{S_{teoric}}{S} \quad (3.10)$$

where NO_0 is the inlet concentration of nitrogen monoxide ($\mu\text{L/L}$), NO is the outlet concentration of nitrogen monoxide ($\mu\text{L/L}$), $NO_{2,0}$ is the inlet concentration of nitrogen dioxide ($\mu\text{L/L}$), NO_2 is the outlet concentration of nitrogen dioxide ($\mu\text{L/L}$), t is the time of removal operation (min), t_{irr} Time of irradiation (min), f is the flow rate converted into that at the standard state (0°C , 1.013 kPa) (L/min), $NO_{x,0}$ is the inlet concentration of NOx ($\mu\text{L/L}$), NO_x is the outlet concentration of NOx ($\mu\text{L/L}$), S is the real surface of samples (m^2), S_{teoric} is the surface teoric of the sample (49 cm^2). W_{irr} is the irradiation potency over the sample per surface unit (W/m^2) and W_{teoric} is the teoric irradiation potency over the sample per surface unit (10 W/m^2).

$$NOx_{removed} (\%) = 100 \cdot \left[\frac{(C_B - C_L)}{C_B} \cdot \frac{I_N}{I} \cdot \frac{S_N}{S} \right] \quad (3.11)$$

where C_B is the measured concentration of NOx in dark conditions (ppb), C_L is the measured concentration of NOx in light conditions (ppb), I_N is the nominal irradiance (20 W/m^2), I is the measured irradiance (W/m^2), S_N is the nominal surface of the sample (64 cm^2) and S is the measured area of the sample.

3.4.2 Rhodamine (RhB) discoloration (UNI 11259:2008)

RhB UNI standard was developed to measure the photocatalytic self-cleaning activity by materials based on hydraulic binders. The determination of the photocatalytic activity was done by measuring the colour intensity of the organic colorant rhodamine B on the surface of the sample, where higher photocatalytic activity corresponds to a higher colour intensity decrease. The colour was measured according to the CIELAB colour space (see Figure 3.19) by a portable spectrophotometer (CM-2300d-Konika Minolta, Figure 3.20b), that was also used for measuring the reductive inks test.

According to the UNI standard, due to the red color of RhB, the chromatic coordinate a^* from CIELAB colour space is used to assess the oxidation of dye during light exposure. Furthermore, the value of a^* at 0 min, $a^*(0)$, must be at least of 12.

0.5 ml of RhB aqueous solution (distilled water) with a concentration of $0.05\text{ g/l} \pm 0.005\text{ g/l}$ was used as ink. In the performed test used a higher initial concentration of RhB compared to the standard (3 ml of RhB solution 0.0083 g/l) to assure a homogeneous layer of the dye with this minimum characteristic value of $a^*(0) \geq 12$. The samples were coloured on the surface by RhB according to the following procedure: A circular area of

22 cm² was delimited on the sample surface by a silicone base hydrophobic product that was let to dry over the night. 1.5 ml of solution was extended over the surface letting the water to evaporate. The addition of solution was repeated a second time resulting in a total addition of 3 ml solution. The resulting amount of RhB on the surface was 0.066 g/m² ($137 \cdot 10^{-6}$ mol/m²). The samples were stored 24 hours at 57% RH and 21°C before the initiation of the irradiation of the samples.

The experimental setup consists of the radiation source placed vertically above the tested samples. The tests were performed in a chamber (MP control –MP CLIM, Figure 3.23) with controlled humidity and temperature ($20 \pm 1^\circ\text{C}$ and a relative humidity of $60 \pm 10\%$). The UVA irradiance intensity used in this test must be 3.75 ± 0.25 W/m².



Figure 3. 23 Imagens of the chamber with MP control –MP CLIM used in RhB tests.

In this work, the RhB test was performed using an aluminium plate with 9 LEDs perimeter 365 nm-LEDs, which ensure a homogeneous light supply (Figure 3.24). The intensity of the irradiance was measured placing the top window of the UVA sensor in the same height as the sample surface. The distance adjustment was done by placing the samples on top of elevation tables adjusting the height. For accurate intensity measurements, the sensor was placed having its top window in the same height as the sample surface and in a location corresponding to the centre of the sample surface. The irradiance was let to stabilize 15 minutes before performing the irradiance measurements.

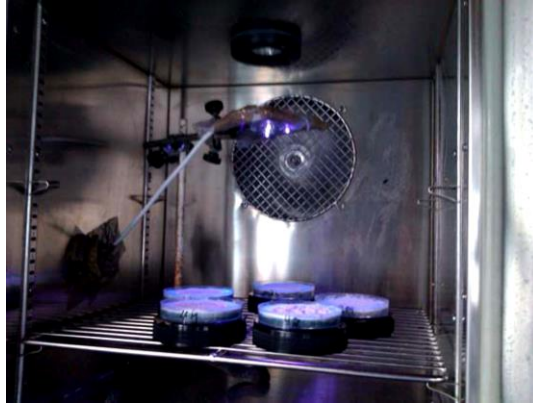


Figure 3. 24 Image of 365 nm LEDs illumination system used in RhB tests.

The colour measurements were performed in the 3 different points of coloured area, repeated 3 times on each sample and the mean value was calculated. If a result exceeds more than $\pm 10\%$ variation with respect to another, the result is discarded and the measurement is repeated.

The rate of decrease of a^* is calculated after 4 h (R_4) and 26 h (R_{26}) exposition time (Eq. 3.12 and 3.13).

$$R_4(\%) = \frac{a^*(0) - a^*(4)}{a^*(0)} \cdot 100 \quad (3.12)$$

$$R_{26}(\%) = \frac{a^*(0) - a^*(26)}{a^*(0)} \cdot 100 \quad (3.13)$$

Where: $a^*(0)$ is the colour intensity coordinates of specimens before the UV irradiation, and $a^*(4)$ and $a^*(26)$ are the colour intensity a^* coordinates of specimen at 4 hours and 26 hours of irradiation respectively.

Table 3. 9 Summary of the main performed photocatalytic proposed and standardized tests on selected construction materials and irradiance conditions used.

Sample type*	Name Sample	Proposed developed methods		Standard methods for determination of photocatalytic activity	
		METHOD 1: Hydroxyl radical quantification using terephthalic acid fluorescence probe method	METHOD 2: Electron yield measurement using Rz and NBT ink method	photocatalytic oxidation of gaseous NO to nitric acid (ISO 22197-1:2007 and UNI 11247:2010)**	Rhodamine (RhB) discoloration (UNI 11259:2008)
(a)	#C1	5 W/m ²	5 W/m ²	10 W/m²	3.75 W/m ²
	#C2	5 W/m ²	5 W/m ²	10 W/m²	3.75 W/m ²
	#C3	5 W/m ²	5 W/m ²	10 W/m²	3.75 W/m ²
	#C4	5 W/m ²	5 W/m ²	10 W/m²	3.75 W/m ²
	#C5	5 W/m ²	5 W/m ²	10 W/m²	3.75 W/m ²
	#C6	5 W/m ²	5 W/m ²	10 W/m²	3.75 W/m ²
	#C7	5 W/m ²	5 W/m ²	10 W/m²	3.75 W/m ²
	#C8	10 W/m ²	-	10 W/m ²	-
	#C9	10 W/m ²	-	10 W/m ²	-
	#C10	10 W/m ²	-	10 W/m ²	-
(b)	#E1	5 W/m ²	5 W/m ²	10 W/m²	3.75 W/m ²
	#E2	5 W/m ²	5 W/m ²	10 W/m²	3.75 W/m ²
	#E3	5 W/m ²	5 W/m ²	10 W/m²	3.75 W/m ²
(c)	#L1	5 W/m ²	5 W/m ²	10 W/m²	3.75 W/m ²
	#L2	5 W/m ²	5 W/m ²	10 W/m²	3.75 W/m ²
	#L3	10 W/m ²	-	10 W/m ²	-
	#L4	10 W/m ²	-	10 W/m ²	-
	#L5	10 W/m ²	-	10 W/m ²	-
(d)	#L6	10 W/m ²	-	20 W/m ²	3.75 W/m ²
	#L7	10 W/m ²	-	20 W/m ²	3.75 W/m ²
	#L8	10 W/m ²	-	20 W/m ²	3.75 W/m ²
	#L9	10 W/m ²	-	20 W/m ²	3.75 W/m ²
	#L10	10 W/m ²	-	20 W/m ²	3.75 W/m ²
	#L11	10 W/m ²	-	20 W/m ²	3.75 W/m ²
	#L12	10 W/m ²	-	20 W/m ²	3.75 W/m ²

*Construction samples used in this work were of four different types: (a) commercial hardened cement-based materials, (b) commercial emulsion coatings, (c) lab-made cement-based samples, and (d) lab-made coloured mortars. Table 3.2 provided the details on formulation of all products tested. **Bold type indicated ISO 22197-1:2007 test. The other ones were performed according UNI 11247:2010 standard.

As a summary, Figure 3.25 gives a schematic diagram of the design of this PhD's project.

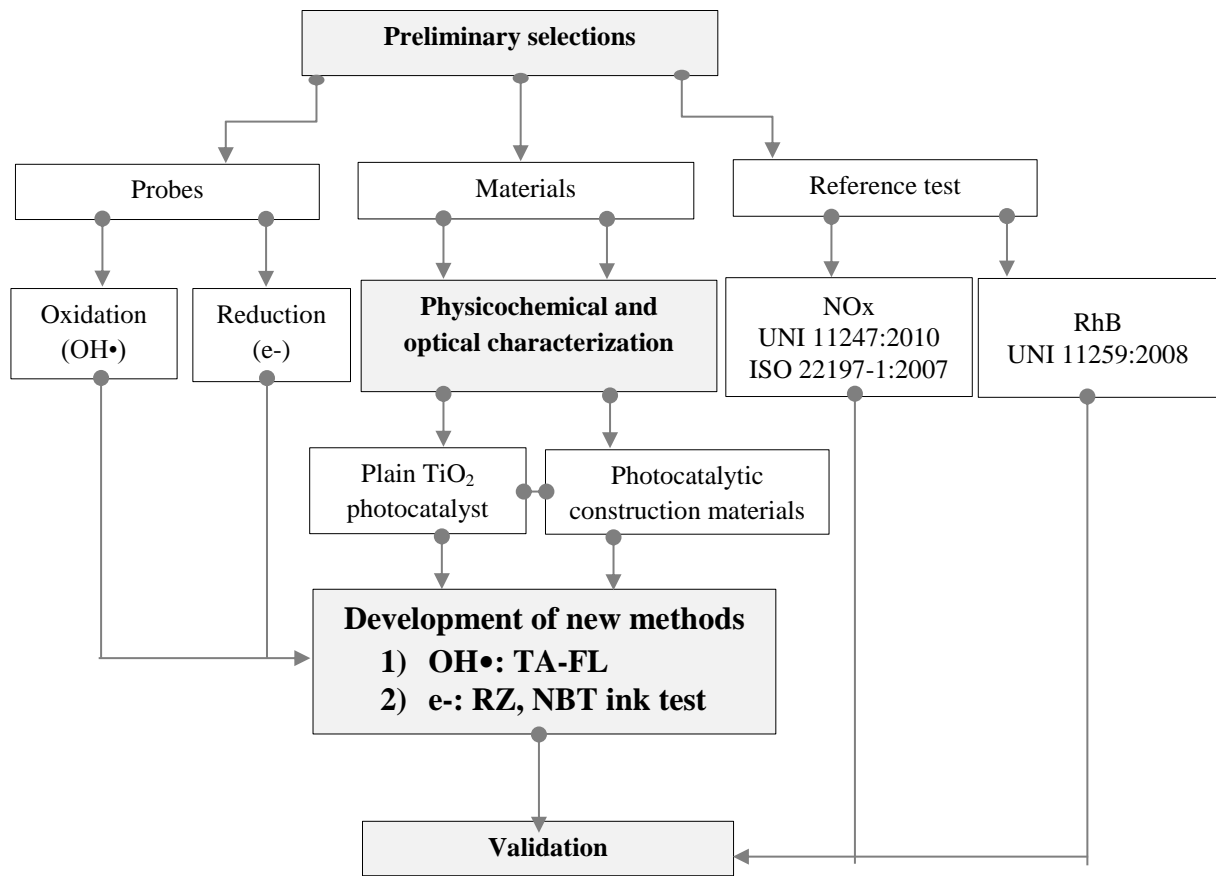


Figure 3. 25 Schematic diagram of this PhD's project.

CHAPTER 4

Results and discussion

4.1 Selection of probes

As explained in the experimental part, previous to the application of probes on the photocatalytic processes, a preliminary selection of probes was performed in order to choose the optimum one to be used in a further analysis of the active species formed in photocatalytic construction materials.

To evaluate the suitability of the different probes, the first step was to make a calibration curves in function of the concentration, measuring it in function of their fluorescence intensity. In all cases, except for the TA probe, all of selected probes reacted with the active species leading to a decrease of their concentration; thus, the concentration calibration curves were performed using different concentration of each probe. TA is a special case as this probe was calibrated using the standard product TAOH. As previous explained, 2-hydroxyterephthalic (TAOH) fluorescence product results from the selectively reaction of TA probe with $\text{OH}\cdot$. Figure 4.1 presents all of calibration concentration curves.

From these calibration curves, the optimum concentration of the probes for the further experiments was selected. All of these optimum concentrations were localized in the higher range or linearity of the calibration curves in order to ensure a wider working range during the photocatalytic oxidative degradation. Accordingly, to this ranges, concentration values chosen for the probes were $70\mu\text{M}$, $1.25\mu\text{M}$, $800\mu\text{M}$ for FC, RhWT respectively. YA and PH were discarded because they did not presented linearity in the tested conditions (Figure 4.1c-d). For TA, the relationship between fluorescence (FL) intensity at 425 nm and the concentration of TAOH is given in (Figure 4.1f). Solutions of standard TAOH presented a linear relationship between FL intensity and concentration up to $2.5\mu\text{M}$ concentration. The negative deviations observed at higher concentrations in a are considered to be caused by TAOH absorption and/or fluorescence quenching [168]. In this case, the concentration of TA was $6.2\mu\text{M}$.

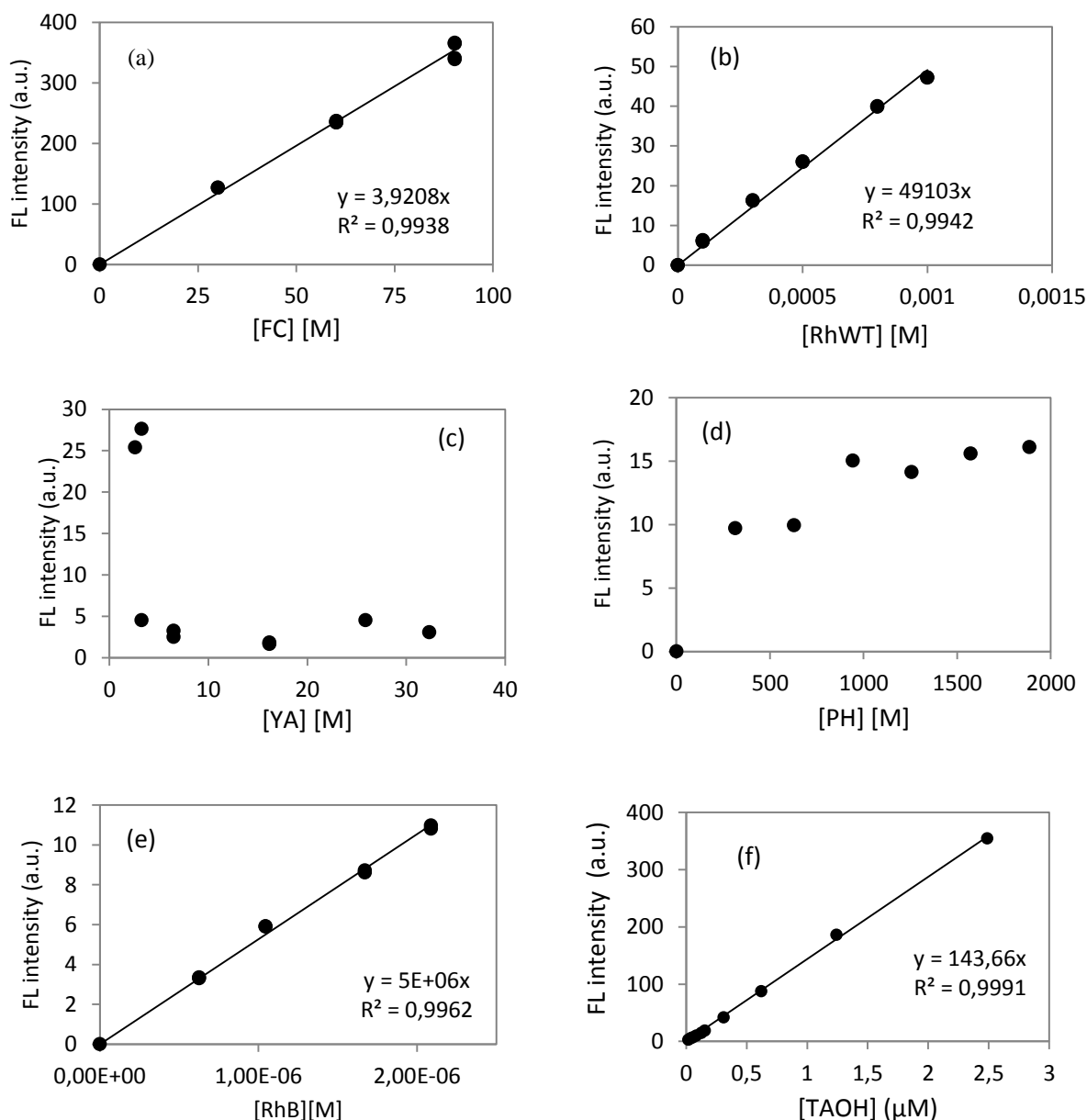


Figure 4. 1 Fluorescenc calibration curves in function of probes concentration. (a) Fluorescein (FC), (b) Rhodamina WT (RhWT), (c) Yellow alizarin (YA), (d) Phenolphthalein (PH), (e) Rhodamine B (RhB), and (f) terephthalic acid (TA)

Considering the importance of the $\text{OH}\cdot$ production on the photocatalytic process, all of oxidative probes were calibrated in function of the $\text{OH}\cdot$ concentration. Several concentrations of $\text{OH}\cdot$ were investigated, generating them through Fenton's reaction. 100 ml of each probe were mixed with 2 mg of $\text{FeSO}_4\cdot 7\text{H}_2\text{O}$ and different know quantities of H_2O_2 (30% v/v). After waiting for 10 minutes, fluorescence intensity was immediately measured [169, 170]. In Figure 4.2, the variation of concentration in function of H_2O_2 concentration (μL) is presented for TA and FC. RhB was discarded because has a very

small detection range; this would limit its use as a detection probe of active species on further photocatalytic experiments. RhWT probe was discarded because no linear relationship found between the amount of $\text{OH}\cdot$ and fluorescence changes in the conditions analysed. The results for TA and FC showed that for obtaining linear fluorescence emission intensity, at least $200\mu\text{l}$ and $300\mu\text{L}$ of H_2O_2 were required respectively. At high concentrations ($>650\mu\text{l}$, 35 mM) the rate production of TAOH and concentration decrease of fluorescein was diminished. The decrease in the rate production of TAOH is consistent with observations made by Kowaska et al. (2004) who state that a decrease in the rate production under UV with $\sim 30\text{ mM}$ H_2O_2 is due to reaction between $\text{OH}\cdot$ and H_2O_2 [171]. Furthermore, it is likely that at higher concentrations of H_2O_2 , the detection of $\text{OH}\cdot$ is reduced due to an increase in the number of $\text{OH}\cdot$ recombinations [172]. In addition, from this Figure 4.2, it can be observed that the TA probe are more sensitive for the $\text{OH}\cdot$ production that the FC probe. Beside this, the production of $\text{OH}\cdot$ can be directly quantitative by TA using the standard TAOH product yield.

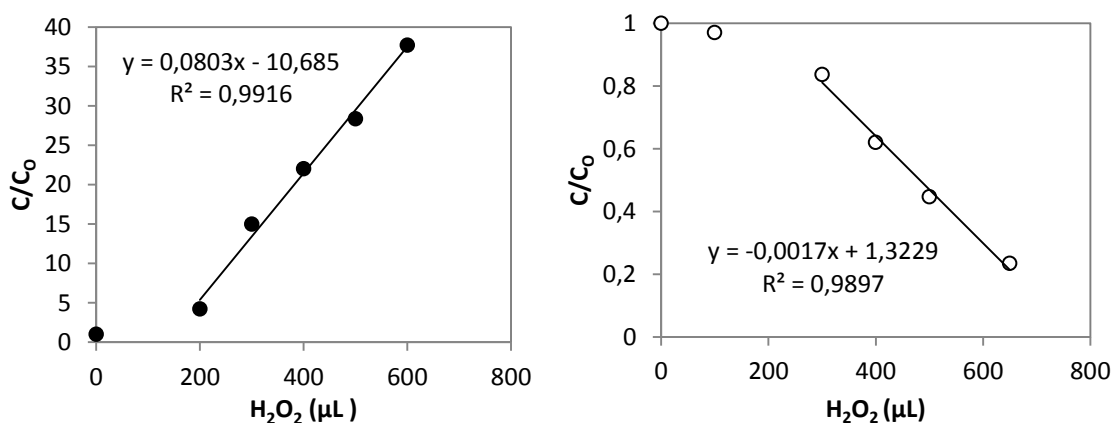


Figure 4. 2 Variation of probe concentration(C/C_0) in function of the addition of H_2O_2 of (a) TA and (b)FC.

Taking into account these results, it has been considered that TA probe is more suitable to further experiments for the determination of active species formed during the photocatalytic process on construction materials.

The probe TA was selected due to has been found to serve as adequate probe for the quantification of $\text{OH}\cdot$, translating the results of fluorescence intensity emission in terms of concentration through a calibration curve of the quantifiable hydroxylation, 2-hydroxyterephthalic (TAOH) product resulted from the reaction of TA probe with $\text{OH}\cdot$. It seems to comply the requirements to be an adequate probe to detect the generated $\text{OH}\cdot$ during the photocatalytic process as previously described on [15, 98, 99]. The application of this method allows monitor the production rate of $\text{OH}\cdot$, which is usually considered as the main reactive oxygen specie of oxidative photocatalytic reaction [64]. Usually, the photo-generated $\text{OH}\cdot$ has two kinds of forms, that is, free $\text{OH}\cdot$ in solution and surface-bound $\text{OH}\cdot$ on sample surface [13, 14]. Various authors suggest that TA could probe only the free $\text{OH}\cdot$ and it cannot react with h^+ or the adsorbed $\text{OH}\cdot$ [13, 14].

In the case of reductive probes (Rz and NBT), considering that they are the only ones able to monitor the reductive photocatalysis (RP) process, both were considered in this work. As previously mentioned, most research on photocatalytic systems focus on either the oxidative photocatalysis, OP, or less the reductive photocatalysis, RP, although both equally take part on photocatalyzed redox reactions. In this way, using both selected probe type of methods (TA-FL and reductive probes) it will be possible to correlate the measured rates of the both different photocatalytic processes, as will be discussed later.

Apart from Rz dye, in this work, for the first time, NBT has also been used. This probe has been generally used as a molecular probe to identify the generation of $O_2^{\bullet-}$ in photocatalytic processes [20, 21]. However, the enhanced oxidation properties of tetrazolium salts induced by UV-irradiation, as is the case of NBT, demonstrated that electrons originating from the photochemical reactions are the dominant species for tetrazolium based probes reduction under O_2 -free conditions. In other words, the tetrazolium salts were turned into strong oxidants by the UV irradiation, which can extract electrons (e^-) directly from neighbouring substances other than selectively from the $O_2^{\bullet-}$ [111]. This work is the first one proposing the NBT probe to monitor the e-reductive rate during a photocatalytic process.

Among the variety of dyes used, Rz and NBT dyes were selected as both present certain interesting characteristics: both dyes during the reduction process change the colour (Rz - from blue to pink, and NBT - from pale yellow to purple). The visible colour change is preferable because it provides an easier detection method. On the other hand, it is also very stable under UV light, a requirement indispensable to be an adequate probe to evaluate a photocatalytic process.

This work is the first one proposing these three probes (TA, Rz and NBT) to monitor the photocatalytic process on construction materials. These probes fulfil all the relevant requirements vinculated with the probe (*see Chapter 3, Figure 3.2*).

4.2. Optimization of selected probes

Previous the application of probes to quantitatively measure the OH^{\bullet} production rate and the e^- reduction yield of a TiO_2 photocatalytic process, a specific study on the selected probe was carried out for the calibration of probes, optimization of the concentration and establishment of the selectivity.

4.2.1 Calibration of probes

The calibration curve of TAOH standard was previously displayed in the *Section 4.1 – selection of probes*, Figure 4.1(f). The absorbance calibration curve of Rz is shown in Figure 4.3. From the slope of Abs_{600} on irradiation time, the generation of e^- (R_{e^-} , $\mu\text{mol}/\text{min}$) on irradiated TiO_2 photocatalyst can be evaluated by comparing the Abs_{600} to that of the standard Rz solution using the e^- reaction mechanism of Rz summarized in Eq. 4.1.

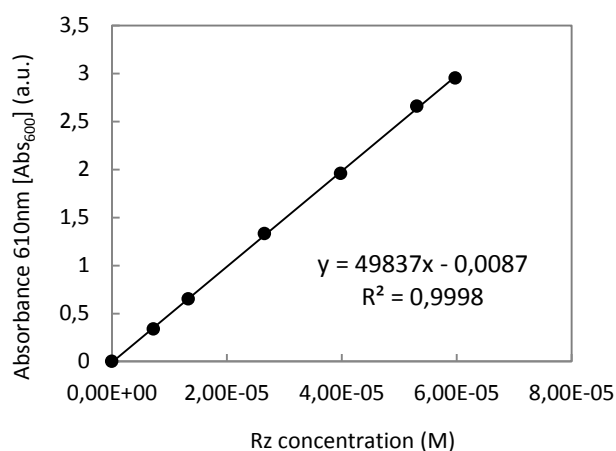


Figure 4. 3 Absorbance curve in function of Rz probe concentration.

4.2.2 Optimal probe concentration

Figure 4.4 (a-b) shows the production rate of TAOH as a function of the TA probe concentration in contact of a reference photocatalytic system (150 mg of the photocatalyst Aeroxide® TiO_2 -P25 from Evonik suspended in 100 ml of TA). A constant photocatalytic production system of active species was obtained, which allows to determine the $\text{OH}\cdot$ detection capability of the probe in function of the used concentration. At low concentrations of the probe, the amount of product increased, which indicates that TA concentration was the limiting factor in the $\text{OH}\cdot$ detection. From 2 mM TA, an increase in the concentration did not change the product yield. These data indicate that no additional product could be achieved by increasing the concentration of TA. As a result, in the plateau region concentrations, the moles of product are proportional to the moles of $\text{OH}\cdot$ produced. Under these conditions, assuming a 35% yield of the reaction of TA with $\text{OH}\cdot$ [102, 150], the probe allows the detection of up to $0.073 \pm 0.004 \mu\text{moles OH}\cdot/\text{min}$. Based on these results, and taking into account the fluorescence background of TA and its solubility, a concentration of 2 mM TA was chosen for further experiments with selected plain photocatalyst and construction materials.

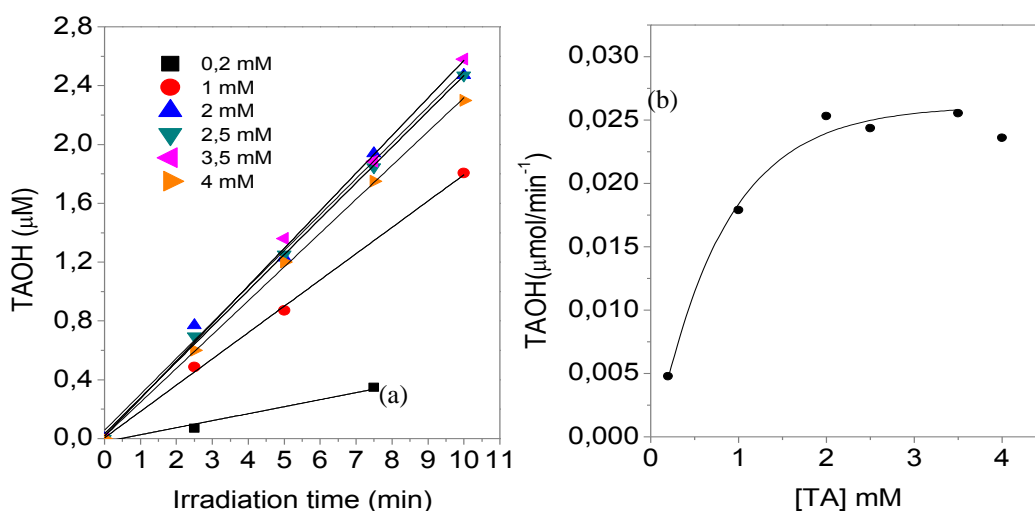


Figure 4. 4 (a) Irradiation time dependence of the TAOH concentration in function of TA probe concentration (0.2-3.5 mM) and (b) Formation rate of TAOH calculated from the corresponding slope of TAOH concentration on irradiation time in function of [TA].

In the case of reductive probes (Rz and NBT) the concentration of probes used was selected following the previously formulation described in literature [119] with some modifications that will be specifically explained in each corresponding section.

4.2.3 Selectivity analysis

The selected concentration of TA ($2 \cdot 10^{-3}$ M) and the pH of the solution has been tuned to be high (\sim pH12) favours the reaction with OH^\bullet [161]. The reaction between the photo-generated h^+ and the probe to form TAOH is unlikely because, unless the concentration of the probe molecules is quite high (in the range of 10^{-1} - 10^{-2} M), aromatic compounds like TA are oxidized by OH^\bullet more rapidly than by h^+ [99, 173, 174]. Even so, the selectivity of the previous selected concentration (2mM) was evaluated using the previous reference photocatalytic system (150 mg of the photocatalyst Aeroxide® TiO_2 -P25 from Evonik suspended in 100 ml of TA). Here DMSO was used as OH^\bullet scavenger, and EDTA as h^+ scavenger. The results are presented in Figure 4.5, where it can be deduced that DMSO inhibited completely TAOH formation, which means that the hydroxylation of TA proceeds exclusively through OH^\bullet . The inclusion of EDTA in the system implied a 16% less of fluorescence, which again means that most of the reaction is due to OH^\bullet . Additionally, quenching of the h^+ might have led to a smaller formation of OH^\bullet due to equilibrium between these species[175]. Combining these results, it can be deduced that oxidation of the probe through h^+ can be neglected at the experimental conditions used.

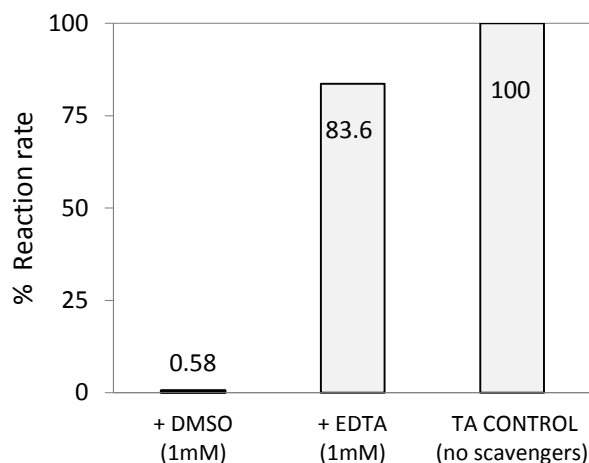


Figure 4. 5 Effect of various scavengers on percentage of TAOH formation rate at the selected concentration of TA (2mM).

The selectivity of reductive probes (Rz and NBT) was evaluated using a reference photocatalytic system (5.5 mg of the photocatalyst UV 100 from Hombikat suspended in 50 ml of Rz or NBT). Here the suspensions were exposed to irradiation under continuous agitation and the absorbance variation of both probes was also monitored under irradiation in a Pyrex glass cell under N_2 -conditions (1 L/min) and ambient conditions. Thus, comparing the reduction yield after different irradiation times under N_2 -conditions and ambient conditions, it is possible to define potential participation of the $O_2^{\cdot-}$ into the reductive yield of inks or interference of O_2 in the experimental conditions via competition of the dissolved O_2 with the ink (Eq. 3.7). The reduction yield was determined in function of the absorbance decreased at 600 nm and 259 nm [20] for Rz and NBT respectively after different irradiation time after centrifugation of photocatalyst.

As shown in Figure 4.6, the concentration was decreased in both probes on TiO_2 suspensions under UV irradiation no matter whether it was in a N_2 -saturated or ambient (oxygen atmosphere). This means that the reduction of Rz and NBT occur *via* electron participation and not by $O_2^{\cdot-}$ from photocatalyst. Beside this, in Figure 4.6, the reduction yield in ambient conditions (O_2 atmosphere) was even lower than those under N_2 -saturated conditions. From these results, it is clear that the rate of reaction 4.2 is reduced when O_2 is present for both inks. Thus, it can be concluded that the reduction yield in O_2 atmosphere for both inks is lower than those under N_2 -saturated conditions is attributed to the direct competition via the reaction of dissolved O_2 with the photo-generated electrons (Eq. 3.7). This could explain the phenomenon shown in Figure 4.6. The results of this work are relevant due to the increasing number of researchers that are using NBT to assess the production of $O_2^{\cdot-}$ on photocatalytic samples [20, 165, 176]. Since reaction defined as Eq. 3.7 is a competitive background, in this work, it was decided that, the study of selected materials that further presented was going to be carried out in ambient

conditions, which ultimately are the actual operational "real world" conditions of this materials. This analysis will be again performed in the experimental condition used on photocatalytic construction materials.

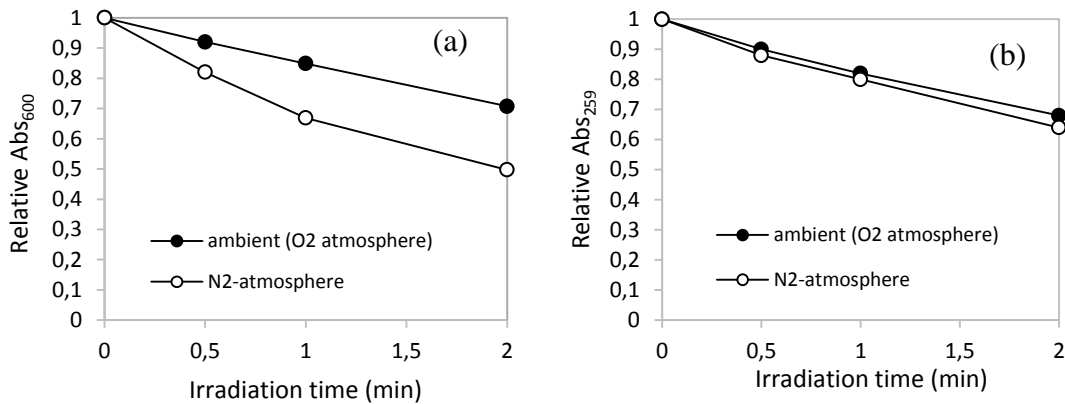


Figure 4. 6 Decay in relative absorbance at 560 and 259 nm of Rz and NBT probes under ambient conditions (O₂ atmosphere and N₂ atmosphere)

4.3 Preliminary study: application of selected probes on plain TiO₂ photocatalyst nanoparticles in aqueous dissolution

Prior to application the proposed methods on construction materials, the selected probes were applied on plain TiO₂ photocatalyst in order to better understand the behavior of these probes in a pure TiO₂ photocatalytic system, thus avoiding any type of interference of the matrix or support of selected construction materials on the measurements.

4.3.1 TiO₂ photocatalyst characterization

Figure 4.7 presents the XRD patterns of the TiO₂ samples. From this XRD results, the average crystallite sizes of anatase and rutile were determined according to the *Scherrer* equation, Eq.3.2 [177] and the percentages of anatase and rutile crystalline phases have been semi-quantified employing the *Spurr* equation, Eq.3.3[153]. Table 4.1 summarizes the main physical properties obtained from pure TiO₂ photocatalyst powders using XRD, together with the BET analysis.

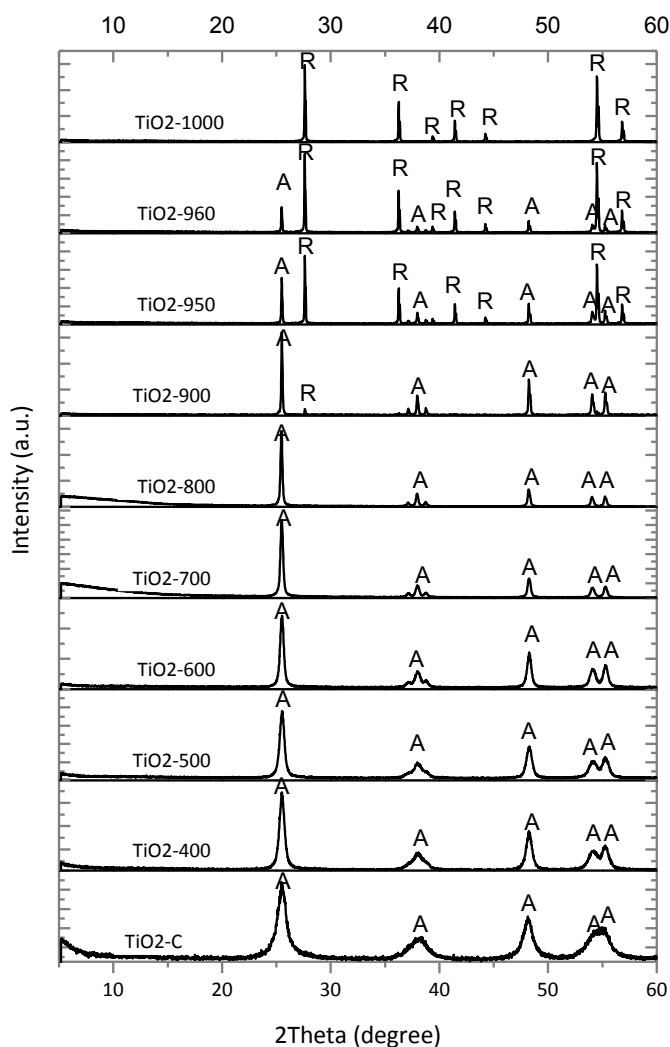


Figure 4. 7 XRD patterns of TiO_2 samples calcined at different temperatures

As evident from Figure 4.7 and Table 4.1, the diffraction peaks of $\text{TiO}_2\text{-C}$ are broader than the rest and correspond to the anatase phase of TiO_2 having a crystallite size around 8 nm. Broad diffraction peaks indicate the presence of small grain size and large grain boundary, containing large number of defects, that produce strain and prevent growth of the nanocrystallite [178, 179]. Rutile structure slightly appears for the samples heated at 900°C (1 %), and clearly at 950°C (51%) and 960°C (71%). Finally, the anatase structure completely disappeared at 1000°C . Thus, TiO_2 Hombikat ($\text{TiO}_2\text{-C}$) photocatalyst used as TiO_2 precursor powder sample shown extremely high crystalline phase stability, consistent with literature results[180]. Based on the *Scherrer* equation from the broadening of anatase (101) reflection and rutile (110) reflection, the crystalline sizes of anatase increase from 8.14 to 90.71 nm as the calcination temperature increases until formation of rutile. On the contrary, the crystallinity and crystalline size for rutile phase not follow a particular pattern in function of calcination temperature. The increases

of calcination temperature are also accompanied by decrease in the surface area of samples, as shown in Table 4.1.

Figure 4.8 (a-b) presents the results obtained by diffuse reflectance spectroscopy (DRS) of TiO₂ nanoparticles. From this figure, it can be observed a progressive red shift of absorption edges of TiO₂ samples in function of calcination temperature. At lower temperature than 900°C, the change in the absorption edges of TiO₂ samples is slight, while a progressive reduction in the absorption of light can be observed at UV wavelengths, which can be attributed to the enhanced scattering of light with larger crystalline size [181]. A higher progressive red-shift in the band edge was observed at temperatures higher than 900°C due to a gradual transition from anatase to rutile. The absorption edge of TiO₂-950 and TiO₂-960 mixed samples showed two absorption shoulders; the second hump between 375-425 nm may be due to the presence of Ti³⁺ or oxygen vacancies generated during the process of phase conversion from anatase to rutile [179]. Absence of absorption hump in the other samples not indicated that defects are absent. The absorption at around 330nm on is due to phonon assisted indirect transition from edge to the center of Brillion zone [179]. This indirect transition decreased during the calcination process, until its disappearance in samples that clearly content rutile phase. The results of DRS are in good accordance with the previous described XRD results.

The band gap (E_g) of TiO₂ powder samples were obtained by plotting the *Kubelka–Munk* (*K-M*) optical absorption coefficients [F(R)] using *Tauc* relation (Eq. 3.4 and 3.5). The plot $(F(R)hv)^{1/n}$ (n=2 for indirect band gaps like TiO₂) vs hv follows a linear dependence in the region of the valence band to conduction band (VB-CB) transition, and the linear extrapolation to the abscissa gives the E_g value. The values of the band gap of the samples are also given in Table 4.1. The E_g values of samples closely match with the E_g of anatase (3.2 eV) for TiO₂-C to TiO₂-900 or rutile (3.0 eV) from TiO₂-950. Notice that all the calcined samples have a band gap lower than the original TiO₂-C. The lowering of band edge in TiO₂ photocatalytic samples can be due to the presence of localized defect states in the forbidden zone of TiO₂-photocatalyst near the bottom/top of its CB-VB.

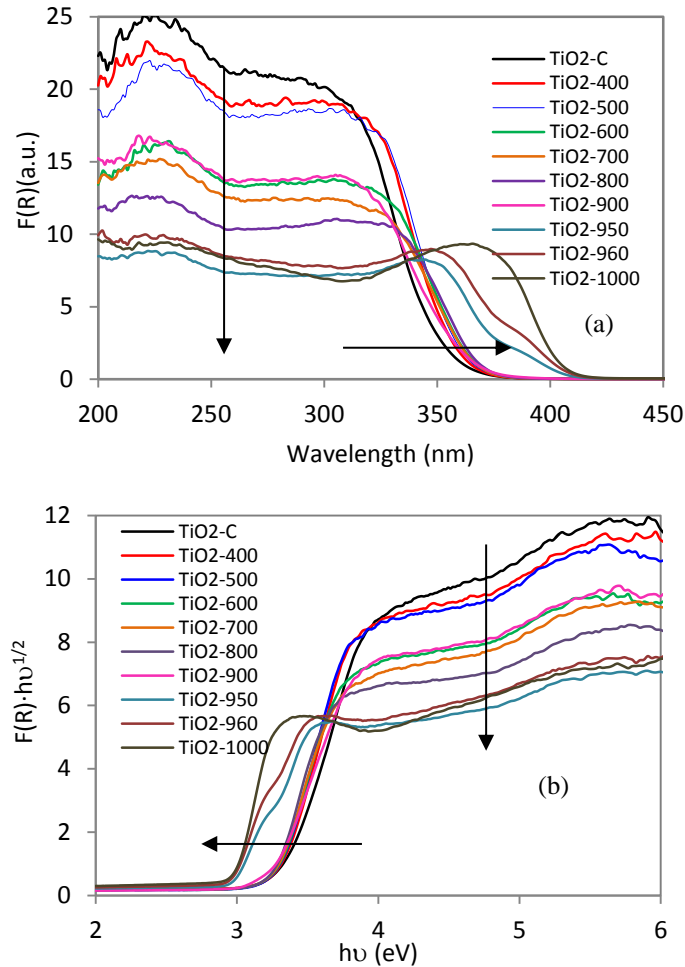


Figure 4. 8 (a) absorption spectra obtained via DRS of TiO_2 calcinated powder samples, the absorbance was plotted as the Kubelka–Munk function (FR) (b) Tauc plot of $(\text{FR}h\nu)^{1/2}$ vs the energy (eV) of the incident photon. Extrapolating the tangent of the band edge curve to the energy axis obtains the indirect bandgap energy (values included in Table 4.1).

Table 4. 1 Summary of physicochemical and optical properties of TiO_2 samples. A: anatase; R: rutile.

Samples	Phase percentage (%) [*]		Crystallite size(nm) [*]		FWHM (°) [*]		BET Surface area (m ² /g)	Band gap (eV)
	A	R	A	R	A	R		
TiO₂-C	100	-	8.14	-	0.99	-	310.08	3.32
TiO₂-400	100	-	11.25	-	0.65	-	109.50	3.30
TiO₂-500	100	-	16.5	-	0.51	-	79.41	3.29
TiO₂-600	100	-	32.48	-	0.37	-	48.79	3.26
TiO₂-700	100	-	49.1	-	0.26	-	26.73	3.25
TiO₂-800	100	-	69.17	-	0.18	-	12.88	3.22
TiO₂-900	99.1	1	75.29	163	0.17	0.074	9.52	3.22
TiO₂-950	44.9	51.1	90.07	138.33	0.18	0.075	3.37	2.94
TiO₂-960	28.5	71.5	90.71	135.85	0.21	0.076	3.25	2.91
TiO₂-1000	-	100	-	136.60	-	0.075	2.75	2.99

^{*}Estimated from the broadening of anatase (101) reflection and rutile (110) reflection in XRD

4.3.2 Quantitative formation rate of OH• on irradiated TiO₂ photocatalyst using terephthalic acid probe (TA)

Figure 4.9 shows fluorescence (FL) spectra obtained from supernatant liquid of the irradiated TiO₂-500 suspension for various duration times with 2 mM TA as an example. All observed FL spectra are identical to FL spectrum of TAOH [64, 99]. So, it can be deduced that fluorescent products generated during photocatalysis process in samples were due to the specific reaction between OH• and TA.

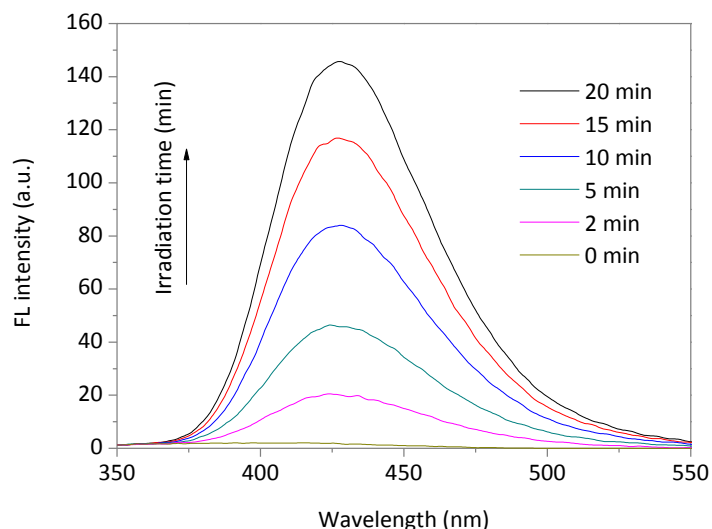


Figure 4. 9 Fluorescence spectra at various irradiation periods that are obtained from supernatant liquid of the irradiated TiO₂-500 suspension containing 2mM of TA probe.

Figure 4.10(a) presents linear relationship between the FL intensity and the duration of UV-irradiation of TiO₂ suspension samples. To quantitatively determine the concentration of TAOH, the calibration curve by plotting FL intensity at 425 nm against concentration of standard TAOH was used ($FL(a.u.) = 143.66 \cdot [TAOH](\mu M)$) (Figure 4.1(f), [64]). From the slope of FL intensity on irradiation time, the formation rate of OH• ($\mu mol/min$), was calculated by comparing the FL intensity obtained to that of the calibration curve using a trapping factor of 35% (Figure 4.10(b)). From this figure, it can be seen that when increasing the temperature of the treatment, the $R_{OH\bullet}$ increases rapidly up to the samples heat-treated to 700-800°C. Above 800°C, $R_{OH\bullet}$ decreases rapidly in coincidence with the appearance of rutile.

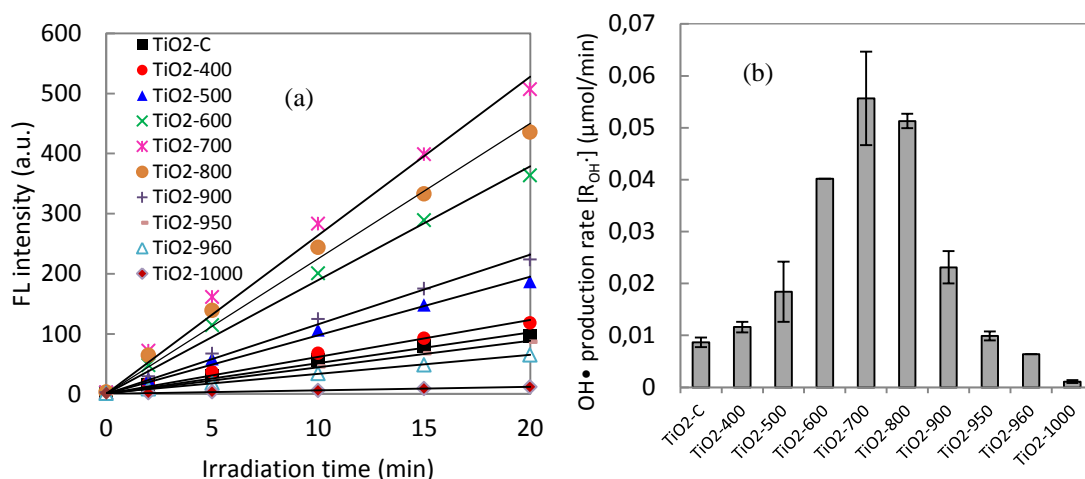


Figure 4. 10 (a) Time dependence of FL intensity of TiO₂ samples (average of two measurements) and (b) Formation rate of OH• (μmol/min) calculated from the corresponding slope of FL intensity on irradiation time (Figure 4.10 (a)) by comparing the FL intensity obtained to that of the calibration curve, FL (a.u.)=143.66·[TAOH](μM), using a trapping factor of 35%.

4.3.3 Formation rate of e⁻ on irradiated TiO₂ photocatalyst using Resazurin ink

The formation rate of e⁻ at photo-illuminated photocatalyst/water interface was detected by the UV-Vis absorbance technique using Rz as a probe molecule. Resazurin (blue) readily reacted with e⁻ to produce Resorufin (Rf, pink). Rf can be reduced subsequently to its colorless counterpart dihydroresorufin (HRf). However, previous studies demonstrated that the reduction of Rz ink by TiO₂ photocatalysis was first order, and the time for Rf to HRf reduction is at least 3.5 times more larger than the first reduction step [115]. As such, the rate of degradation of the Rz to Rf can be determined to by assessing the decrease in absorbance at 600 nm at early times (i.e. times in which the rate of decrease is linear). The linear changes of Abs₆₀₀ of all TiO₂ suspensions with the irradiation time are shown in Figures 4.11(a-b) using Rz probe with and without glycerol respectively. The nonlinear decrease with the increase of irradiation time in the more active TiO₂ suspension is attributed to the exhaustion of the Rz. Consequently, it could be inferred that the produced e⁻ at the TiO₂ surface was proportional to the irradiation time. From the slope of Abs₆₀₀ on irradiation time, the generation of e⁻ (R_{e⁻}, μmol/min) on irradiated TiO₂ photocatalyst can be evaluated by comparing the Abs₆₀₀ to that of the standard Rz solution (calibration curve, Figure 4.3) using the e⁻ reaction mechanism of Rz summarized in Eq. 4.1.

Herein, the e^- production rates using both Rz probe formulations, which were calculated from lines in Figure 4.11(a-b), are given in Figure 4.11c, where the percentages of recombination have also been included as calculated through Eq. 4.2. From this figure, it can be seen that the production rate of e^- in TiO_2 suspensions shows marked differences in function of Rz probe formulation with increasing heat treatment temperature between 400-1000°C due to the differences on the e^- measurement on hole scavenger system (glycerol) or Rz without glycerol. Image of colour change of Rz probe in function of irradiation time of TiO_2 -700 sample was included in Figure 4.12.

$$e^- \text{ Recombination } (\%) = 100 \cdot [Re- (\text{with glycerol}) - Re- (\text{without glycerol}) / Re- (\text{with glycerol})] \quad (4.2)$$

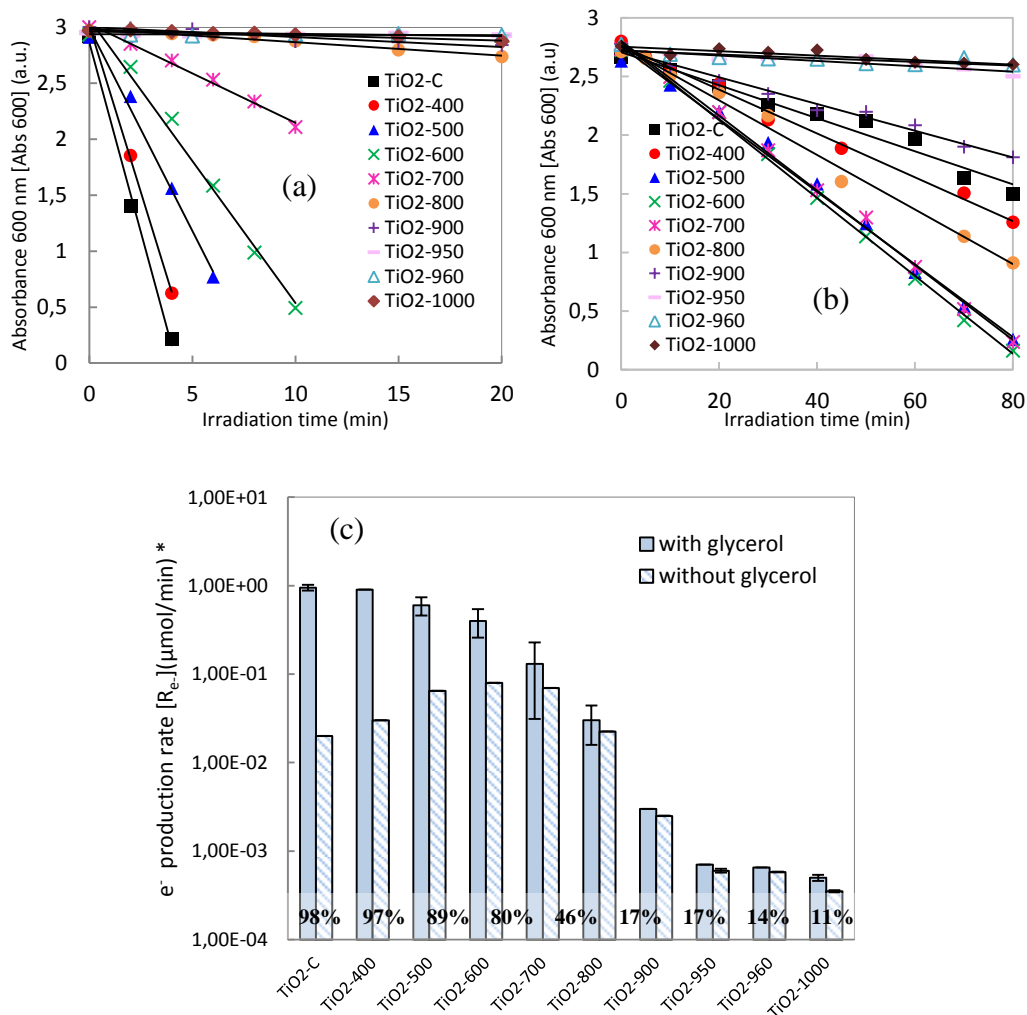


Figure 4. 11 Variation of the absorbance (Abs₆₀₀) due to irradiation time of all TiO_2 samples suspensions using Rz probe (a) with glycerol and (b) without glycerol, and (c) formation rate of e^- (R_{e^-}). The percentages of surface e^- recombination were also included using the Eq. 4.2.

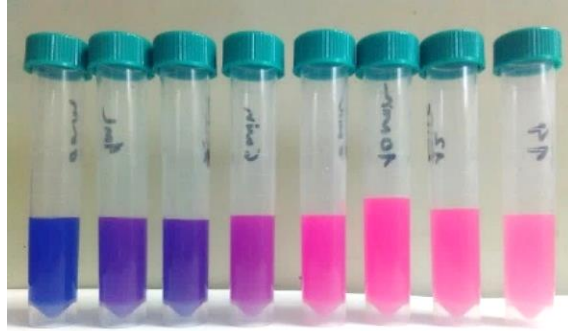


Figure 4.12 Image of Rz with glycerol probe degradation in function of irradiation time of samples TiO₂-700°C (measures each 2 minutes, final time 14 minutes).

4.3.4 Rhodamine B discolouration test

In Figure 4.13a the relative evolution of RhB concentration in water in function of the time of irradiation is shown for every sample. From the slope of the lines in Figure 4.13a, the rate of RhB degradation (K_{RhB} , min^{-1}) has been determined, and has been plotted in Figure 4.13b. As higher is the temperature of the calcination, higher is the rate constant K_{RhB} until reaching around 700-800°C, when it starts to decrease in coincidence with the appearance of rutile, as the rate of $\text{OH}\cdot$ formation ($R_{\text{OH}\cdot}$).

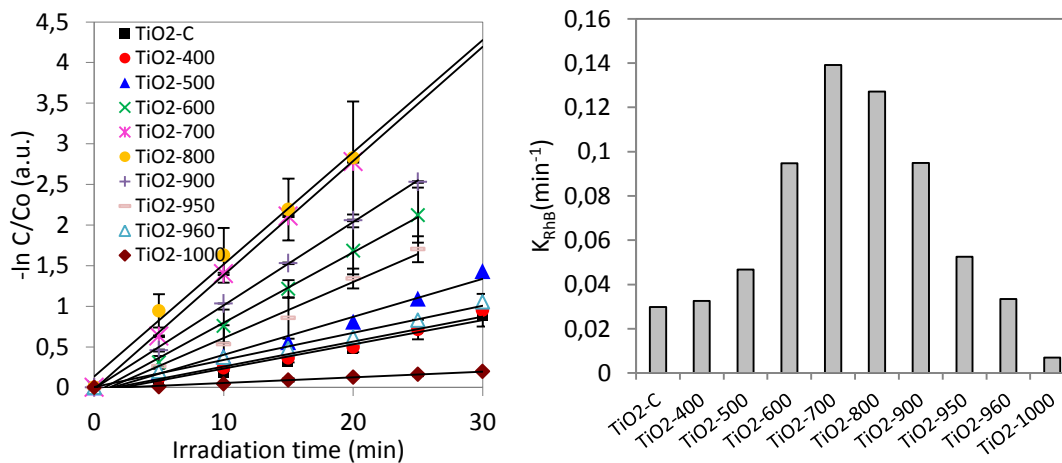


Figure 4.13 (a) RhB photo-degradation and (b) pseudo first order kinetic rate constant (K_{RhB}) for RhB degradation in the presence of TiO₂ samples (average of two measurements).

Different calcination temperatures induce significant effects on the intrinsic properties of the material, such as crystal size, type of phase present and content, surface area, which have an important influence on the photocatalytic activity. Figure 4.14 (a-c) presents the kinetic constant of degradation of RhB versus the size of the crystallites, BET area and percentages of each phase (anatase or rutile).

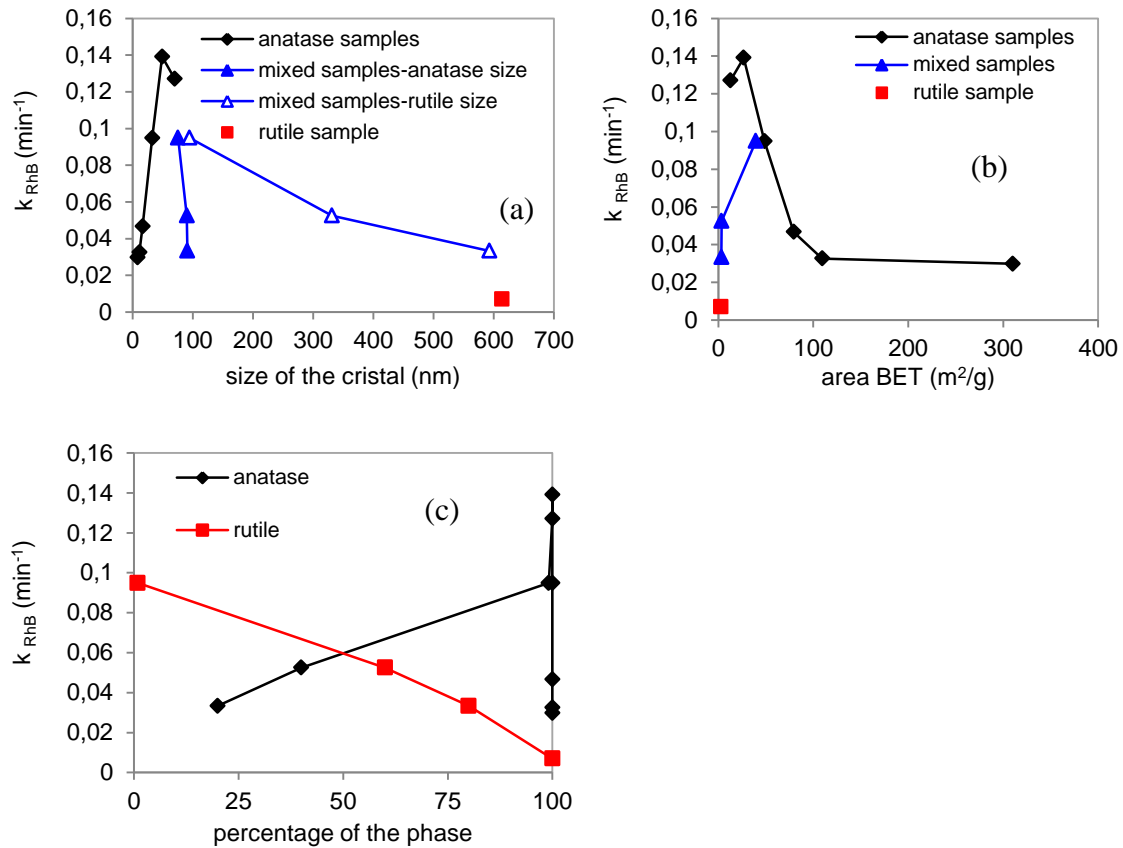


Figure 4. 14 Kinetic constant of degradation of RhB versus (a) Crystallite size, (b) BET area and (c) percentages of each phase (anatase or rutile).

In terms of general catalysis theory, the smaller the particle size, the larger the surface area, and therefore higher concentration of active sites per square meter as well as higher absorbance of the pollutant on the catalyst surface, that should lead to higher reactivity area[182]. In the present research (see Figure 4.14a), for pure anatase samples, as temperature of the treatment increases, leading to higher size of crystallites, the efficiency of the RhB decomposition increases following a linear trend. When rutile starts to be present in the samples, for both phases, the trend becomes the opposite than those having anatase as the only phase. Consequently, the same behavior takes place concerning BET area. Photocatalytic efficiency increases as long as BET area increases for rutile and anatase-rutile mixed samples while the trend is the opposite for pure anatase. From figure 4.14c it is clear that for pure anatase, the efficiency increases as the temperature of the treatment increases until rutile is formed, when the efficiency decreases almost linearly with the increase of the percentage of rutile.

Concerning the active species formed, the results of RhB photo-degradation and $\text{OH}\cdot$ production rate follow the same trend for all samples, with independence of microstructural parameters. In Figure 4.15, the correlation between $R_{\text{OH}\cdot}$ and K_{RhB} is given, showing a quite good linear relationship. These results may suggest that the higher RhB degradation of samples should be attributed to the higher photo-induced $\text{OH}\cdot$ production process due to correlation between them. These results are in accordance with the previously reports [72, 183].

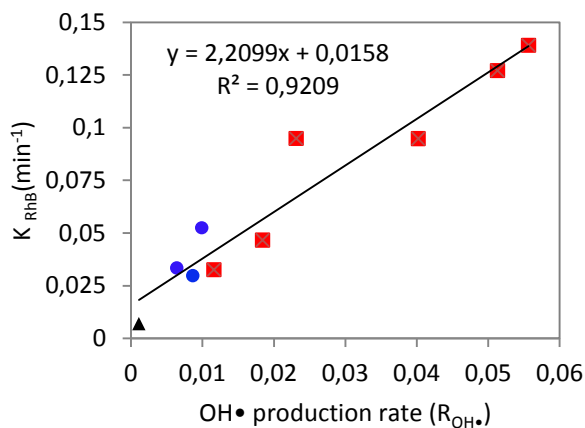


Figure 4. 15 Dependences of rate constant for RhB decomposition (K_{RhB}) on the rate of $\text{OH}\cdot$ formation ($R_{\text{OH}\cdot}$) of TiO_2 samples (geometric symbols: square: anatase, circle: anatase-rutile mixed, and triangle: rutile)

Concerning electrons, e^- (Re^-), in Figure 4.16(a-b) the rates of formation of electrons, as detected by the probes, both with and without glycerol are presented. From this figure, it can be deduced that there is not a clear relationship between e^- (Re^-) and degradation of RhB. However, in Figure 4.16b, it can be seen that the results determined by RhB degradation seem to follow the same trend with those determined by a Rz without glycerol. These results are a sign that although e^- participate on RhB, the complexity of the process involved on RhB degradation make the results show a large dispersion between both parameters, not allowing a clear relationship.

On the other hand, provided that the e^- production rate obtained using Rz with glycerol allows to measure the total photo-generated electrons transfer to surface after absorption light and before e^-h^+ recombination process, and the e^- rate obtained with Rz ink without glycerol gives the actual amount of e^- located onto the photocatalyst surface after the recombination process, and serve as redox sources for react with adsorbed reactants (RhB in our case), it seems to be reasonable that only the e^- rate obtained with Rz ink without glycerol showed some relationship with the photocatalytic oxidation of RhB. These results confirm again the importance of e^-h^+ recombination rate as a limiting factor in photocatalytic process.

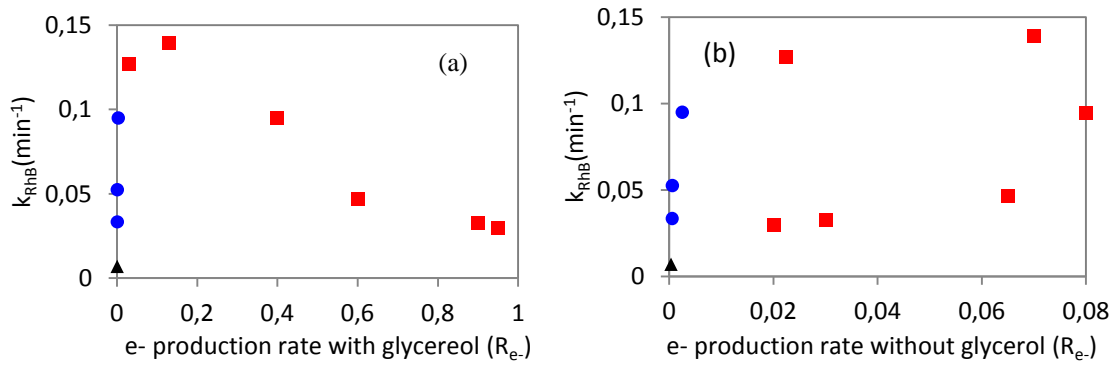


Figure 4. 16 Rate of degradation of RhB versus formation of electrons, as detected by the probes both (a) with, and (b) without glycerol. (geometric symbols: square: anatase, circle: anatase-rutile mixed, and triangle: rutile)

As said, from the different number of electrons detected depending on the use of glycerol, the percentage of recombination of electrons has been calculated. The dependence of the degradation of RhB with the percentage of e^- recombination is presented in Figure 4.17, where it can be observed that the e^- recombination is different for samples with different crystal phase composition. Samples of pure anatase present the higher amount of recombination, finding an inverse linear relationship between the k_{RhB} and the e^- recombination rate. In rutile-containing samples, although the surface recombination percentage was much lower than for anatase samples, this parameter do not seems to determine the final photocatalytic activity.

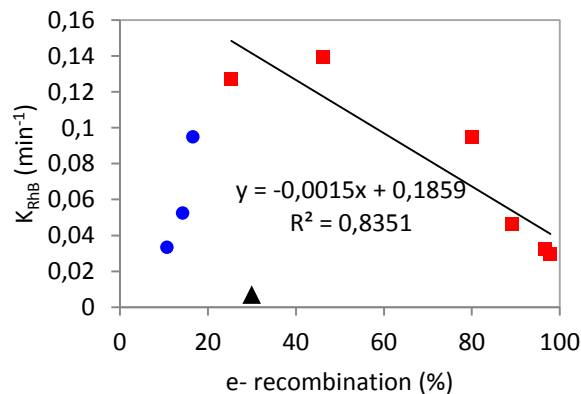


Figure 4. 17 Rate of degradation of RhB versus the percentage of e^- recombination (geometric symbols: square: anatase, circle: anatase-rutile mixed, and triangle: rutile)

In nanocrystalline semiconductor particles, when particle size decrease the e^- h^+ recombination becomes an important process, and therefore the photoconductivity and electron lifetimes increase with increasing particle size [184, 185]. Thereby in anatase samples, even though BET area diminishes with higher crystal size, increasing the temperature of calcination implies lower surface recombination, which seems to have a

dominant influence with respect to the crystallographic aspects. Under these circumstances, it is impossible to study the sole effect of a parameter. However, it is important to remark that the e^- production with controlled e^-h^+ recombination (R_{e^-} with glycerol) was higher when decreased the particle size due to a higher photonic efficiency, as expected; however, the limiting factor of e^-h^+ recombination reversed trend on pure TiO_2 anatase, as observed on results of e^- production rate without glycerol (uncontrolled e^-h^+ recombination). The possibility of trend reversed originated for different recombination rate corroborates the important influence of the dynamics of e^-h^+ recombination on the anatase samples. It is important also to notice that when rutile is present in the sample, the amount of $OH\cdot$ measured is higher than electrons detected using both probes with and without glycerol, which is not possible if every electron is being detected.

In explaining this experimental observation, it is necessary to take into account that: (1) $OH\cdot$ can be generated also as a result of a multistep reduction of oxygen [96]; however, taking into account that the probe for detection of electrons should avoid the reduction of oxygen, in these experiments, $OH\cdot$ are considered as generated from oxidation of water by the holes; (2) considering its behaviour as charge carriers, three type of electrons have been described: deeply trapped electrons in defects, shallowly trapped electrons in the mid-gap states and free electrons in the conduction band; (3) in anatase, free and shallowly trapped electrons are in equilibrium and have a lifetime longer than 1 ms, being highly reactive. In rutile, most electrons are deeply trapped, not been reactive with O_2 [186]. Therefore, it can be deduced that the method of quantitatively analyse electrons using Rz probe, is not detecting deeply trapped electrons, which cannot be considered a drawback of the method, as only reactive electrons, and then, those susceptible of participate in the redox reactions, are detected.

As a summary, the results obtained from this research have been depicted together in Figure 4.18, where the photocatalytic degradation rate of RhB, the production rate of $OH\cdot$ ($R_{OH\cdot}$), free and shallowly trapped electrons, e^- (R_{e^-}) before and after recombination and percentage of recombination (%), have been presented in function of the temperature of the calcination, BET area, phase content and anatase crystalline size.

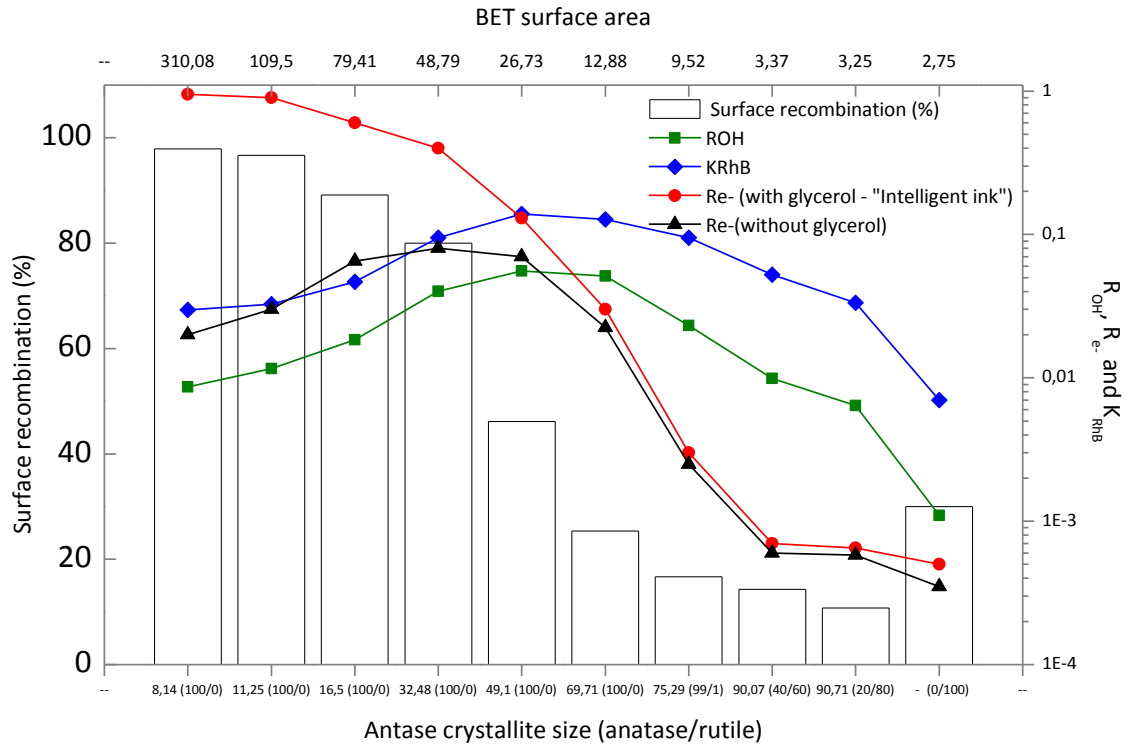


Figure 4. 18 Production rate of OH^\bullet (R_{OH} , $\mu\text{mol}/\text{min}$), free and shallowly trapped electrons (R_e , $\mu\text{mol}/\text{min}$), e^- surface recombination (%) and RhB photo-degradation (K_{RhB} , min^{-1}) in function of the temperature of calcination, BET surface area, anatase/rutile percentage content and anatase crystallite size.

4.4 Development of methods on construction materials

4.4.1 Characterization of construction materials

4.4.1.1 Composition -XRD and FRX

Figure 4.19-4.22 presents the XRD patterns of the samples tested. Taking into account that in some cases the TiO_2 phases associated to the photocatalyst are undetectable due to the high amount of aggregates mask the TiO_2 signals, images at the right side of Figure 4.19-4.22 displayed the zooms to be able to observe the small peaks of TiO_2 crystallite phases.

Figure 4.19 includes the commercial cement-based samples (#C1-#C10) spectra. In this figure, it can be seen the peak of the typical compounds present on cementitious materials: calcite, quartz, dolomite and portlandite. According to the results, it can be seen that the aggregates are siliceous for all the samples with the exception of #C7 and #C9 which include dolomite. Calcite also is shown in all samples. Concerning TiO_2 phases associated to the photocatalyst, it can be observed the main peak corresponding with anatase TiO_2 (101 , $2\theta \sim 25.4$) in all samples except for the non-photocatalytic sample

(#C6) and sample #C9. Rutile phase, only could be detected (110 , $2\Theta \sim 27.5$) in samples #C1-#C4, #C8 and #C10. The absence of TiO_2 crystallite peaks in the photocatalytic sample #C9 do not mean that any TiO_2 crystallite phases are present; provided #C9 this is a bilayer sample, and only includes the photocatalyst in a fine surface layer, the detection is quite difficult.

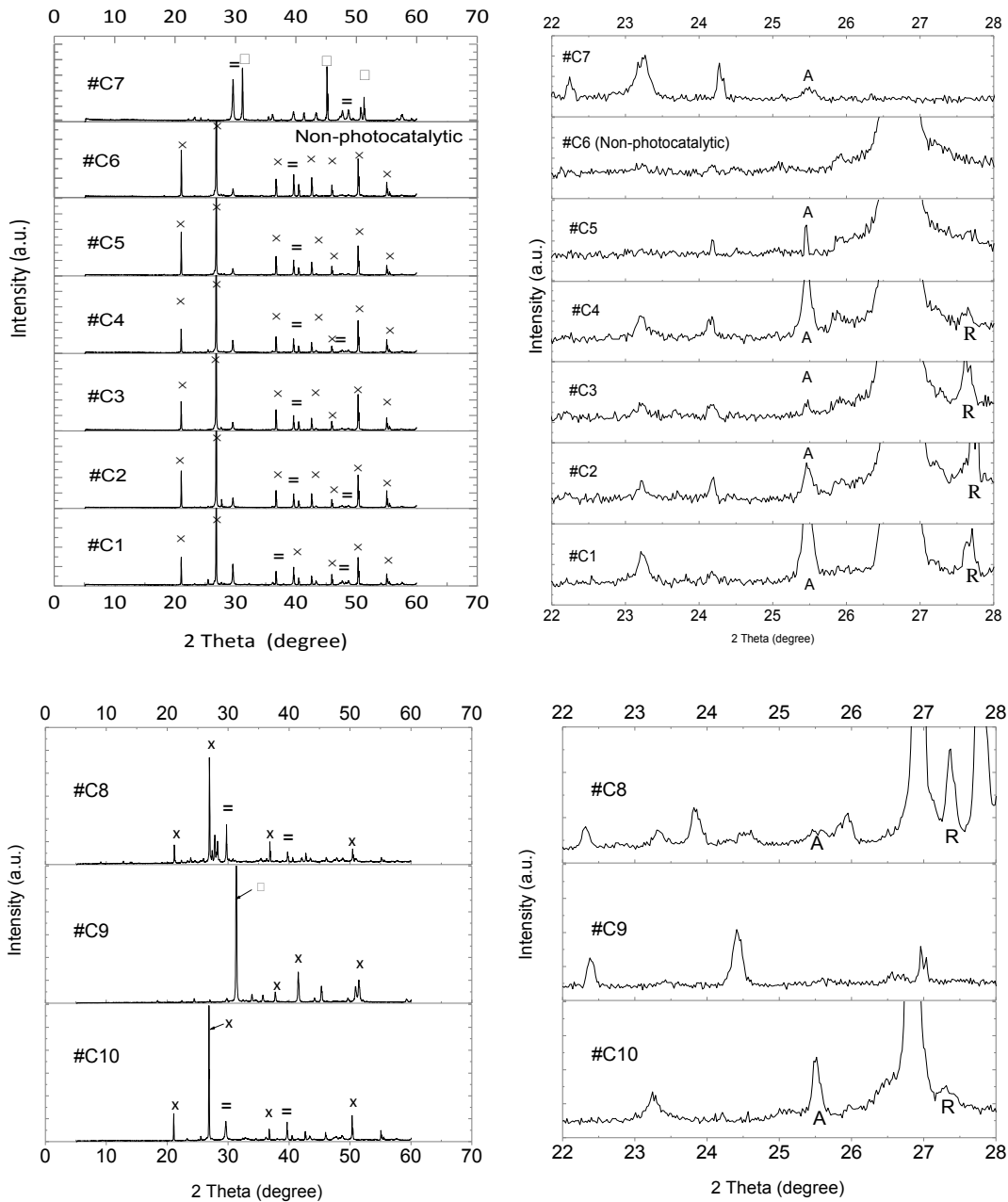


Figure 4. 19 XRD of hardened cement-based samples. The right-hand side images are a detail of the XRD spectra at the left in order to identify the crystal phases of TiO_2 . (\times Quartz, $=$ Calcite, \square Dolomite, A Anatase and R Rutile).

Figure 4.20a includes the XRD of the emulsion coatings applied on Portland bases support via aerosol spray (#E). Similar to previous results, the analysis of the powder of

the bulk sample, only allow detect calcite and quartz components, which may be assumed that correspond with the cementitious base, and are not related to the emulsions composition; Thereby, all emulsion coatings samples shown the same XRD spectra. In this case, the cement-based supports of the emulsion coatings are compound of quartz (characteristics of siliceous aggregates) and portlandite. In order to avoid the masking of the signal due to the presence of cement-based support, the three emulsions were dispersed on a glass support (Figure 4.20b). From this analysis, it can be observed a high amorphous signal corresponding with the glass slide, although it can be intuited that the TiO₂ crystal form of sample #E2 and #E3 is anatase. In contrast, in sample #E1 is hard to find a TiO₂ crystalline phase although that data sheet supplied by the producers indicated that this product contains anatase.

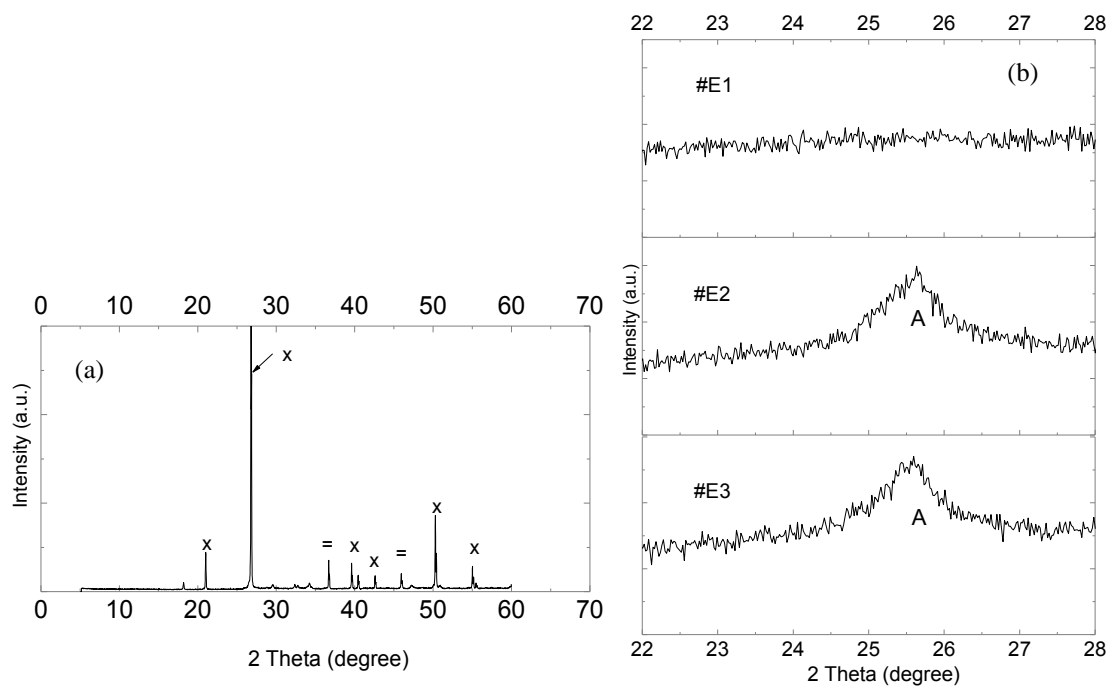


Figure 4. 20 XRD spectra of (a) cement-based support of emulsion coating samples. and (b) emulsion coating dispersed on glass support. (× Quartz, = Calcite and A Anatase).

Figure 4.21 presents the XRD spectra of lab-made cement-based samples, where quartz (from the siliceous aggregates), portlandite and calcite coming are present. Regarding the TiO₂ phases, in the case of samples #L1 and #L2, none crystalline phase could be detected. Note that in these samples, 2 % of weight of cement of TiO₂ Aeroxide P25 from Evonik (75% anatase - 25% rutile) was added as photocatalyst into the cementitious matrixes. #L3-#L5, the signal corresponding with anatase can be observed. Regarding rutile, none signal can be observed in this type of samples.

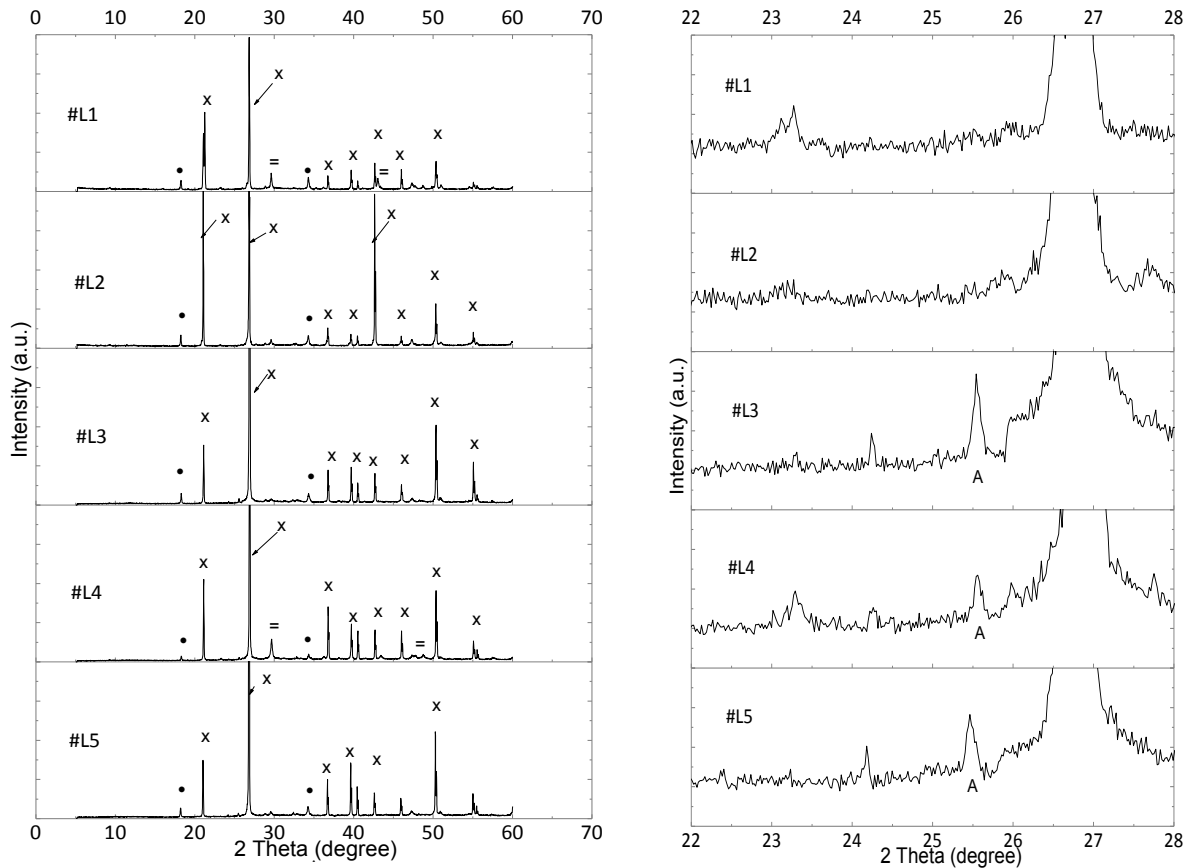


Figure 4. 21 XRD of lab-made cement based samples. The right-hand side images are a detail of the XRD spectra at the left in order to identify the crystal phases of TiO_2 . (\times Quartz, $=$ Calcite, \bullet Portlandite and A Anatase).

Figure 4.22 included the XRD of lab-made coloured mortars (#L6-#L12). All samples shown the same composition of cement; thereby the same signal peaks were shown. The mineralogical composition of these samples is quartz, dolomite and calcite. Concerning TiO_2 phases, only in the sample #L7 (red sample) anatase could be detected. As previously mentioned, the absence of TiO_2 signals, does not necessary mean that TiO_2 phases are not present.

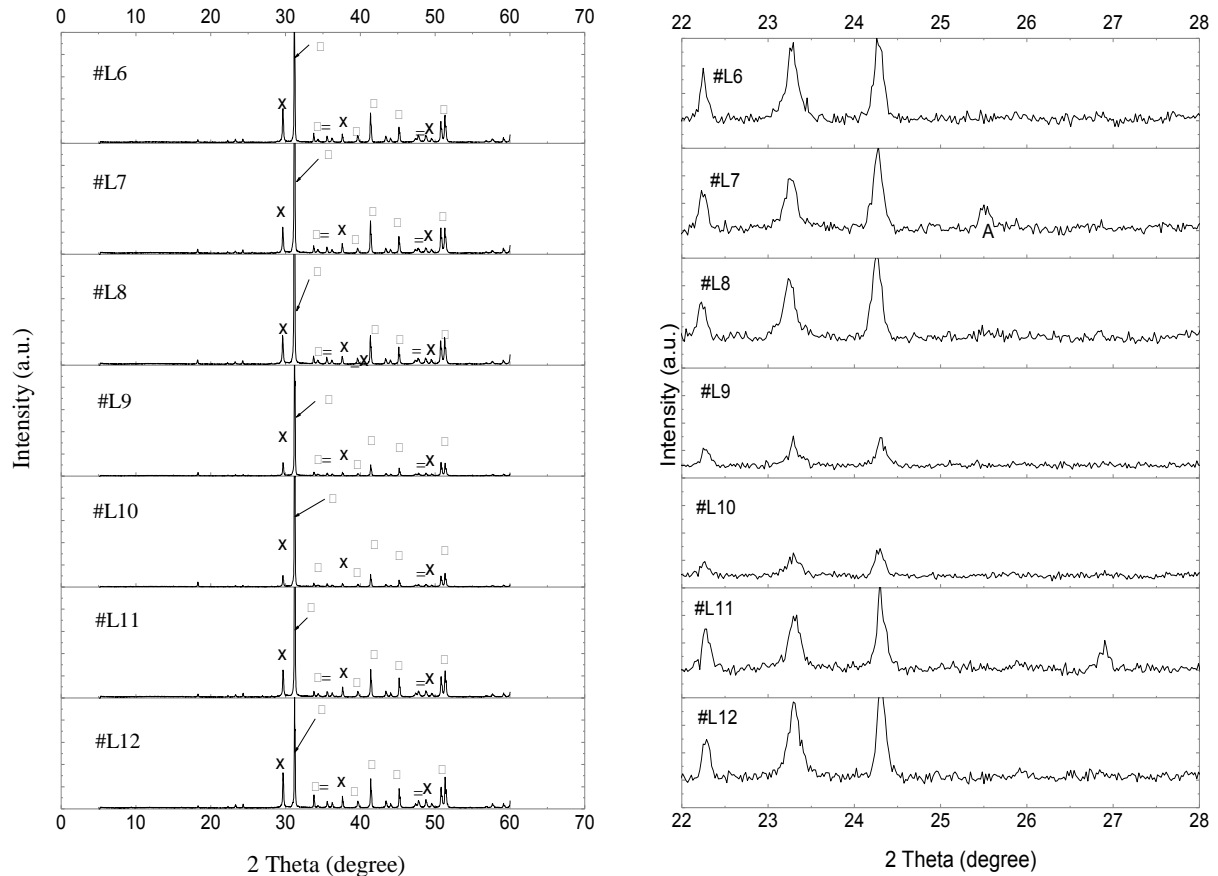


Figure 4. 22 XRD of lab-coloured mortar samples. Right-hand images are a detail of the XRD spectra in order to visualize the crystallite phase of TiO_2 (x Quartz, = Calcite, □ Dolomite and A Anatase).

Taking into account the XRD results, it can be said that the selected samples shown a representative selection of the wide variety of compositions found in the currently market, especially for higher widely used TiO_2 crystalline phases (anatase and rutile). A summary of the TiO_2 phases detected by XRD is given in the table (Table.4.2).

In the case of lab-coloured mortars samples, apart from the analysis of the entire hardened samples, the original iron oxide based pigments used were also characterized by XRD and FRX. These results were included in the *APPENDIX B (Effect of iron oxide based pigment on photocatalytic performance parameters of construction parameters)*, where a complete discussion about the effect of pigment addition of photocatalytic activity parameters was included.

Table 4. 2 TiO₂ phases detected by XRD analysis of selected construction samples.

Sample	TiO ₂ phases detected
#C1	Anatase ; rutile
#C2	Anatase ; rutile
#C3	Anatase ; rutile
#C4	Anatase ; rutile
#C5	Anatase
#C6	Non-photocatalytic samples
#C7	Anatase
#C8	Anatase ; rutile
#C9	No peak detected
#C10	Anatase ; rutile
#E1	No peak detected
#E2	Anatase
#E3	Anatase
#L1	No peak detected
#L2	No peak detected
#L3	Anatase
#L4	Anatase
#L5	Anatase
#L6	No peak detected
#L7	Anatase
#L8	No peak detected
#L9	No peak detected
#L10	No peak detected
#L11	No peak detected
#L12	Non-photocatalytic samples

4.4.1.2 BET Surface area and porosity- physical gas absorption and mercury intrusion porosimetry (MIP)

A summary of microstructure results obtained by MIP and BET are given in Table 4.3 Figure 4.23–4.26 illustrated the cumulative and incremental pore size distribution of all selected construction samples. The samples selected shown a wide variety of microstructural values. In the case of emulsion coatings applied on Portland base support via an aerosol spray (#E), as previously occurred in XRD analysis, all the emulsion samples (#E1-#E3) showed the same microstructural characteristics that correspond to the cementitious base, and does not vary in function of the emulsion type used; Thereby in Figure 4.24 only displayed one cumulative and incremental pore size distribution example.

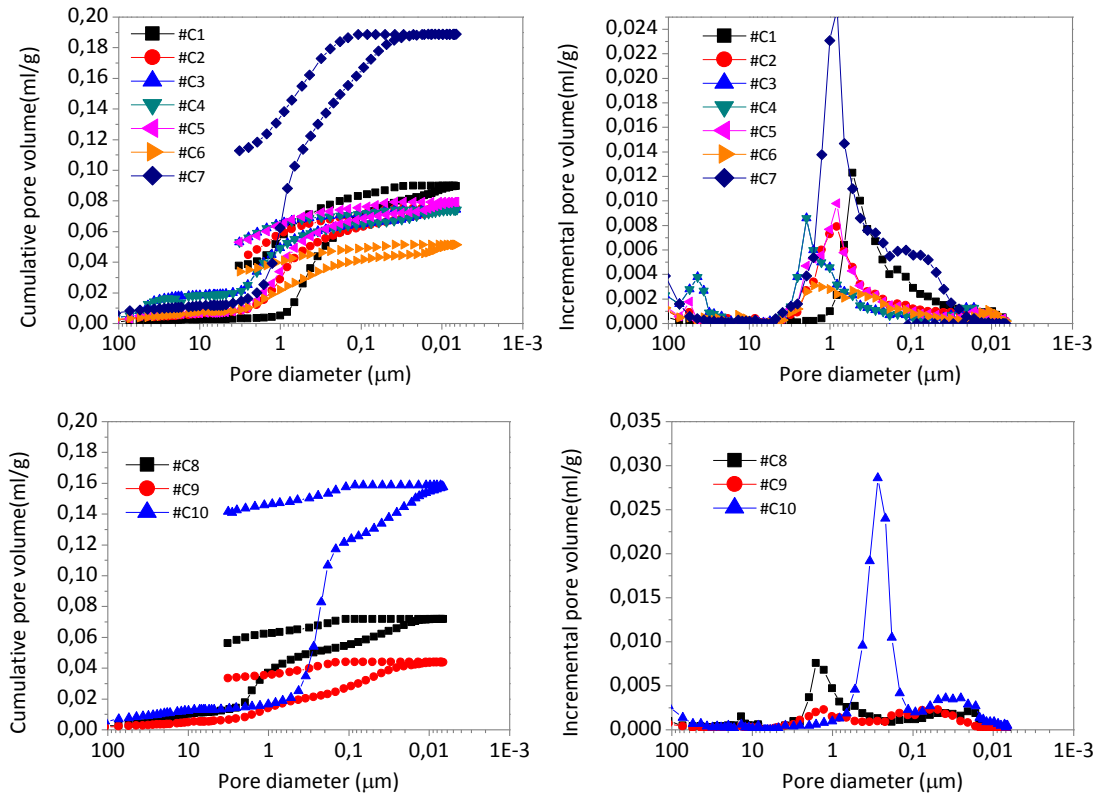


Figure 4. 23 Cumulative and incremental pore size distribution of commercial hardened cement-based samples.

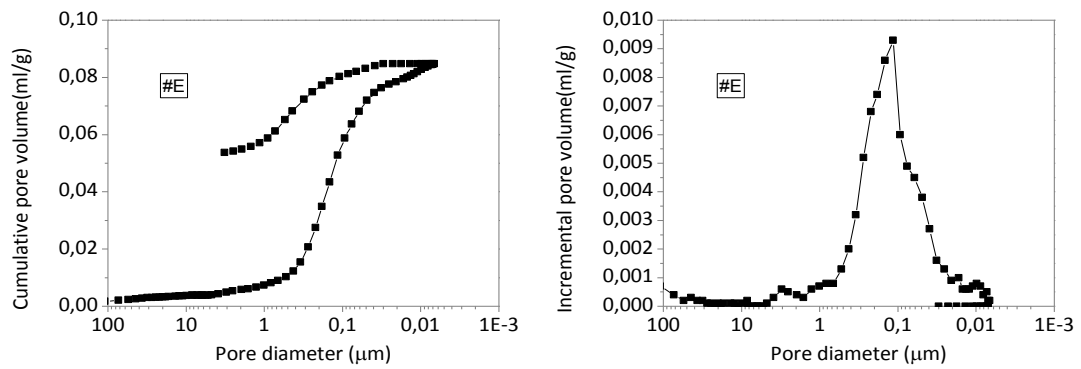


Figure 4. 24 Cumulative and incremental pore size distribution of cement-based support of commercial emulsions.

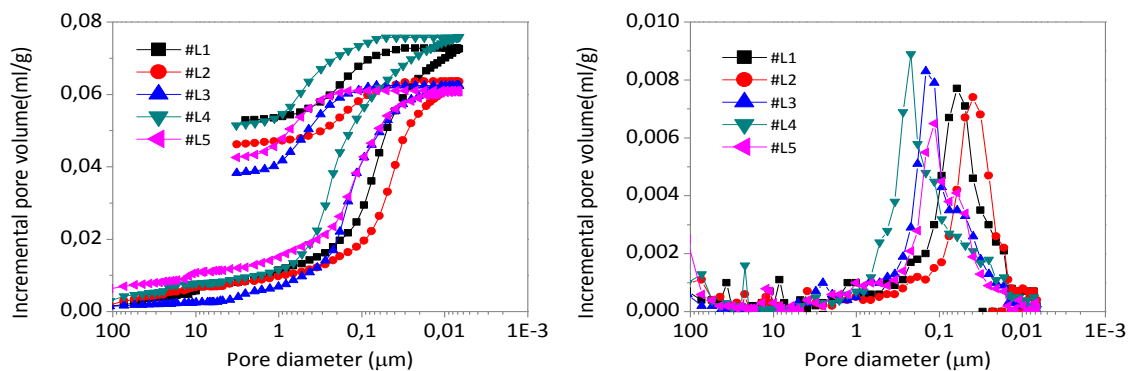


Figure 4. 25 Cumulative and incremental pore size distribution of lab-made cement-based samples.

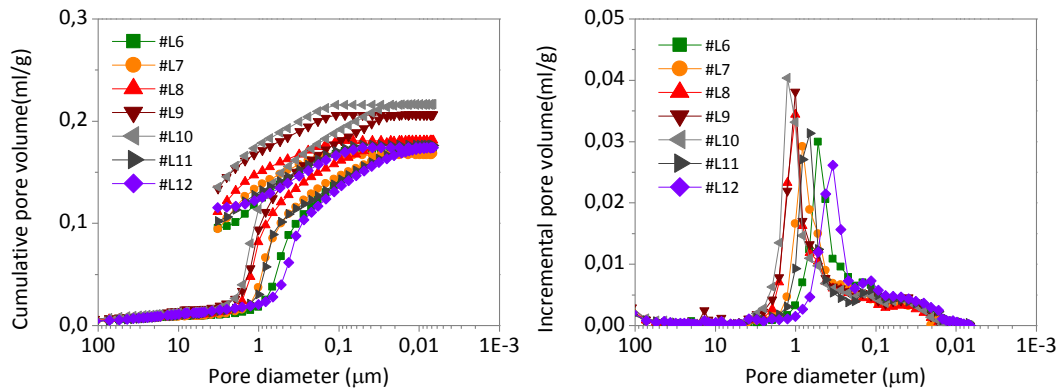


Figure 4. 26 Cumulative and incremental pore size distribution of coloured lab-made mortar samples.

Table 4. 3 Summary data of characterization parameters by MIP and physical gas absorption measurements

Sample	Average pore diameter - 4V/A- (µm)	Bulk density (g/ml)	Porosity (% vol)	BET surface area (S _{BET}) (m ² /g)	Pore volume (cm ³ /g)	Average pore diameter (nm)*
#C1	0.0802	2.1086	18.9431	5.7396	0.022715	15.8300
#C2	0.1081	2.1712	16.3124	4.0892	0.017047	16.6753
#C3	0.1395	2.1613	16.0994	4.1239	0.018026	16.6735
#C4	0.1056	2.1454	16.9565	4.2822	0.017728	16.5602
#C5	0.1085	2.1396	16.9869	3.0117	0.014976	19.8898
#C6	0.0724	2.2400	11.5586	3.0111	0.001545	18.6795
#C7	0.2397	1.7528	33.1387	2.8939	0.017240	23.8294
#C8	0.1119	2.1642	15.5408	4.3447	0.000121	-
#C9	0.0771	2.371	10.4111	3.7417	0.000177	-
#C10	0.0869	1.709	27.0282	11.4852	0.000702	-
#E	0.0694	2.0496	17.3778	6.1582	0.02482	15.6421
#L1	0.0469	2.0842	15.1386	6.2694	0.023865	14.9874
#L2	0.0383	2.1263	13.4989	3.3290	0.020137	24.1957
#L3	0.0803	2.129	13.2911	11.6097	0.032612	11.2363
#L4	0.0795	2.069	15.7247	12.8321	0.3034194	10.6590
#L5	0.0992	2.149	13.0642	3.9319	0.000085	-
#L6	0.1383	1.7833	30.74	4.1994	0.000072	-
#L7	0.2109	1.7817	31.08	3.5637	0.000164	-
#L8	0.2464	1.7524	32.74	-	-	-
#L9	0.22325	1.6967	35.01	-	-	-
#L10	0.23805	1.66405	35.31	-	-	-
#L11	0.1236	1.77885	31.57	-	-	-
#L12	0.106	1.7975	30.99	-	-	-

* Average Pore Diameter (4V/A by BET)

4.4.1.3 Optical properties - UV-Vis diffuse reflectance (DRS)

The absorption spectra of the samples has been obtained from reflectance data (R) using the *Kubelka -Munk* equation (Eq. 3.4, [156]), (Figure 4.27 – Figure 4.30). Assuming that every material tested contained TiO₂ as photocatalyst, that is an indirect semiconductor, the plots of the modified Kubelka-Munk function using *Tauc* relation (Eq. 3.5), $[F(R)h\nu]^{1/2}$ versus the energy of absorbed light ($h\nu$) can be depicted, and are given in the right side of Figure 4.27-4.30 [187, 188]. However, it is important to note that these samples are complex mixed matrices and not are pure semiconductor photocatalyst; thus, the value in the formula of E_g , will be denoted as “apparent photoabsorption edge (PE_{app})” in composite materials [158, 189]. An example of PE_{app} estimation is illustrated in the inset diagram of Figure 4.27c and 4.27d.

From UV-Vis absorbance analysis, it can be observed that all the samples, regardless of the type of samples, present higher absorbance in the UV (<400 nm) than in the visible light range. Only the samples #C8 (Figure 4.27), #E3 (Figure 4.27), and #L2; #L5 (Figure 4.29) showed some absorption in the visible range. However, this enhancement of visible light absorption can be attributed to the grey colour of these samples; in comparison with the other ones (white or light grey samples). In the case of lab-made coloured samples (Figure 4.30), distinctive visible light absorbance is also displayed in function of the colour characteristic of samples. For example, the red sample (#L7) spectrum exhibits most light absorption in the visible region except the red end. From these absorbance results, it can be also observed significant differences in the UV range spectrum of samples, which may account for the different results of photocatalytic activity. The absorbance area of UV range was calculated by integrating the spectra over the wavelengths between 200-400 nm. The calculated numerical values are listed in Table 4.4.

The values of PE_{app} determined from plots of $[F(R)h\nu]^{1/2}$ versus $h\nu$ of all samples are also given in Table 4.4. From these data, it can be observed that all commercial hardened cement-based samples (#C) showed similar values 3.25 ± 0.1 , except the sample #C8 and #C9 that showed a shifted value to lower energies (2.66 and 2.49 eV respectively). Values ca. 3.25 eV are consistent with data reported elsewhere for TiO₂ anatase phase band gap [190]. The emulsion coatings showed more dispersed values of PE_{app} (3.16-3.40). In the case of samples #L1 and #L2, which included as photocatalyst, 75% anatase- 25% rutile (Aeroxide® TiO₂-P25 from Evonik), the values are very similar, and ca. 3 eV, which is consistent with data reported elsewhere [190]. Pure anatase has a band gap of 3.2 eV, whereas for rutile phase, it is 3.0 eV. However, a mixture of these phases, as is the TiO₂-photocatalyst added, yields lower band gap corresponding to the visible region [191]. The consistence of the values obtained as PE_{app} with the E_g values previously reported in the bibliography for pure photocatalyst samples seem indicate that this measurement is a fairly reliable estimate of the optical behaviour of photocatalyst on complex matrices. The other ones (#L3-#L5) that were prepared using a photocatalytic commercial cement also showed similar values from 3-3.2 eV.

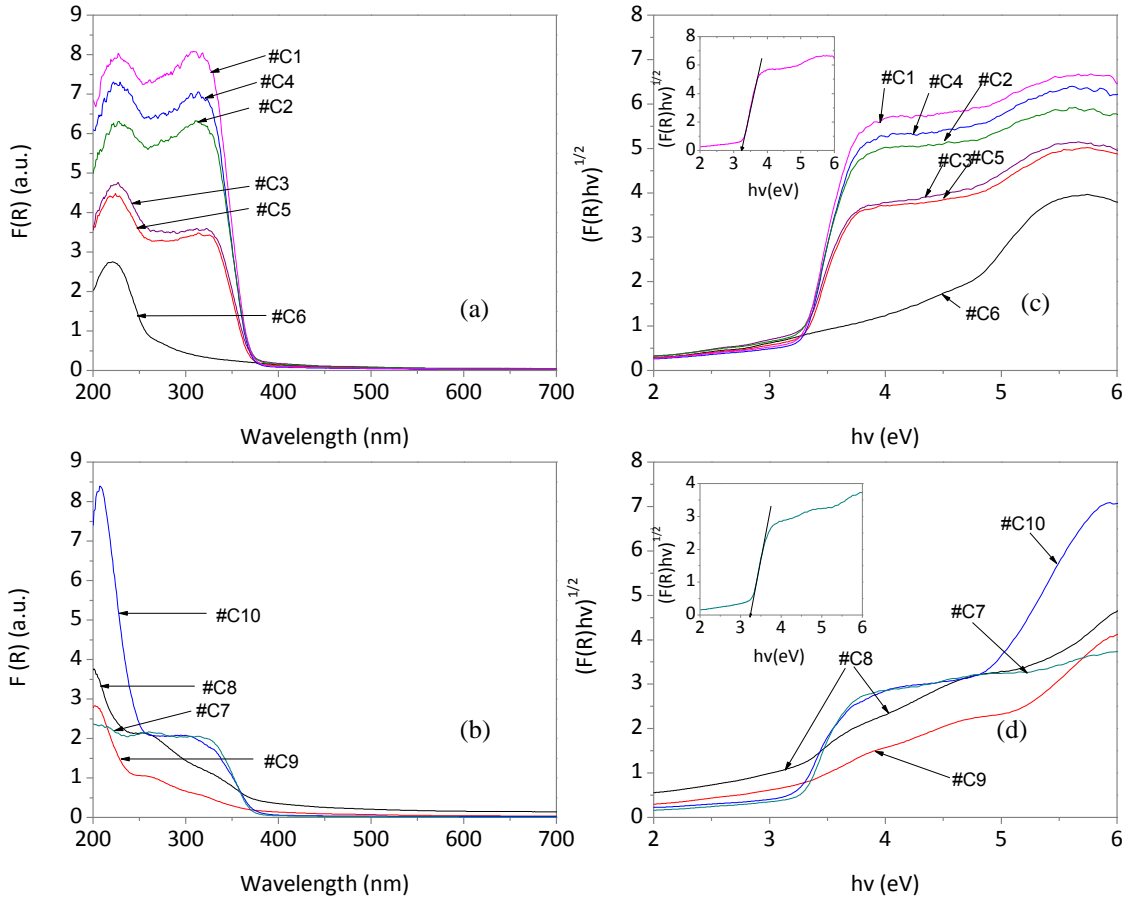


Figure 4. 27 Absorbance spectra in Kubelka Munk units of commercial hardened cement-based samples (a-b). Plot of Tauc's relation versus photoenergy from DRS measurement (c-d). The inset diagram is the example of sample #C1 and sample #C7 apparent photoabsorption edge energy estimation (PE_{app}).

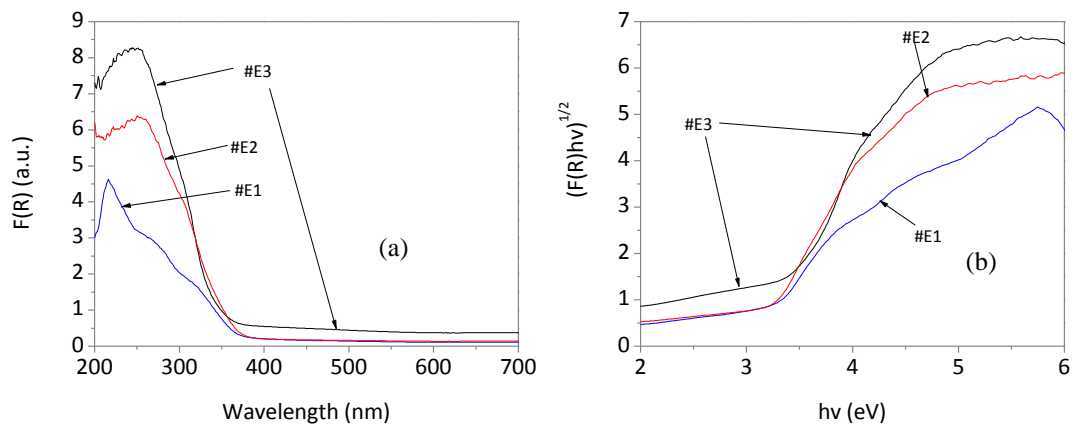


Figure 4. 28 (a) Absorbance spectra in Kubelka Munk units of commercial emulsion coating onto Portland cement –based support and (b) Plot of Tauc's relation versus photoenergy from DRS measurement.

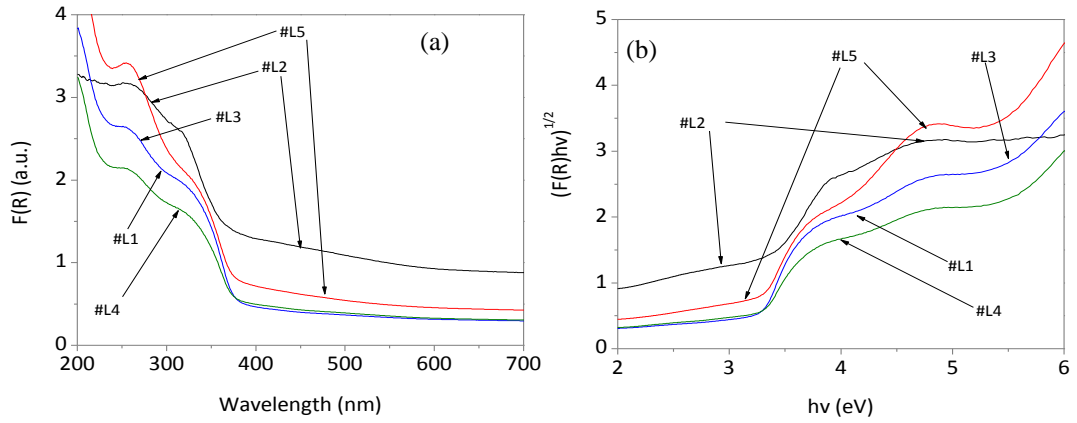


Figure 4.29 (a) Absorbance spectra in Kubelka Munk units of lab-made cement-based samples and (b) Plot of Tauc's relation versus photoenergy from DRS measurement.

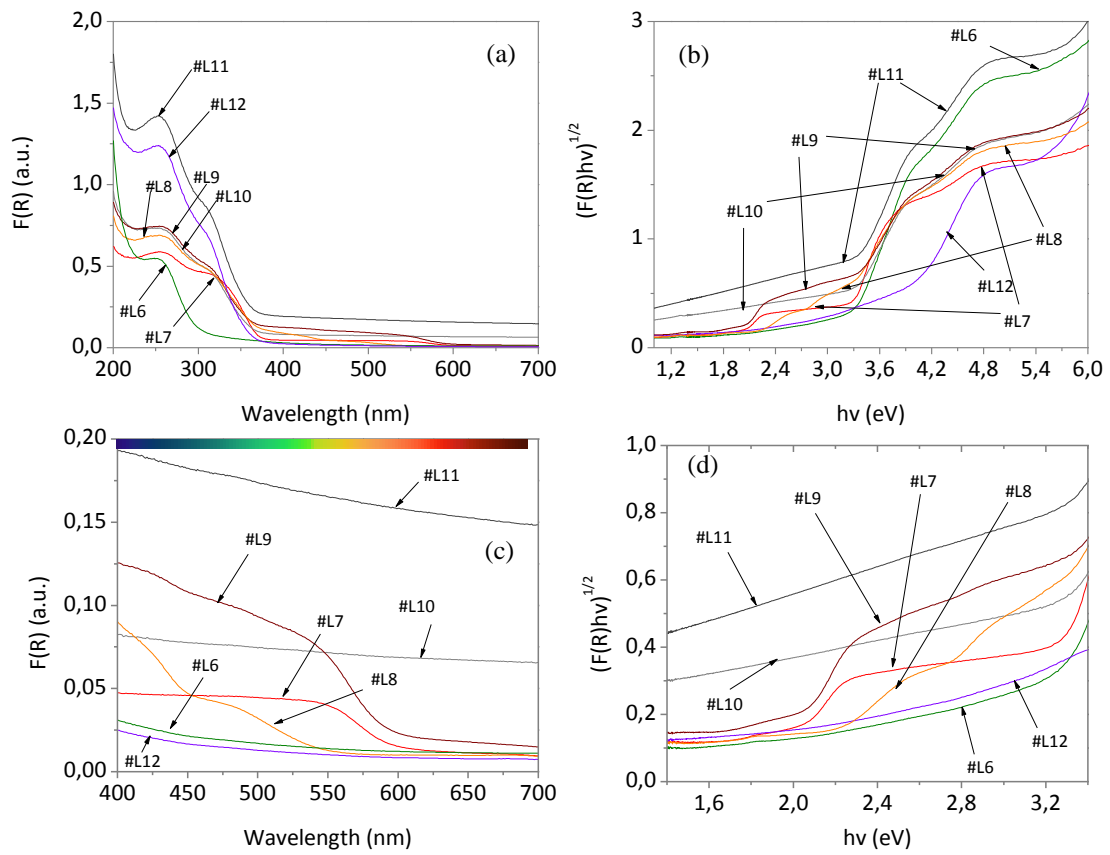


Figure 4.30 (a) Absorbance spectra in Kubelka Munk units of lab-made coloured mortar samples, (b) Plot of Tauc's relation versus photoenergy from DRS measurement, (c) detail of visible range of Figure (a), and (d) detail of visible range of Figure (c).

From the data of lab-made coloured mortars, it is immediately evident that the addition of pigments modifies the absorption energy characteristics of the mortar samples, resulting in an absorption-edge shifted towards lower energy values of all pigment-photocatalytic samples respect to photocatalytic mortar formulation without pigments (#L12). These results are related with the presence of iron-oxides includes as pigments into the cementitious matrix. As previous indicated, the evaluation of the effect of pigment addition of lab-made coloured mortars was included in *APPENDIX B (Effect of iron oxide based pigment on photocatalytic performance parameters)*.

The lowering of the band gap in TiO₂ pure photocatalyst samples can be due to the presence of localized defect states in the forbidden zone of TiO₂ photocatalyst near the bottom/top of its conduction/valence band. This distortion can bring an Urbach type absorption which occurs due to the electron transition between extended band and localized band tail. The structural disorder originates from impurities and defects (Ti³⁺ and oxygen vacancies) produce an absorption tail extending the deep into the forbidden gap [179, 192]. This absorption tail is called Urbach tail and the associated energy (Urbach energy, E_u) is given by the tail region where absorption depends exponentially on the photon energy ($h\nu$) as described by the Eq. 4.3.

$$F(R) = F_0 \exp(h\nu/E_u) \quad (4.3)$$

where F_0 is a constant, E_u is the Urbach energy and $h\nu$ is the photon energy.

For the calculation of E_u , $\ln F(R)$ is plotted against $h\nu$ (eV). The reciprocal of the slope of linear portion, below optical band gap, gives the value of E_u . In composite materials, like the tested materials of this PhD's work, the Urbach energy region was calculated considered the region below the PE_{app} previously calculated. The Urbach energy region of the samples is displayed in Figure 4.31-4.33. The calculated values of E_u from the reciprocal of these slope was included in Table 4.4.

A complete study about the suitability of the determination of optical properties, E_u and PE_{app} in photocatalytic cementitious complex matrixes was published by our group in [158].

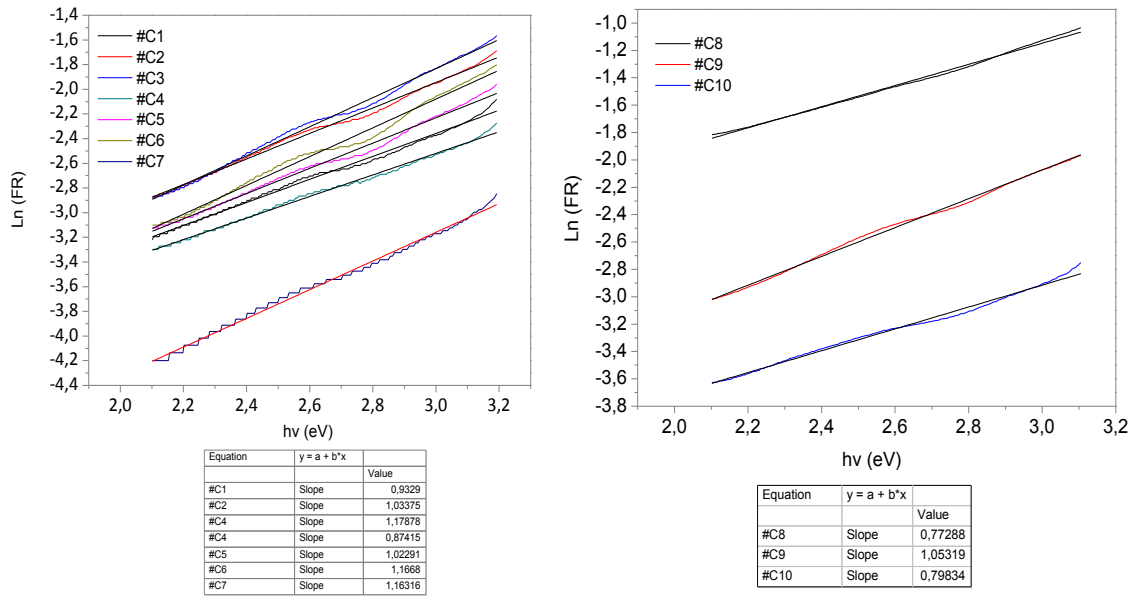


Figure 4. 31 Determination of Urbach energy of photocatalytic commercial cement-based materials

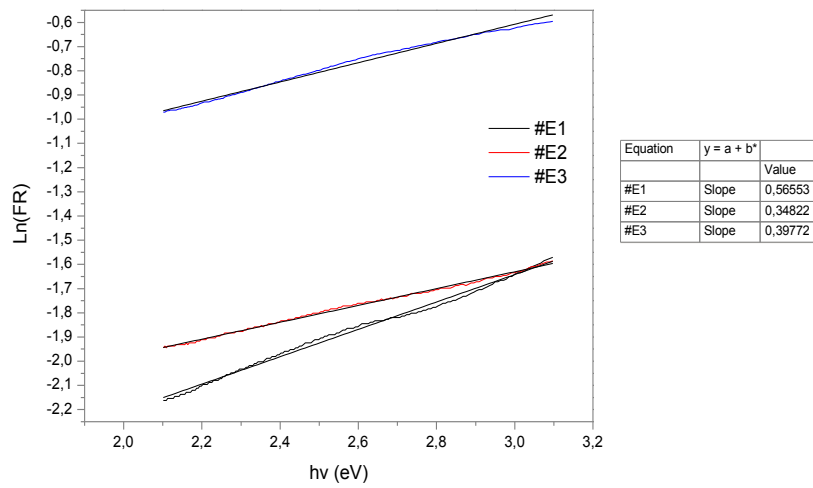


Figure 4. 32 Determination of Urbach energy of TiO_2 photocatalytic commercial emulsions

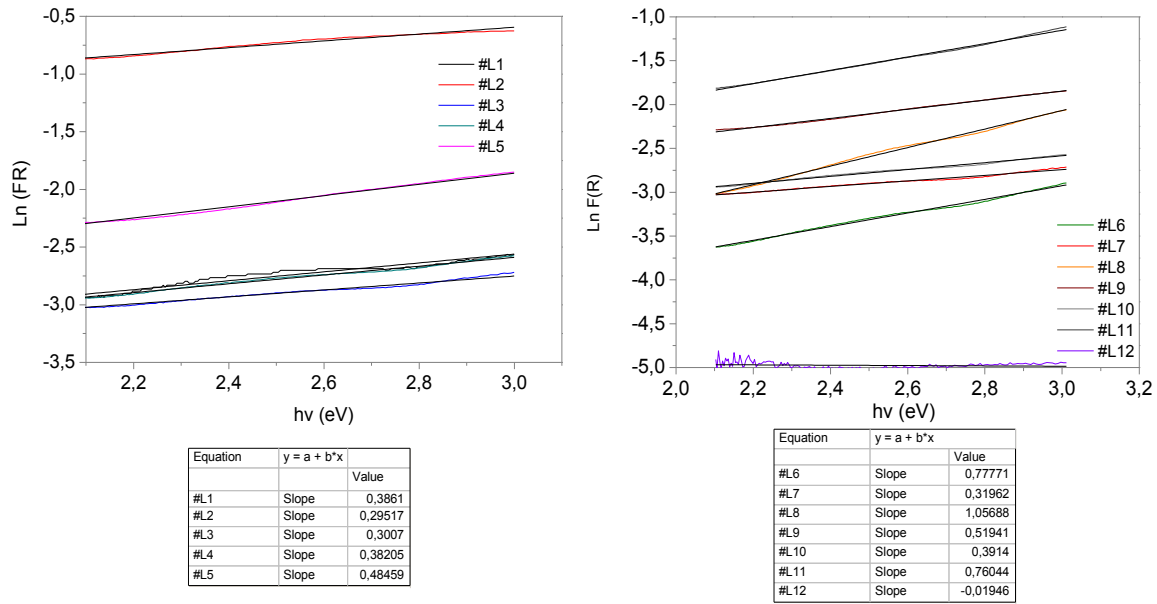


Figure 4. 33 Determination of Urbach energy of TiO₂ lab-cement based samples and lab-coloured mortars

Table 4. 4 Summary of optical parameter calculated of tested samples

Samples	Absorbance -200-400 nm- (a.u.)	PE _{app} (eV)	Eu (eV)
#C1	1146.767	3.26	1.07
#C2	905.817	3.26	0.97
#C3	589.905	3.24	0.85
#C4	1011.544	3.26	1.14
#C5	552.618	3.26	0.98
#C6*	179.364	-	0.86
#C7	320.847	3.23	0.86
#C8	307.455	2.66	1.34
#C9	169.892	2.72	0.96
#C10	487.009	3.25	1.28
#E1	419.747	3.16	1.77
#E2	726.773	3.22	2.87
#E3	895.035	3.40	2.51
#L1	126.416	3.10	2.51
#L2	294.870	3.00	1.81
#L3	200.375	3.19	1.92
#L4	135.937	3.15	2.89
#L5	301.195	3.05	2.21
#L6	141.101	3.20	1.94
#L7	79.864	3.18	1.29
#L8	91.535	2.96	3.13
#L9	98.856	2.93	0.95
#L10	94.588	3.03	1.93
#L11	175.069	2.98	2.55
#L12	56.758	-	1.32

*non-photocatalytic samples

4.4.2 METHOD 1: Hydroxyl radical quantification using terephthalic acid fluorescence probe method (TA-FL)

Figure 4.34 show an example of FL spectra of the probe solutions after irradiation in contact with the tested sample (#L5). The obtained FL spectra of solution have identical shape and wavelengths to TAOH standard solutions. So, it can be deduced that fluorescent products generated during photocatalysis process in samples were due to the specific reaction between $\text{OH}\cdot$ and TA.

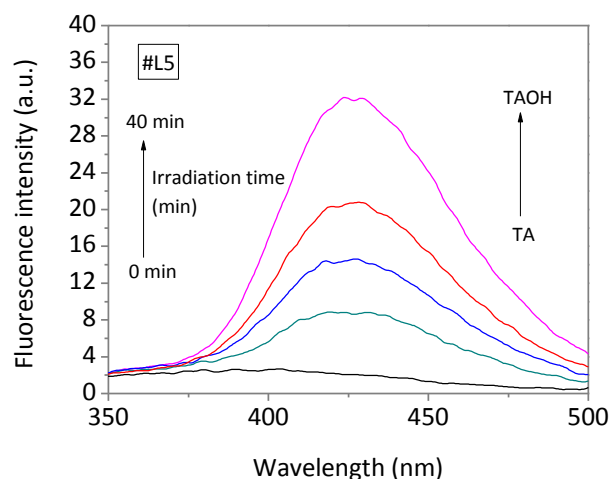


Figure 4. 34 Typical change of fluorescence intensity of TA on irradiated photocatalytic samples (examples of #L5).

Figure 4.35-4.38 (a-b) displayed the FL intensity as a function of irradiation time at 425 nm for every samples, showing a linear increase in FL intensity against irradiation time. So, $\text{OH}\cdot$ produced at the surface of the samples obeyed a zero-order reaction rate kinetic. Using the previous fluorescence calibration curve of TAOH concentration (Figure 4.1(f)) and assuming 35% yield of the reaction of TA with $\text{OH}\cdot$ to produce $\text{OH}\cdot$ [102, 150], the rate of $\text{OH}\cdot$ formation by tested samples could be expressed by the slope of the linear fit of Figure 4.35-4.38(a). The obtained values, expressed per unit of area ($\mu\text{mol}/\text{min}\cdot\text{cm}^2$) are given in their correspondent Figure 4.35-4.38(b). Reference samples not containing TiO_2 (#C6 and # L12) did not lead to any increase of fluorescence, indicating that the probe TA do not suffer any photolysis during the irradiation process.

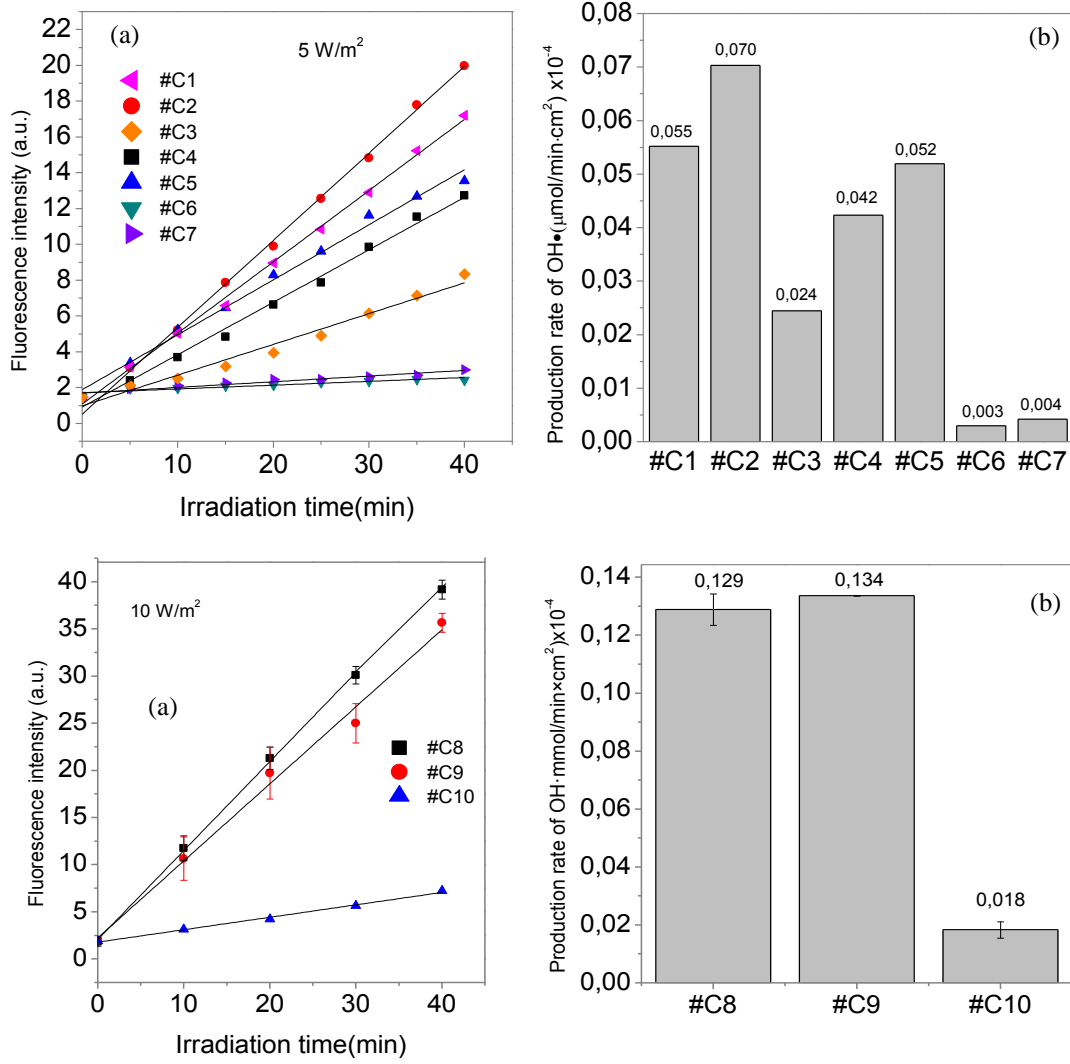


Figure 4. 35 (a) Time dependence of the fluorescence intensity at 425 nm on commercial cement-based samples and (b) production rate of OH• calculated from the corresponding slope of fluorescence intensity on irradiation time of figure (a) using a trapping factor of 35%.

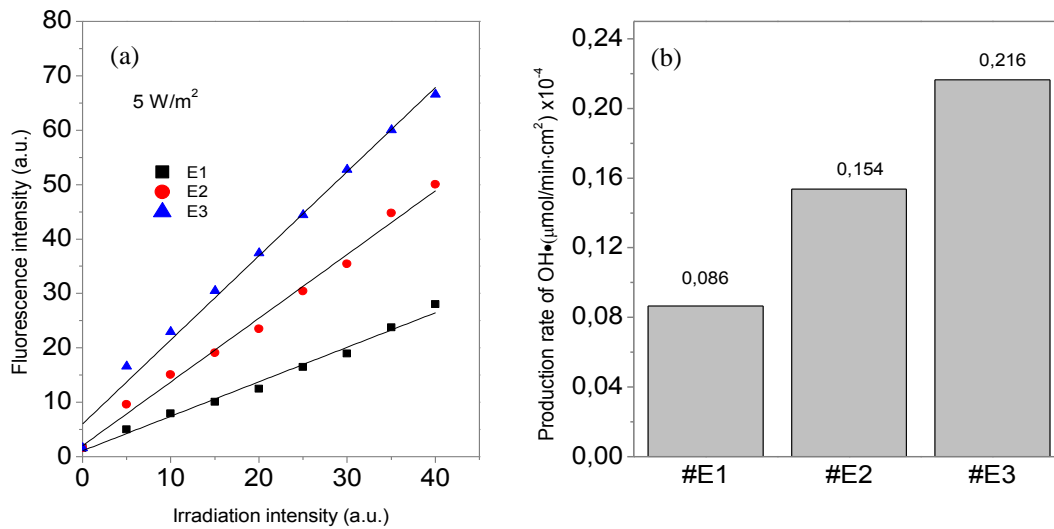


Figure 4. 36 (a) Time dependence of the fluorescence intensity at 425 nm on commercial emulsions samples and (b) production rate of OH• calculated from the corresponding slope of fluorescence intensity on irradiation time of figure (a) using a trapping factor of 35%.

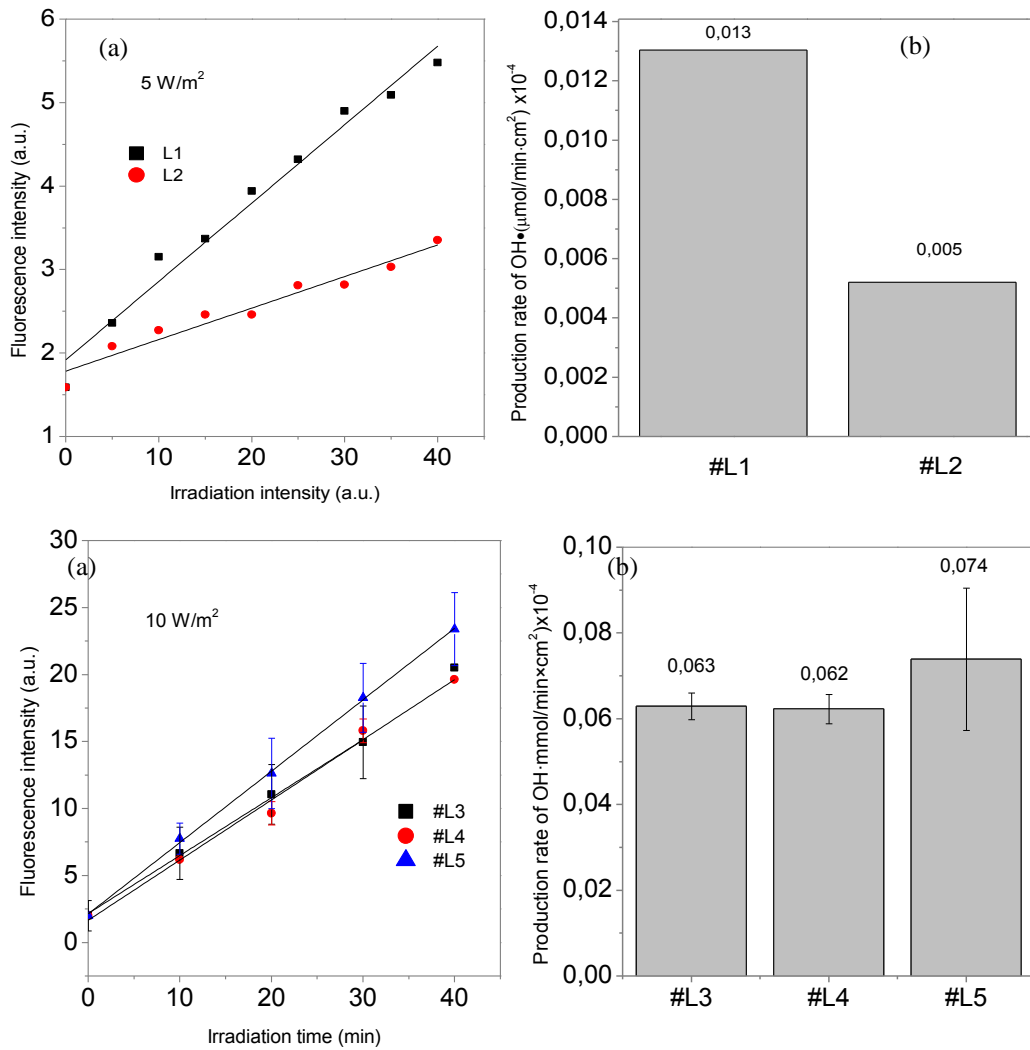


Figure 4.37 (a) Time dependence of the fluorescence intensity at 425 nm on lab-made cement-based samples and (b) production rate of OH• calculated from the corresponding slope of fluorescence intensity on irradiation time of figure (a) using a trapping factor of 35%.

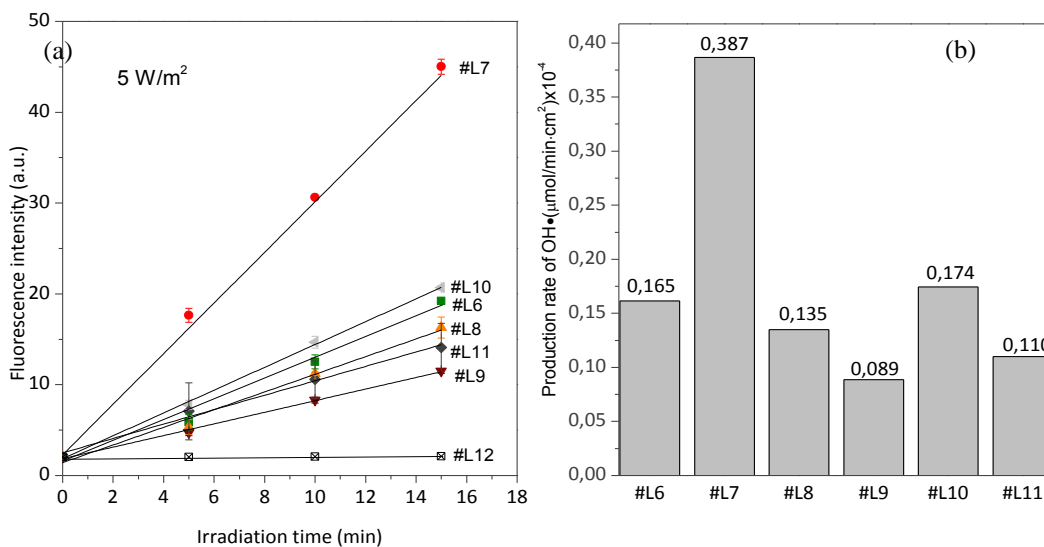


Figure 4.38 (a) Time dependence of the fluorescence intensity at 425 nm on lab-made cement-based samples and (b) production rate of OH• calculated from the corresponding slope of fluorescence intensity on irradiation time of figure (a) using a trapping factor of 35%.

The application of this method on photocatalytic samples allow obtained a new concept of photocatalytic activity measurements, “OH• production rate”, that allow the comparison between the samples. The samples do appear to show different “OH• production rate”, with the activities in the order in function of the light irradiance intensity are:

$$5\text{W/m}^2: \#E3>\#E2>\#E1>\#C2>\#C1>\#C5>\#C4>\#C3>\#C7>\#C6.$$

$$10\text{W/m}^2: \#L7>\#L10>\#L6 >\#L8\sim\#C9>\#C8>\#L11>\#L9 \\ >\#L5>\#L3\sim\#L4>\#C10>\#L12.$$

The differences between the OH• production rate between the samples were analysed in function of the intrinsic characteristic of the samples. In the particular case of lab-made coloured mortars, it is possible to individually evaluate the effect of pigment addition in the OH• production rate (*APPENDIX B*). Although the study of the influence of intrinsic properties of samples on the photocatalytic activity results is out of the scope of this work, the relationships between intrinsic samples parameter and the photoactivity results using all photocatalytic performed tests was included in the *APPENDIX A*.

4.4.3 METHOD 2: Electron (e-) rate measurement using Rz and NBT ink method

4.4.3.1 Optimization of procedure: analysis of interferences of O₂^{•-} or O₂ in the reduction yield of inks by electron

Taking into account that the e- rate measurements using Rz and NBT ink method on construction materials were performed using different experimental conditions (dried spray ink) that the preliminary study on plain TiO₂ photocatalysts (in solution), an analysis of the interferences of O₂^{•-} or O₂ in the reduction yield of inks by electron under this experimental condition was again done.

Figure 4.39 presents the evolution of the UV-Vis absorbance spectra in Kubelka -Munk units of NBT and Rz probes during the irradiation of a typical photocatalytic sample (#C8) under O₂-atmosphere (ambient conditions) and N₂-saturated atmosphere (1 L/min N₂ flow into a reactor). The comparison between these results allowed identifying the interferences of O₂, and the photo-generates O₂^{•-} from O₂, into the reaction of Rz or NBT with the photo-generated e- in the conditions used on the further experiments on selected construction materials. As shown in Figure 4.39, Rf/DH-Rf and formazan were produced in the photocatalytic sample under irradiation no matter whether it was in a N₂-saturated (O₂-free conditions) or in ambient conditions. This indicates that the reduction reaction of RZ and NBT occur *via* electron participation, and not by O₂^{•-}. Figure 4.40, presents the plot of change in relative absorbance in Kubelka Munk units of Rz at 608 nm ($\lambda_{\text{max}} = 608$,

Abs₆₀₈) or formazan product from NBT at 560 nm ($\lambda_{\text{max}} = 560$ nm, Abs₅₆₀) from the previous spectra. From the results illustrated in Figure 4.39, it is clear that the rate of reaction (Eq. 4.4) is reduced when O₂ is present for both Rz and NBT inks. Thus, it can be concluded that the reduction yield in O₂ atmosphere for both inks is lower than those under N₂-saturated conditions that is attributed to the direct competition via the reaction of dissolved O₂ with the photo-generated electrons (Eq. 4.5). This could explain the phenomenon shown in Figure 4.39-4.40. The results of this work are relevant due to the increasing number of researchers that are using NBT to assess the production of O₂^{•-} on photocatalytic samples [20, 165, 176].

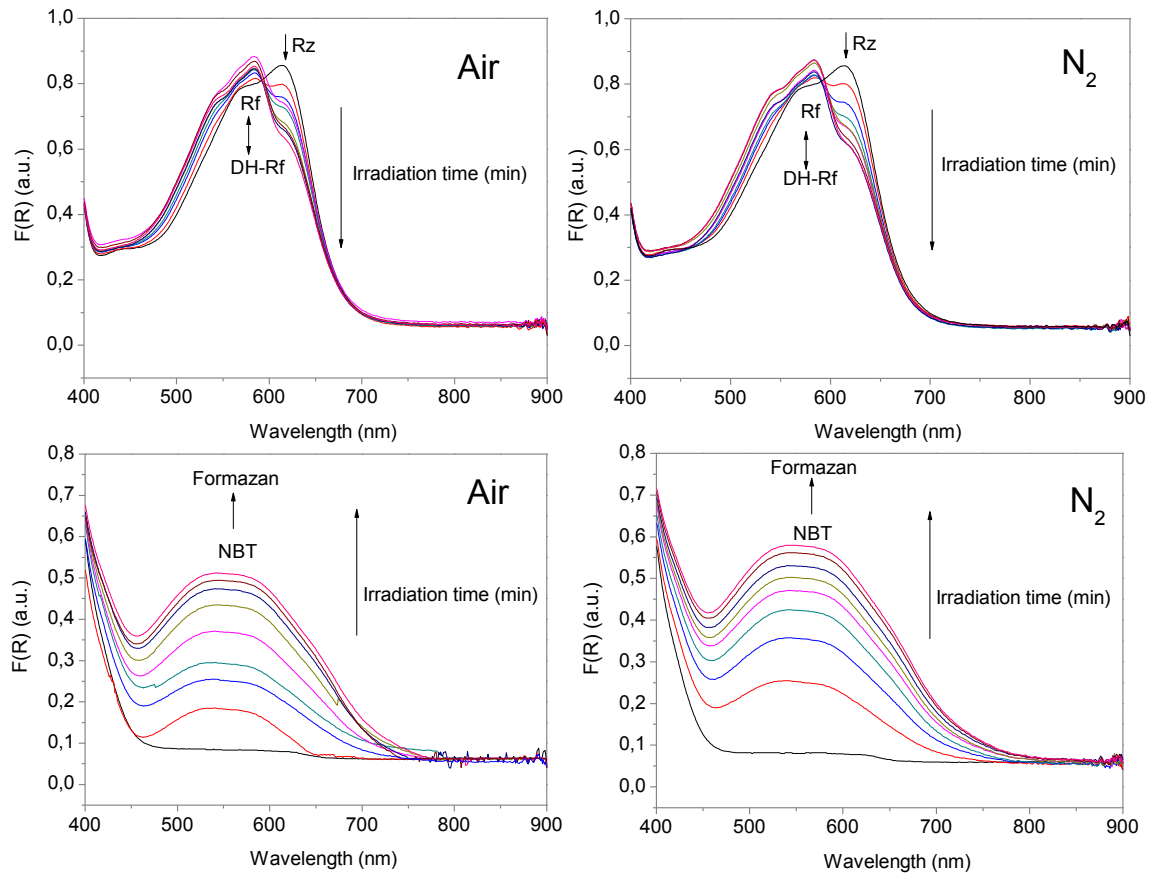
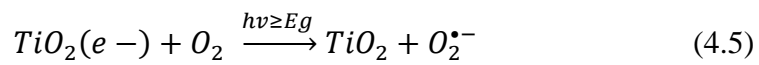


Figure 4. 39 Spectral profiles for the photocatalyzed reduction of Rz and NBT inks under N₂ atmosphere and air-free conditions by a replicate specimen of sample #C7 upon irradiation at 5 W/m².

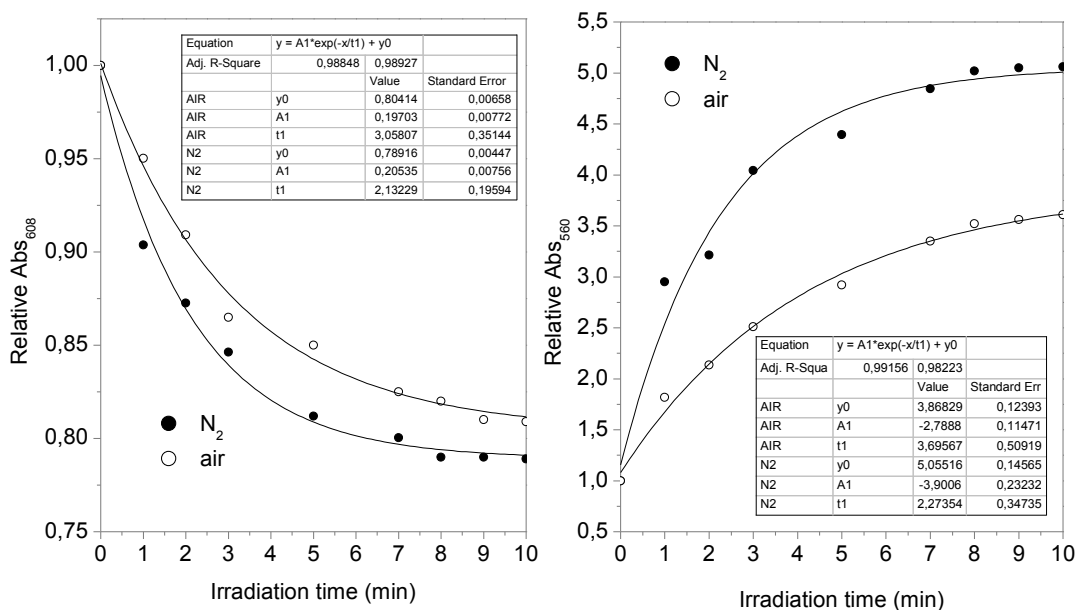


Figure 4. 40 Decay in relative absorbance at 608 nm and 560 nm of Rz and formazan from NBT of data presented in Figure 4.39.

Interestingly, for the two kinetic reactions illustrated in Figure 4.40 for both inks, even in the presence of oxygen, the overall kinetic for reaction remains first order ($R^2 > 0.98$, see Tables inside Figure 4.40). Fortunately, since reaction defined as Eq.4.4 is a constant competitive background kinetic feature that not changes the kinetic order, the e- reduction yields calculated under air conditions, although slower, is comparable with the obtained rate under not-interference oxygen conditions. Thus, in this work, it was decided that, the study of the selected construction materials that further presented was going to be carried out in air. In addition, the obtained results allow to correlate the activity of tested samples using the inks in air, with that measured using a the more traditional methods selected in this work, RhB discolouration and NOx oxidation, both carried out in presence of air.

4.4.3.2 e- reduction rate in photocatalytic construction materials

Before showing the results of Rz and NBT ink tests on the construction samples tested, it is important to indicate that, NBT was a good ink for monitoring the photocatalytic reduction of the tested materials under UV irradiation. In contrast, Rz was found to be unsuitable for assessing the photocatalytic activity due to e- action in emulsions (#E1, #E2, #E3) and lab-made mortars (#L1 and #L2) samples. It can be observed that for this type of samples, in the absence of illumination, the dye changed the colour (to a non-blue colour, usually violet or pink) and the spectra recorded changed its shapes (Figure 4.41). Considering that Rz is a commonly used pH indicator, the first parameter analysed as possible cause of this change in dark conditions was the pH of these samples. A simple test to evaluate the pH of the samples tested is the use of phenolphthalein. This compound is a typical pH indicator. The pH scale of phenolphthalein for acids and alkalis system goes from 0 (strongly acidic) to 14 (strongly alkaline). For it use as an indicator, it was

dissolved in isopropyl alcohol (isopropanol) in a 1% solution. The phenolphthalein indicator solution was applied to a surface of all tested samples.

In the case of the cementitious samples (commercial, #C1-#C7, and lab-made mortars, #L1-#L2), which is commonly highly basic construction materials, only for the samples #L1 and #L2, the original colour of the phenolphthalein indicator changed to pink on contact with the surface, therefore these samples had a basic pH (8.2-12). For the other ones, the indicator maintained their original colour (colourless), thus the pH was ≤ 8.2 in samples #C1-#C7. Thus, RZ ink is pH-sensitive, and the test is not appropriate to highly alkaline materials. The difference of pH displayed for these samples are related with the process of carbonation. All the samples acquired in hardened state to commercial manufactures were carbonated in their surface as it was not any control of ambient conditions before they arrived at our installations. In contrast, the lab-made samples were cured in humid chamber for more than 28 days at $>95\%RH$ and $23\pm 2^\circ C$ inside the moulds, and were kept in this conditions until the tests were performed.

In the case of emulsions, as they were applied on cement-based samples, the analysis of pH with phenolphthalein was first performed on the Portland base surface without the coating. In this case, the indicator maintained their original colour (colourless), thus the pH was ≤ 8.2 for the cementitious support of the emulsions. In line with the previous results, this substrate showed evidences of carbonation. When applying the RZ ink on these surfaces without emulsion coating, RZ was not altered. However, it changed on the emulsions. In this case, which is not due to pH, the conversion of RZ upon contact with emulsion coating in absence of illumination can be related with the chemical composition of them; yet, it is out of the scope of this work a deep characterization of the influence of the composition of emulsions on the RZ ink colour change in absence of illumination, which should require a deep characterization of the broad variety of emulsions with different compositions of the current market in order to evince a clear trend from such compositions.

These facts have pointed out possible limitations in the application of RZ ink method to assess the photocatalytic degradation by electron production rate on samples with very alkaline surface, such as cement-based materials, provided there are no evidences of surface carbonation; and on polymeric emulsion coatings. In real conditions, the application of this method requires then a previous simple verification. If the sample changes the colour of the ink completely (to a non-blue colour, usually pink), instantly, upon contact with the ink in the absence of illumination, the surface is 'reactive' and the test is not appropriate.

The further analysis only included the RZ ink results on photocatalytic samples that not are 'reactive'.

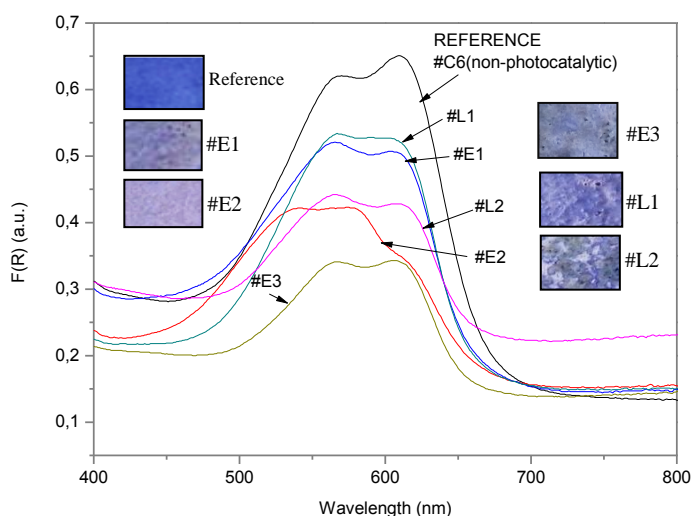


Figure 4. 41 Conversion of absorbance spectra and color of Rz upon contact with the emulsion coating samples (#E1, #E2 and #E3) and lab-made non-carbonated mortar samples (#L1 and #L2) in dark conditions – ‘reactive’ samples. Sample #C6 (non-photocatalytic) also included as reference spectra and color of Rz without any change.

4.4.3.3 Monitoring of the e^- reduction rate using the inks

In this research, three different methods have been compared:

- UV-Vis absorbance using UV-vis spectrophotometer.
- Colour monitoring - CIELAB colour system using UV-vis spectrophotometer.
- Colour monitoring - RGB colour system using digital camera.

4.4.3.3.1 UV-Vis absorbance and colour monitoring using UV-vis spectrophotometer

Subsequent work demonstrated that all the photocatalytic samples tested produced the same changes in the absorption spectrum as previous displayed in Figure 4.39, but with different rates in function of the sample tested. All samples clearly show that the conversion of the Rz (608nm) to Rf (585 nm), and the subsequent reduction of Rf to DH-Rf is occurring. Thus, in order to measure the overall photocatalyzed reduction of Rz as a function of irradiation time, just the change in absorbance at 608 nm, ΔAbs_{608t} , is reported here as a function of irradiation time. For NBT, the change in concentration during the irradiation time was calculated as function of change in absorbance at 560 nm, ΔAbs_{560t} (due to formazan production). In this way, the calculation of the change in absorbance in function of variation (Δ) allows the comparison of change rate between series of samples with different original colour.

Figure 4.42(a-b) shows the data of the variation of absorbance in Kubelka–Munk units at 560 nm and 608 nm, ΔAbs_{560t} or ΔAbs_{608t} (determined with a UV-Vis absorbance measurements), together with the change of a^* coordinate ($a^*>0$ red, $a^*<0$ green), i.e. ΔLab_{at} , and the b^* coordinate ($b^*>0$ yellow, $b^*<0$ blue), i.e. ΔLab_{bt} obtained using a portable spectrophotometer) as a function of irradiation time, t , for RZ and NBT respectively. These colour coordinates had been considered as optimum within the other possibilities considering the range of colours formed by the photocatalytic reduction of inks during the irradiation time [Rz (blue) to Rf (pink) and DH-Rf (colourless) and NBT (pale yellow) to formazan (purple)] and it has been checked that they were the colour values that gave the biggest change over the course of the conversion for each dye.

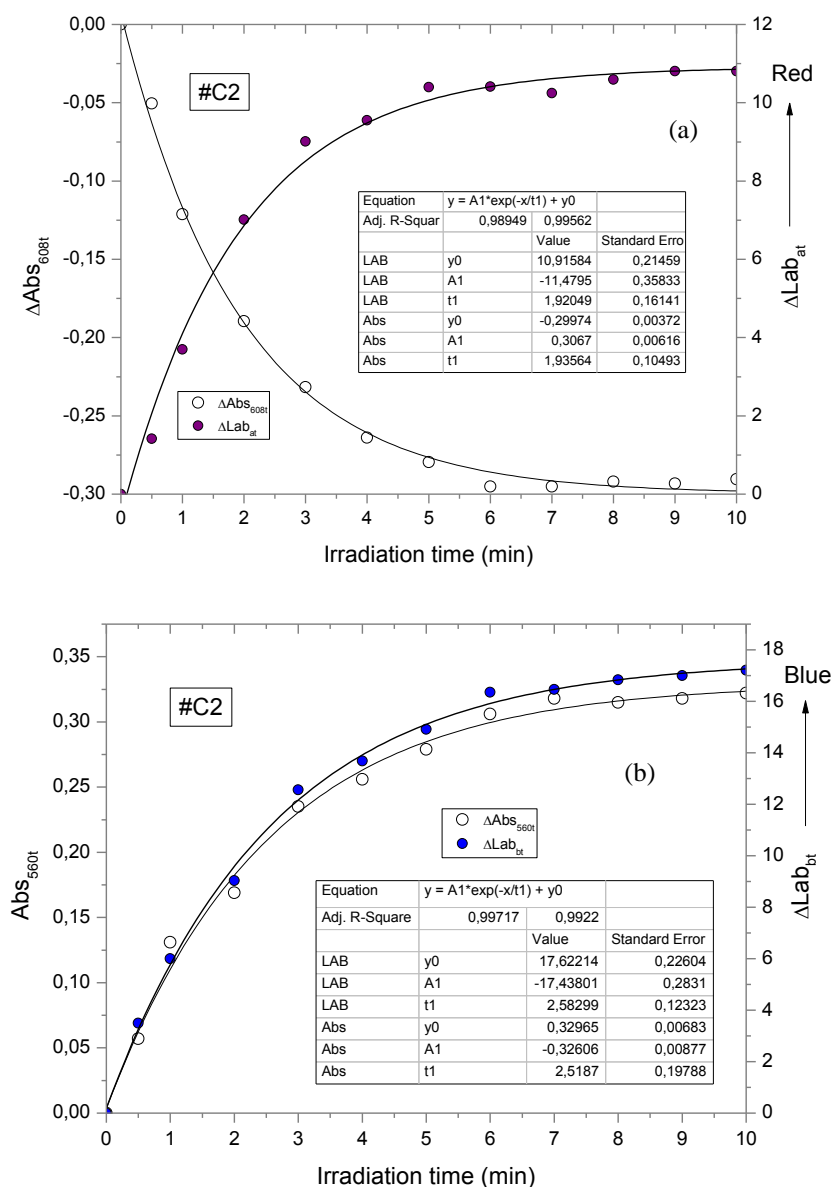


Figure 4. 42 Plot of the change in absorbance Kubelka–Munk units and change of color coordinate of Cielab system in function of irradiation time (a) ΔAbs_{608} and ΔLab_{at} and (b) ΔAbs_{560} and ΔLab_{bt} as a function of irradiation time. The inset graphs are the plot of ΔAbs_t vs ΔRGB_t , showing the linear relationship for both inks.

From Figure 4.42, it can be observed again that for both inks the photocatalytic conversion measured as variation of absorbance or colour during the irradiation appears to be approximately first order kinetics (see the values of adjustment R-square included inside the graph). The collection and adjustment of data over irradiation time for both inks on the all materials tested are included in *APPENDIX C*.

A plot of the data collected for all the samples shown in Figure 4.42 (a-b) and the rest of materials included in the *APPENDIX C* in the form ΔAbs_t vs ΔLAB_t , shown in Figure 4.43 (a-b) for Rz and NBT respectively. These graphs reveal a linear relationship between these two parameters. The linear relationship observed between ΔAbs_t and ΔLAB_t suggests that both parameters can be used to monitor the photo-degradation of the inks, since ΔAbs_t is proportional to ink concentration, and thus allows the monitorization of the rate of degradation.

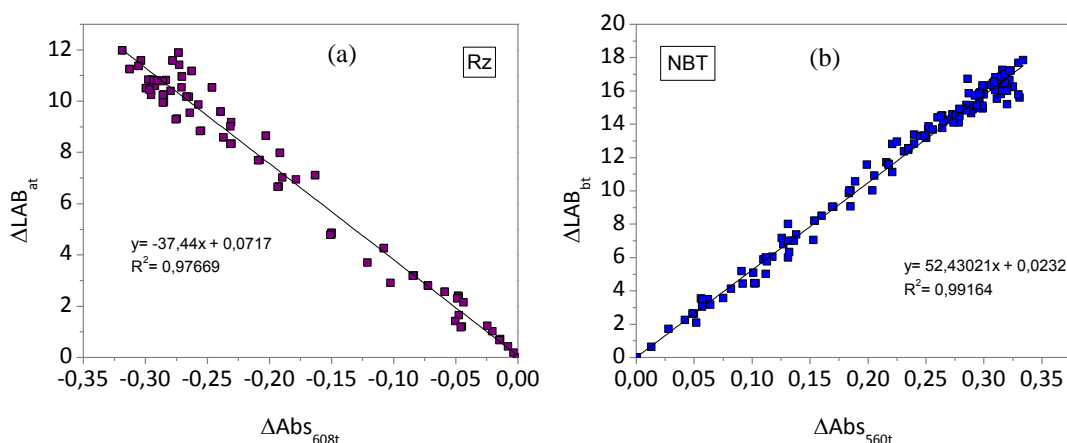


Figure 4. 43 Plot of variation of absorbance and colour measurement of all selected samples for (a) Rz - ΔAbs_{608t} vs ΔLAB_{at} , and (b) NBT- ΔAbs_{560t} vs ΔLAB_{bt}

In the case of the non-photocatalytic sample (#C6) over irradiation time for both inks, no significant changes of absorbance in Kubelka –Munk units during the tests could be observed (Figure 4.44 (a-b)). Thus, it can be considered that the non-photocatalytic process associated with the dye photolysis is negligible for both inks.

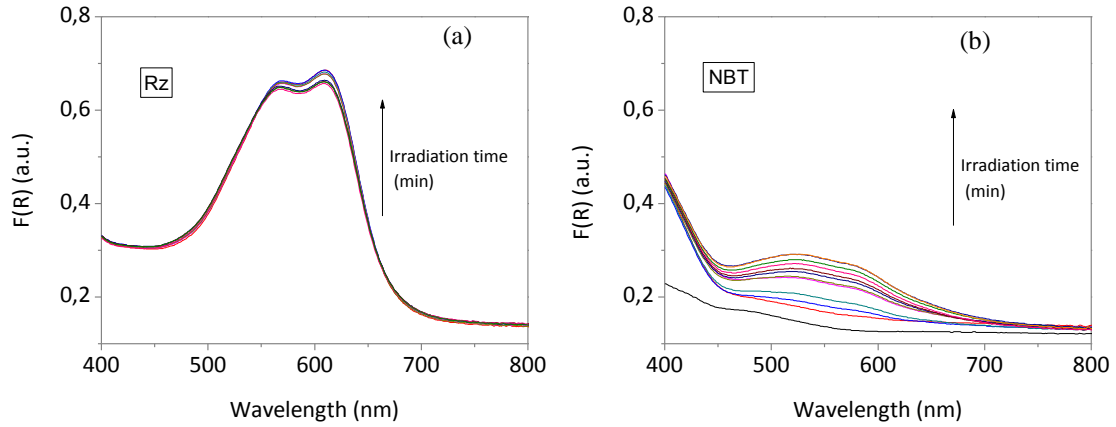


Figure 4. 44 Change in the diffuse reflectance spectrum of the (a) Rz and (b) NBT ink on non-photocatalytic sample #C6, irradiated with UV irradiance at 5 W/m^2 .

4.4.3.3.2 Colour monitoring using image processing of digital photograph

Figure 4.45 (a-b) shows the typical data of image processing over irradiation when illuminating at 5 W/m^2 using a digital camera in a mobile phone as way of monitoring. Specifically, the red or blue components, i.e. RGB_{Rt} or RGB_{Bt} , were used to monitor the change in colour of the Rz and NBT inks at irradiation time taking into account, as in the previous Lab coordinates, the variation of the colour of the ink during the photocatalytic reduction [Rz(blue) to Rf(pink) and DH-Rf (colourless) and NBT (pale yellow) to formazan (purple)]. The normalised $n\text{RGB}_{Rt}$ and $n\text{RGB}_{Bt}$, were calculated using Eq. (4.6) and (4.7) and the measured values of the red, green, and the blue components of the digital image of the ink coating at irradiation time, i.e. RGB_{Rt} , RGB_{Bt} , and RGB_{Bt} . Normalisation of the RGB data in this way helps to compensate for any minor changes in the lighting during the process of taken of the photographs.

$$n\text{RGB}_{Rt} = \frac{\text{RGB}_{Rt}}{(\text{RGB}_{Rt} + \text{RGB}_{Gt} + \text{RGB}_{Bt})} \quad (4.6)$$

$$n\text{RGB}_{Bt} = \frac{\text{RGB}_{Bt}}{(\text{RGB}_{Rt} + \text{RGB}_{Gt} + \text{RGB}_{Bt})} \quad (4.7)$$

Thus, the variation of colour during the irradiation was calculated using the Eq. (4.8) and Eq. (4.9) for Rz and NBT respectively:

$$\Delta\text{RGB}_{Rt} = n\text{RGB}_{Rt} - n\text{RGB}_{R(t=0)} \quad (4.8)$$

$$\Delta\text{RGB}_{Bt} = n\text{RGB}_{Bt} - n\text{RGB}_{B(t=0)} \quad (4.9)$$

As with previous measurements (absorbance in Kubeka-Munk units and the color monitoring using CIELab system), it was also observed that for both inks the photocatalytic conversion of RGB from digital photographs during the irradiation appears again to be approximately first order kinetics.

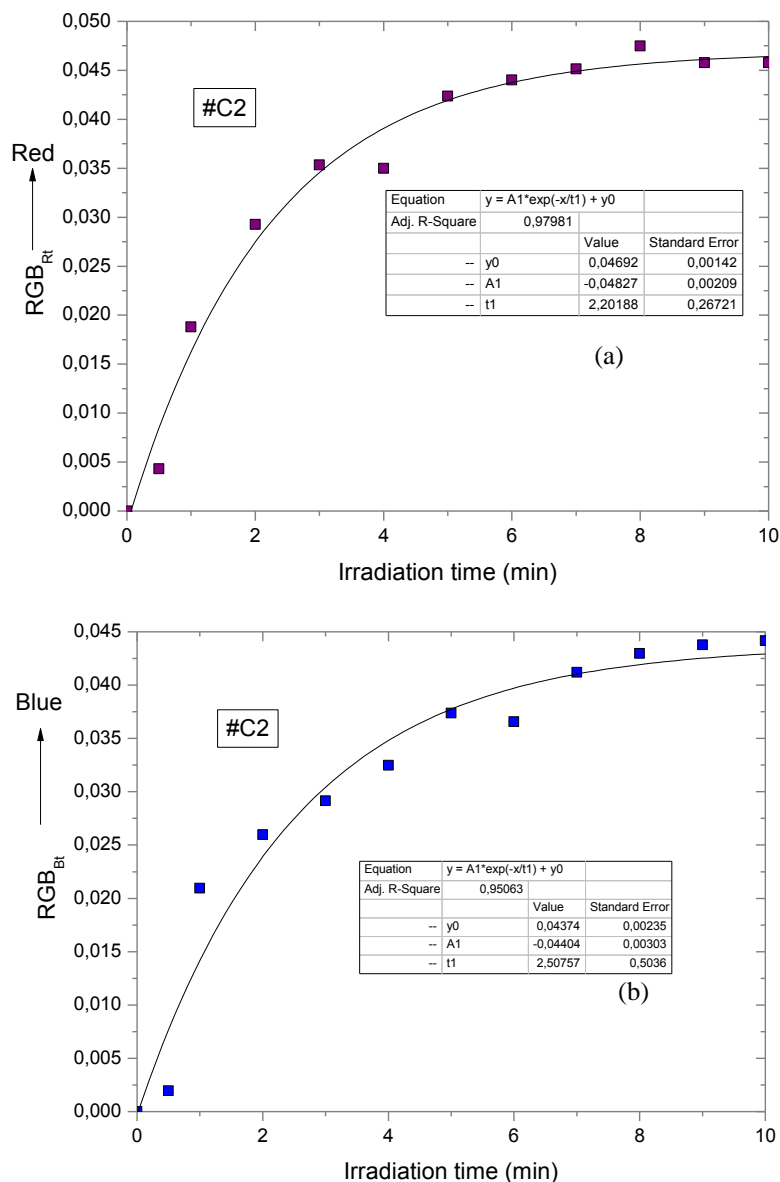


Figure 4. 45 Plots of the variation of the normalized RGB component in function of irradiation time from digital photographs (a) ΔRGB_{Rt} for Rz and (b) ΔRGB_{Bt} for NBT.

The plot of the data in Figure 4.45 (a-b) in the form ΔAbs_{608t} vs ΔRGB_{Rt} and ΔAbs_{560t} vs ΔRGB_{Bt} , presented in Figure 4.46, reveals a linear relationship between the two correlated parameters. The linear relationship observed suggests that the RGB component, derived from digital images using a mobile phone camera also provides a reliable measure of the corresponding ΔAbs_t (Rz- ΔAbs_{608t} or NBT- ΔAbs_{560t}). Therefore, it is possible to quantitatively measure the variation of the dyes concentration during the

photocatalytic process of a wide range of construction materials, not only using a lab-based, diffuse reflectance spectrophotometer, but also, with similar efficiency and much more cheaply, the digital photography. This last method frees the ink from the laboratory and makes it possible to use these tests in field measurements. The data of digital images analysis over irradiation time for both inks on the all materials tested are included in APPENDIX C.

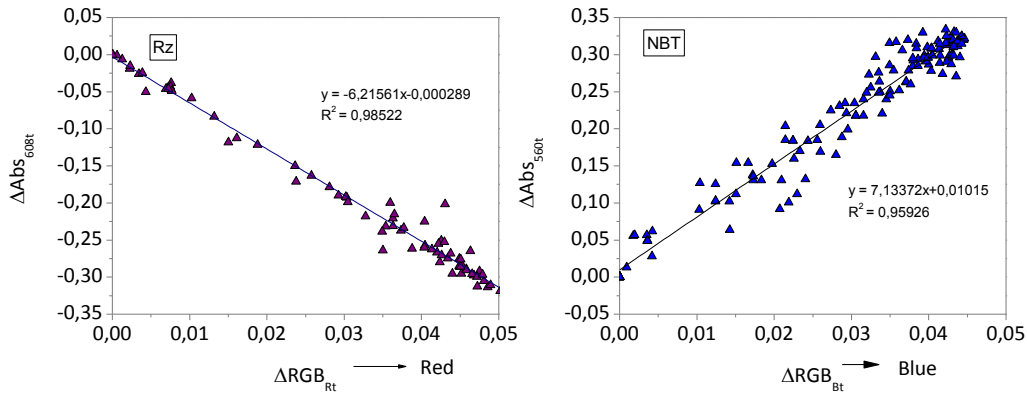


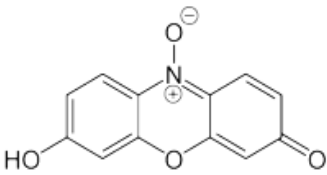
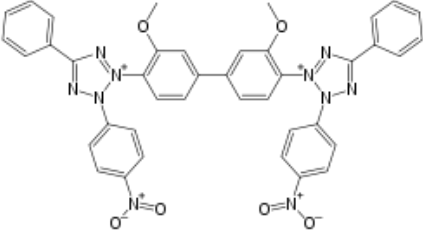
Figure 4. 46 Plot of (a) ΔAbs_{608t} vs ΔRG_{Rt} – RZ and (b) ΔAbs_{560t} vs ΔRG_{Bt} – NBT of all selected samples

Figure 4.47 shows the record of photographs taken for sample #C7 as an example of the change in colour of inks onto the photocatalytic sample as a function of the irradiation time. Table 4.5, as a summary, gives the parameters used to assess the photocatalytic conversion of dyes over the irradiation time.

Time (min)	NBT ink	RZ ink
0		
0.5		
1		
2		
3		
4		
5		
6		
7		
8		
9		
10		

Figure 4. 47 Example of photograph of the colour change of the RZ and NBT inks on sample#C7 upon irradiation at 5 W/m^2 .

Table 4. 5 Summary of parameters used to assess the photocatalytic conversion of dyes over the irradiation time.

Resazurin (Rz)			
	Optimum absorbance wavelength (nm)	608	ΔAbs_{608t}
	Optimum Lab component	a ($a^* > 0$ red, $a^* < 0$ green)	ΔLab_{at}
	Optimum RGB component	R(Red)	$\Delta nGRB_{Rt}$
Nitroblue tetrazolium(NBT)			
	Optimum absorbance wavelength (nm)	560	ΔAbs_{560t}
	Optimum Lab component	b ($b^* > 0$ yellow, $b^* < 0$ blue)	ΔLab_{bt}
	Optimum RGB component	B(Blue)	$\Delta nRGB_{Bt}$

4.4.3.4 Determination of efficiency parameter: Half-life of the ink decomposition

Time-domain parameters that define first-order systems can be expressed in terms of a time constant. The half-life parameter, usually denoted by $t_{1/2}$, is an often used parameter to characterization the response to a step input of a first-order, linear time-invariant system. In our case, $t_{1/2}$ presents the elapsed time required for the dye to lose half its original concentration/colour. The value of $t_{1/2}$ was calculated using the simple multiplication of time constant (t1) for $\ln 2$ ($t_{1/2} = t1 \cdot \ln 2$). The time constant (t1) values were obtained from the exponential adjustment of data collected of absorbance and colour (RGB and CIELAB) measurements for both inks during the photocatalytic test (see values from table of Figures 4.42 and 4.45 and Figures included in APPENDIX C. Half-life time calculation allows the comparison between different time-dominant parameters defined for first order kinetics, such as the case of absorbance or colour changes due to the reduction of Rz and NBT dyes on photocatalytic samples in function of irradiation time.

Table 4.6 gives the $t_{1/2}$ parameters obtained in function of the ink used and monitoring parameter for each photocatalytic sample. As expected from the linearity of the three techniques to monitor the ink degradations, as previously shown in Figure 4.42 and 4.45, the $t_{1/2}$ obtained show equal values with a few inaccuracies. Figure 4.48 (a) included the mean of $t_{1/2}$ of the three-data processed and its corresponding error bars.

Table 4. 6 Elapsed time required for the Rz and NBT to lose half its original concentration/color ($t_{1/2}$) for their reduction on photocatalytic cement-based samples. $t_{1/2}$ were obtained from: ^achange of absorbance in Kubelka–Munk units (from diffuse reflectance monitoring), ^bchange in color of LAB cielab components (from hand-spectrophotometer), and ^cchange in color component of RGB (from digital mobile camera images).

Sample	$t_{1/2}$ (min)		
	$t_{1/2Abs}^a$	$t_{1/2Lab}^b$	$t_{1/2RGB}^c$
Resazurin (Rz)			
#C1	1.47	1.40	1.45
#C2	1.34	1.33	1.53
#C3	2.27	2.29	2.25
#C4	1.39	1.38	1.37
#C5	1.55	1.55	1.49
#C6 (non-photocatalytic)	-	-	-
#C7	2.26	2.30	2.21
#E1	*	*	*
#E2	*	*	*
#E3	*	*	*
#L1	*	*	*
#L2	*	*	*
Nitroblue tetrazolium(NBT)			
#C1	1.84	1.89	1.75
#C2	1.75	1.79	1.74
#C3	2.59	2.63	2.47
#C4	1.60	1.70	1.80
#C5	2.13	2.02	1.81
#C6 (non-photocatalytic)	-	-	-
#C7	2.76	3.10	2.66
#E1	1.30	1.21	1.38
#E2	0.93	0.77	0.77
#E3A	0.66	0.52	0.71
#E3B	0.68	0.59	0.76
#L1	2.47	2.67	2.64
#L2	2.63	2.43	2.33

*Ink changes the colour completely upon contact with the sample in the absence of illumination ('reactive' surface).

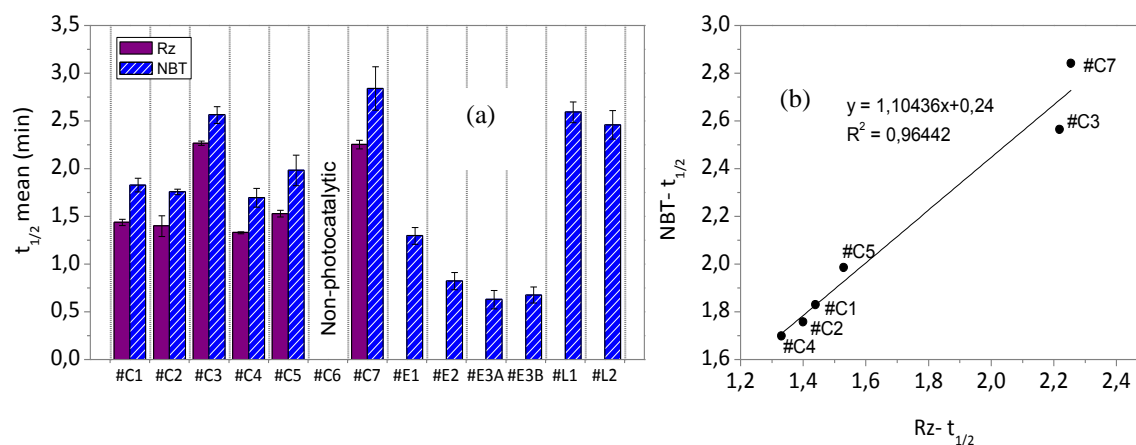


Figure 4. 48 (a) Mean half-life time ($t_{1/2}$ mean) obtained from the $t_{1/2}$ obtained of the three techniques to monitor the photocatalytic reduction of RZ and NBT inks (change of absorbance in Kubelka–Munk units from diffuse reflectance monitoring, change in color coordinate of CIELab form hand-spectrophotometer and change in color component of RGB from digital mobile camera images), and (b) Linear relationship between the $t_{1/2}$ mean obtained for RZ ink vs NBT ink.

The application of this method on the photocatalytic samples has allowed obtaining a new concept of photocatalytic activity measurements, e- photocatalytic reduction yield. In this work, this parameter was quantified as elapsed time required for the dye to lose half of its original concentration/colour “half-life time ($t_{1/2}$)” that allow the comparison between the samples. The ranking of samples according to their “half-life time ($t_{1/2}$)”, under irradiation at $5W/m^2$, is:

$$\#E3A \sim \#E3B > \#E2 > \#E1 > \#C4 > \#C2 > \#C1 > \#C5 > \#L2 > \#C3 \sim \#L1 > \#C7 > \#C6.$$

Requiring the two replicates of sample #E3 the smaller time for ink photocatalytic reduction and the sample #C7 the longest time (#C6 is a non-photocatalytic sample). Although RZ was found to be unsuitable for assessing the photocatalytic activity of “reactive samples” such as emulsion coating samples (#E) and lab-made mortars (#L) as previous explained, it is important to indicate that for non ‘reactive’ samples, both inks in the form $t_{1/2}$ mean (NBT) vs $t_{1/2}$ mean (Rz) reveals a linear relationship between them (Figure 4.48(b)). This means that although RZ need less time to lose half its colour/concentration, the linear relationship indicated that both results are comparable with a ratio $t_{1/2}$ mean(Rz)/ $t_{1/2}$ mean(NBT)=1.10, even though the organic molecule is quite different. An interesting comparison between different redox dye times to change the colour was reported by Mills et al. [114]. This work demonstrated that methyl orange and acid violet dye inks worked equally well, showing the same times to change of colour. In contrast, Basic blue 66 and RZ ink showing different time of reaction.

As previously mentioned, although the study of the influence of the intrinsic properties of samples on the photocatalytic activity results is out of the scope of this work, the differences between the e⁻ reduction yields between the samples in function of the intrinsic characteristic of the samples was also included in *APPENDIX A (Effect of physicochemical and optical properties of the materials on photocatalytic performance parameters)*.

4.5 Validation of the methods

To prove the validity of the proposed tests (TA-FL probe method and reductive ink methods) as procedures to assess the photocatalytic activity, the results obtained of their application on the different selected construction materials was compared with the photocatalytic activity performance obtained on the same materials using the standards: photocatalytic oxidation of gaseous NO to nitric acid (ISO 22197-1:2007 and UNI 11247:2010) and Rhodamine (RhB) discoloration (UNI 11259:2008). Furthermore, as both methods have been developed with the objective to assess the photocatalytic efficiency, it was thus decided to also correlate their results.

4.5.1 Photocatalytic activity results using photocatalytic oxidation of gaseous NO to nitric acid (ISO 22197:1-2007 and UNI 11247:2010) and Rhodamine (RhB) discoloration (UNI 11259:2008)

The profiles of NO_x (NO and NO₂) concentration of all selected construction materials in function of time are included in the *APPENDIX D*. From this data, the removal rate (%) of NO_x of the samples were determined as described in *Section 3.4.1*, Eq. (3.8-3.10) for the set of experiments based on the requirement of ISO 22197:1-2007 standard and Eq. (3.11) for the experiment based on the UNI 11247:2010 standard. The values of removal rate obtained are given in Figure 4.49.

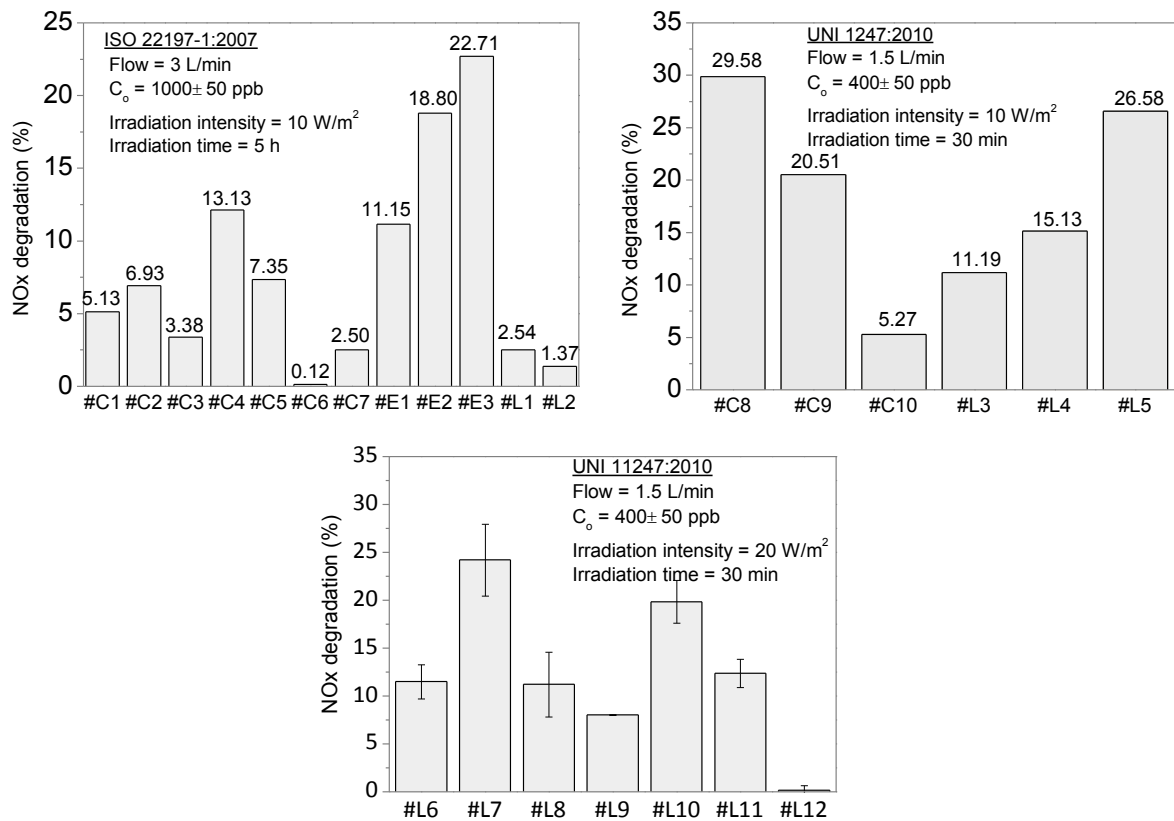


Figure 4. 49 Photocatalytic removal rate (%) of gaseous NO to nitric acid using the test conditions defined on the standard: (a) ISO 22197-1:2010 and (b) UNI 11247:2010 at 10 W/m^2 and (c) UNI 11247:2010 at 20 W/m^2 .

The summary results of RhB test were included in Figure 4.50. In the particular case of lab-coloured mortars, a homogeneous distribution of dye film was not easy to be achieved, leading to results with substantial bias. To buffer this, the test was performed on 3-5 different specimens and the values reported for each specimen is the mean of at least 3 different measurements in the coated area of the sample. Nonetheless, as the values of degradation at 4 hours showed higher deviations, the results not have been included in this work. The homogeneity of the dye film on the samples surface can be related with the higher hydrophobic characteristic of these samples that difficulties the homogeneous distribution of the RhB. On the other hand, since RhB degradation is calculated as the decreased in the intensity of the a^* (red) colour coordinate, there is necessarily an underestimation in samples #L7 (red sample) and #L9 (brown sample) due to the fact that loss of the colour of RhB implies the emergence the original colour of substrate (reddish). This reduces the reliability of such experimental procedure for photocatalytic performance comparison between the differently coloured mortars, in comparison with NOx degradation or the proposed methods of this work (TA-FL and reductive inks), whose results are independent of the colour substrate. Considering the previous indicated constraints of RhB test, the further correlations of photocatalytic results only included the samples white or light grey colour.

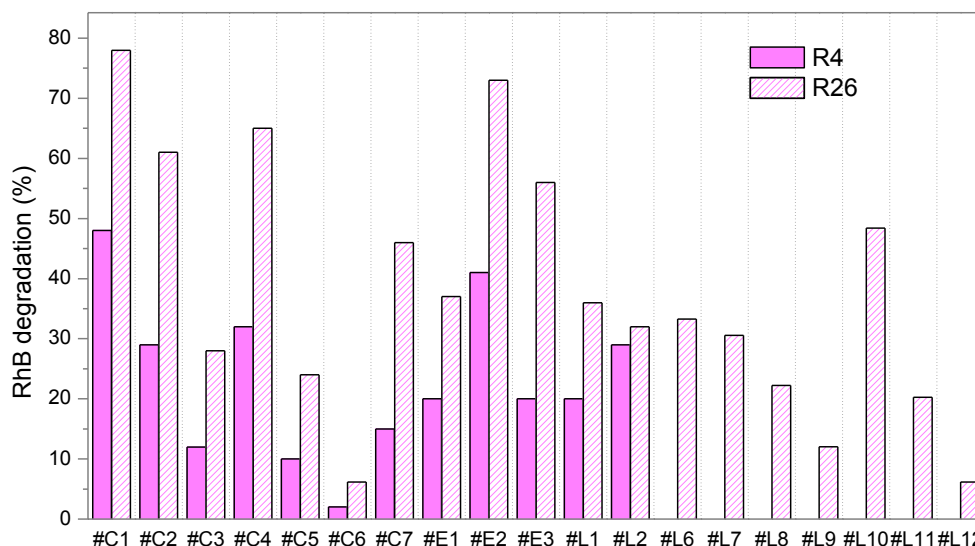


Figure 4. 50 Percentage of RhB degradation (UNI 11259:2008) of selected samples.

4.5.2 Comparative between methods: TA-FL method, reductive ink tests, photo-oxidation of gaseous NO to nitric acid (ISO 22197:1-2010 and UNI11247:2010) and RhB discoloration (UNI 11259:2008)

4.5.2.1 NOx degradation vs RhB discoloration

In order to validate the proposed methods as techniques to assess the performance of photocatalytic materials, both proposed methods (reductive ink tests and TA-FL method) have been correlated with the two sets of photocatalytic activity results of standards of photo-oxidation of NO_x and RhB discoloration.

Before these comparisons, both standardized methods are also compared between them in Figure 4.48 (a-c). From these figures, it can be seen that these two set of results (RhB and NO_x) do not show a clear relationship, being the differences between methods higher if compared the NO_x degradation with the RhB discoloration results at 4 hours (R₄). The differences between both photocatalytic tests may be related to three parameters:

- (1) The different type of radiation used (UV and UV-Vis light for RhB and NO_x test respectively)
- (2) The underlying mechanism of reaction
- (3) The intrinsic characteristics of samples.

It is important to note that all considered samples in Figure 4.51 are white or light grey; therefore, the deviations of RhB measurements due to variation of colour substrate are discarded. Beside this, as observed from UV-Vis absorbance analysis, all considered samples only shown absorbance in the UV range (<400 nm); therefore, the aspect related with the difference light activation could be also ruled out. Thus, it seems that the anomalies in the correlation are related with the underlying degradation mechanism of contaminant as well as the intrinsic samples characteristics of the wide variety of materials tested. Similar results also were reported on previous studies[193, 194]. These results highlight the problems that previously indicated about the comparison of photocatalytic activity results between materials using the current standardized methods. Herby the test method may favour certain materials and have negative influence on others, or in the case of RhB test can give “false positive or negative”. Note that the RhB test method (UNI 11259:2008) estipulate that the material tested is considered photocatalytic if the percentages of color decrease are greater than 20% and 50% at 4 and 26 hours respectively. Taking into account these results, the comparison between the standardized test and the proposed tests will be individually done.

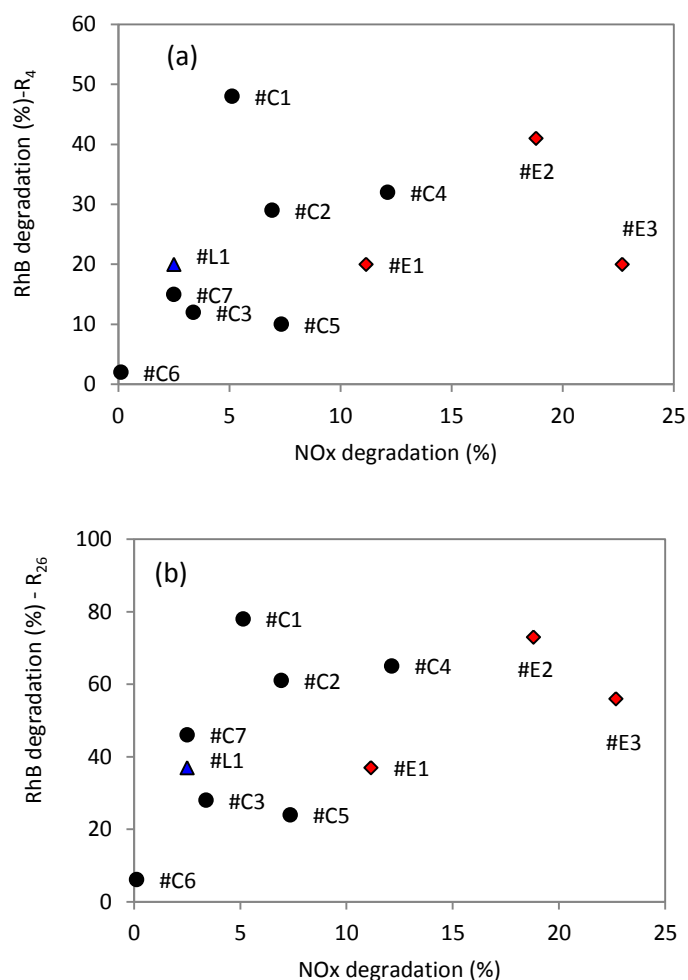


Figure 4. 51 Comparison between the photoactivity results determined by NOx (ISO 22197-1:2010) and RhB degradation upon irradiation at (a) 4 hours and (b) 26 hours.

4.5.2.2 TA-FL vs reductive inks

It is important to point out again that in both developed tests (TA-FL and reductive inks) and in NO_x air purification standard test, the light source used is the same and their results are independent of the colour substrate. Therefore, in the different comparisons made using these results, the correlation remains unaffected by these parameters, as will be briefly further discussed.

The results of both developed methods are correlated and shown in Figure 4.52. It can be seen that in spite of a wide range of the significant TiO₂ selected construction materials, a reasonably good relationship has been achieved. These results are of particular importance as they demonstrate that an effective photocatalyst for oxidation reaction through OH• will also be effective for reductive reaction by e⁻, as the measured rates of the different processes are related directly to each other.

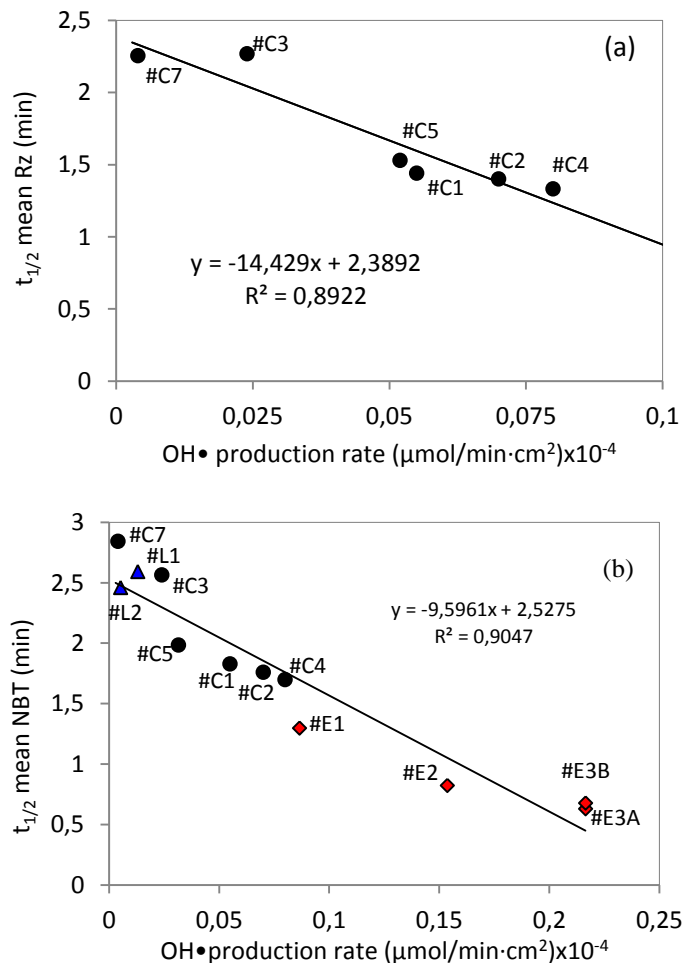


Figure 4. 52 Plot of OH• production rate ($\mu\text{mol}/\text{min cm}^2 \times 10^{-4}$) vs time taken for Rz (a) and NBT (b) to lose half its color ($t_{1/2}$) on photocatalytic samples. $t_{1/2}$ mean is the average value of data collected by absorbance and color (RGB and CIELAB) measurements for both inks.

4.5.2.3 NO_x degradation vs TA-FL and reductive inks

The results of the methods (TA-FL and reductive inks) are correlated with the NO_x results in Figure 4.53 (a-c) and 4.54 (a-b) respectively. It can be seen that in spite of having different TiO₂ photocatalytic materials, the results of both types of methods correlated very well with the NO_x degradation results, with an almost linear relationship, indicating that the greater formation rate of OH•/ e- reduction yield (lower time taken for Rz and NBT to lose half its colour ($t_{1/2}$)), the higher photocatalytic degradation of NO_x. The less value of R² lineal adjustment of Rz can be attributed to less number and low variability of samples tested. The correlation obtained encourages the validation of both proposed tests as methods for determination of the photocatalytic performance, considering that the NO_x air purification test is considered as reference in the evaluation of the photo-activity of photocatalytic samples, due to the high importance of the decontamination of outdoor air.

It can be noted that NO_x degradation results were obtained using two different procedures (ISO 22197:2010 and UNI 11247:2010 standards). Both NO_x tests present large differences in their experimental conditions that make different numeric linear adjustment with the photocatalytic activity results obtained using the development tests; thus, the comparison between the NO_x standardized tests and the new proposed test will be individually presented in different graphs.

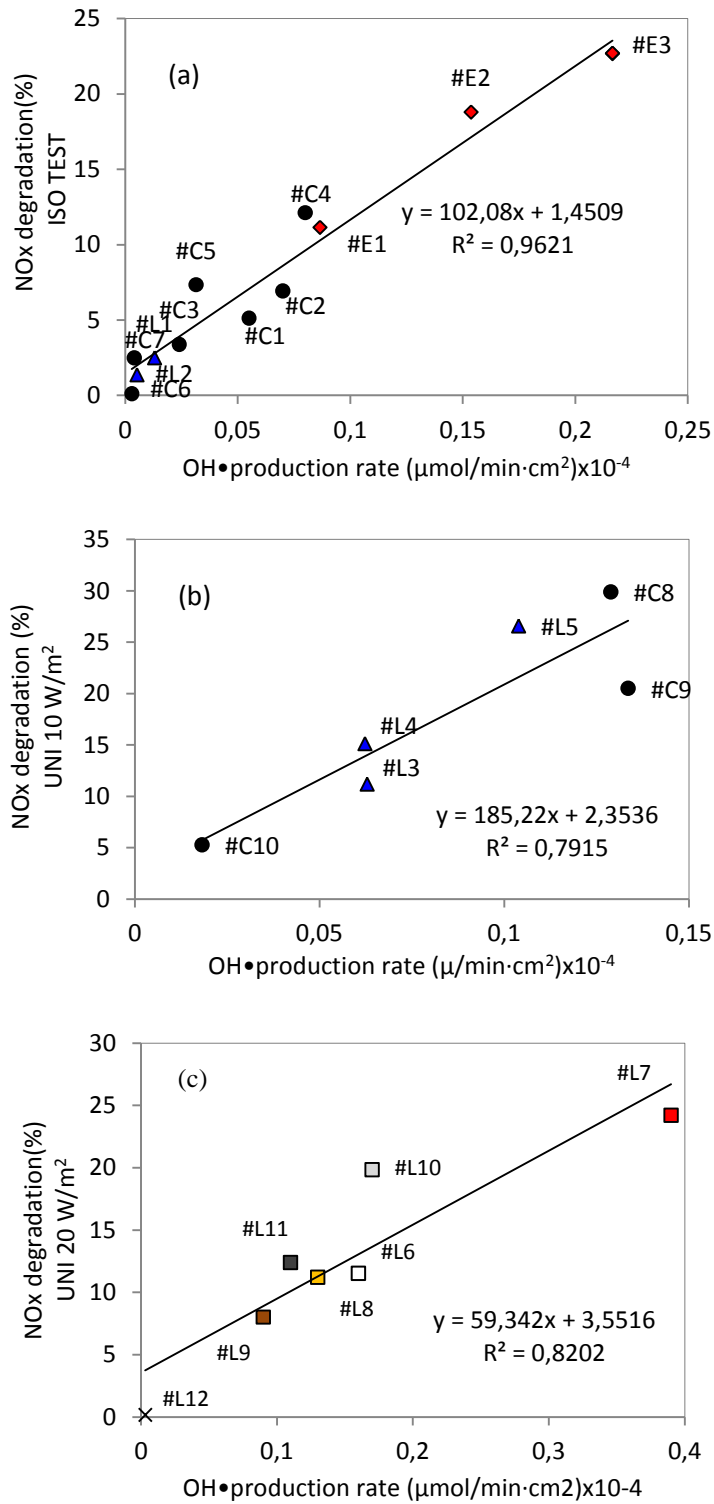


Figure 4. 53 Plot of OH• production rate ($\mu\text{mol}/\text{min cm}^2 \times 10^{-4}$) of photocatalytic samples vs NOx degradation (%). $t_{1/2}$ mean is the average value of data collected by absorbance and color (RGB and CIELAB) measurements for both inks.

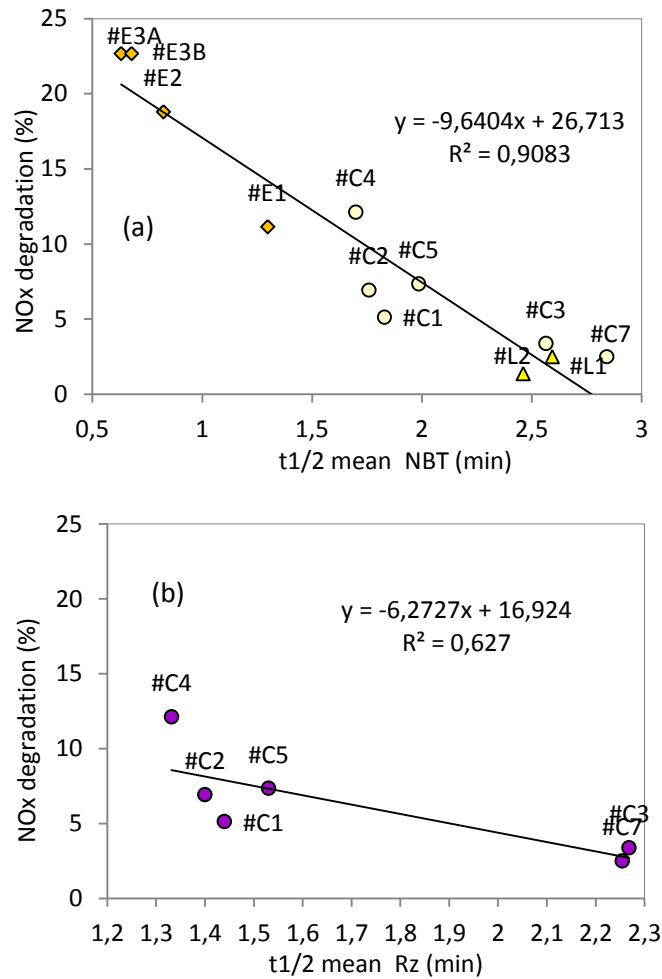


Figure 4. 54 Plot of time taken for Rz and NBT to lose half its color ($t_{1/2}$) on photocatalytic samples vs NOx degradation (%). $t_{1/2}$ mean is the average value of data collected by absorbance and color (RGB and CIELAB) measurements for both inks.

On the other hand, these results may suggest that the higher NOx degradation of samples should be attributed to the higher photo-induced e^- or OH^\bullet production process, due to correlation between them, as verified in Figures 4.53 and 4.54. In order to clarify these relationships, additional results were presented in Figure 4.55. In this figure, it was compared the NOx degradation ability, in $\mu\text{mol}/\text{min}\cdot\text{cm}^2$ units of the data shown in Figure 4.53(b), with the OH^\bullet formation rate ($\mu\text{mol}/\text{min}\cdot\text{cm}^2$) determined by TA-FL method. Both set of experiments was performed at $10 \text{ W}/\text{m}^2$ in order to ensure an adequate comparative of the data.

It is generally accepted that the photocatalytic degradation of NO_x on TiO₂ proceeds mainly via direct OH• oxidation [5, 195, 196], following Eq. (4.10) and (4.11). Several authors have also reported that superoxide radical (O₂•⁻), may also contribute to the conversion process (Eq. (4.12) and (4.13) [197, 198].



From the Figure 4.55, it can be deduced that again there is a clear proportionality between the OH• production rate and NO_x degradation parameters. This good relationship might induce to think that the photocatalytic oxidation of NO_x takes place mainly through the OH• generated (following Eq. (4.10) and (4.11)). However, as simplified approximation using the previous Eq (4.10-4.11), it could be said that to degrade a given number of moles of NO_x, 3 times more of OH• are stoichiometrically needed. Therefore, based on the results of Figure 4.55 [NO_x (μmol/min·cm² × 10⁻³) = 1.04 OH• (μmol/min·cm² × 10⁻⁴)], the obtained NO_x degradation rate was ca. 30 times larger than the OH• detected, considering that degradation of NO_x had taken place all through OH•. These experimental results suggest that other species in equilibrium with OH• must be involved into the NO degradation process.

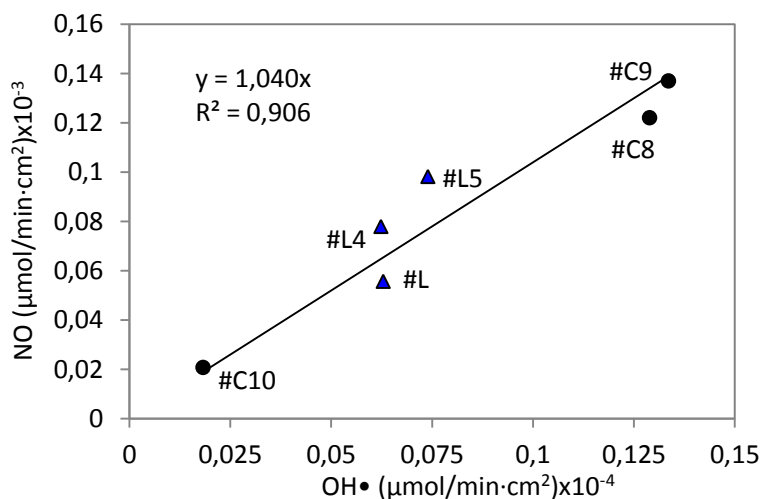


Figure 4. 55 NO_x removal (UNI 11249:2010) vs production rate of OH• on μmol/min· cm² units.

To evaluate if the $O_2^{\cdot-}$ could be the responsible of all the part of the degradation that is not produced by OH^{\cdot} , a series of RhB oxidative tests were carried out on the same samples using scavengers for OH^{\cdot} (DMSO) and $O_2^{\cdot-}$ (deoxygenating the system by purging with argon (Ar)). This oxidative test has been proved to be an effective technique to identify the oxygen active species generated [199-201]. For this, the cementitious samples were grounded and 150 mg of powder of each sample was suspended in 25 ml of RhB aqueous solutions (1ppm). The suspensions were kept in dark under magnetic stirring for 5 hours in an aerated Pyrex glass cell until the adsorption–desorption equilibrium was reached. After that, the suspensions were exposed to irradiation on continuing stirred conditions and the decrease of colour after different irradiation times was determined measuring the variation of the a^* coordinate of the supernatant liquid after recovering the mortar powders by centrifugation. The results are given in Figure 4.56, where the percentage of degradation of RhB with respect to the test without scavengers after 30 minutes of irradiation is given (RhB discolouration without any scavenger is considered 100%). In this figure, the production of the corresponding radical species by photocatalytic sample involves a decreasing of degradation when removed its activity by the addition of corresponding scavenger. As expected, the degradation rates exhibited significant decrease in the presence of DMSO, meaning that OH^{\cdot} were generated for all samples. This experiment was repeated in the anaerobic conditions, with larger degradation due to $O_2^{\cdot-}$ in all the cases except for #C1, that had a negligible effect of RhB degradation compared without scavenger under otherwise identical conditions, indicating that $O_2^{\cdot-}$ was not generated by this sample. These results demonstrated that the surplus in the amount of NOx degraded in relation to the amount of OH^{\cdot} produced (around 30 times) cannot be attributed exclusively to the contribution of $O_2^{\cdot-}$.

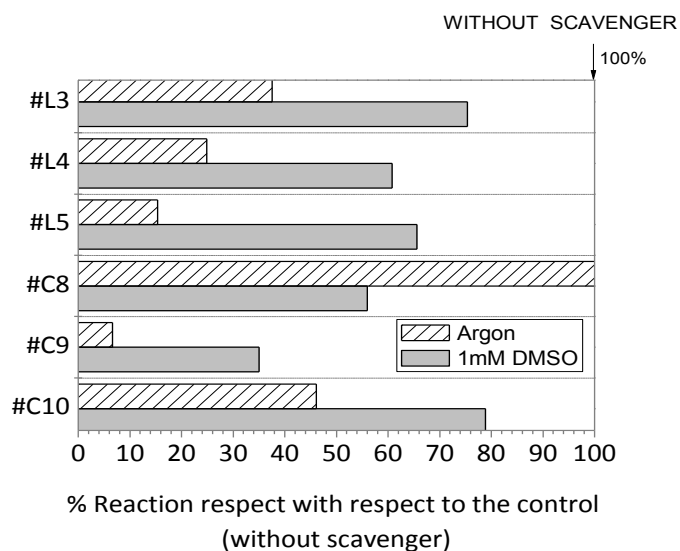


Figure 4. 56 Percentage of degradation of RhB with respect to control test without scavenger.

In order to confirm these previous results of RhB oxidative test with scavengers, XPS measurement of three samples were performed. In this way, it is possible to calculate the position of valence band of the TiO₂ photocatalyst into the cement matrix. This technique has been proved to be an effective technique to calculate the position of valence band (VB) of the TiO₂ cement complex matrix [158]. The VB spectrum of selected samples is presented in Figure 4.57. Beside this, for the VB-XPS it can be seen a VB tail induced by structural disorders in all samples [158, 192, 202], more pronounced in the case of samples #C8 and #C9. The structural disorder originates from impurities and defects (Ti³⁺ and oxygen vacancies) produce an absorption tail extending the deep into the forbidden gap near the bottom/top of its conduction/valence band. The presence of tails can result in a decrease of the band gap of photocatalytic samples [179, 192].

The conduction band (CB) bottom of samples was calculated by subtracting the value of apparent photoabsorption edge (PE_{app}, from absorbance measurements, Table 4.4) from VB position (Eq. 4.14). Table 4.7 included the all values for this calculation. From these values, a probable band energy diagram is displayed in Figure 4.58.

$$CB (eV) = VB (eV) - PE (eV) \quad (4.14)$$

Figure 4.56 clearly shows that although most of the samples show a potential energy of CB position for reduction of O₂ to O₂^{•-}, the sample #C8 not shown enough potential energy for this reaction. These results confirmed the above obtained results using RhB oxidation test with scavengers, that evidenced the sample #C8 is not producing O₂^{•-}.

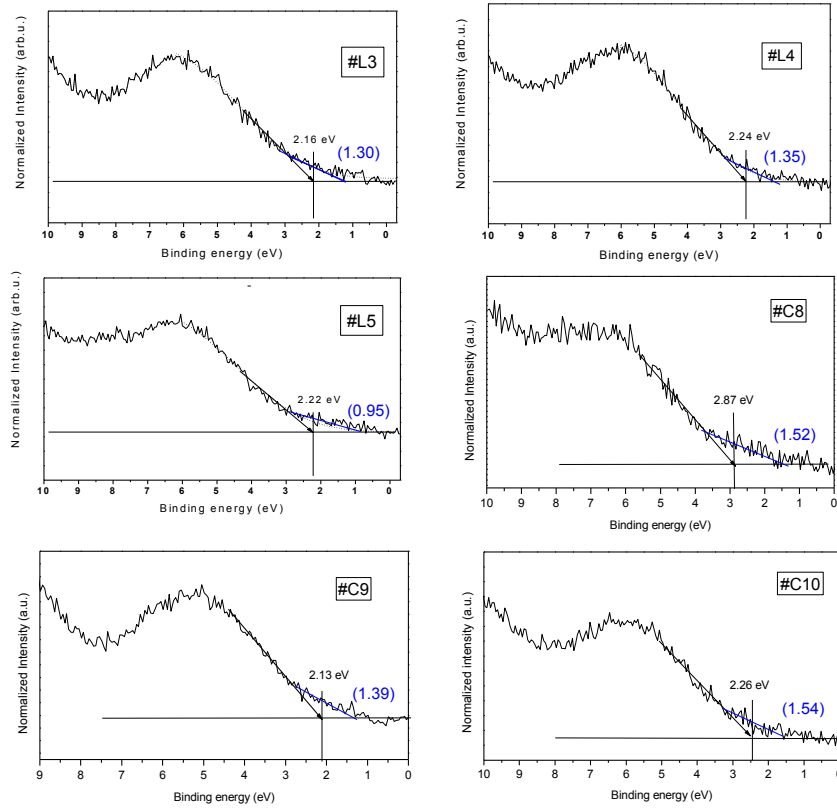


Figure 4. 57 XPS Valence Band (VB) spectra of selected samples. The values presented in the figure indicated the maximum energies associated with the BV and band tails. The band tail energies were shown using parentheses.

Table 4. 7 Calculation of the probable position of VB and CB of TiO₂ samples.

Samples	PE ¹ (eV)	VB position ² (eV)	CB position (eV)	VB position tail ² (eV)
#L3	3.19	2.16	-1.03	1.30
#L4	3.15	2.24	-0.91	1.35
#L5	3.05	2.22	-0.83	0.95
#C8	2.66	2.87	0.21	1.52
#C9	2.72	2.13	-0.59	1.39
#C10	3.25	2.26	-0.99	1.54

¹ data obtained from reflectance and ² from XPS measurements

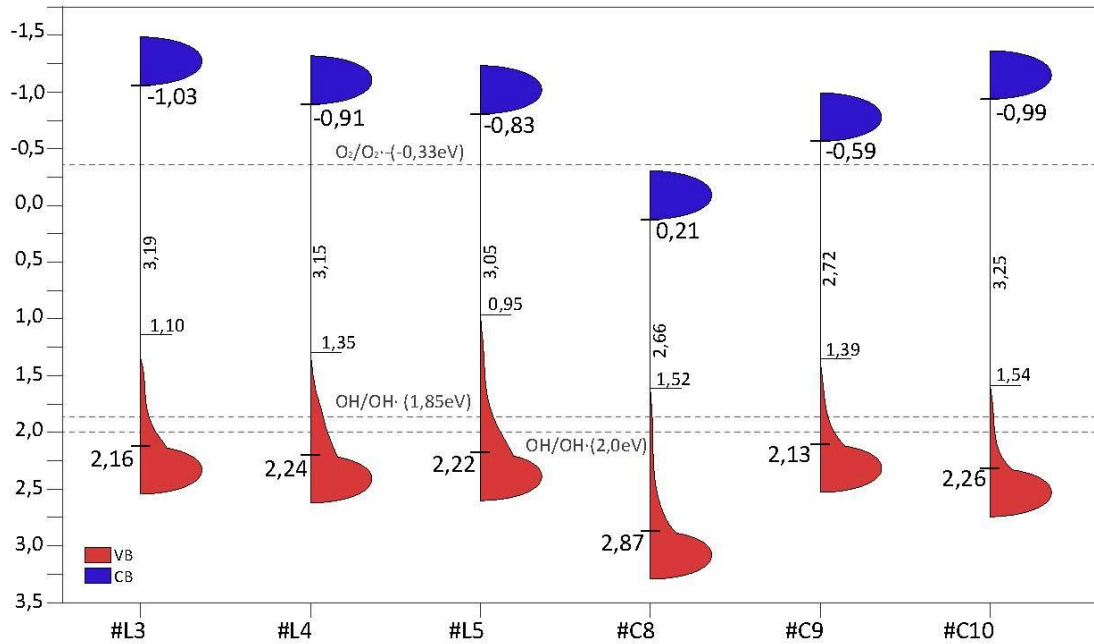


Figure 4. 58 Schematic illustration of approximate position of conduction band (CB), valence band (VB) and band tail of VB of selected samples.

Additionally, Looking at the Pourbaix diagram of potential versus pH (Figure 4.59, adapted from [17]) for nitrogen species and the couples $\text{OH}^-/\text{OH}\cdot$ and $\text{O}_2/\text{O}_2\cdot^-$ it is clear that the potential of the couple $\text{OH}^-/\text{OH}\cdot$ is significantly higher (more oxidant) than nitrogen couples, indicating that all oxidation steps of nitrogen species are easily performed by $\text{OH}\cdot$. Figure 4.59 shows that at the basic pH of cement-based samples $\text{O}_2\cdot^-$ it is able to oxidize NO_2 to NO_3^- but higher pH is needed, not reached by every binder with $\text{pH} > 13.6$), to give the reaction for the couple NO_2^-/NO .

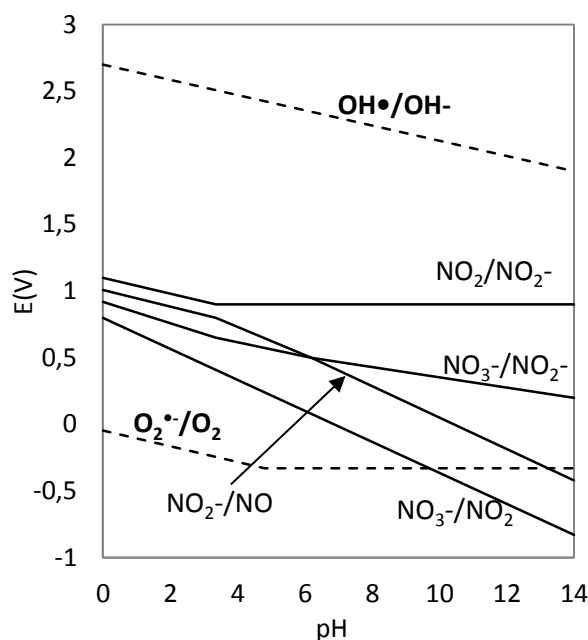
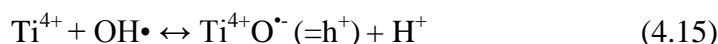


Figure 4. 59 Pourbaix diagram for nitrogen species together with the equilibrium lines corresponding to $\text{OH}\cdot/\text{OH}^-$ and $\text{O}_2^{\cdot-}/\text{O}_2$.

Therefore, taking into account all of above results, the surplus in the amount of NO_x degraded in relation to the amount of $\text{OH}\cdot$ produced cannot be attributed exclusively to the contribution of $\text{O}_2^{\cdot-}$. However, $\text{OH}\cdot$ must then be in equilibrium with the main specie responsible for this oxidation process, in a way that, despite the absolute value of production of $\text{OH}\cdot$ is not stoichiometric related to the mineralization of NO_x , it is proportional to it. In fact, through pulse radiolysis experiments [32] it was found that there is an equilibrium between free $\text{OH}\cdot$ produced by irradiation in TiO_2 suspension and surface trapped h^+ (Eq. 4.15).



The correlation between the photocatalytic activity and the $\text{OH}\cdot$ formation therefore could be explained due to equilibrium between h^+ and free $\text{OH}\cdot$ ($\text{OH}\cdot \leftrightarrow \text{h}^+$). According to the results in this research, this equilibrium must be significantly shifted towards the surface trapped h^+ (about 30 times, as previously explained). These results coincide with those obtained in previous studies. Ishibashi et al. [18] reported that the quantum yield of $\text{OH}\cdot$ production during TiO_2 photocatalysis was estimated to be $7 \cdot 10^{-5}$ in aqueous solution by means of a method using TA-FL probe method. This value is much lower than the quantum yield of ordinary photocatalytic reactions ($\sim 10^{-2}$). Conversely, the quantum yield of h^+ generation estimated by iodide ion oxidation was equivalent ($5.7 \cdot 10^{-2}$) to that of ordinary photocatalytic reactions. This implies that oxidative reactions on TiO_2 photocatalyst occur mainly via photo-generated h^+ , not *via* $\text{OH}\cdot$. Zhang et al. [203] already found for decomposition of acetaldehyde to CO_2 , the equilibrium is significantly shifted to the surface trapped (about 10^3 times) than that of the $\text{OH}\cdot$ formation.

Based on the experimental results from the present study, a mechanism for NO_x conversion to NO₃⁻ is proposed, which is shown in Figure 4.60.

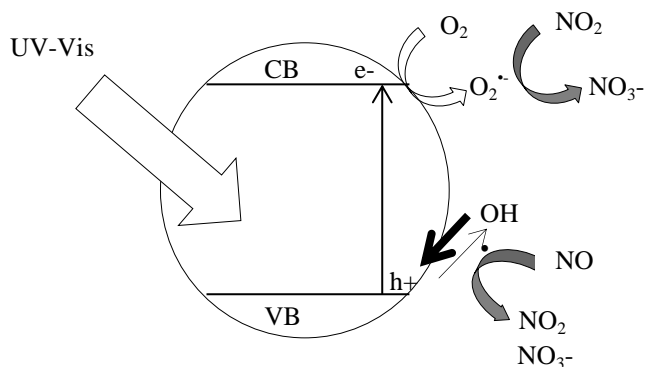
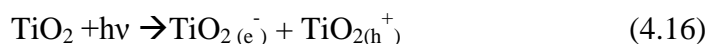


Figure 4. 60 Schematic illustration of reaction mechanism proposed based on the detection of OH• and NO_x removal.

The assumption about the direct participation of h⁺ in the NO_x degradation process also is in accordance with the good linear relationship of NO_x test with the reductive ink methods (NBT and Rz, Figure 4.54). In fact, during photocatalytic processes, when a semiconductor absorbs a photon with equal or higher energy than its band gap energy, it results in the formation of an e⁻-h⁺ pair [h⁺ in the VB and an e⁻ in the CB], according to Eq. 4.16. Therefore, it might be expected that the rates of e⁻ and h⁺ photo-generated are comparable.



Thus, the results of this work provide support that it might be indicate that an effective photocatalyst for oxidation reaction by OH•/h⁺ will also be effective for reductive e⁻ reaction, i.e., the measured rates of the different processes would be related one to another. Figure 4.61 presents a schematic diagram of the relationship between methods and the species determined for each one of them.

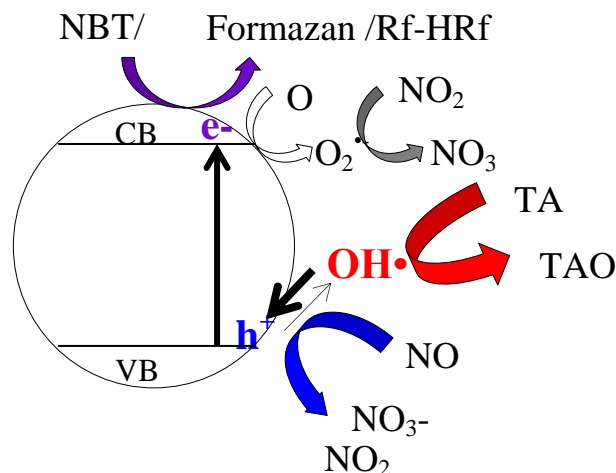


Figure 4. 61 Schematic diagram of relationship between methods.

4.5.2.4 RhB discoloration vs TA-FL and reductive inks

Concerning the second set of comparisons, the data from the developed methods vs RhB discoloration test (UNI 11259:2008) are shown in Figure 4.62. As before, the retained samples for the comparative are white or light grey and only shown absorbance in the UV range (<400 nm); therefore, the aspects related with the possible deviations in the comparison related with the colour substrate and light activation should be ruled out. As expected, taking into account the previous correlations, the proposed tests and the RhB discoloration show much deviation respect to the linearity (Figure 4.62). In addition, as indicated in the previous comparison between both standardized tests (Figure 4.51), the approach seems different in function of irradiation time of RhB discoloration at 4 hours (R_4) or at 26 hours (R_{26}). Although it is true that for $\text{OH}\cdot$ the same trend can be seen, indicating that the higher the $\text{OH}\cdot$ production rate, the higher the RhB degradation. In the case of e^- reduction yield, no correlation can be found, in agreement with the tests with plain powder photocatalyst.

The non-correlation in the data may be attributed to the underlying degradation mechanism of the contaminant as well as to the intrinsic characteristics of the wide variety of materials tested. However, the fact that is the only one method whose results follows a different tendency in comparison with the others, make us believe that the deviations are mainly related with the underlying RhB mechanism degradation, rather than the intrinsic characteristic of the samples. The oxidative degradation pathway of RhB under UV light by TiO_2 photocatalytic samples may involves the participation of mainly $\text{O}_2\cdot^-$, h^+ and $\text{OH}\cdot$ [165-167]. Thus, it is reasonable to think that the fact of the RhB dye degradation results depends on more complex redox reactions that the other proposed tests, which only depend of yield production of one active species (e^- yield – reductive inks and $\text{OH}\cdot$ production – TA-FL method), can explain the deviations of comparative results with respect to the linearity shown in Figure 4.62. As previous

explained, it is considered that the linearity of the other standard test (NO_x air purification test) is possible as the photo-generated holes would dominate the photocatalytic NO_x degradation, and thereby the direct relationship of them with the e- and OH• detected by the others proposed methods allows this direct correlation with low deviations.

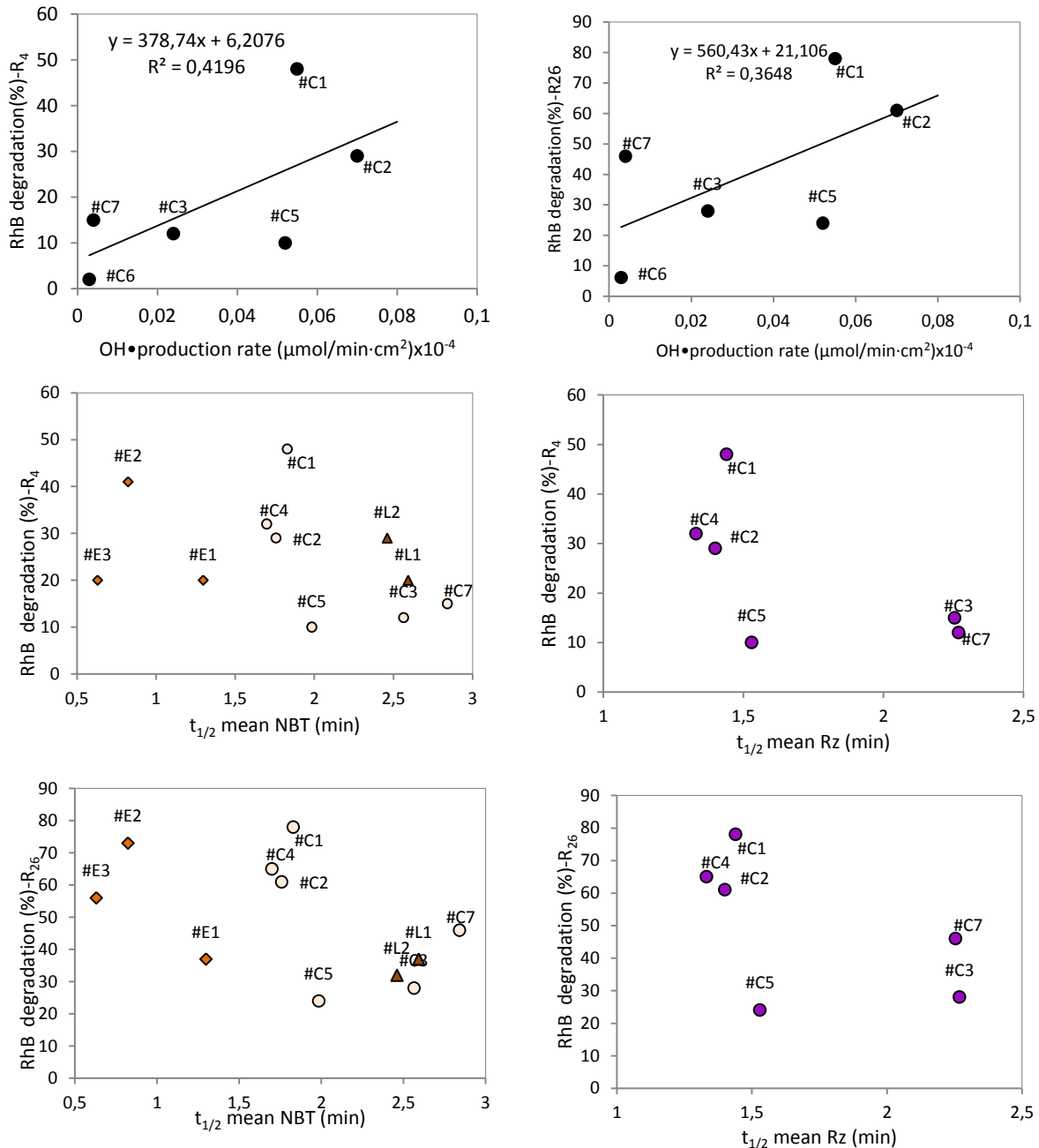


Figure 4. 62 Plot of OH• production rate from TA-FL measurements and time taken for Rz and NBT to lose half its color ($t_{1/2}$) on photocatalytic samples under an irradiance vs percentage of RhB discoloration at 4 hours (a, c and d) and 26 hours (b, e and f). RhB test performed using the procedure defining on UNI 11259: 2008 standards. $t_{1/2}$ mean is the mean value of data collected by absorbance and color (RGB and CIELAB) measurements for both inks.

Concerning RhB, Watanabe and co-worker[204] reported that degradation pathways of RhB is established by two parallel different pathways: cleavage of whole conjugated chromophore and N-de-ethylation under UV-Vis radiation, although it is important to note that it was not considered the effect of dye -sensitization in this results [72] as no Vis light was used. Natarajan et al.[205] established that the same two parallel pathways occur under UV-LEDs (see Figure 4.63). Cleavage is associated with invariance in the main absorbance peak position followed by progressive decrease in the intensity. N-de-ethylation of RhB is characterized by steps of successive blue shift in the absorbance peak of photodegraded dye, in which five main different levels are associated with different stage of photo-degradation [206, 207]. Characteristic peak of RhB at 554 nm is progressively shifted to 539 nm (N,N,N'-Triethylrhodamine), 522 nm (N,N'-Diethylrhodamine), 510 nm (N-Ethylrhodamine) and 498 nm (Rhodamine) (Figure 4.64).

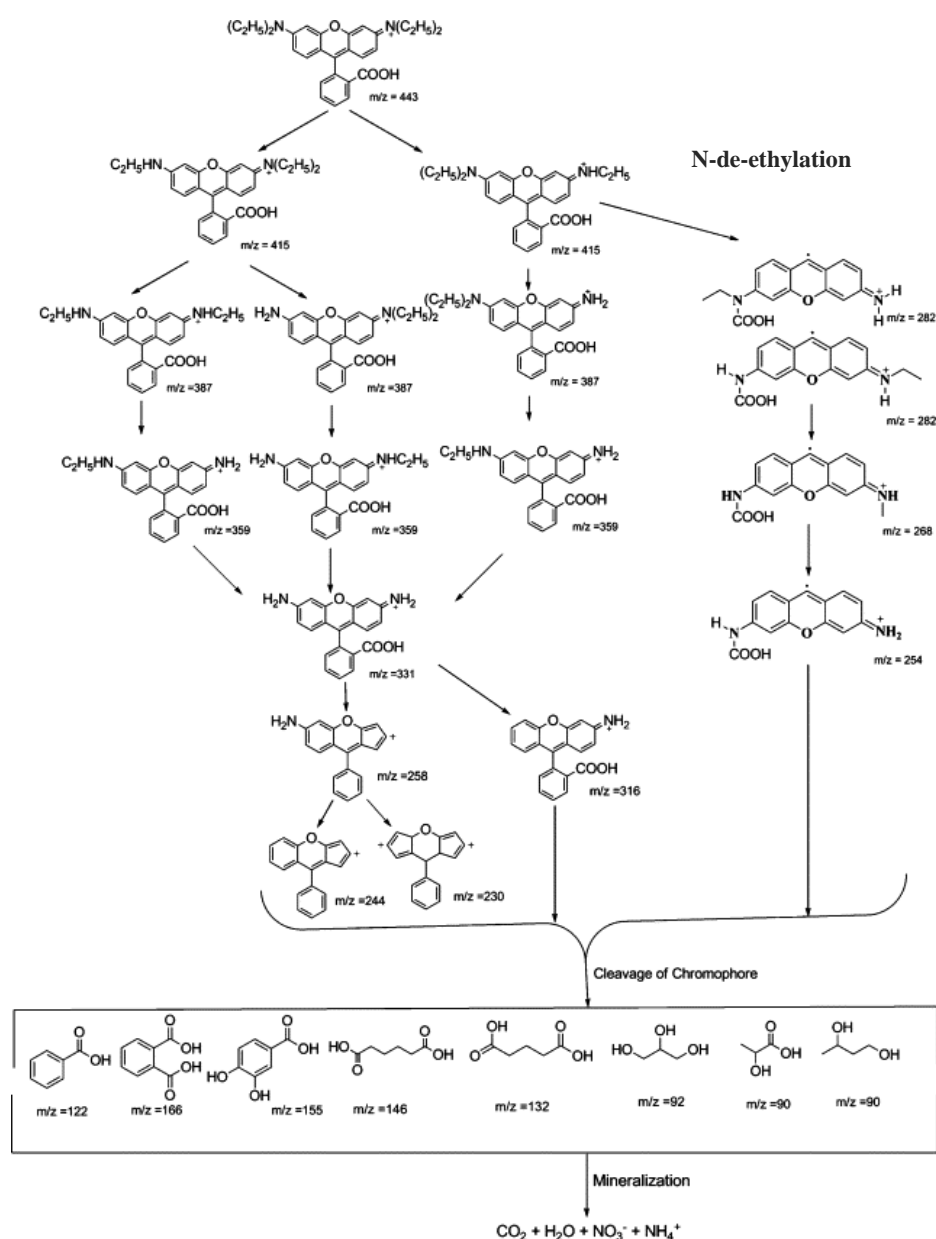


Figure 4. 63 Probable mechanism for the photocatalytic degradation of RhB dye (Taken from [205]).

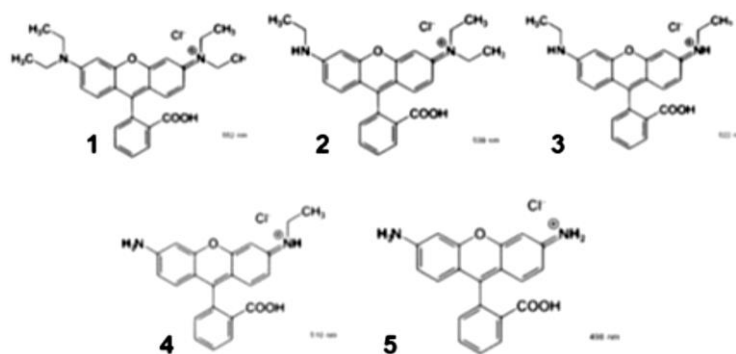


Figure 4. 64 Configuration of mainly degraded RhB molecules on N-de-ethylation process. ¹ 554 nm RhB, ² 539 nm (N,N,N'-Triethylrhodamine), ³ 522 nm (N,N'-Diethylrhodamine), ⁴ 510 nm (N-Ethylrhodamine) and ⁵ 498 nm (Rhodamine)[207].

Many workers reported that the N-de-ethylation process occurs sequentially, and this process is competing with the chromophore destruction[193, 208]. However, Zhuang et al [209] considered that the irradiated TiO₂ with both the N-de-ethylation (incomplete) and cycloreversion of RhB, resulting in the higher mineralization efficiency. Also is interesting to note that other works [210, 211] demonstrated that the effect of N-de-ethylation process predominates during the initial radiation period.

Concerning the participation of the primary active species in each degradation pathway, h⁺ and OH• yielded are beneficial for the cleavage of benzene from RhB, and superoxide from photo-generated electron and molecular oxygen are beneficial for the removal of ethyl [211]. Wu et al. [72] considered that the N-de-ethylation reaction of RhB by OH• is mostly induced by the OH• at the surface of the TiO₂ film whereas oxidative degradation of the dye chromophore (cycloreversion of RhB) is mainly caused by the free OH• in the bulk solution. This fact is in agreement with the linear relationship previously found in the preliminary study for TiO₂ plain photocatalysts in solution, between OH• detected using the TA probe and RhB degradation (see Figure 4.14). According to the absorbance spectra of RhB dye tested under plain TiO₂ photocatalysts, the maximum absorption of the dye spectrum decreased gradually with irradiation time and no peak shift was observed in all plain photocatalysts samples analyzed, which confirm that only cycloreversion route of RhB degradation occurred (some examples of spectrum are included in the APPENDIX E).

In contrast, according results of this work, the absorbance spectra of RhB dye tested under action of the selected construction materials during UV-365 nm LEDs irradiation shown very different behaviors. In some cases, the maximum absorption of the dye decreased gradually with irradiation time and no peak shift was observed (Figure 4.65a, example of sample # C7). However, other samples showed the two types of change, decrease in absorbance and the other shift in the absorbance maximum (Figure 4.65b, example of sample #C2). In this sample, the shift in wavelength maximum of RhB

corresponds to an incomplete de-ethylation of RhB to give N, N, N' Triethylrhodamine (~540 nm). Thereby, these results demonstrated the different TiO₂ samples tested shown different reaction routes of RhB degradation. Therefore, the final values of RhB degradation not only depend of the amount of photo-generated active species, but also the predominant route that follow, which may make it difficult to correlate the RhB degradation results with the other methods.

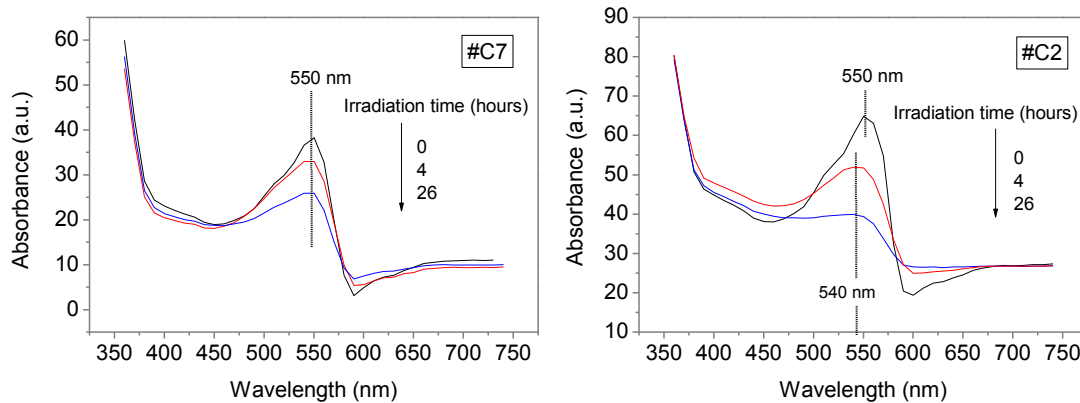


Figure 4. 65 Examples of temporal absorbance spectral changes of RhB dye by #C7 and #C2 samples.

Other interesting aspect is shown in in Figure 4.66 where the change in RhB degradation vs. irradiation time for all the samples compared. From it, one relevant aspect needs to be reported, as the rate of decomposition in function of the time do not follow the same tendency in all samples, e.g. the initial rate of degradation (R_4) by #L2 and #C2 is the same, however the further degradation rate of #C2 is much faster than the one photocatalyzed by the #L2 sample. This may again indicate that the TiO₂ samples tested shown different mechanisms of degradation, even in function of irradiation time and that the different routes may be change during the time as previously indicated.

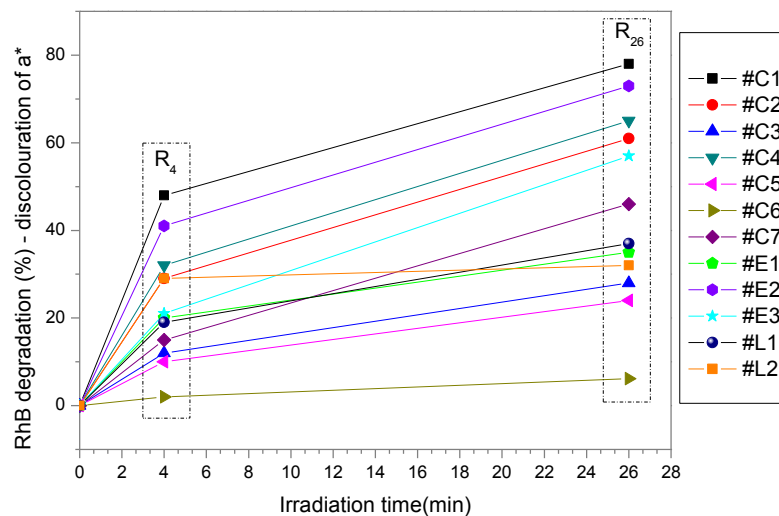


Figure 4. 66 RhB degradation of all analyzed samples in function of irradiation time.

Other cause that can explain the differences in the degradation rate of RhB and the other photocatalytic performance results can be related with the parameter considered during the RhB test. It must be keep in mind that dye degradation calculated in function of the loss of colour (coordinate a^* CIELab system) for evaluation of self-cleaning performance on UNI 11259:2008 standard performed test, only gives an indication of the breakup of the molecule due to the breaking of chromophores. During the N-de-ethylation, additional chromophoric compounds are formed, which complicate the quantification of RhB degradation based on the loss of color. In fact, is probably that there is an underestimation of RhB discolouration on samples that shown N-de-ethylation due to the appearance of N-de-ethylated chromophores. Therefore, for an adequate measurement of photocatalytic kinetics of RhB, techniques as Total Organic Carbon (TOC) measurements and mass spectrophotometry should be used.

As a summary, three aspect may be considered that as possible causes to the divergences between the RhB test (UNI 11259:2008) and the other photocatalytic tests (TA-FL, reductive inks and NO_x air-purification) on construction materials: The first is the more complex underlying mechanism of dye test degradation, which is dependent of the participation of various photo-generated active species (mainly h^+ , OH^\bullet and $O_2^{\bullet-}$), the second is the presence of two parallel different pathways, that even may change during the irradiation time. And the third can be related with the parameter considered during the RhB test (red color, coordinate a^* CIELab system), that is not appropriate parameter to monitor the RhB degradation due to the interferences that may suffer the estimated values by the appearance of other N-de-ethylated chromophores. This fact again underscores the dangers of extrapolating photocatalytic performance results from RhB dye discolouration tests to other photocatalytic tests. Even, the serious limitations of results comparison between different samples analyses only with RhB test.

In order to get more insights about the relationship between the photocatalytic degradation rate of reductive ink tests and RhB standard method, a simpler comparison using replicated specimen of same sample (#C7) under different irradiances intensity was performed. In this way, the effect of intrinsic properties on the underlying mechanism of degradation of both tests was annulated. To do this, RhB discolouration and Rz ink conversion tests were performed using the coating procedure described in the standard of RhB discolouration (UNI 11259:2008, described detail in *Section 3.4.2*). As the coating procedure is different as previous test (spray coating), some modification of Rz probe formulation was required in order to obtain a homogeneous layer covering the entire surface of the photocatalytic material with a clearly visible characteristic colour of the ink (blue). The probe was made from ultrapure water (4 mL), hydroxyethyl cellulose polymer (0.2 g, 1.5 wt. % aqueous solution, glycerol (0.3 g) and Resazurin (4 mg). The amount of probe deposited onto the sample was 500 microliters. A glass rod was used to spread out the probe layer onto the samples.

The portable spectrophotometer (Figure 3.20b) was used to measure the variation of colour and the absorbance in function of irradiation time of coated replicates of sample #C7(#C7A, #C7B, #C7C, #C7D, #C7E) subjected to different UV irradiances (0–3.75 W/m²). The corresponding identification of samples in function of the irradiation intensities used was displayed in Table 4.8. This sample was selected because previously, through the application of the RhB standardized test, showed that the RhB degradation pathway was the chromophore degradation route, and not N-de-etylation pathway was observed. In this way, the underlying mechanism of both processes can be easily understanding, and the the RhB degradation monitoring can be estimated avoiding the interferences that may suffer by the appearance of other N-de-etylated chromophores.

Each data was then analysed to determine the value of kinetic degradation rate in form abs/min. Under these experimental conditions of coating procedure and maxima irradiance intensity of 3.75 W/m², the rate of conversion of Rz to Rf was slower than in the previous performed tests (using a light of 5W/m² and the spray coating procedure). In order to gain a measure of the dependence of the degradation rate with the light intensity, avowing the possible interferences of the second step of reduction (Rf to DH-Rf), which also show different kinetic rate (at least 3.5 times more larger than the first reduction step [115]), the kinetic rate of degradation of the Rz to Rf can be determined to by assessing the decrease in absorbance at 608 nm at early times (i.e. times in which the rate of decrease is linear). The results during irradiation time (#C7E, sample irradiated at 3.75 W/m²) are given in Figure 4.67. The rate of conversion of Rz to Rf (R_{Rz}) and degradation of RhB (R_{RhB}) were calculated using the variation in the absorbance at 608 nm and 550 nm respectively during 120 min of irradiation. The results plotted in the form of relative absorbance vs. time under different irradiation intensity are illustrated in Figure 4.67(c and d) for Rz and RhB respectively. From the slope of the dependences of these figures, both rates (abs/min) were calculated. The values obtained are presented in Table 4.8.

Figure 4.68 shows the chronological series of images recorded for the replicated specimens of sample #C7 at different irradiation intensities. This figure evidence the more noticeable visible change of Rz ink in less time that RhB.

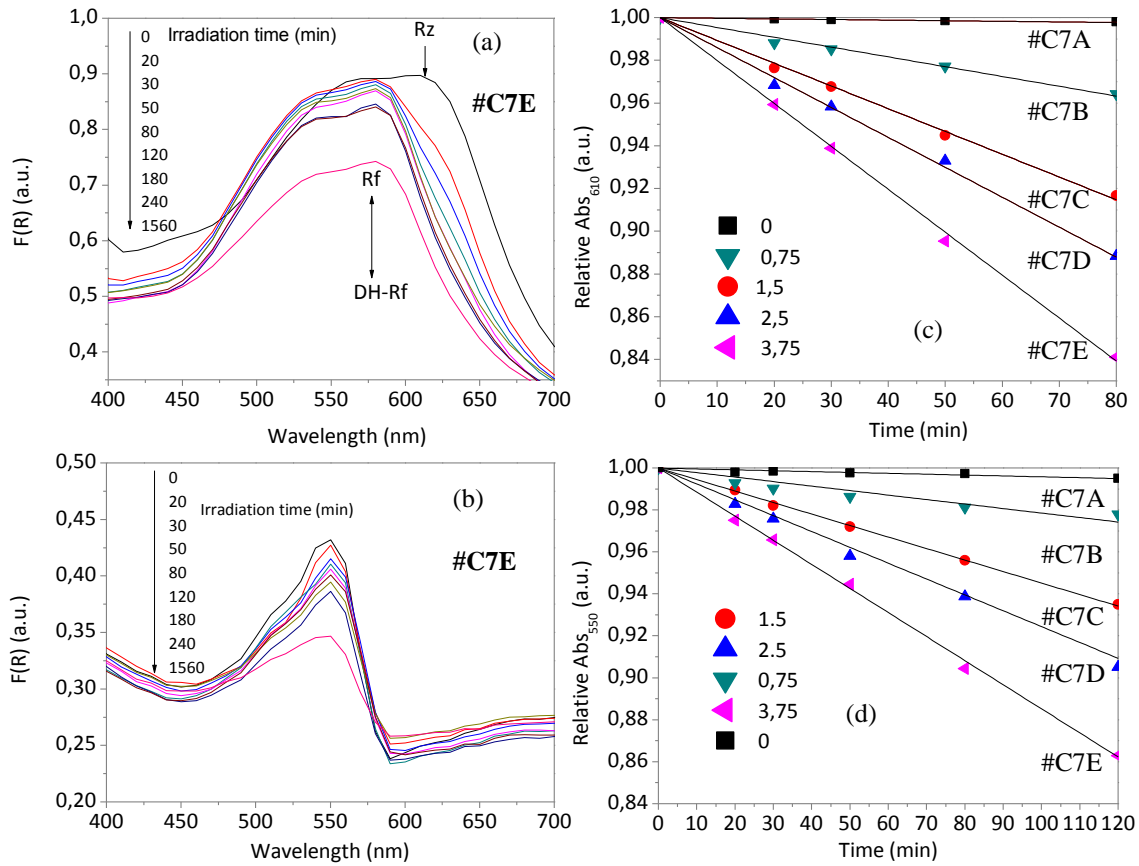


Figure 4. 67 Variation of UV–Vis absorbance spectra of the (a) Rz and (b) RhB probe deposited onto a sample of replicated specimen of sample #C7 (#C7E) as a function of irradiation time at 3.75 W/m² (b) Plot of the relative Abs₆₁₀ vs. irradiation time of (c) Rz and (d) RhB onto replicated specimens of sample #C7 at different irradiation intensity (0-3.75 W/m²).

Table 4. 8 Identification of samples and results of analysis of Rz and RhB degradation on photocatalytic replicated samples (#C7A-#C7E).

Sample	Irradiance intensity (Wm ⁻²)	R _{Rz} (Abs/min)	R _{RhB} (Abs/min)
#C7A	0	0.00001	0.00002
#C7B	0.75	0.00052	0.00030
#C7C	1.5	0.00107	0.00035
#C7D	2.5	0.00131	0.00049
#C7E	3.75	0.00190	0.00081

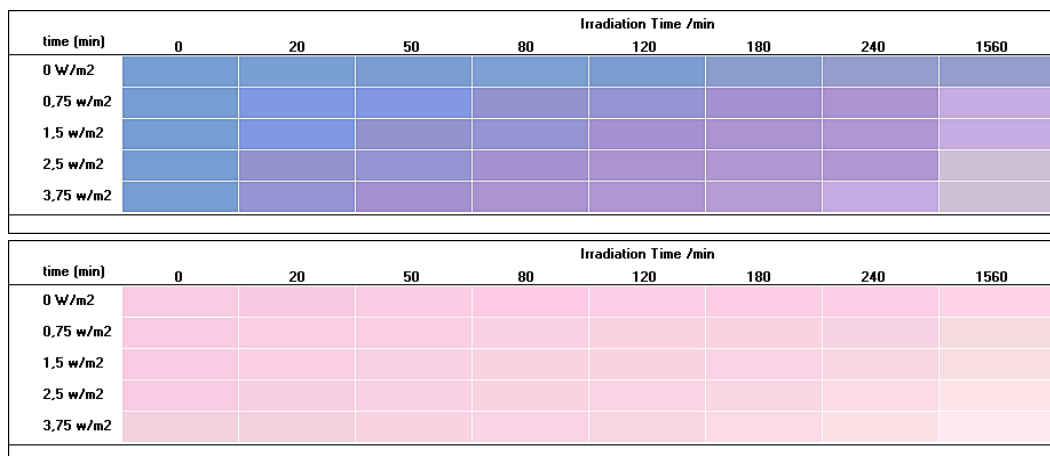


Figure 4. 68 Chronological series of images recorded for the replicated specimens of sample #C7 at different irradiation intensity.

The results of R_{Rz} and R_{RhB} (data from Table 4.8) vs. irradiance intensity (W/m^2) are shown in Figure 4.69 (a). These plots reveal that the degradation rates of both probes are directly proportional to the UV irradiance intensity, whose linear correlation is 0.9838 and 0.9424 for Rz and RhB respectively. The relationship between these results in the form of abs/min is shown in Figure 4.69 (b). In contrast to previous results performed using different samples, from this data, the degradation of RhB, was found to be proportional to Rz ink conversion. These results confirm the previous discussion, as sample #C7 not showed degradation by N-de-ethylated pathway; therefore, the possible deviations between tests related to the presence of two parallel degradation pathways, and the appearance of N-de-ethylated chromophores can be excluded. On the other hand, these tests were performed using replicated specimen of the same piece of cement based sample (#C7 under different UV irradiances intensities); thereby, under these experimental conditions, the divergences in the correlation between both tests by the different intrinsic properties of samples, as important as, the type of photocatalyst or surface properties (BET, porosity, etc.) can be excluded.

Therefore, it could be said that the good linear relationship between both tests, when the tests were done using replicated specimen by the same sample (#C7), demonstrated that a direct relationship between the electron yield rate and the oxidative rate of RhB existed. Considering that the underlying mechanism of RhB dye degradation is more complex than the Rz conversion by electron due to the photocatalytic oxidation by RhB is dependent of the participation of various oxidative photo-generated active species (mainly h^+ , OH^\bullet and $O_2^{\bullet-}$) [165-167]; This relationship can be explained considering the same explanation used previously that allows that the three methods results (NO_x air purification test, TA-FL and inks test) are comparable (see Figure 4.61). Thereby, based on these results, it might consider that the photocatalytic oxidation of RhB take place mainly through the h^+ or OH^\bullet generated, and the direct relationship between the species ($e^- \leftrightarrow h^+ \leftrightarrow OH^\bullet$) allows that the results of RhB and Rz are comparable in this case. Note again that this direct

correlation only is possible under these conditions because the possible deviations by the intrinsic properties of samples and degradation by N-de-ethylated pathway are not present. These results also are in agreement with [211], that demonstrated that h^+ and $OH\bullet$ yielded are related with the cleavage of benzene from RhB.

These results although allows some clarify the complex mechanism of RhB, but continues to show the limitations of extrapolating photocatalytic performance results from RhB dye discoloration tests to other photocatalytic tests.

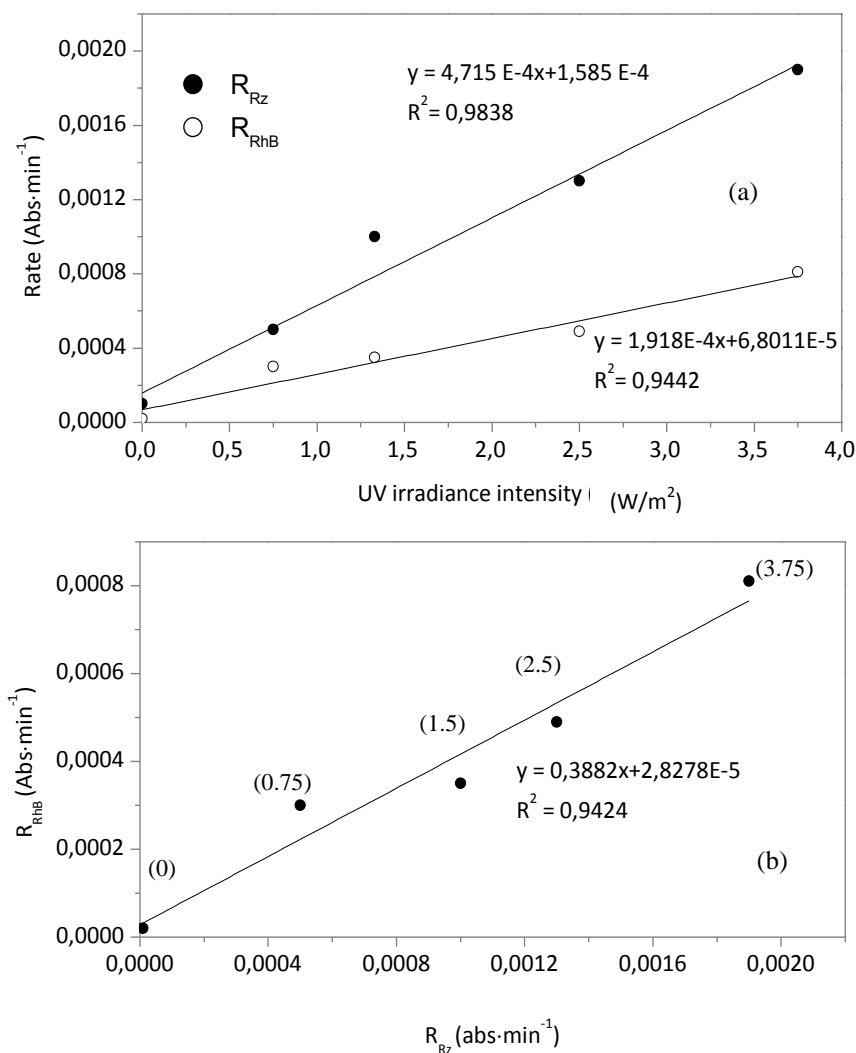


Figure 4. 69 (a) R_{Rz} and R_{RhB} vs. irradiance intensity (W/m^2) and (b) Relationship between R_{Rz} and R_{RhB} . The numbers in parenthesis indicated the values of irradiance intensity used (W/m^2).

As a summary, it is important to emphasise that the comparisons between the different tests are very interesting due to each test follow markedly different underlying reaction mechanism and different physical and chemical form of dye/probe/contaminant used during the test, i.e. NO_x (inorganic compound) is a gas-phase test, RhB and reductive inks dried film organic dye-test, and TA-FL method used a liquid probe. Table 4.9 underline the main differences of the different procedures.

Since all the tests are semiconductor photocatalyzed redox reactions, and the reaction rate directly depends on the amount of reactive oxygen species (ROS) or charge carriers (e^- - h^+ pairs) present, and these ROS are generated from the holes-electron pairs, then it could be assumed that an effective photocatalyst for oxidation reactions by ROS would also be effective for reductive reactions through electron, i.e. that the measured rates of the different processes will be related to one another. Rz and NBT ink test, which is based on the reduction of the ink (and concomitant oxidation of glycerol), is also correlated with the ability of photocatalytic samples to oxidative degradation of an inorganic (NO_x) compounds, and even with the TA-FL probe method that only react with the oxidative specie OH•. In this case, the results have supported this affirmation due a direct relationship of the main active species involved on the degradation pathways. However, RhB do not show a clear direct relationship with another photocatalytic tests, due to mainly the more complex underlying mechanism of dye test degradation.

Therefore, from one isolated photocatalytic test on a specific contaminant, no general conclusions of the general expected photocatalytic performance of photocatalytic materials must be derived. The results of this work are relevant to the high number of researches that only determined the photocatalytic activity of new photocatalyst using one single method [212-215].

In addition, the good correlation between the new developed tests (TA-FL and reductive ink) with both NO_x degradation tests, which are made following the standard ISO 22197:2007 and UNI 11247:2010 are of particular importance to extrapolate directly the photocatalytic results of TA-FL probe method and reductive ink tests to NO_x degradation tests, which are generally considered as the standard reference tests for determination of photocatalytic activity on photocatalytic materials, in particular in the construction field.

Table 4. 9 Summary of the main differences between photocatalytic performed test.

Test/standard name	probe/contaminant	Physical form of probe/contaminant during the test	Inorganic/organic composition of probe/contaminant	Reaction mechanism	Results independent of colour subtract
Reductive ink tests	(Rz or NBT) +glycerol+HC	Dried film onto surface sample	Organic	electron(e ⁻) reduction	yes
Rhodamine (RhB) discoloration (UNI 11259:2008)	Rhodamine B (RhB)	Dried film onto surface sample	Organic	Active species oxidation (OH•, O ₂ ⁻ , h ⁺) Two routes (N-de-etylation and cleavage chromophore)	no
photo-oxidation of gaseous NO to nitric acid (ISO 22197-1: 2007)	Nitrogen oxides (NO _x =NO+NO ₂)	Gas	Inorganic	Active species oxidation (h ⁺ , OH• and O ₂ ⁻)	yes
Terephthalic acid fluorescence probe (TA-FL) method	Terephthalic acid (TA)	liquid	Organic	OH• oxidation	yes

These results are also encouraging as the timescale for obtaining both ink tests (~10 minutes) and TA-FL probe method results (~20-40 min) results, is considerably smaller than that both conventional standardized photocatalytic activity tests (photo-oxidation of gaseous NO to nitric acid - ISO 22197-1: 2007(~6 hours) and UNI 11247:2010 (1 hour), and therefore offers advantages as a quick test. Note that the time presented in parenthesis not includes the longer time that requires the NO_x-air purification tests. Beside this, the possible use of the reductive ink technology for assessing the photocatalytic activity as a simple and inexpensive manner *in situ* using a digital camera make them as more attractive method for testing such materials. In addition, both proposed test can be performed under ambient conditions without any control of temperature and humidity conditions. This type of measurement it's possible due to the short time require for the proposed test.

The importance of the results of the present work, is that the photocatalytic activity calculated using Rz and NBT, was obtained in a wide range of photocatalytic construction materials (cement-based materials and emulsion coatings), with different photocatalytic activities and intrinsic properties (physicochemical and optical properties), even with different crystallite forms (anatase and rutile).

CONCLUSIONS - CONCLUSIONES

Conclusions

This research has made it possible the **development of new methods for evaluating the photocatalytic activity of TiO₂ construction materials based on the detection of the active species formed during the photo-activation process**, which is the global objective postulated for this PhD's work. Specifically, **one method for detecting hydroxyl radicals** have been developed; the Terephthalic Acid (TA) Fluorescence (FL) probe method, and **two methods that detect the available electrons**; the Resazurin (Rz) and NitroBlueTetrazolium (NBT) ink methods.

As part of this general conclusion, the following partial ones have also been derived:

1. The application of the TA-FL probe method and NBT /RZ ink method on photocatalytic construction samples has allowed to obtain a new concept of photocatalytic activity measurements, the "OH• production rate" and "e-reductive yield", which allows the comparison between the samples independently of a specific contaminant.
2. The TA-FL probe method allows quantifying the photocatalytic OH• formed in the bulk solution, while the ink method detects free and shallowly trapped electrons, which are the only one susceptible of participate in the redox reactions.
3. The characterization of the reductive (e-) and oxidative (OH•) production rate of activated photocatalytic materials give fundamental information for better understanding the mechanisms of the processes and therefore further development of highly efficient photocatalyst.
4. TA and NBT were good probes for monitoring the photocatalytic activity of every tested materials. In contrast, Rz was found to be unsuitable for assessing the photocatalytic activity on samples with very alkaline surface, such as cement-based materials, provided there are no evidences of surface carbonation; and on polymeric emulsion coatings.
5. The reduction reaction of NBT under the analysed condition occur via electron participation, and not via O₂^{-•}, like as numerous previous literature indicate.
6. A good relationship between both developed methods with NOx degradation tests was observed when probing the photocatalytic efficiency on construction materials, which is of particular importance to extrapolate directly the photocatalytic results of TA-FL probe method and reductive ink tests to NOx degradation tests, which this are generally considered as the standard reference tests for determination of photocatalytic activity on photocatalytic construction materials.

7. The results demonstrated that the photocatalytic degradation of NO_x photo-oxidation occur mainly via photo-generated h⁺. Thus, the relationship between the active species monitored on proposed methods, e⁻ and OH• with the generated h⁺ makes it possible the positive correlation between methods.
8. The comparison of photocatalytic activity when determined using the developed methods and NO_x standard with RhB discoloration standard not indicates an encouraging correlation using a range of different construction samples was analysed. The possible causes to the divergences between the RhB test (UNI 11259:2008) and the other photocatalytic tests (TA-FL, reductive inks and NO_x air-purification) are related to the more complex underlying mechanism of RhB dye test degradation; among them, the presence of two parallel different degradation pathways, and the interferences that may suffer the estimated discoloration values by the appearance of other N-de-etylated chromophores.
9. These results outline the danger of extrapolating photocatalytic performance results from RhB discoloration tests to other photocatalytic tests, especially when the physic-chemical properties of samples are different. Therefore, from one isolated photocatalytic test on a specific contaminant, no general conclusions of the general expected photocatalytic performance of photocatalytic materials must be derived. These findings should be considered when the standardization methods will be proposed.
10. The potential to “simple-to-use”, the short timescale involved, clear visible change (only for ink tests) and inexpensive measurement give the proposed tests significant advantages over conventional photoactivity tests contaminant based. Beside this, RZ –NBT ink test allows assessing the activity of photocatalytic construction materials using just a portable spectrophotometer or digital camera to record the change in colour, making it ideal for testing these materials “in situ”—a capability which is currently not available using the conventional tests.
11. The use of these methods opens the door to improve significantly the degree of quality control of commercial photocatalyst products, and to speed up research work on the photocatalytic field.

Conclusiones

Esta investigación ha permitido el **desarrollo de nuevos métodos de evaluación de la actividad fotocatalítica de los materiales de construcción con nano partículas de TiO₂ en función de la producción de especies activas durante el proceso de fotoactivación**, que es el objetivo global postulado para este trabajo de doctorado. Específicamente, se ha desarrollado **un método para detectar radical hidroxilo**; El método de la sonda de fluorescencia (FL) del ácido tereftálico (TA), y **dos métodos que detectan los electrones disponibles**; Los métodos de tinta Resazurin (Rz) y a nitroazul de tetrazolio (NBT).

A partir de esta conclusión general, también se han derivado las siguientes conclusiones parciales:

1. La aplicación del método de la sonda TA-FL y el método de la tinta NBT / RZ sobre las muestras de construcción fotocatalíticas ha permitido obtener un nuevo concepto de mediciones de la actividad fotocatalítica, la "tasa de producción de radicales hidroxilos (OH•)" y el "rendimiento de producción de electrones (e-)", lo que permite la comparativa entre las muestras independientemente de un contaminante específico.
2. El método de la sonda TA-FL permite cuantificar el OH• formados en la solución, mientras que el método de la tinta detecta electrones libres y atrapados superficialmente, que son los susceptibles de participar en las reacciones redox.
3. La caracterización de la tasa de producción reductora (e-) y oxidativa (OH•) de los materiales fotocatalíticos activados proporciona información fundamental para una mejor comprensión de los mecanismos involucrados en el proceso fotocatalítico y, por tanto, el desarrollo de fotocatalizadores altamente eficientes.
4. TA y NBT fueron sondas adecuadas para monitorizar la actividad fotocatalítica de todos los materiales ensayados. Por el contrario, se encontró que Rz no era adecuada para evaluar la actividad fotocatalítica en muestras con superficies muy alcalinas, tales como materiales a base de cemento, siempre que no existan evidencias de carbonatación superficial; y tampoco en revestimientos de emulsión poliméricos.
5. La reacción de reducción del NBT bajo las condiciones de análisis ocurre por la reacción con los electrones formados, y no por la participación de los superóxidos (O₂^{•-}) formados en el fotocatalizador, como indica numerosa bibliografía previa.
6. Una buena correlación entre los resultados de ambos métodos desarrollados y las pruebas de degradación de NO_x cuando se determinó la eficiencia fotocatalítica en materiales de construcción fue obtenida, lo cual es de particular importancia

para extrapolar directamente los resultados fotocatalíticos de los métodos TA-FL y pruebas reductoras de tinta, a las pruebas de degradación de NO_x (óxidos de nitrógeno), que generalmente se consideran como las pruebas de referencia para la determinación de la actividad fotocatalítica sobre materiales de construcción fotocatalíticos.

7. Los resultados demostraron que la degradación fotocatalítica de la foto-oxidación de NO_x se produce principalmente a través de h⁺ (hueco) foto-generado. Por lo tanto, la relación entre las especies activas monitoreadas en los métodos propuestos (e⁻ y OH•) con el h⁺ generado hace posible la correlación positiva entre los métodos.
8. La comparación de los resultados de actividad fotocatalítica determinados usando los métodos desarrollados y los métodos estandarizados de NO_x, con el test de decoloración de RhB (rodamina B) no mostro una correlación alentadora usando las diferentes muestras de construcción ensayadas. Las posibles causas de las divergencias entre la prueba RhB (UNI 11259: 2008) y las otras pruebas fotocatalíticas (TA-FL, tintas reductoras y purificación de aire por NO_x) están relacionadas con el mecanismo subyacente más complejo de la degradación del colorante RhB; Entre ellos, la presencia de dos vías de degradación diferentes paralelas y las interferencias que pueden sufrir los valores de decoloración estimados por la aparición de otros cromóforos N-de-etilados.
9. Estos resultados demostraron el peligro de extrapolar los resultados del rendimiento fotocatalítico de las pruebas de decoloración de RhB a otras pruebas fotocatalíticas, especialmente cuando las propiedades físico-químicas de las muestras son diferentes. Por lo tanto, a partir de una prueba fotocatalítica aislada sobre un contaminante específico, no deben derivarse conclusiones generales del rendimiento fotocatalítico esperado de los materiales fotocatalíticos. Estos hallazgos deben considerarse cuando se propongan los métodos de normalización.
10. El potencial de "uso simple", la corta escala de tiempo implicada, el cambio visible (sólo para pruebas de tinta) y la medición económica otorgan a las pruebas propuestas ventajas significativas sobre las pruebas de foto-actividad convencionales basadas en contaminantes. Además de esto, la prueba de tinta RZ-NBT permite evaluar la actividad de los materiales de construcción fotocatalíticos usando sólo un espectrofotómetro portátil o cámara digital para registrar el cambio de color, lo que lo hace ideal para probar estos materiales "in situ" -una capacidad que actualmente no está disponible utilizando las pruebas convencionales.
11. El uso de estos métodos puede abrir una puerta para mejorar significativamente el grado de control de calidad de los fotocatalizadores comerciales y acelerar los trabajos de investigación en el campo fotocatalítico.

***SCIENTIFIC PRODUCTION AND
DISSEMINATION***

The results included in this PhD Thesis work give rise to scientific diffusion on: **4 published articles** and **4 in preparation**, **5 collective publications**, **presentation at congress and courses or seminaries**. Apart from these, resulted in a **1 patent** application.

As a final point, the following is a list of these production and scientific diffusion activities derived from this Doctoral Thesis along with relevant information about them.

Published articles on specialist journal or books

SCI journals

TITLE: Characteristics and efficiency of photocatalytic cementitious materials: Type of binder, roughness and microstructure

AUTHORS: **E. Jimenez-Relinque**, J.R. Rodriguez-Garcia, A. Castillo, M. Castellote

REF. JOURNAL: Cement and Concrete Research 71 (2015) 124–131

DOI: 10.1016/j.cemconres.2015.02.003

TITLE: Quantification of hydroxyl radicals on cementitious materials by fluorescence spectrophotometry as a method to assess the photocatalytic activity

AUTHORS: **E. Jimenez-Relinque**, M. Castellote

REF. JOURNAL: Cement and Concrete Research 74 (2015) 108–115

DOI: 10.1016/j.cemconres.2015.04.011

TITLE: Photocatalytic behavior of colored mortars containing TiO₂ and iron oxide based pigments

AUTHORS: A. Laplaza, **E. Jimenez-Relinque**, J. Campos, M. Castellote

REF. JOURNAL: Construction and building materials 144 (2017) 300-310

DOI: 10.1016/j.conbuildmat.2017.03.146

TITLE: TiO₂ cement-based materials: Understanding optical properties and electronic band structure of complex matrices.

AUTHORS: **E. Jimenez-Relinque**, I. Llorente, M. Castellote.

REF. JOURNAL: Catalysis Today, 287(2017)203–209

DOI: 10.1016/j.cattod.2016.11.015

Collective publications

SPEA7; 7th European Meeting on Solar chemistry&Photocatalysis: Environmental applications. Abstract Book Volume pp101. ISBN 978-989-97667-3-0

TITLE: Assessing The Feability Of Using «Other» Probes To Quantify By Fluorescence Spectroscopy The OH· Formed In Photocatalysis Of TiO₂ Based construction Materials

AUTHORS: **E. Jiménez-Relinque** and M. Castellote.

FOURTH International Conference on Semiconductor Photochemistry (SP4). Abstract Book Volume. pp106. ISBN 978-80-7080-854-2

TITLE: Efficiency of TiO₂ enriched photocatalytic construction materials based on their production of active species

AUTHORS: **E. Jiménez-Relinque** and M. Castellote.

14 th International Congress on the Chemistry of Cement (ICCC 2015). Abstract Book Volume 1[C]. 2015

TITLE: Influence of Chemical Composition of Cementitious Matrix, Surface Roughness and Microstructure on Photocatalytic activity of TiO₂ Mortars

AUTHORS: **E. Jimenez-Relinque**, J.R. Rodriguez-Garcia, A. Castillo and M. Castellote.

Second International Conference on Concrete Sustainability. Abstract Book Volume. pp 229. ISBN 978- 84-945077-8-6

TITLE: Influence of Physicochemical and Microstructural Properties of TiO₂ Cementitious materials on Photocatalytic Pollution Degradation

AUTHORS: **E. Jimenez-Relinque** and M. Castellote.

Advanced Courses 2015 Eduardo Torroja. ISBN: 978-84-7292-395-9. Published by: Institute of Construction Science Eduardo Torroja. CSIC, Serrano Street, 4. 28033. Madrid (Spain). pp 84-96.

TITLE: Seminar 11. Healthy Building for a Better Environment: Air quality and Photocatalysis in Construction. Photocatalysis in Construction. Fundament and Measured Method.

AUTHORS; **Eva Jimenez Relinque**

Communications at congress, seminar or courses

Seminar or courses

Curso de especialización del CSIC “Cursos Avanzados Eduardo Torroja: Evaluación, Intervención y Mantenimiento de Edificios y Estructuras.”, IETcc, 2014.

TITLE: Seminario S6: Construcciones Sanas para un Entorno Mejor: Gestión, Prevención, Diagnóstico y Descontaminación. Taller de fotocatalisis en construcción (2 h)

Curso de “Construcción Sostenible” Organizado por AECID (Embajada Española en Uruguay) y CSIC (MINECO), 2014.

TITLE: Módulo IV: Construcciones sanas para un entorno mejor. Calidad de ambiente interior, descontaminación y utilización de materiales fotocatalíticos (3 h).

Curso de especialización del CSIC “Cursos Avanzados Eduardo Torroja: Durabilidad, Rehabilitación y Sostenibilidad.”, Organizado por el IETcc, 2015.

TITLE: Seminario S11: Calidad del aire interior y fotocatalisis en construcción. La Fotocatalisis en Construcción: Fundamentos y métodos de medida (1 h).

Curso de “Construcción Sostenible” Organizado por AECID (Embajada Española en Guatemala) y CSIC (MINECO), 2015.

TITLE: Módulo III: Construcciones sanas para un entorno mejor. Calidad de ambiente interior, descontaminación y utilización de materiales fotocatalíticos (3 h).

Congress

Photocatalytic and Advanced Oxidation Technologies for Treatment of Water, Air, soil and surfaces.

November 2010; San Diego (California).

PARTICIPATION TYPE: Poster

TITLE: Photocatalytic activity determination by tobacco extracts removal by self-cleaning surfaces: A parametric study

AUTHORS: M. Castellote, N. Bengtsson and **E. Jiménez**

2nd European Symposium on Photocatalysis (JEP 2011).

September 2011; Burdeos (French)

PARTICIPATION TYPE: Poster

TITLE: Degradation of a tobacco extract in self-cleaning surfaces: kinetic based transposition of results in any experimental condition to the wanted reference and prediction in different scenarios.

AUTHORS: N. Bengtsson, **E. Jiménez** and M. Castellote

SPEA7; 7th European Meeting on Solar chemistry&Photocatalysis: Environmental applications.

June 2012; Porto (Portugal)

PARTICIPATION TYPE: Poster

TITLE: Assessing The Feasibility Of Using «Other» Probes To Quantify By Fluorescence Spectroscopy The OH· Formed In Photocatalysis Of TiO₂ Based construction Materials

AUTHORS: **E. Jiménez-Relinque** and M. Castellote

FOURTH International Conference on Semiconductor Photochemistry (SP4).

June 2013; Prague (Czech Republic)

PARTICIPATION TYPE: Poster and oral communication

TITLE: Efficiency of TiO₂ enriched photocatalytic construction materials based on their production of active species

AUTHORS: **E. Jiménez-Relinque** and M. Castellote

3rd European Symposium on Photocatalysis (JEP 2013).

September 2013; Portoroz (Slovenia)

PARTICIPATION TYPE: Poster

TITLE: Photocatalytic mineralization of VOCs as a function of the conditions of the air in air conditioning installations.

AUTHORS: **Eva Jiménez-Relinque** y Marta Castellote

3rd European conference on environmental applications of advanced oxidation processes

October 2013; Almeria (Spain)

PARTICIPATION TYPE: Poster

TITLE: Turning Waste Into Valuable Resources: Potential of Electric Arc Furnace Dust As Photocatalytic Material.

AUTHORS: María Sapiña, **Eva Jiménez-Relinque** and Marta Castellote

8th European meeting on solar chemistry and photocatalysis: Environmental Applications.

June 2014; Thessaloniki (Greece)

PARTICIPATION TYPE: Oral

TITLE: Cleaning the Air we Breathe: Degradation of Allergens of Pollen by Heterogeneous Photocatalysis

AUTHORS: **Eva Jimenez-Relinque**, Maria Sapiña, Roman Nevshupa, Elisa Román and Marta Castellote

XXXV Meeting of electrochemistry of the Spanish royal society of chemistry and 1st E3 mediterranean symposium: electrochemistry for environment and energy.

July 2015; Burgos (Spain)

PARTICIPATION TYPE: Oral

TITLE: Detection and quantification of reactive oxygen species (ROS) on photocatalytic construction materials

AUTHORS: **Eva Jimenez-Relinque**

V Encuentro-edificación sobre rehabilitación de edificios (RIR)

March 2015; Madrid (España)

PARTICIPATION TYPE: Oral

TITLE DEL TRABAJO: Fotocatálisis en construcción: tecnología eco-sostenible y rehabilitación eficiente

AUTHORS: **E. Jimenez-Relinque**

The third International Conference on Photocatalytic and Advances Oxidation Technologies for treatment of Water, Air, Soil, and Surfaces (PAOT-3)

September 2015; GDSANK (Polonia)

PARTICIPATION TYPE: Oral

TITLE: photocatalytic materials put in place: In situ Laboratory Comparison and durability of the efficiency

AUTHORS: Maria Sapiña, **E. Jimenez-Relinque** and M. Castellote

International Congress on the Chemistry of Cement (ICCC 2015)

October 2015; BEIJING (China)

PARTICIPATION TYPE: Oral

TITLE: Influence of Chemical Composition of Cementitious Matrix, Surface Roughness and Microstructure on Photocatalytic activity of TiO₂ Mortars

AUTHORS: **E. Jimenez-Relinque**, J.R. Rodriguez-Garcia, A. Castillo and M. Castellote

The 20th International Conference on Semiconductor Photocatalysis & Solar Energy Conversion (SPASEC-20)

November 2015; San Diego (California)

PARTICIPATION TYPE: Oral

TITLE: Photocatalytic Construction Materials' Potential to Diminish Gramineae Allergens Airborne

AUTHORS: M. Sapiña, **E. Jiménez-Relinque**, R. Nevshupa, E. Roman y M. Castellote.

The 20th International Conference on Semiconductor Photocatalysis & Solar Energy Conversion (SPASEC-20)

November 2015; San Diego (California)

PARTICIPATION TYPE: Oral

TITLE: Photocatalytic Performance on TiO₂ Cement-Based Materials in Function of Hydroxyl Radicals Production

AUTHORS: **E. Jimenez-Relinque** y M. Castellote

French Conference on Catalysis (FCCAT)

May 2016; Frejus (Francia)

PARTICIPATION TYPE: Poster

TITLE: Quantitative characterization of electrons produced by various photocatalysts

AUTHORS: **E. Jimenez-Relinque** y M. Castellote

French Conference on Catalysis (FCCAT)

May 2016; Frejus (Francia)

PARTICIPATION TYPE: Poster

TITLE: Pollen allergens removal by photocatalysis

AUTHORS: Maria Sapiña, **E. Jimenez**, R. Nevshupa , E.Roman, M.Castellote

Second International Conference on Concrete Sustainability

June 2016; Madrid (Spain)

PARTICIPATION TYPE: Oral

TITLE: Influence of Physicochemical and Microstructural Properties of TiO₂ Cementitious materials on Photocatalytic Pollution Degradation

AUTHORS: **E. Jimenez-Relinque** y M. Castellote

9th European Meeting on Solar Chemistry and Photocatalysis: Environmental Applications(SPEA9)

June 2016; Strasburg (France)

Participation type: Poster

Title: TiO₂ Cement-based Materials: Understanding Optical Properties of Complex Matrixes for Optimal Photocatalytic Performance

AUTHORS: **E. Jimenez-Relinque**, I. Llorente y M. Castellote

Patents

DISPOSITIVO PORTATIL DE MEDIDA DE ACTIVIDAD FOTOCATALITICA Y PROCEDIMIENTO DE MEDIDA DE ACTIVIDAD FOTOCATALITICA



Justificante de presentación electrónica de solicitud de patente

Este documento es un justificante de que se ha recibido una solicitud española de patente por vía electrónica, utilizando la conexión segura de la O.E.P.M. Asimismo, se le ha asignado de forma automática un número de solicitud y una fecha de recepción, conforme al artículo 14.3 del Reglamento para la ejecución de la Ley 11/1986, de 20 de marzo, de Patentes. La fecha de presentación de la solicitud de acuerdo con el art. 22 de la Ley de Patentes, le será comunicada posteriormente.

Número de solicitud:	P201631716	
Fecha de recepción:	30 diciembre 2016, 09:48 (CET)	
Oficina receptora:	OEPM Madrid	
Su referencia:	ES1641.1273	
Solicitante:	CONSEJO SUPERIOR DE INVESTIGACIONES CIENTIFICAS	
Número de solicitantes:	1	
País:	ES	
Título:	DISPOSITIVO PORTATIL DE MEDIDA DE ACTIVIDAD FOTOCATALITICA Y PROCEDIMIENTO DE MEDIDA DE ACTIVIDAD FOTOCATALITICA	
Documentos enviados:	Descripción-1.pdf (7 p.) Reivindicaciones-1.pdf (3 p.) Resumen-1.pdf (1 p.) Dibujos-1.pdf (3 p.) OLF-ARCHIVE.zip FEERCPT-1.pdf (1 p.)	package-data.xml es-request.xml application-body.xml es-fee-sheet.xml feesheet.pdf request.pdf
Enviados por:	C=ES,O=PONS PATENTES Y MARCAS INTERNACIONAL SL,2.5.4.97=#0C0F56415445532D423834393231373039,CN=50534279 J ANGEL PONS (R: B84921709),SN=PONS ARIÑO,givenName=ANGEL,serialNumber=IDCES-50534279J,description=Ref.AEAT/AEAT0297/PUESTO 1/40639/05102016093524	
Fecha y hora de recepción:	30 diciembre 2016, 09:48 (CET)	
Codificación del envío:	56:22:F2:D1:E9:D4:3E:A6:2B:63:4A:7B:F0:84:FE:E2:82:73:FA:41	

AVISO IMPORTANTE

Las tasas pagaderas al solicitar y durante la tramitación de una patente o un modelo de utilidad son las que se recogen en el Apartado "Tasas y precios públicos" de la página web de la OEPM (http://www.oepm.es/es/propiedad_industrial/tasas/). Consecuentemente, si recibe una comunicación informándole de la necesidad de hacer un pago por la inscripción de su patente o su modelo de utilidad en un "registro central" o en un "registro de internet" posiblemente se trate de un fraude. La anotación en este tipo de autodenominados "registros" no despliega ningún tipo de eficacia jurídica ni tiene carácter oficial.

En estos casos le aconsejamos que se ponga en contacto con la Oficina Española de Patentes y Marcas en el correo electrónico informacion@oepm.es.

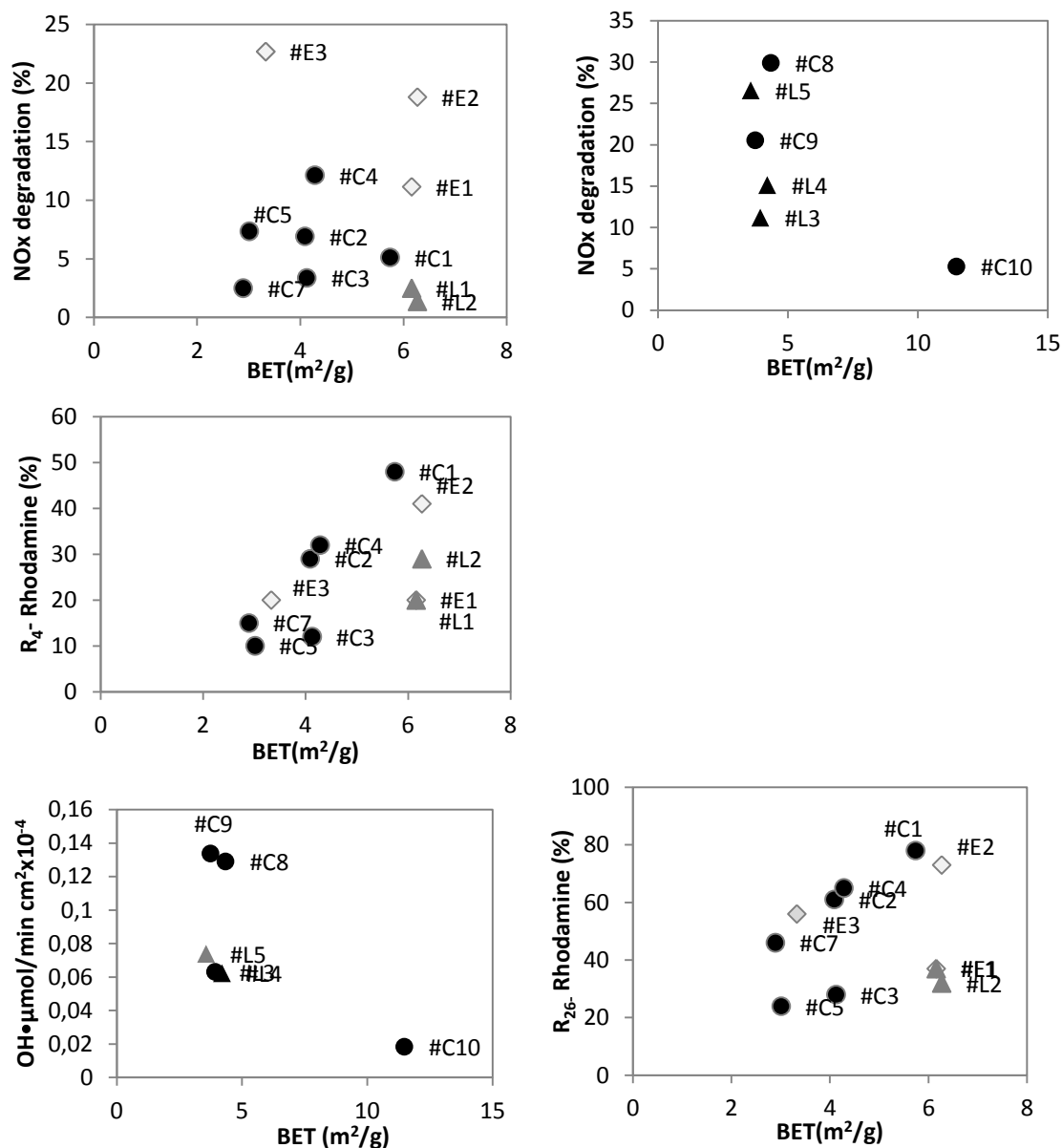
ADVERTENCIA: POR DISPOSICIÓN LEGAL LOS DATOS CONTENIDOS EN ESTA SOLICITUD PODRÁN SER PUBLICADOS EN EL BOLETÍN OFICIAL DE LA PROPIEDAD INDUSTRIAL E INSCRITOS EN EL REGISTRO DE PATENTES DE LA OEPM, SIENDO AMBAS BASES DE DATOS DE CARÁCTER PÚBLICO Y ACCESIBLES VÍA REDES MUNDIALES DE INFORMÁTICA. Para cualquier aclaración puede contactar con la O.E.P.M.

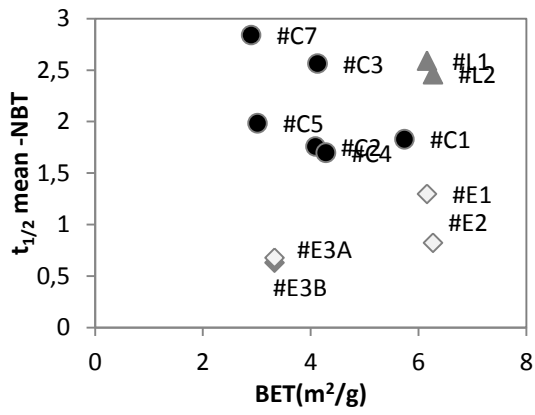
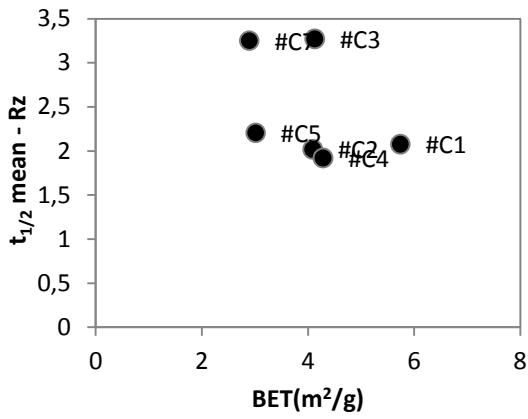
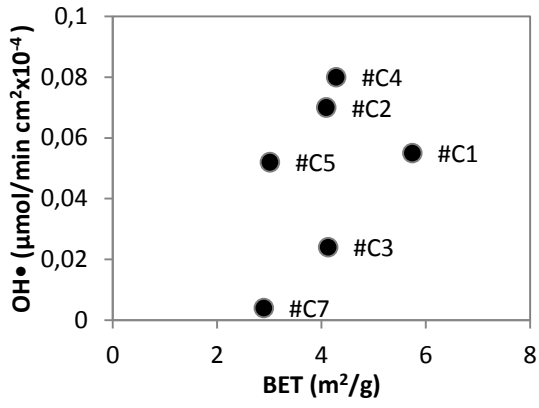
/Madrid, Oficina Receptora/

APPENDIX

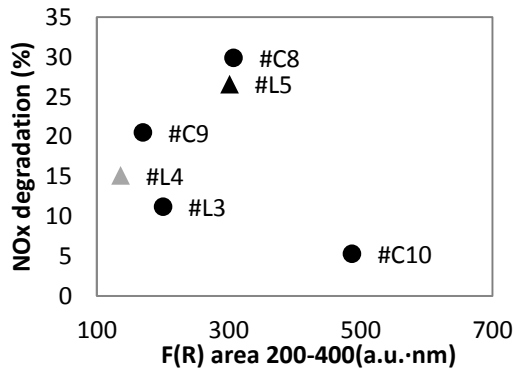
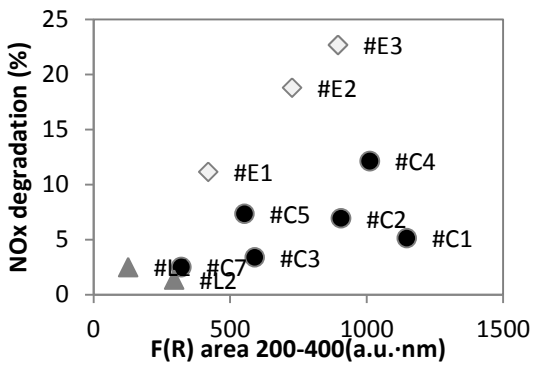
Appendix A Effect of physicochemical and optical properties of the materials on photocatalytic performance parameters

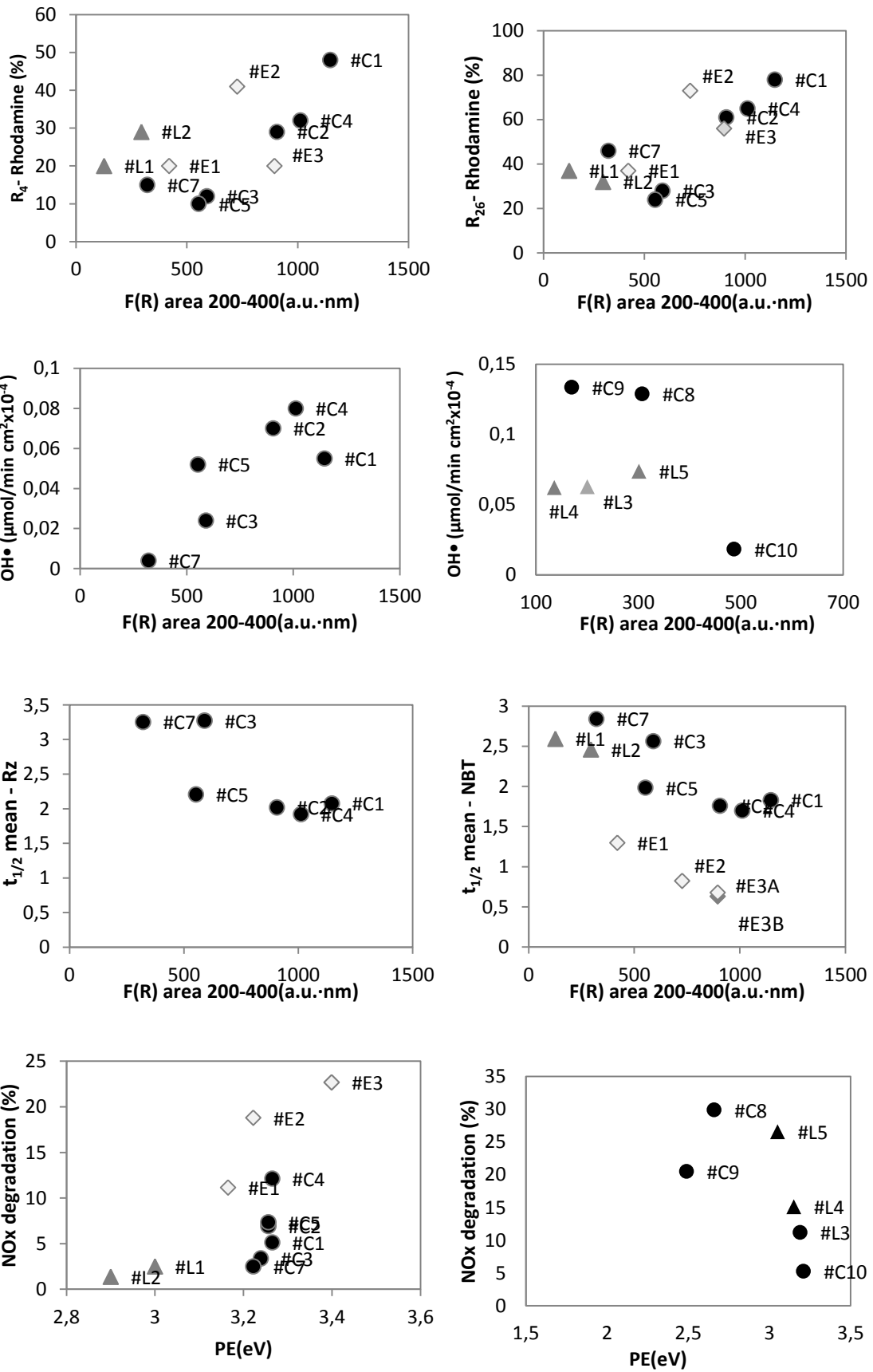
A.1 Physical parameters

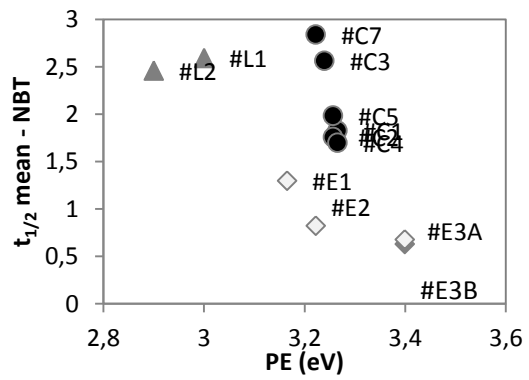
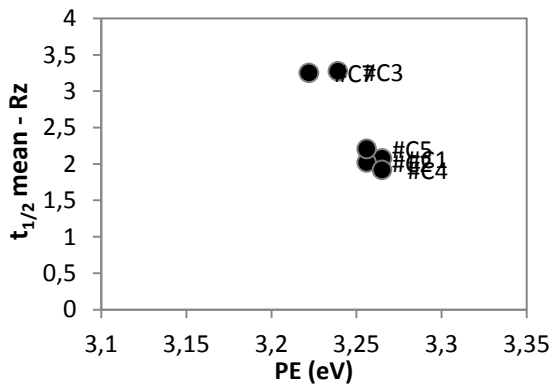
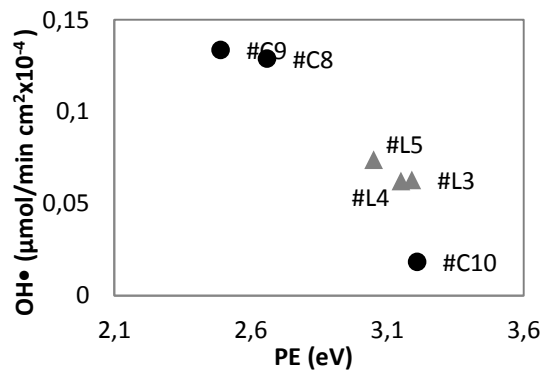
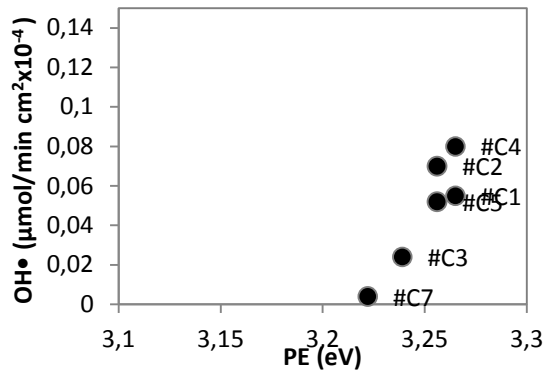
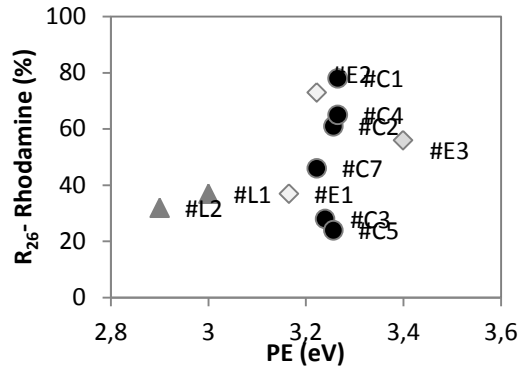
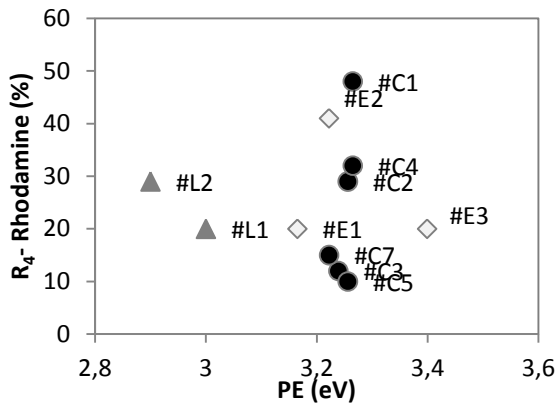




A.2 Optical properties







Appendix B Effect of iron oxide based pigment on photocatalytic performance parameters

From the series of lab-made photocatalytic coloured mortar (samples type (d) on *Chapter 4*) is possible to evaluate the effect of iron-based pigment addition on the photocatalytic performance parameters (RhB discoloration, NO_x degradation and OH• production rate). More detail about this study in [216].

B.1 Iron oxide based pigment characterization-XRF and XRD

In the case of lab-coloured mortars samples, apart from the analysis of the entire hardened samples (included in *Chapter 4*), the original iron oxide based pigments used were also characterized by XRD and FRX. From XRD pigments patterns (Figure B.1), it can be said that the composition of red pigment is mostly hematite (Fe₂O₃), goethite (FeOOH) mainly composes the yellow pigment, and magnetite (Fe₃O₄) is used as black pigment. Brown pigment, is a mixture of red and yellow pigment (hematite and goethite), and also includes calcite (CaCO₃) in their composition.

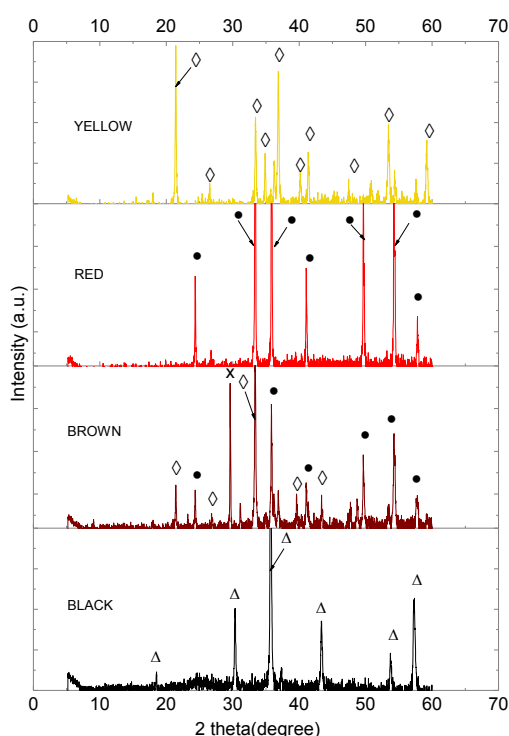


Figure B.1 XRD of iron oxide based pigments used as addition on lab-made coloured mortars. (\diamond = Goethite, \bullet = Hematite, x = Calcite and Δ = Magnetite).

XRF elemental composition (Figure B.2) analysis has revealed that the highest amount of Fe corresponds to the red pigment (96.47%) followed by the yellow one (86.35 %), then the brown one (65.66 %), quite close to the black one (60.95 %). Consequently, the loss on ignition of the pigments, that refers mainly to the amount of calcite in their composition, shows important differences, being the smaller one the corresponding to the red pigment (0.5 %) and the higher one that of the black pigment (33%). Additionally, it must be remarked the 1% of equivalent TiO_2 of the black pigment.

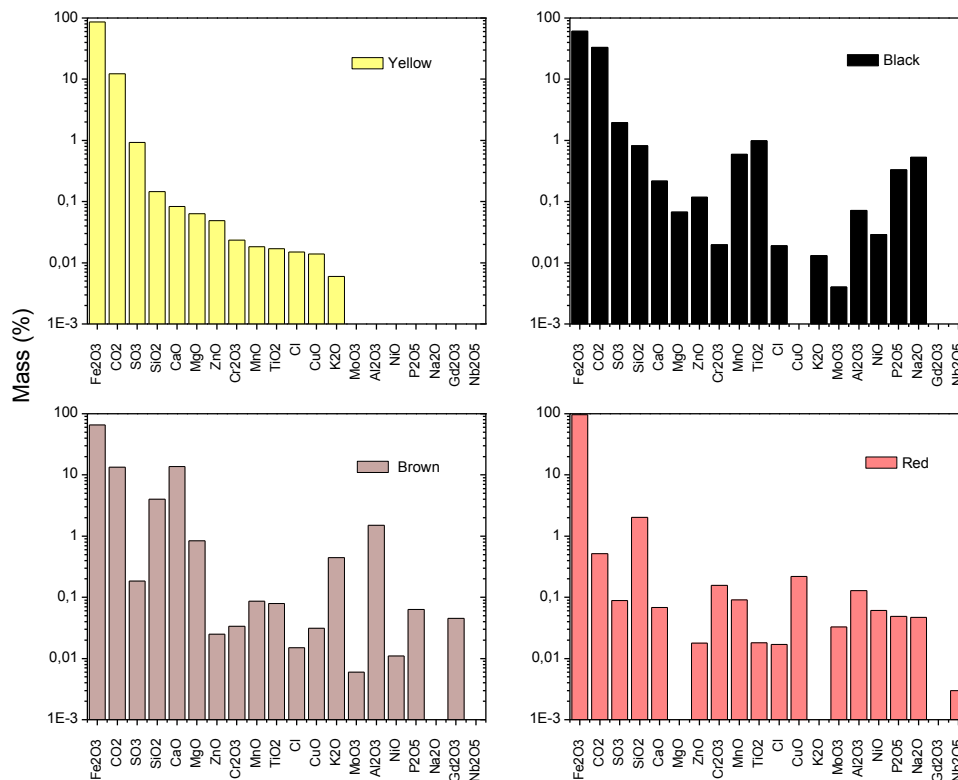


Figure B.2 Elemental composition of the pigments, referred to the corresponding oxide.

B.2 Effect of iron oxide based on photocatalytic parameters

Considering the previous results about the reduced reliability of RhB UNI 11259:2009 experimental procedure for photocatalytic performance comparison between differently colored mortars, in comparison with NO_x and OH^\bullet degradation previous test, whose results are independent on the color of the substrate, the following evaluation of the effect of iron-based pigment addition on TiO_2 mortar will be based on the results of these last test.

Previous studies postulated different theories about the effect of iron-based pigments addition on photocatalytic activity of photocatalytic coloured mortars (PHCMs). One kind of explanation assumed that the pigments could physically occupy the active sites on the surface of TiO_2 particles, which consequently would modify the TiO_2 particles activation [43, 217], and even may block the pores in the concrete surface layers, this shielding affecting the diffusion of gas pollutants into the active sites [217]. This physical factor, might incurred in a reduction of the photocatalytic activity. In contrast, some other authors claimed that the presence of iron-based oxides may improve the TiO_2 performance under visible light irradiation by shifting the absorption spectra to a lower energy region [218-220]. In addition, several experimental works have probed an enhanced of photocatalytic activity by limiting the recombination of the photogenerated electron-hole pairs at the interface of iron oxide–semiconductor for cases such $\text{TiO}_2/\text{FeOOH}$ [221], $\text{Fe}_3\text{O}_4/\text{SiO}_2/\text{TiO}_2$ [218] and $\text{Fe}_2\text{O}_3/\text{TiO}_2$ nanocomposites [220, 222].

To understand the behaviour of PHCMs, is necessary to address the metal oxide (pigment)-substrate (TiO_2 based mortar) heterojunctions under visible and UV irradiation light. Generally, when metal oxide nanoparticles were coupled to the surface of photocatalyst, both compounds can lead to metal oxide-semiconductor heterojunction. This composite structure can absorb light energy separately; the total photon energy absorbed can be enhanced effectively. Furthermore, with suitable electronic band structure, the photo-generated e^- and h^+ can be separated effectively due to photo-induced electrons tend to transfer to the higher energy CB to the lower energy CB of the other material or *viceversa*, thus promoting the charge separation and improving the photocatalytic performance.

Evident modifications of the absorption energies characteristics of mortar samples with the introduction of pigment were observed, which could lead to a shift of the absorption-edge towards lower energy values with respect to photocatalytic mortar formulation without pigments (See *Chapter 4*, Table 4.4). In order to easily see this effect, the shifts of the PE with respect to the photocatalytic mortar without pigment addition (#L6) were presented in the Figure B.3. However, it was noticeable that a lower photo-absorption apparent band edge (PE_{APP}) did not lead to a higher NO_x photocatalytic degradation (see Figure B.4). The $\text{OH}\cdot$ production rate obtained lead to the same behavior due to direct correlation between the NO_x and $\text{OH}\cdot$ results (see *Chapter 4*, Figure 4.51c).

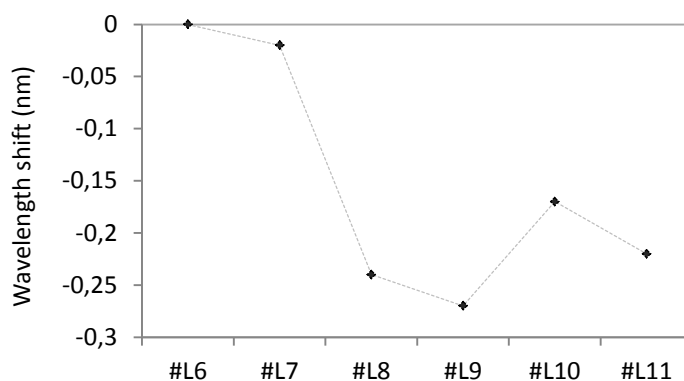


Figure B.3 Wavelength shift (nm) of PE calculated of PHCMs with respect to the reference photocatalytic mortar without pigment addition (#L6). #L7 red pigment, #L8 yellow pigment, #L9 brown pigment, #L10 grey pigment (0.015/0.1), #L11 grey pigment (0.03/0.1). Parenthesis numeric values indicated pigment proportion (% weight of dry mortar/% weight of cement). More detail about the composition of samples in *Chapter 3, Table 3.2*.

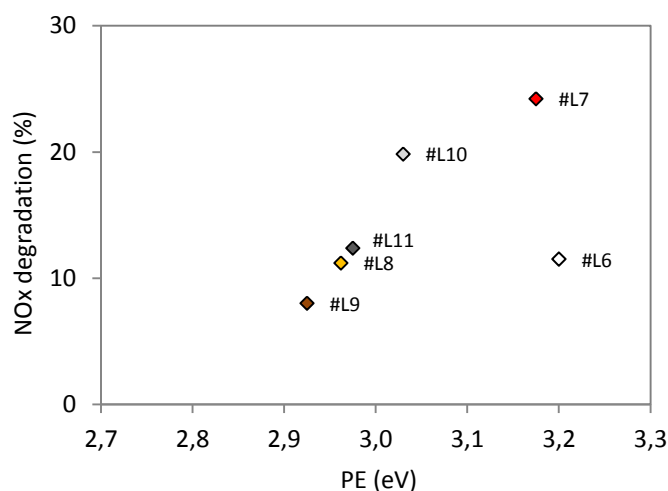


Figure B.4 NOx degradation of photocatalytic samples in function of the absorption band edge energy (eV). Photocatalytic samples (#L6 without pigment, #L7 red pigment, #L8 yellow pigment, #L9 brown pigment, #L10 grey pigment (0.015/0.1), #L11 grey pigment (0.03/0.1)). Parenthesis numeric values indicated pigment proportion (% weight of dry mortar/% weight of cement). More detail about the composition of samples in *Chapter 3, Table 3.2*.

Therefore, the photocatalytic activity performance of these mortars could be depending on the behavior of the coupling structure iron oxide–semiconductor of PHCMs. As previous explained the metal oxide-semiconductor heterojunction, iron oxide pigment-TiO₂ mortar in our case, could lead to promoting the charge separation, resulting in a decreasing of e⁻-h⁺ recombination rate, and therefore improving the photocatalytic performance.

During photocatalytic processes, when a semiconductor absorbs a photon with equal or higher energy than its band gap energy, it results in the formation of h^+ in the VB (valence band) and an e^- in the CB (conduction band), according to reaction (1). It was commonly accepted that h^+ was quickly converted to OH^\bullet upon oxidation of chemisorbed water or OH^- on the catalyst surface, according to reaction (2). The yield of OH^\bullet depended on the competition between oxidation of water adsorbed on the surface (reaction (2)) and e^-h^+ recombination according to reaction (3). Therefore, it can be assumed that the greater the formation rate of OH^\bullet the higher separation efficiency of e^-h^+ pairs. Furthermore, previous works demonstrated that there is an equilibrium between free OH^\bullet produced by irradiation in TiO_2 suspension and surface trapped h^+ (reaction 4) [64, 161].



Therefore, providing the type and concentration of the photocatalyst is the same in the different PHCMs, the previous measurement of the OH^\bullet formation rate calculated using the proposed method TA-FL can be a useful measure to evaluate the effect of pigment addition as limiting or enhancing the e^-h^+ pairs recombination.

Accordingly to the previous result using the TA-FL probe method (see Figure 4.38), it could be said that only #L7-red pigment (0.387, 24.22) and #L10-Grey pigment (0.174, 19.84) mix formulations resulted in an improved charge separation in comparison with the samples without pigment, #L6 (0.161, 11.51), which leads to a higher OH^\bullet production rate, and beneficial effect on NOx degradation (%). The above parenthesis values indicated the mean values of OH^\bullet production rate ($\mu\text{mol}/\text{min}\cdot\text{cm}^2 \times 10^{-4}$) and NOx degradation (%) respectively. The other colored samples did not show this efficiency improvement.

Taking into account that the ability of promoting the charge separation into the coupling structure iron oxide–semiconductor, and thereby the reduction of e^-h^+ recombination, depend on the bands energy positions of coupling structure iron oxide–semiconductor, the approximated position of the VB and CB can be seen in Figure B.5. The energy position of all VB and CB have been calculated through equations (Eq. 5 and 6) [223].

$$CB (V \text{ vs. NHE}) = 1.23 - PE (eV)/2 \quad (5)$$

$$VB (V \text{ vs. NHE}) = 1.23 + PE (eV)/2 \quad (6)$$

These equations have been applied to the experimental apparent photo-absorption band edges (PE_{APP}) obtained in DRS measurements (see Table 4.4). At the typical pH levels of mortar samples (pH 12-14), the hole in the VB of all the samples can oxidize the H_2O/OH^- leading to OH^\bullet ($H_2O/OH^- /OH^\bullet = 2-1.85$ vs NHE at pH 12-14). However only #L6 (without pigment) and #L7 (red pigment) can reduce the O_2 leading to $O_2^{\bullet-}$ ($O_2/O_2^{\bullet-} = -0.33$ eV vs NHE, at pH 12-14).

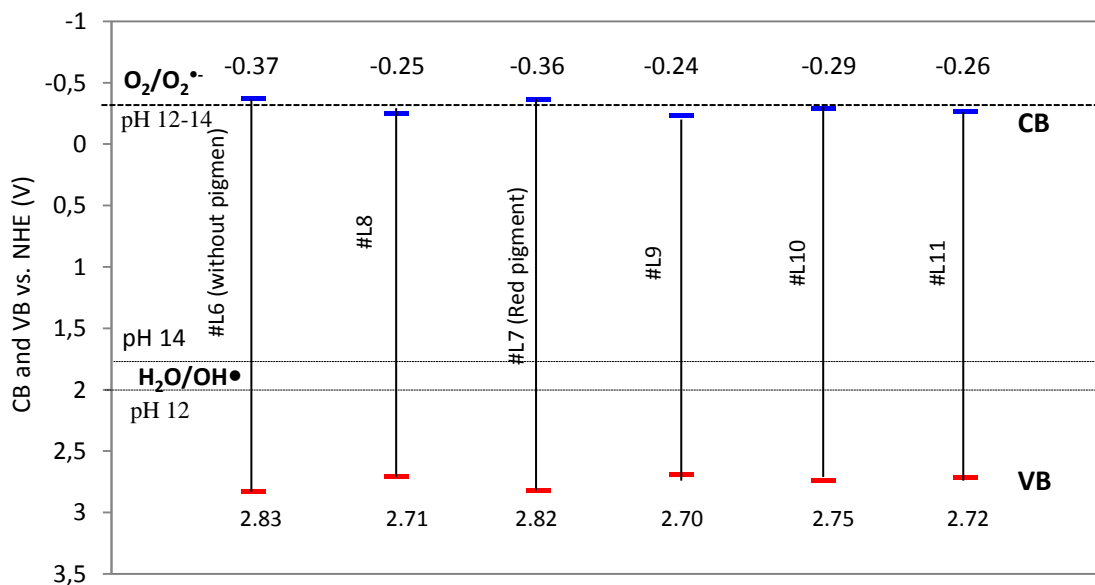


Figure B.5 Approximated band-edge position of valence bands (VB) and conduction bands (CB) for the different mortars and equilibrium lines corresponding to OH/OH^\bullet and $O_2/O_2^{\bullet-}$ at pH 12-14. Photocatalyst samples (#L6 without pigment, #L7 red pigment, #L8 yellow pigment, #L9 brown pigment, #L10 grey pigment (0.015/0.1), #L11 grey pigment (0.03/0.1)). Parenthesis numeric values indicated pigment proportion (% weight of dry mortar/% weight of cement). More detail about the composition of samples in Chapter 3, Table 3.2.

Based on the calculated CB positions of the different mixes, it can be said that the observed photocatalytic production rate of $\text{OH}\cdot$ of the coloured samples was found to decrease linearly with the CB energy position (Figure B.6), which verifies the significance of the energy band position in the heterostructure iron-based pigment– TiO_2 -mortar. This relationship might be attributed to an easier electron-hole recombination process due to unfavorable energetic bands positions of the heterostructure for the electron transfer from the iron based pigment to TiO_2 semiconductor.

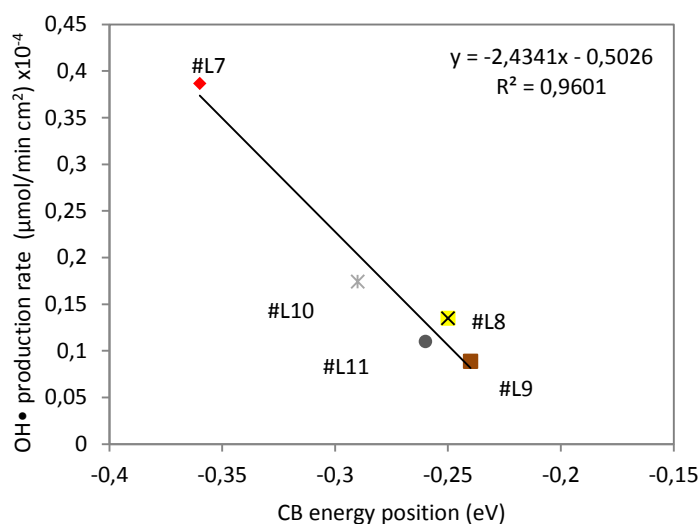


Figure B.6 Production rate of $\text{OH}\cdot$ for PHCMs in function of the CB energy position.

Specifically, in the case of hematite, that are the main component of the used red pigment, includes high-energy acceptor states [219, 220, 222, 224] in the CB. Thus, under visible light irradiation e^- can promote from the VB of Fe_2O_3 into its CB, including their high-energy region. Therefore, this same behavior may also apply to analyze the influence of red pigment addition of PHCMs, which is mainly composed of Fe_2O_3 , on the photocatalytic parameter obtained under irradiation with the UV-Vis lamp (Philips actinic BL, see the spectra on *Chapter 3, Figure 3.15*). Despite that a large fraction of photoelectrons at low-energy levels could rapidly recombine, the photo-generated e^- promoted at higher energy levels to the CB of Fe_2O_3 pigment, can be subsequently transferred to the TiO_2 -based mortar CB, resulting in an improved charge separation. In this way, h^+ generated in the Fe_2O_3 pigment VB can oxidize adsorbed contaminants, as well as generate reactive $\text{OH}\cdot$ that can further contribute to the decomposition of contaminants. In addition, adsorbed oxygen can be reduced by photo-generated electrons leading to $\text{O}_2\cdot^-$ ($\text{O}_2/\text{O}_2\cdot^- = -0.33\text{eV}$ vs NHE, see Figure B.5), which can further promote the photocatalytic degradation of adsorbed compound. In a different way, UV light can induce e^-h^+ pair formation in TiO_2 -based mortar. In this case, the transfer of photo-generated e^- occurs from TiO_2 -based mortar CB to Fe_2O_3 pigment CB. Under the condition used in this study, which comprises both UV and visible radiation, the two processes can synergistically occur. The effectively charge separation and transfer on

interface TiO_2 -based mortar and Fe_2O_3 red pigment under UV-Vis that might be responsible for the observed higher NO_x photocatalytic activity and $\text{OH}\cdot$ production rate in comparison with the others PHCMs and the reference sample without pigment (#L6). Moreover, the main effect on photocatalytic activity is believed to be the transfer of photo-generated e^- from iron oxide pigment CB to TiO_2 -based mortar CB. This would justify that RhB test performed only under UV light show degradation rate much lower than expected, even than mortar samples without pigment (#L6), in comparison with $\text{OH}\cdot$ production rate and NO_x degradation rate under UV-Vis light. In addition to this, as previously mentioned, in the case of red samples, an underestimation of the degradation of RhB due to the emergence of the original color of substrate may occur.

A schematic mechanism for the e^- transfer mechanism of #L7-red pigment sample is proposed in Figure B.7.

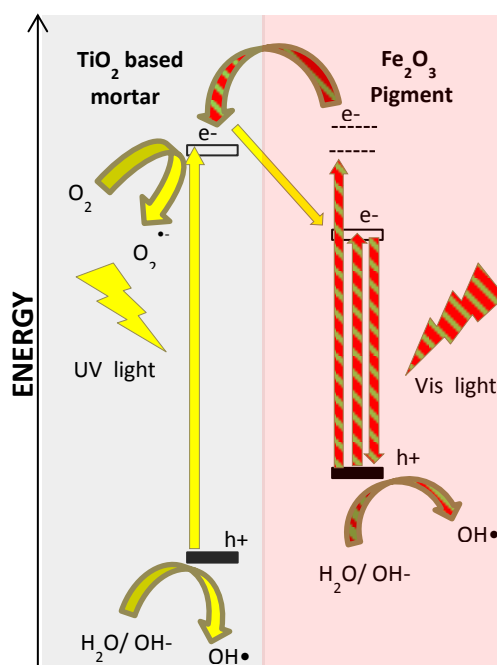


Figure B.7 Schematic of the proposed process for transfer and spatial separation of UV-visible excited electrons in #L7 (red pigment samples).

Other important parameter that regulates the electron transfer ability is the content of iron with respect to TiO_2 particles, as demonstrated by the different efficiency of grey samples (#L10 and #L11), which present different black pigment proportions. #L10 grey pigment (0.015/0.1) and #L11 grey pigment (0.03/0.1). Parenthesis numeric values indicated pigment proportion (% weight of dry mortar/% weight of cement). Previous experimental works [225, 226] reported that there was an optimum doping content in TiO_2 particles for the most efficient separation of photo-induced electron-hole pairs; as the Fe/TiO_2 ratio

increased, the $\text{OH}\cdot$ formation rate first increased and then drastically decreased. So, an optimum loading of pigments must exist. Figure B8 shows the results of production rate of $\text{OH}\cdot$ in function of Fe/Ti content (data obtained from the X-ray fluorescence analysis of the mortar samples) finding a clear potential relationship. In this case, only ratios $\text{Fe}/\text{TiO}_2 < 0.35$ (#L10 and #L7) led to enhanced photocatalytic activity with respect the samples with only TiO_2 (#L6).

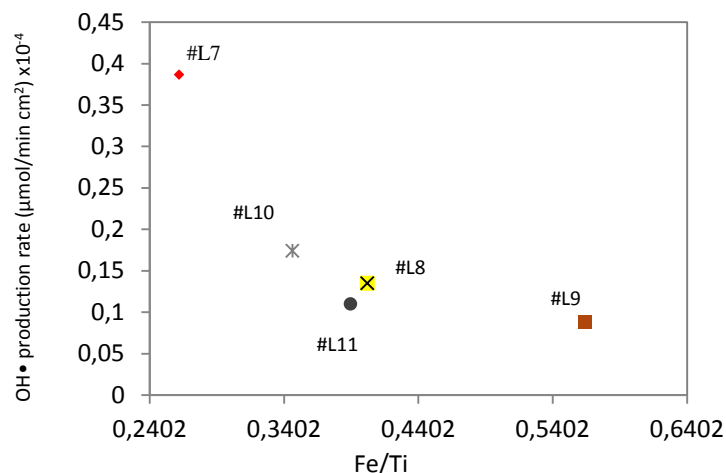
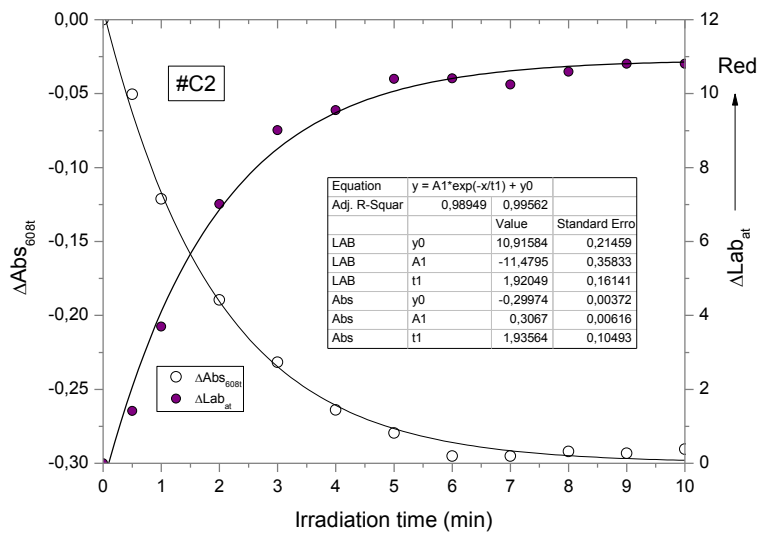
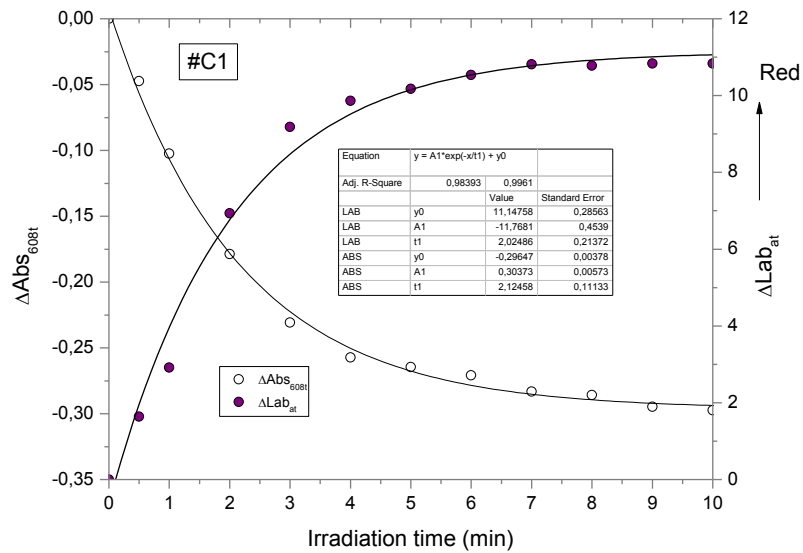


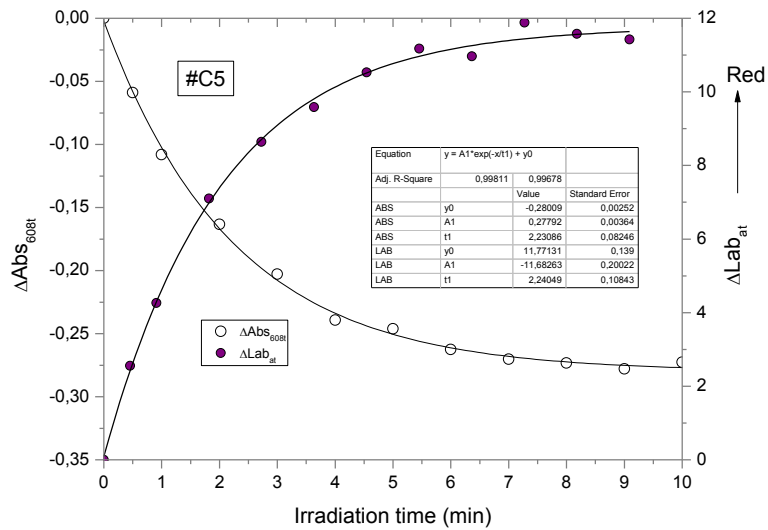
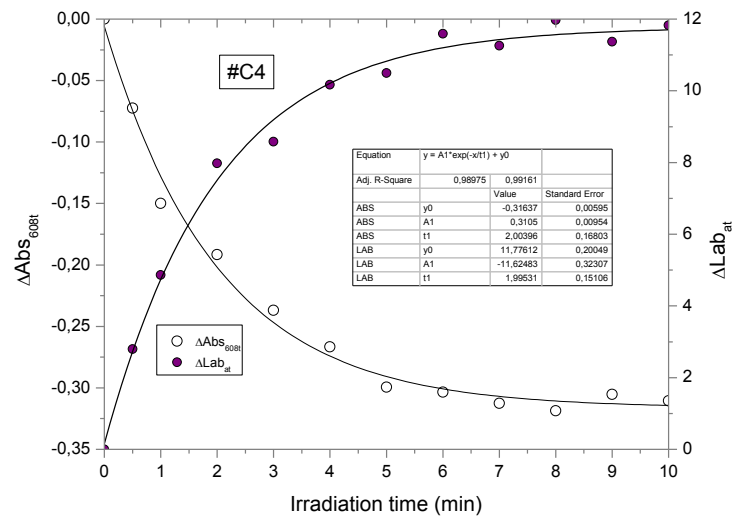
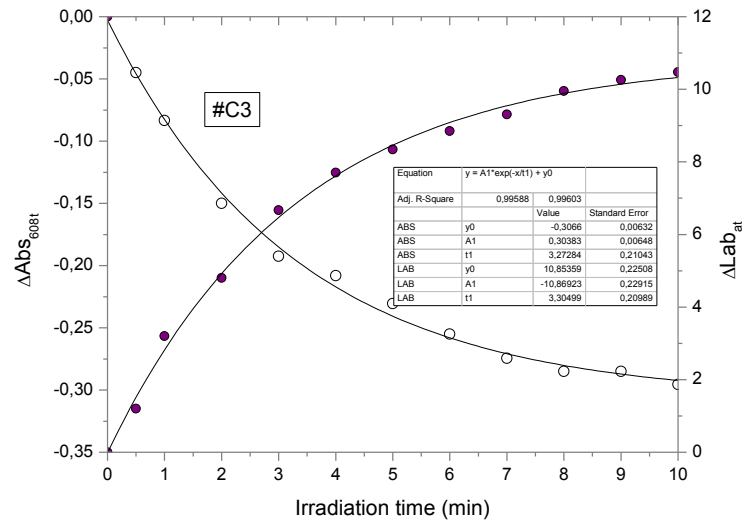
Figure B.8 Production rate of $\text{OH}\cdot$ for PHCMs in function of Fe/Ti. Photocatalysts samples (#L6 without pigment, #L7 red pigment, #L8 yellow pigment, #L9 brown pigment, #L10 grey pigment (0.015/0.1), #L11 grey pigment (0.03/01). Parenthesis numeric values indicated pigment proportion (% weight of dry mortar/% weight of cement). More detail about the composition of samples in *Chapter 3, Table 3.2*.

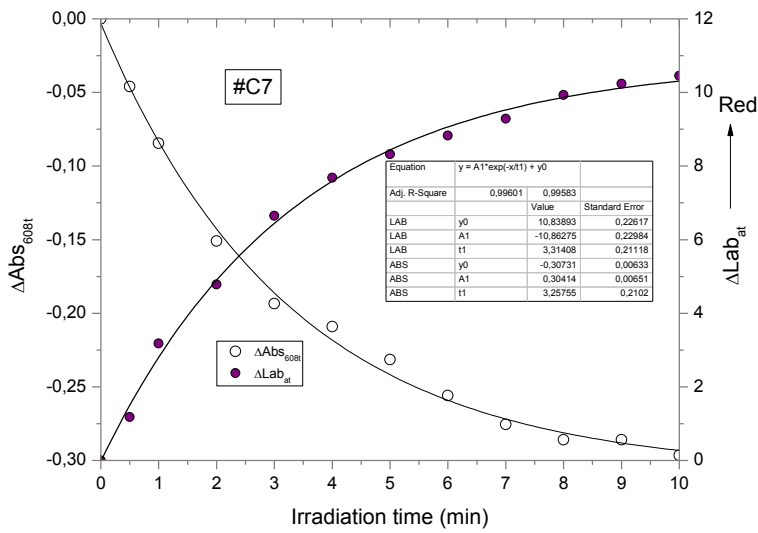
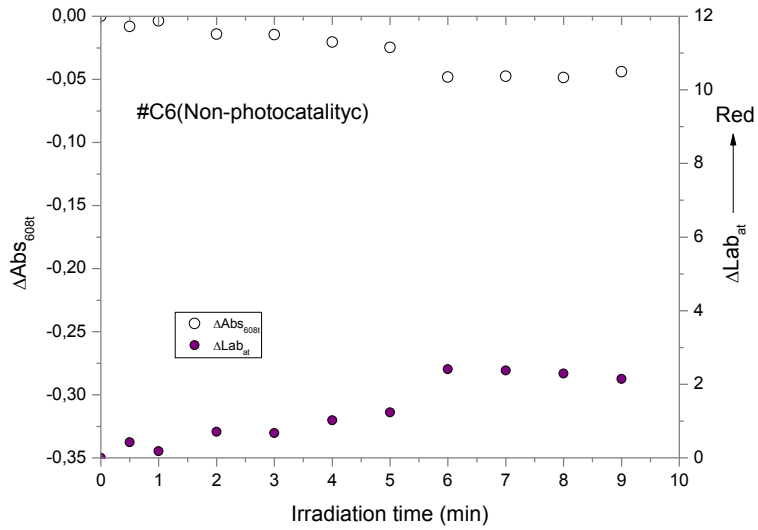
Therefore, from the series of lab-made photocatalytic coloured mortar (PHCMs) analysis in this work, it can be considered that the photoreactivity of photocatalytic colored mortar under UV-Vis light appears to be a complex function of the band-edge structure and thus of e^-h^+ recombination rate. The possibility of e^- transfer between the CB of iron oxide-based pigments and TiO_2 -mortars and *viceversa* seems to be a key parameter to enhance the efficiency of coloured mortars. The ratio Fe/Ti in the final formulation has also demonstrated to be an important parameter regarding the electron transfer ability with respect to the e^-h^+ recombination rate.

Appendix C Collection and adjustment of data over irradiation time for RZ and NBT inks on the all materials tested

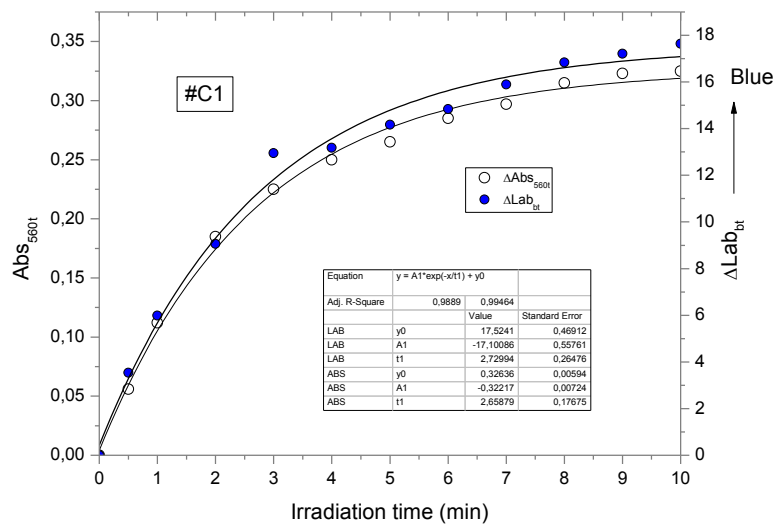
C.1 RZ ink – Absorbance and CIELAB colour

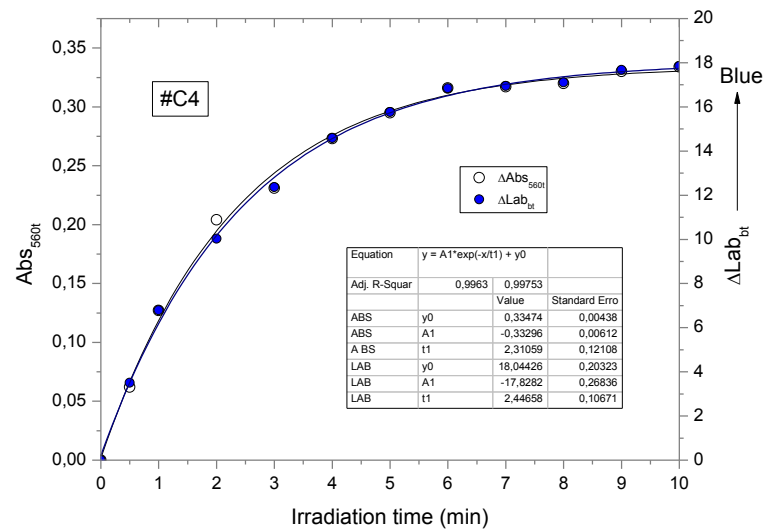
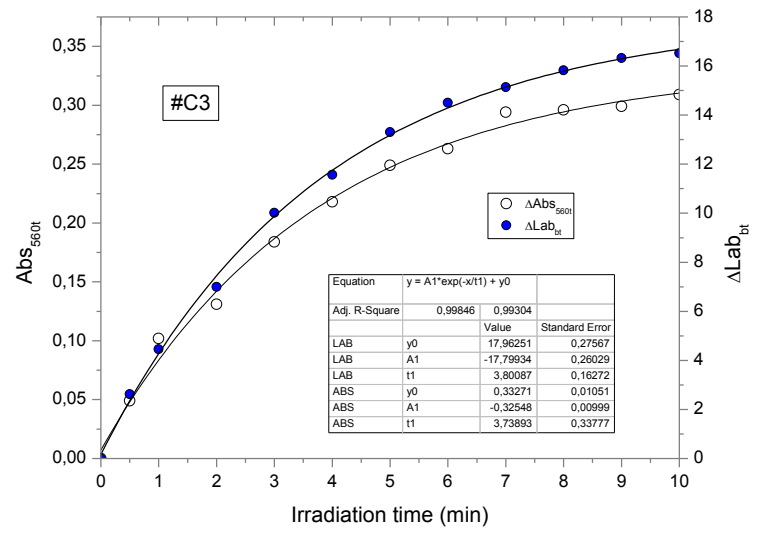
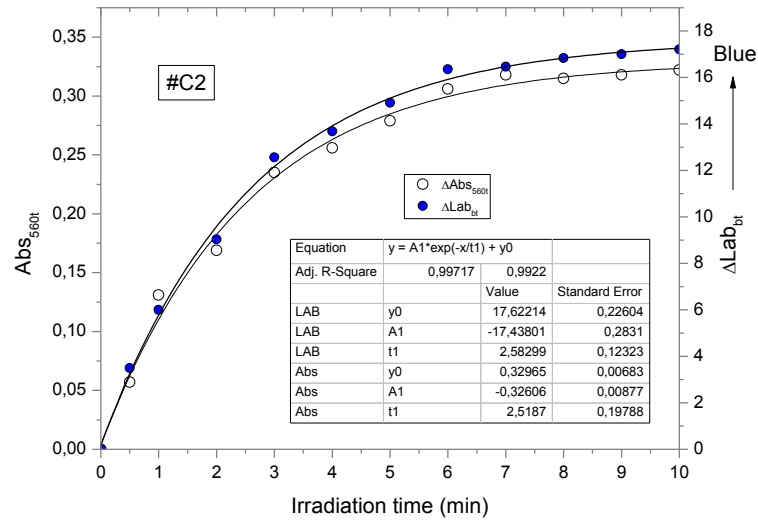


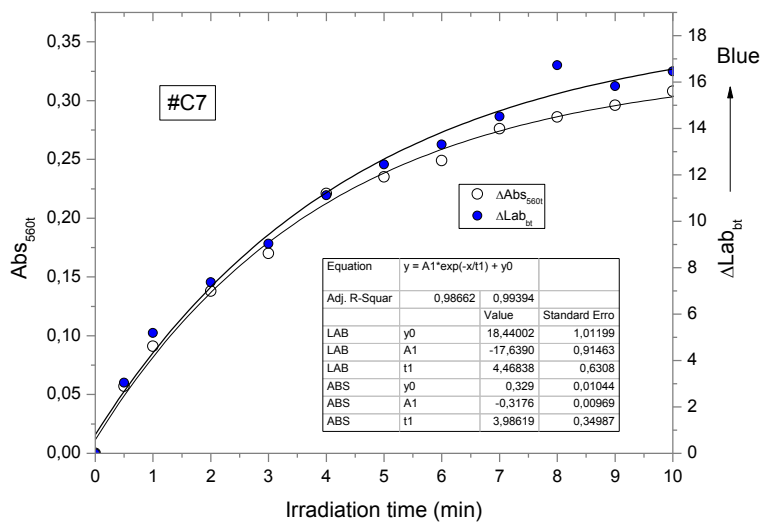
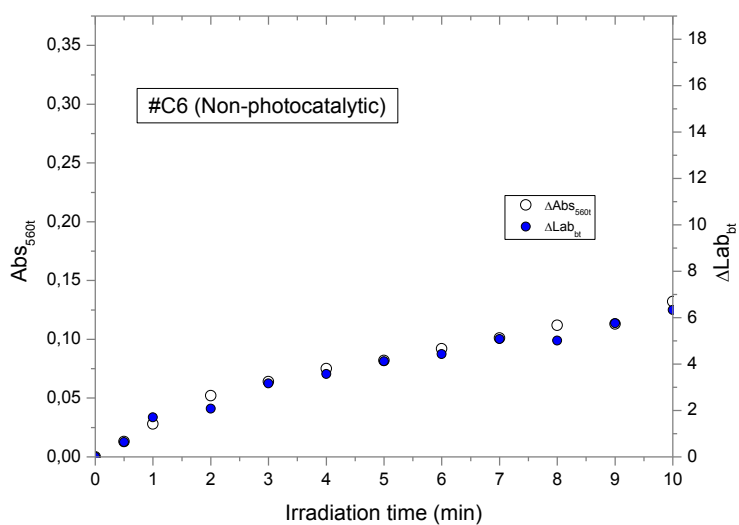
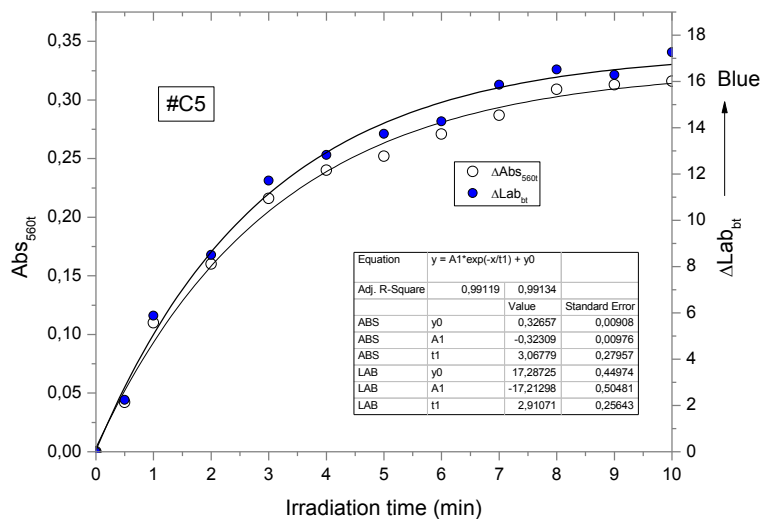


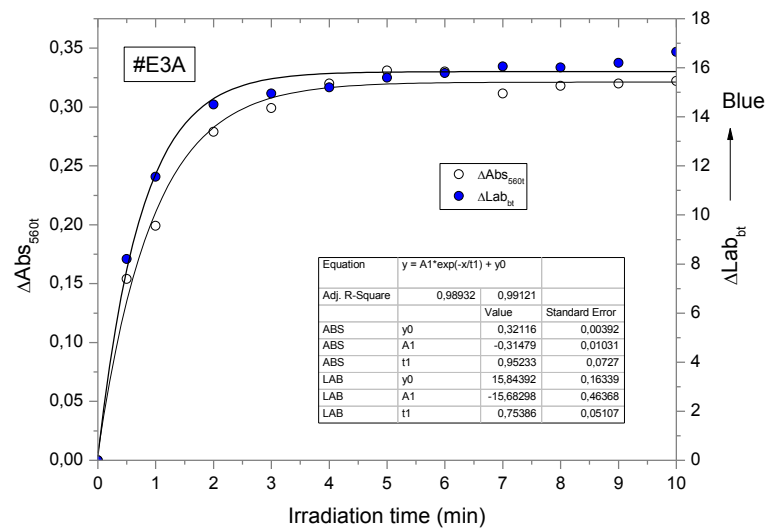
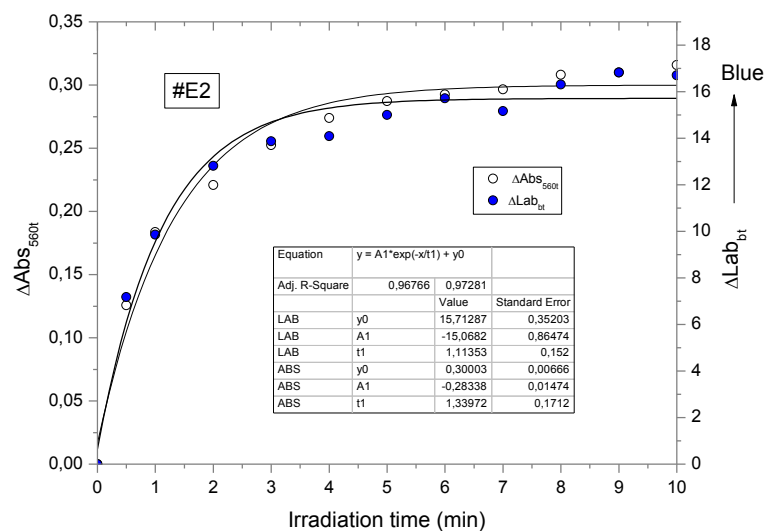
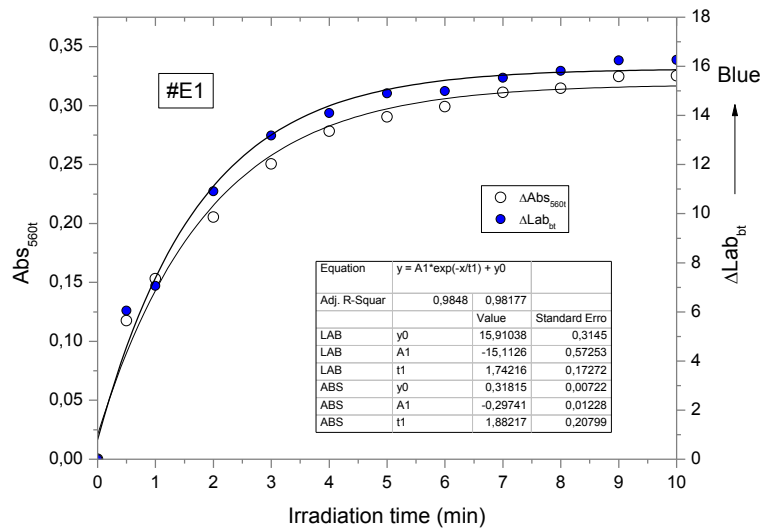


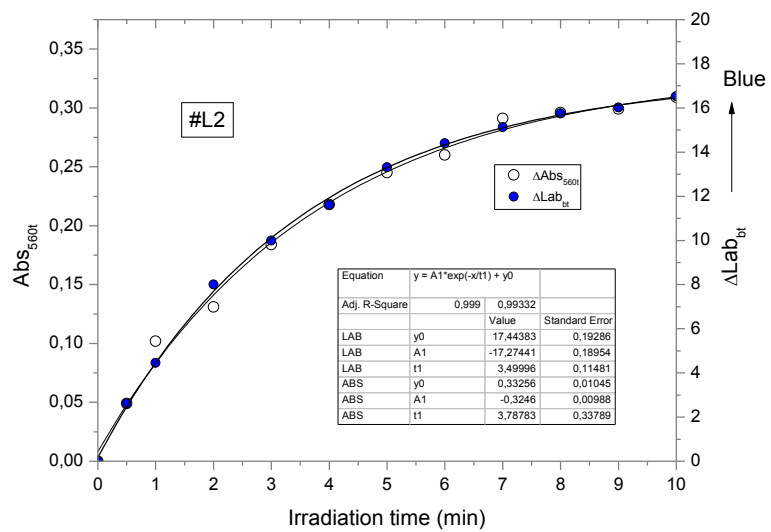
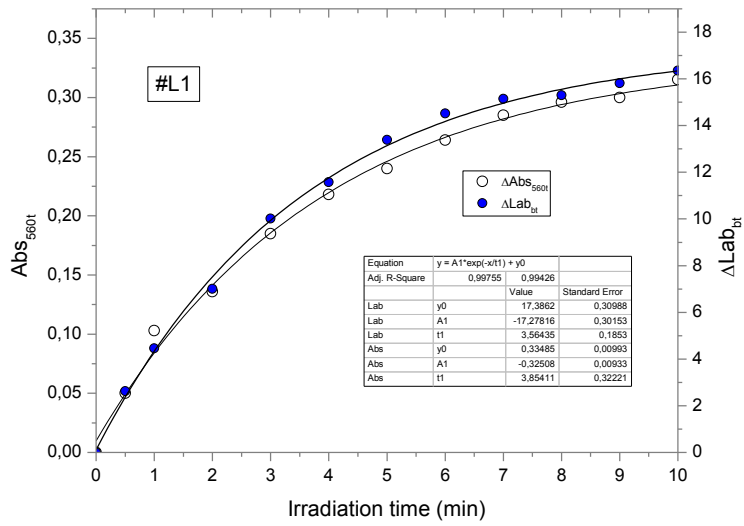
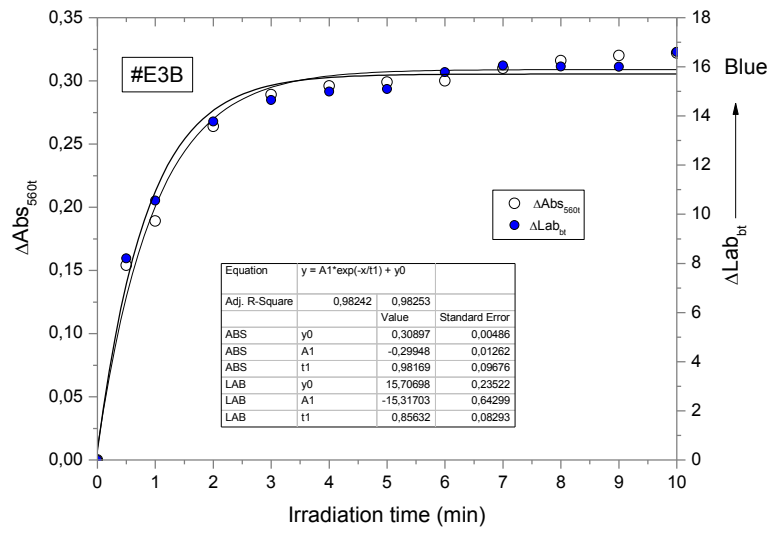
C.2 NBT ink – Absorbance and CIELAB colour



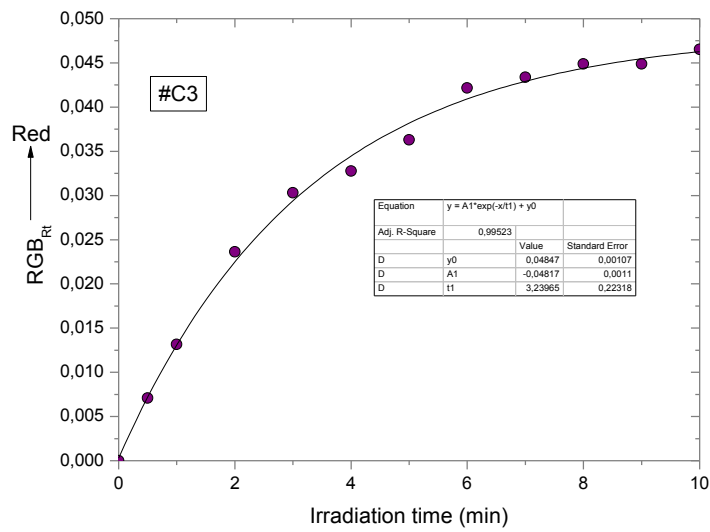
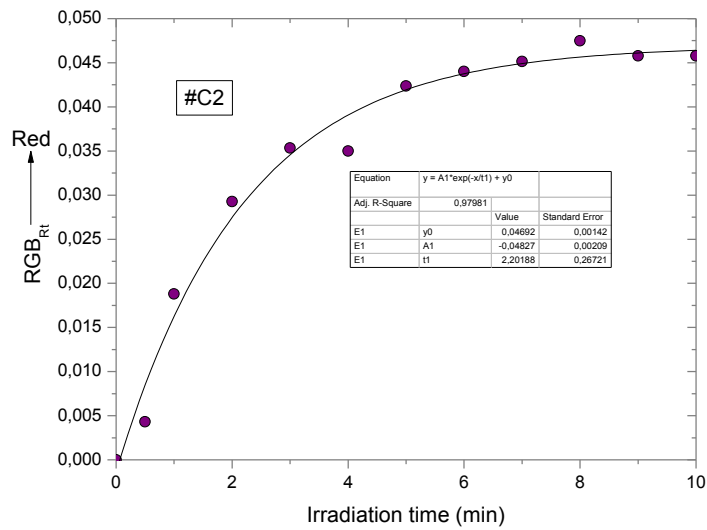
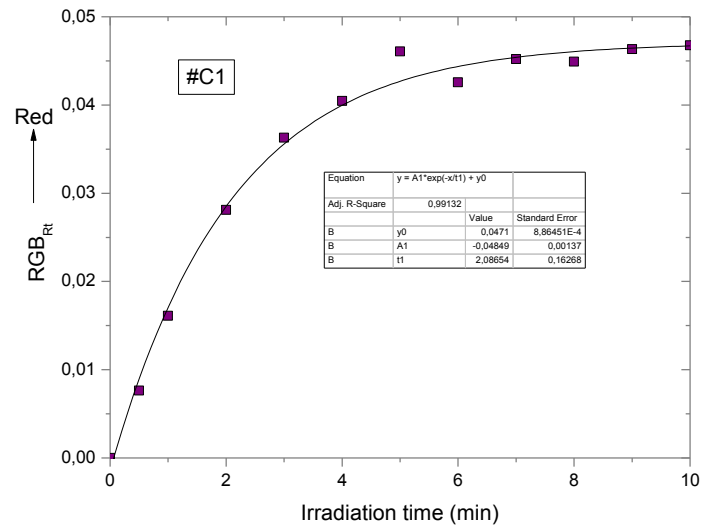


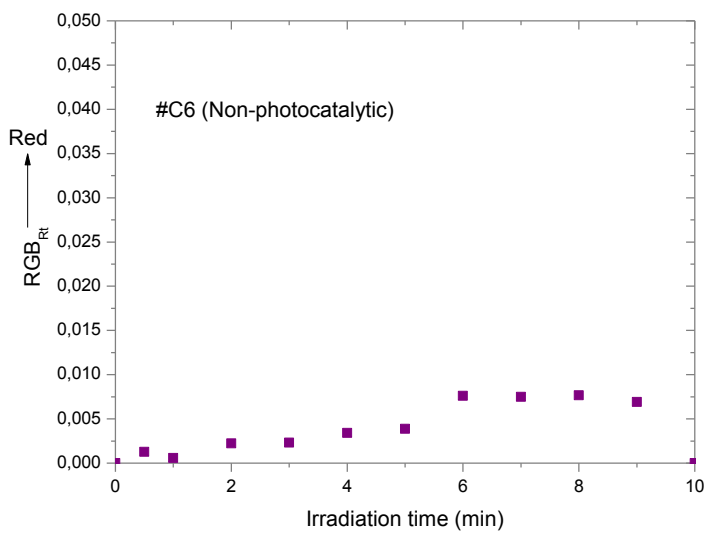
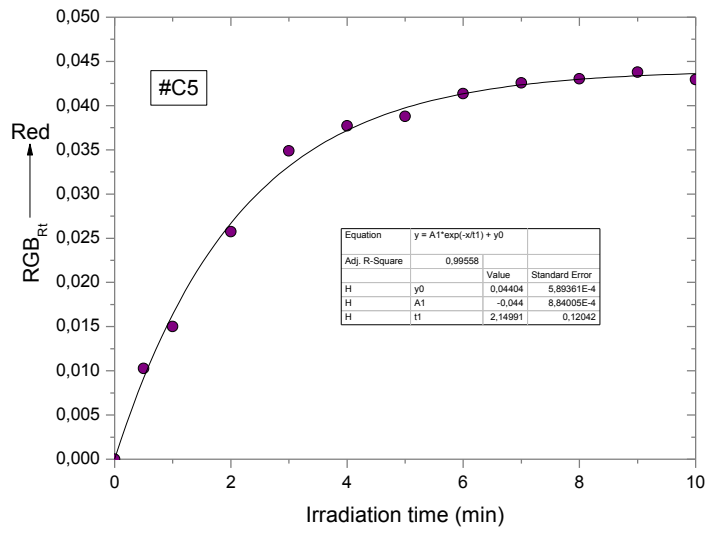
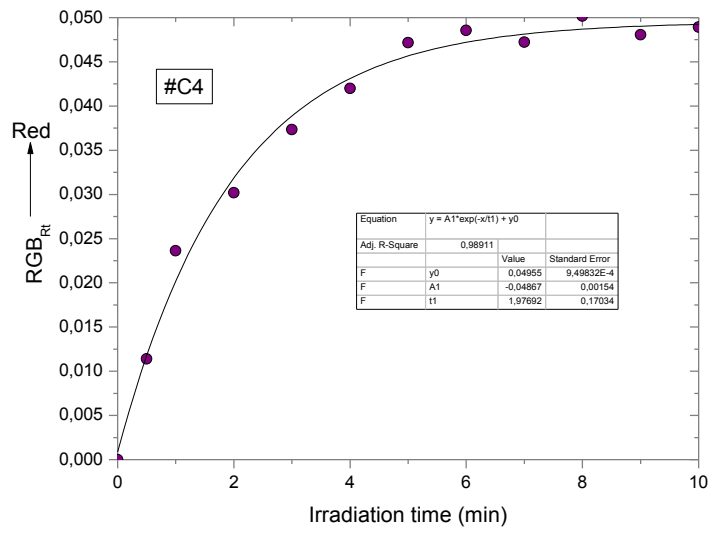


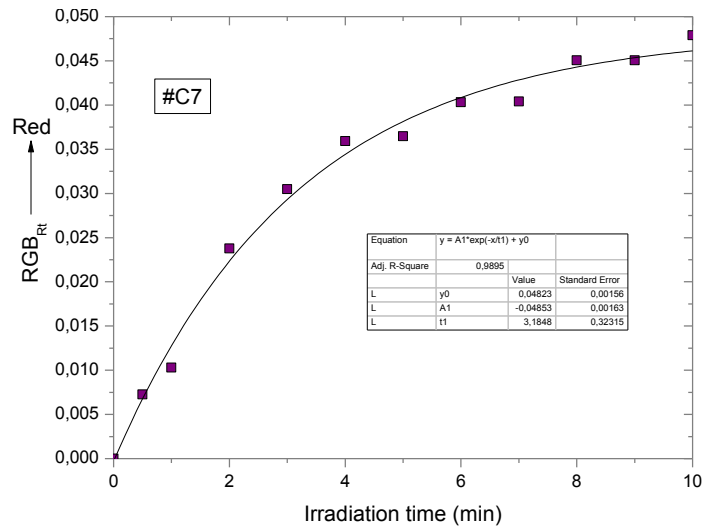




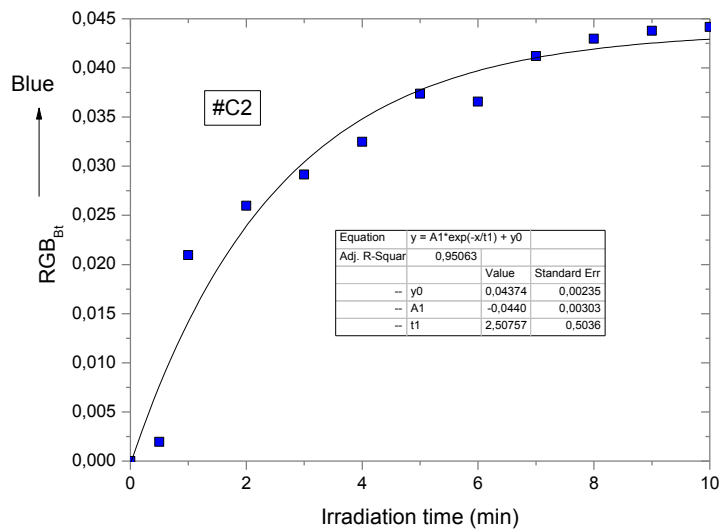
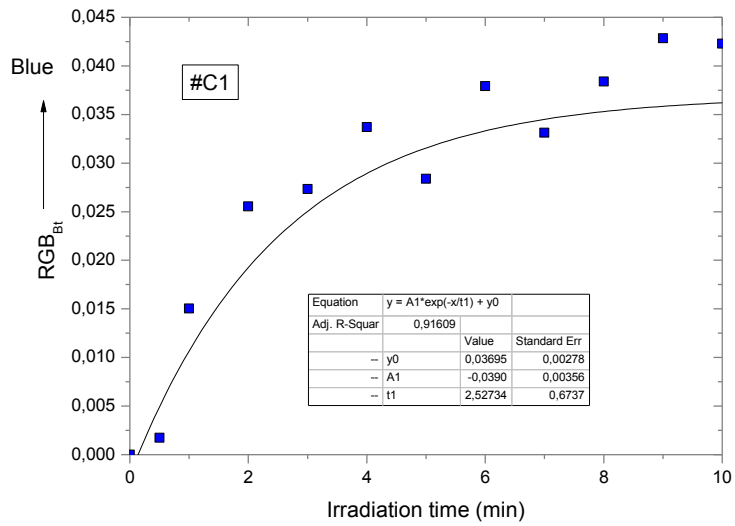
C.3 Rz ink – RGB from images

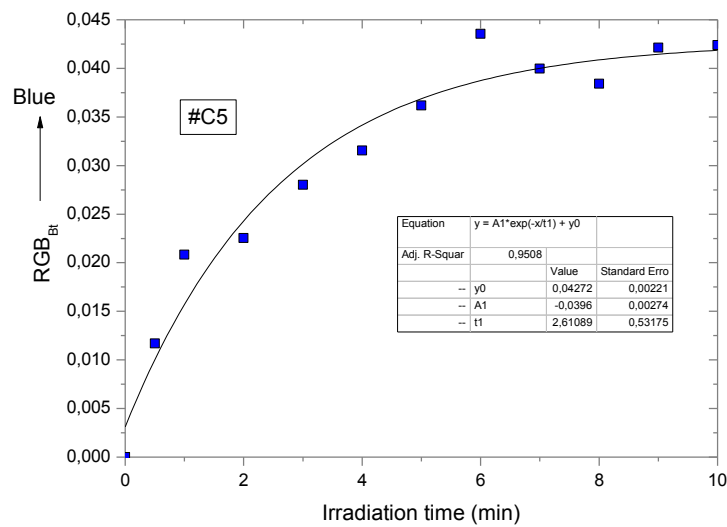
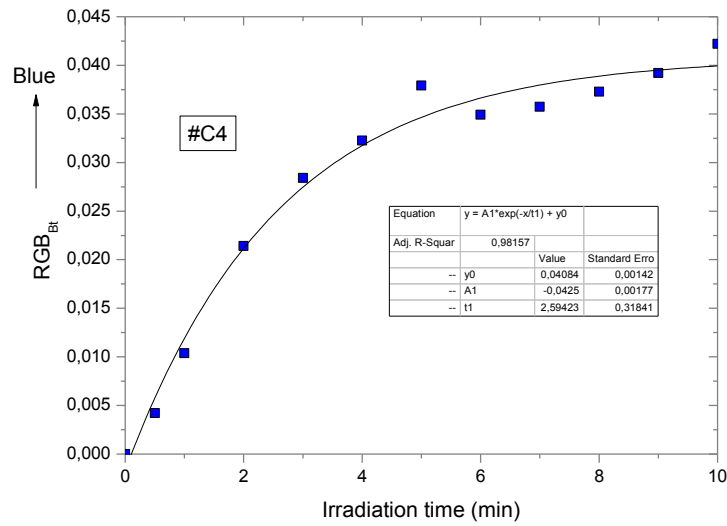
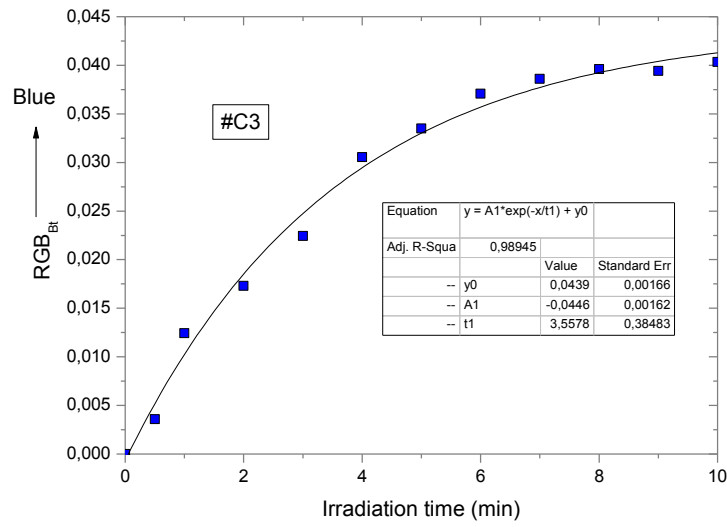


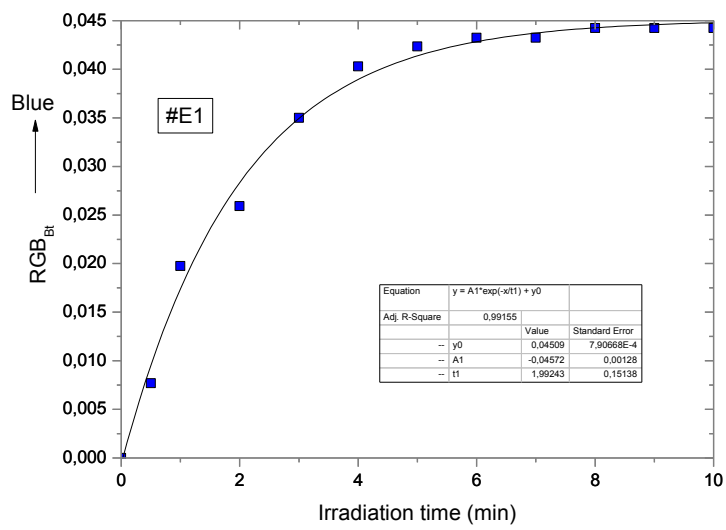
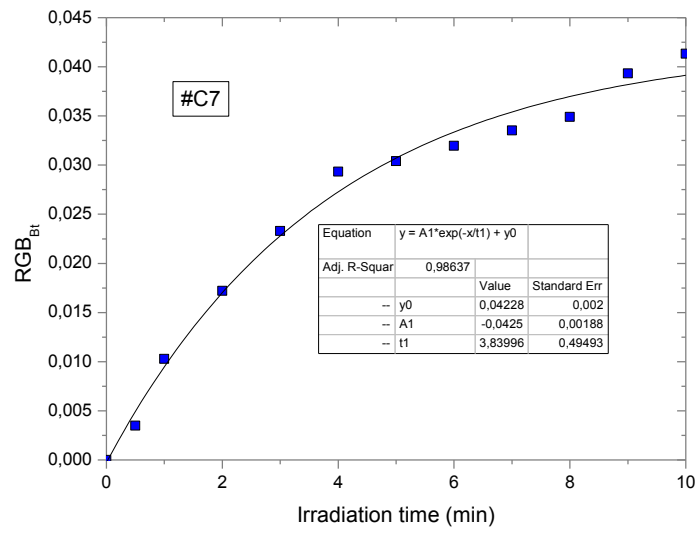
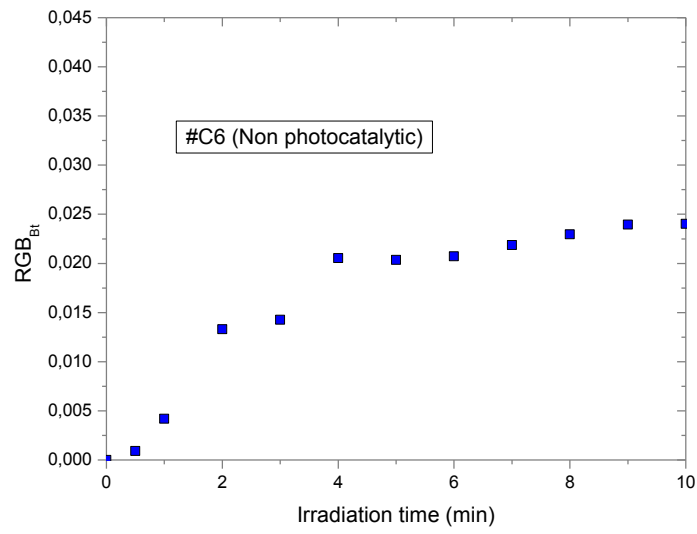


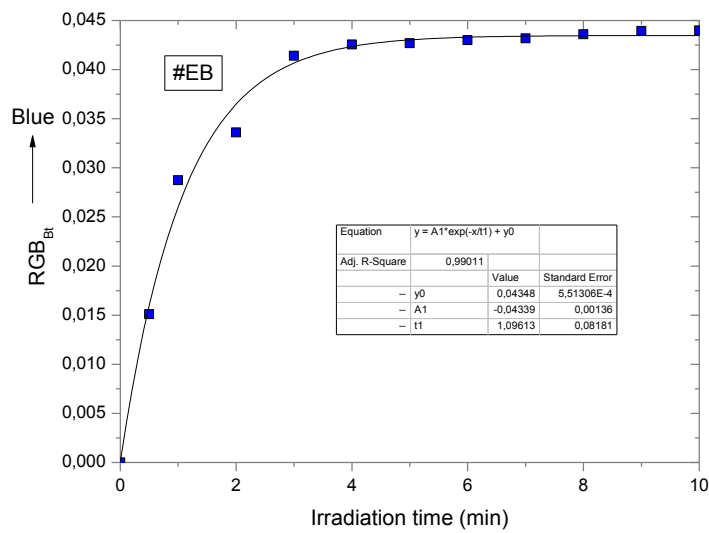
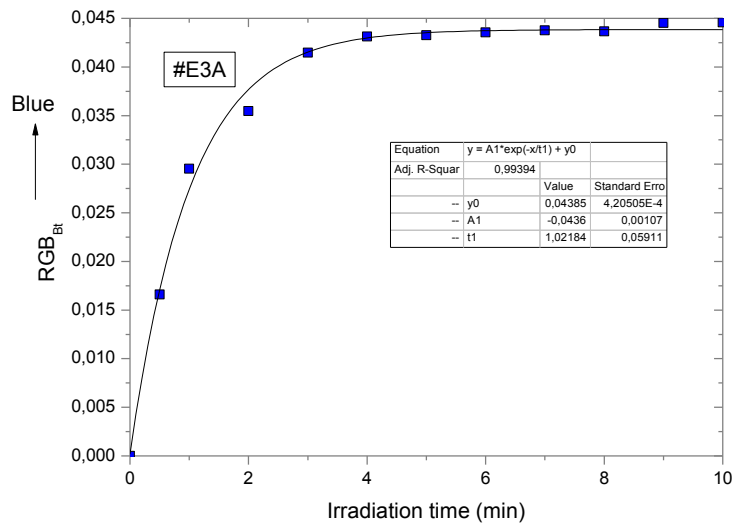
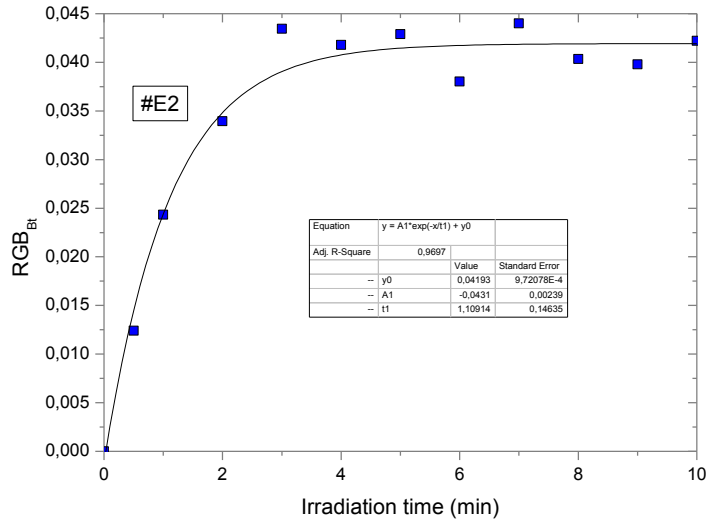


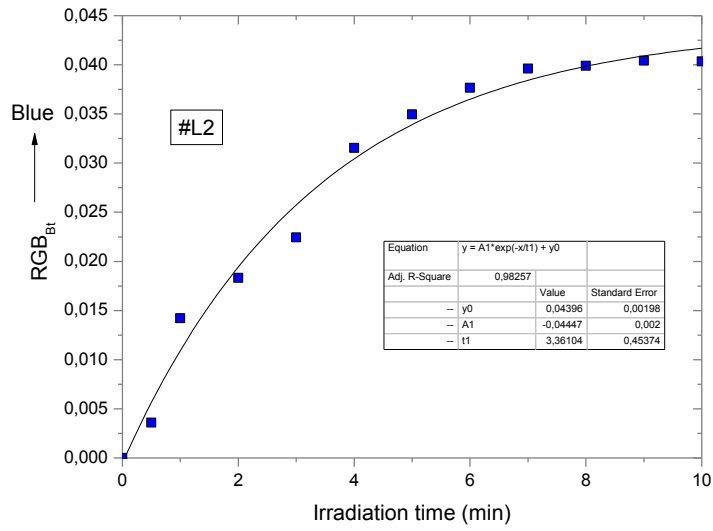
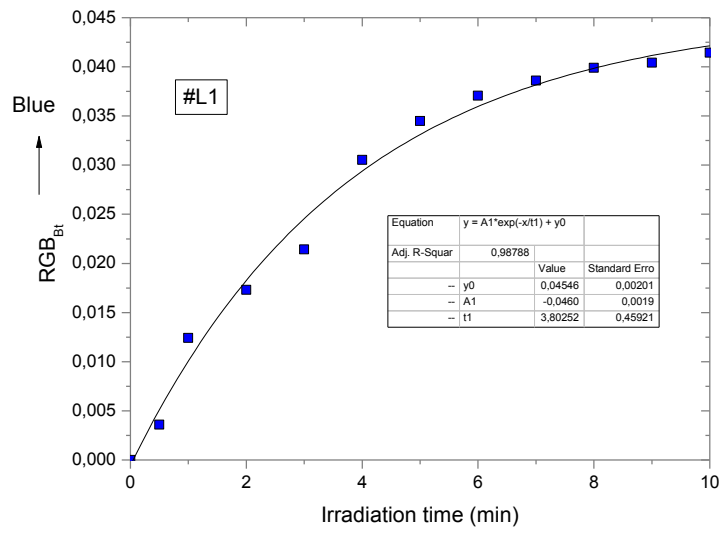
C.4 NBT ink – RGB from images



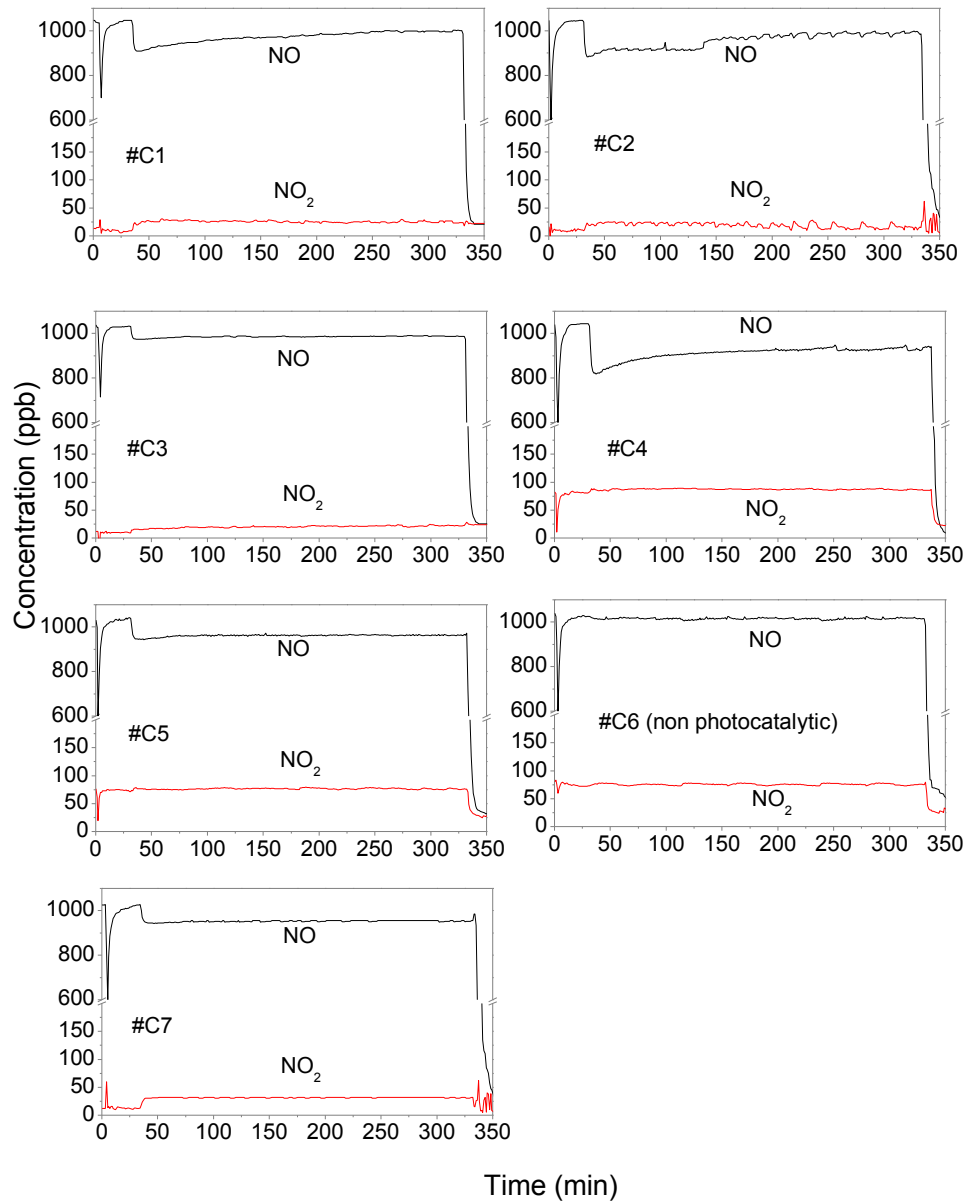


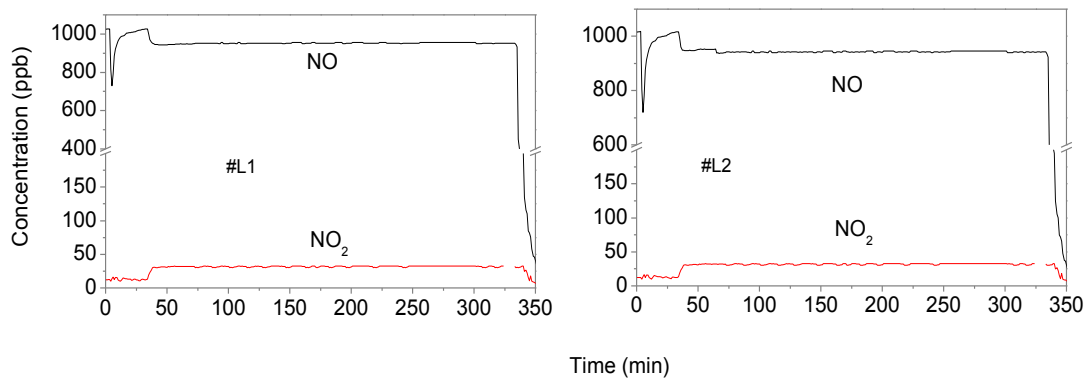
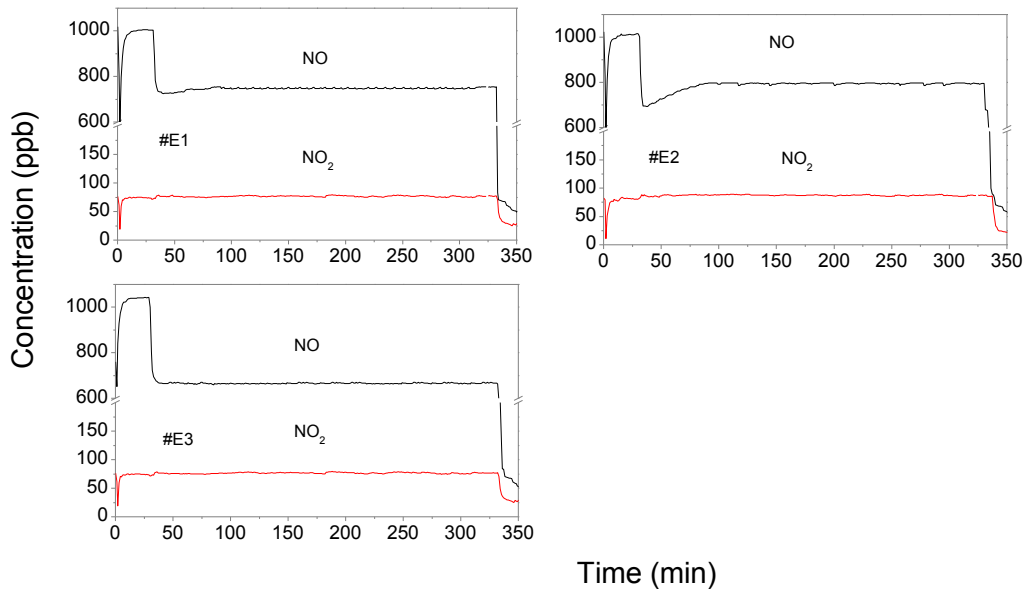
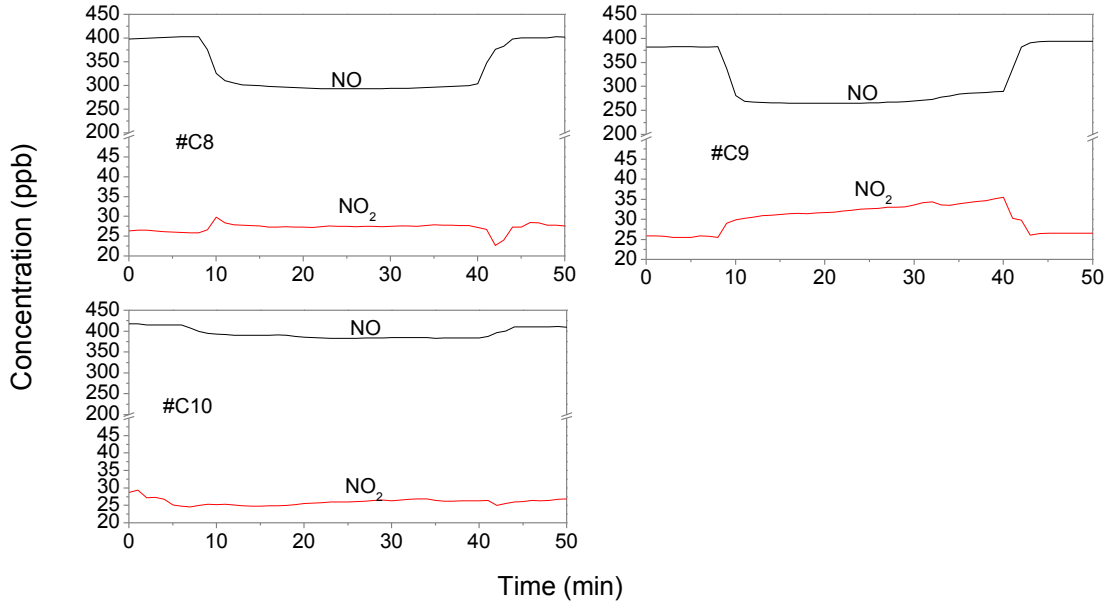


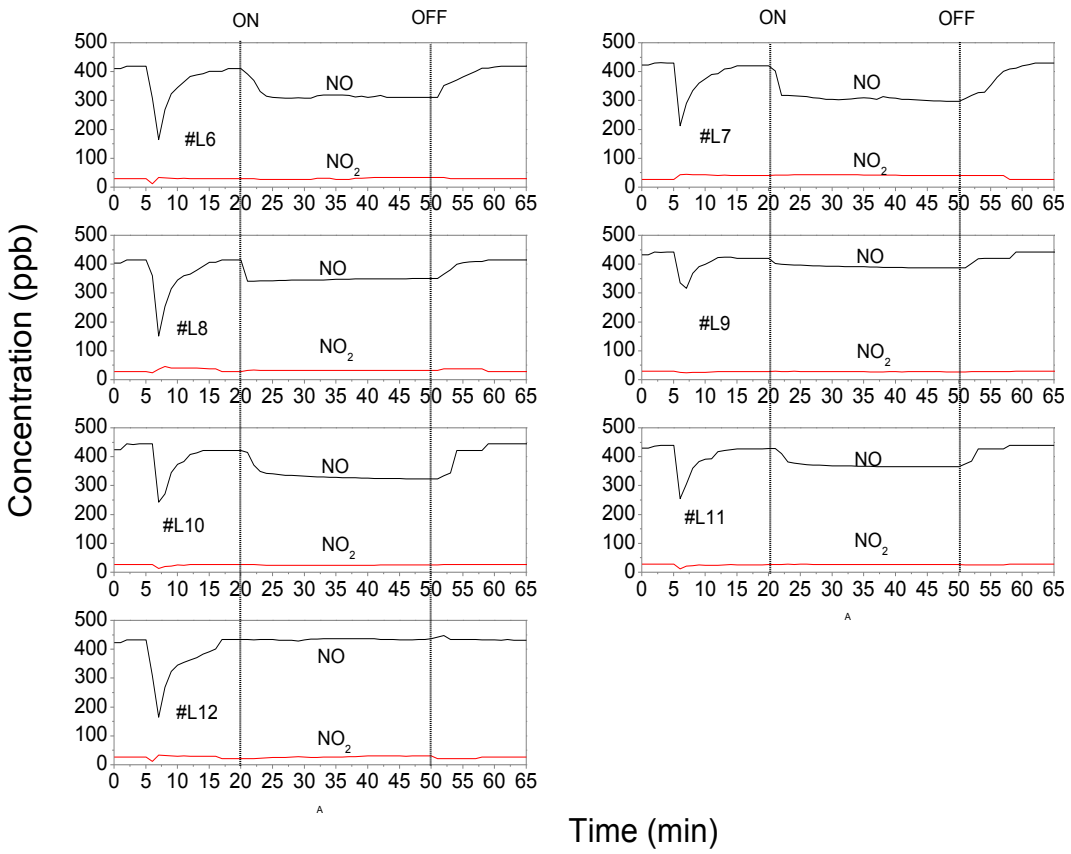
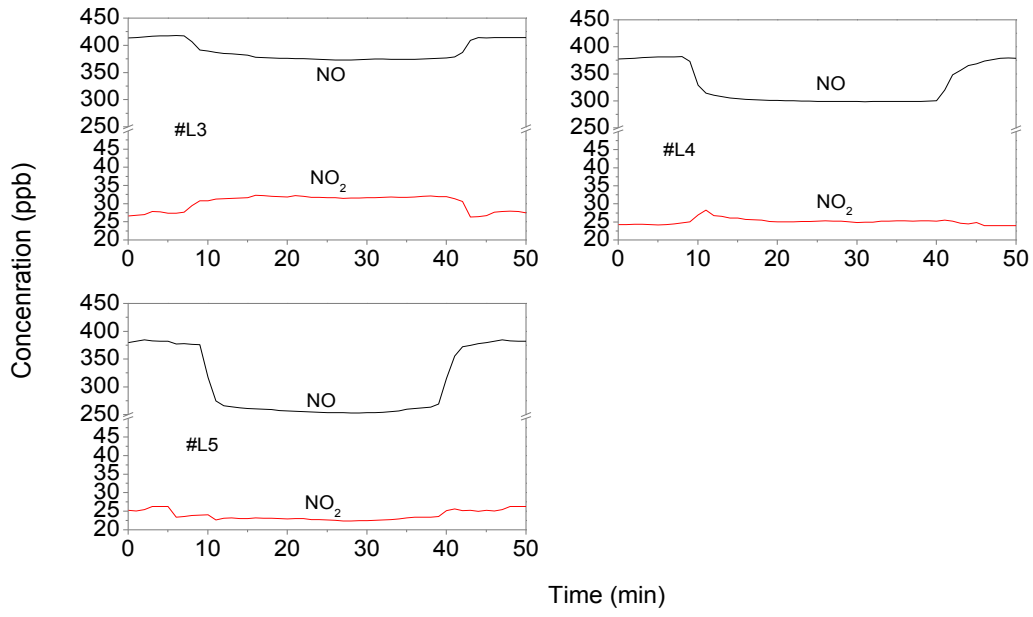




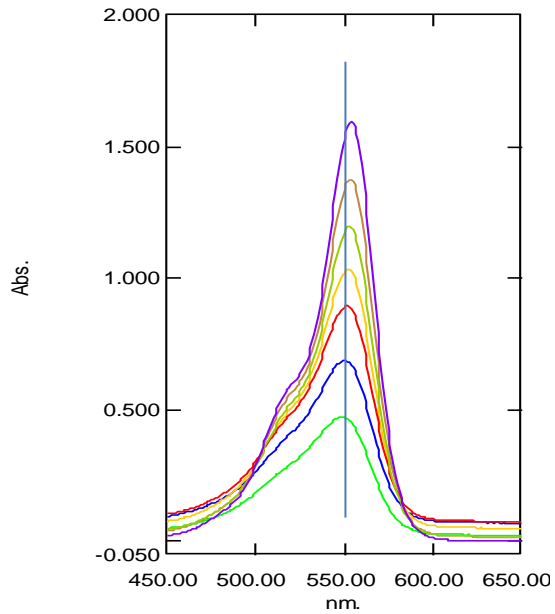
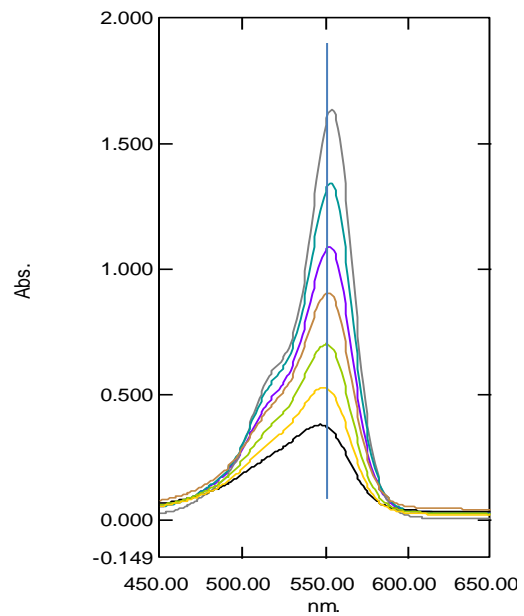
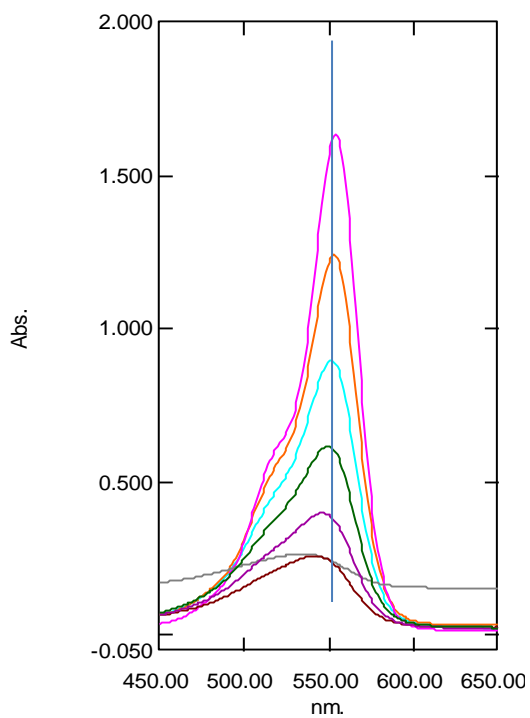
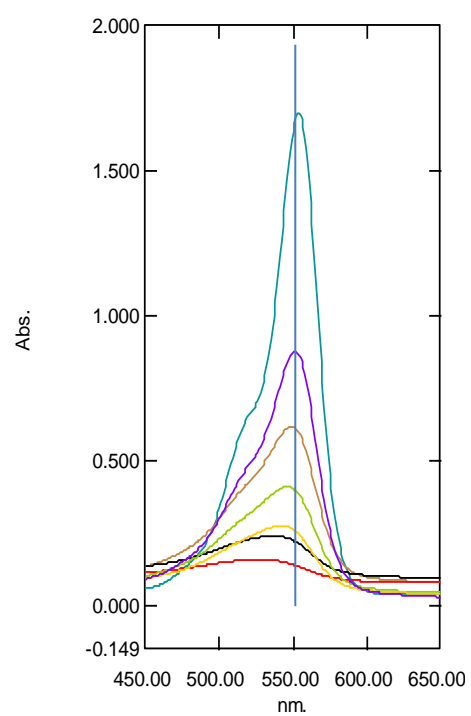
Appendix D Photocatalytic activity results using photocatalytic oxidation of gaseous NO to nitric acid (ISO 22197:1-2007 and UNI 11247:2010)

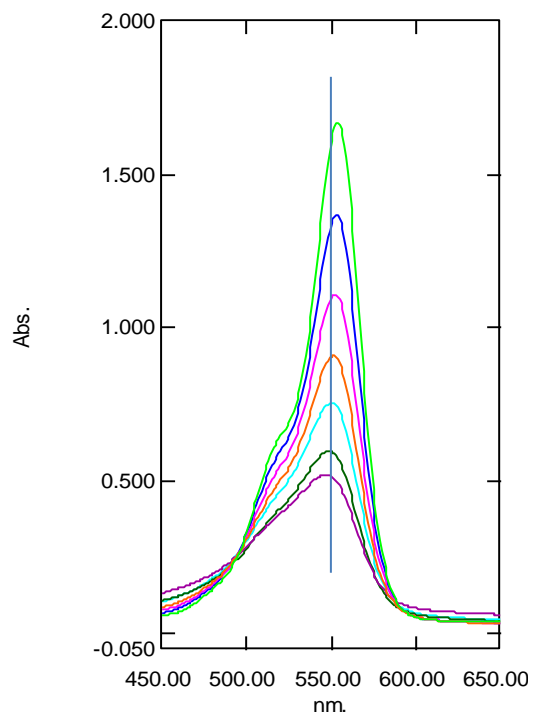
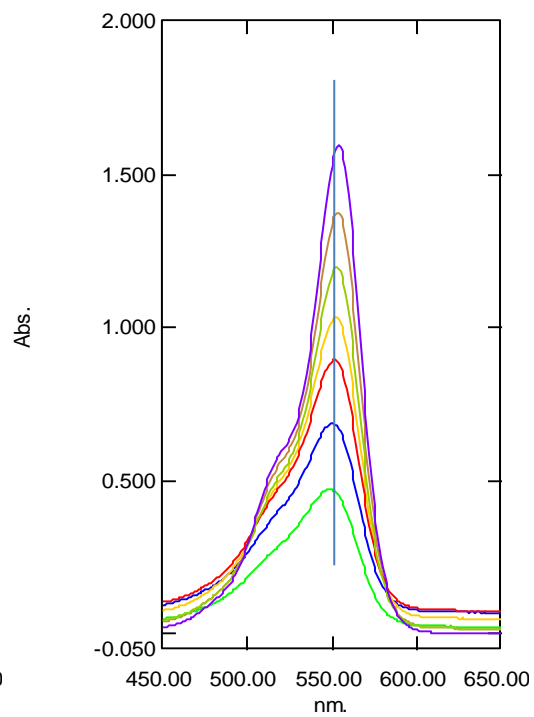
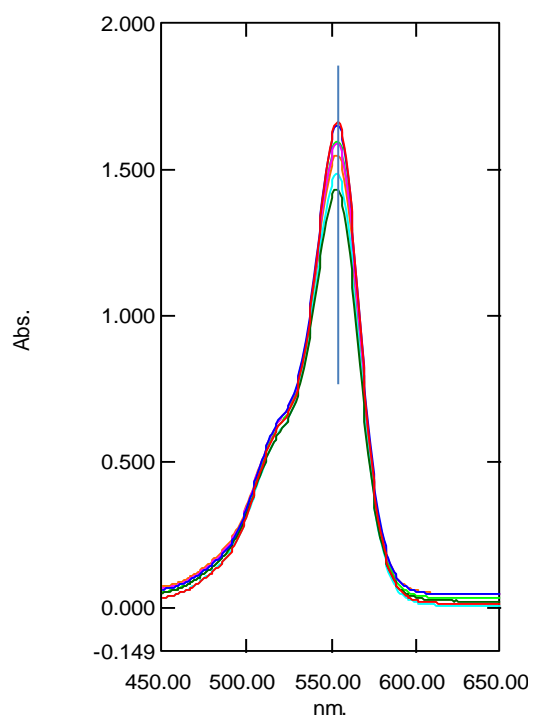






Appendix E Absorbance spectra variation of RhB dye tested under plain TiO_2 photocatalysts

 TiO_2 -400 **TiO_2 -500** **TiO_2 -600** **TiO_2 -700**

TiO₂-950***TiO₂-960******TiO₂-1000***

References

- [1] Dimitris I. Kondarides, Photocatalysis, in Catalysis, Encyclopedia of Life Support Systems (EOLSS), Ed. Gabriele Centi, Developed under the Auspices of the UNESCO, EOLSS Publishers, Oxford, UK., 2010.
- [2] N. Serpone and E. Pelizzetti, Photocatalysis : fundamentals and applications, Wiley, New York, 1989.
- [3] A.L. Linsebigler, G. Lu and J.T. Yates, Chemical Reviews, 95 (1995) 735.
- [4] A. Fujishima, K. Hashimoto and T. Watanabe, TiO₂ Photocatalysis: Fundamentals and Application, Tokyo, 1999.
- [5] J. Chen and C.-s. Poon, Building and Environment, 44 (2009) 1899.
- [6] M.R. Hoffmann, S.T. Martin, W. Choi and D.W. Bahnemann, Chemical Reviews, 95 (1995) 69.
- [7] A. Mills and S. Le Hunte, Journal of Photochemistry and Photobiology A: Chemistry, 108 (1997) 1.
- [8] R.H. Austin and S.-f. Lim, Proceedings of the National Academy of Sciences, 105 (2008) 17217.
- [9] X. Chen and S.S. Mao, Chem. Rev, 107 (2007) 2891.
- [10] A. Fujishima, X. Zhang and D.A. Tryk, Surface Science Reports, 63 (2008) 515.
- [11] T. Ohno, K. Sarukawa and M. Matsumura, The Journal of Physical Chemistry B, 105 (2001) 2417.
- [12] A. Fujishima, T.N. Rao and D.A. Tryk, Journal of Photochemistry and Photobiology C: Photochemistry Reviews, 1 (2000) 1.
- [13] T. Hirakawa and Y. Nosaka, Langmuir, 18 (2002) 3247.
- [14] Q. Xiang, J. Yu and P.K. Wong, Journal of Colloid and Interface Science, 357 (2011) 163.
- [15] Q. Xiao and L. Ouyang, Chemical Engineering Journal, 148 (2009) 248.
- [16] K.-i. Ishibashi, A. Fujishima, T. Watanabe and K. Hashimoto, Journal of Photochemistry and Photobiology A: Chemistry, 134 (2000) 139.
- [17] E. Jimenez-Relinque, Rodriguez-Garcia, J.R, Castillo, A., Castellote, M., Cement and Concrete Research, (2015).
- [18] K.-i. Ishibashi, A. Fujishima, T. Watanabe and K. Hashimoto, Journal of Photochemistry and Photobiology A: Chemistry, 134 (2000) 139.
- [19] H. Goto, Y. Hanada, T. Ohno and M. Matsumura, Journal of Catalysis, 225 (2004) 223.
- [20] X. Xu, X. Duan, Z. Yi, Z. Zhou, X. Fan and Y. Wang, Catalysis Communications, 12 (2010) 169.
- [21] H. Goto, Y. Hanada, T. Ohno and M. Matsumura, Journal of Catalysis, 225 (2004) 223.
- [22] K. Rajeshwar, Journal of Applied Electrochemistry, 37 (2007) 765.
- [23] A. Olivo, V. Trevisan, E. Ghedini, F. Pinna, C.L. Bianchi, A. Naldoni, G. Cruciani and M. Signoretto, Journal of CO₂ Utilization, 12 (2015) 86.

- [24] R. Wang, K. Hashimoto, A. Fujishima, M. Chikuni, E. Kojima, A. Kitamura, M. Shimohigoshi and T. Watanabe, *Advanced Materials*, 10 (1998) 135.
- [25] A. Fujishima, X. Zhang and D.A. Tryk, *International journal of hydrogen energy*, 32 (2007) 2664.
- [26] A. Fujishima and X. Zhang, *Comptes Rendus Chimie*, 9 (2006) 750.
- [27] F. Toma, G. Bertrand, D. Klein and C. Coddet, *Environmental Chemistry Letters*, 2 (2004) 117.
- [28] W.-K. Jo, J.-H. Park and H.-D. Chun, *Journal of Photochemistry and Photobiology A: Chemistry*, 148 (2002) 109.
- [29] E. Jimenez-Relinque and M. Castellote, *Environmental Science and Pollution Research*, 21 (2014) 11198.
- [30] R.M. Harrison, *Pollution: causes, effects and control*, Royal Society of Chemistry, 2001.
- [31] A. Folli, C. Pade, T.B. Hansen, T. De Marco and D.E. Macphee, *Cement and Concrete Research*, 42 (2012) 539.
- [32] M. Zinzi, E. Carnielo and S. Agnoli, *Energy and buildings*, 50 (2012) 111.
- [33] P.-C. Maness, S. Smolinski, D.M. Blake, Z. Huang, E.J. Wolfrum and W.A. Jacoby, *Applied and environmental microbiology*, 65 (1999) 4094.
- [34] C.A. Linkous, G.J. Carter, D.B. Locuson, A.J. Ouellette, D.K. Slattery and L.A. Smitha, *Environmental Science and Technology-Columbus*, 34 (2000) 4754.
- [35] M.-Z. Guo, T.-C. Ling and C.-S. Poon, *Cement and Concrete Composites*, 36 (2013) 101.
- [36] M. Sapiña, E. Jimenez-Relinque and M. Castellote, *Environmental science & technology*, 47 (2013) 11711.
- [37] M. Sapiña, E. Jimenez-Relinque, R. Nevshupa, E. Roman and M. Castellote, *Journal of Chemical Technology & Biotechnology*, 92 (2017) 210.
- [38] E. Jimenez-Relinque, M. Sapiña, R. Nevshupa, E. Roman and M. Castellote, *Chemical Engineering Journal*, 286 (2016) 560.
- [39] P. Amezaga-Madrid, G. Nevarez-Moorillon, E. Orrantia-Borunda and M. Miki-Yoshida, *FEMS Microbiology Letters*, 211 (2002) 183.
- [40] K. Hashimoto, H. Irie and A. Fujishima, *Japanese journal of applied physics*, 44 (2005) 8269.
- [41] H. Irie, K. Sunada and K. Hashimoto, *Electrochemistry*, 72 (2004) 807.
- [42] S. Laufs, G. Burgeth, W. Duttlinger, R. Kurtenbach, M. Maban, C. Thomas, P. Wiesen and J. Kleffmann, *Atmospheric Environment*, 44 (2010) 2341.
- [43] M. Diamanti, B. Del Curto, M. Ormellese and M. Pedferri, *Construction and Building Materials*, 46 (2013) 167.
- [44] M.V. Diamanti, M. Ormellese and M. Pedferri, *Cement and Concrete Research*, 38 (2008) 1349.
- [45] A. Strini, S. Cassese and L. Schiavi, *Applied Catalysis B: Environmental*, 61 (2005) 90.
- [46] J. Chen, S.-c. Kou and C.-s. Poon, *Building and Environment*, 46 (2011) 1827.

- [47] F. Vallee, B. Ruot, L. Bonafous, L. Guillot, N. Pimpinelli, L. Cassar, A. Strini, E. Mapelli, L. Schiavi and C. Gobin, RILEM International Symposium on Environment-Conscious Materials and Systems for Sustainable Development 2004.
- [48] G.L. Guerrini and E. Peccati, Newsletter, (2016).
- [49] A. Beeldens, L. Cassar, N. Pimpinelli and G. Guerrini, (2007).
- [50] W. Zhu, P.J. Bartos and A. Porro, Materials and Structures, 37 (2004) 649.
- [51] G. Guerrini, A. Plassais, C. Pepe and L. Cassar, Newsletter, (2016).
- [52] C.E. Bygott, J.E. Maltby, J.L. Stratton and R. McIntyre, Newsletter, (2016).
- [53] M. Lackhoff, X. Prieto, N. Nestle, F. Dehn and R. Niessner, Applied Catalysis B: Environmental, 43 (2003) 205.
- [54] A. Nazari, S. Riahi and S. Riahi, Journal of American Science, 6 (2010) 98.
- [55] M.V. Diamanti, F. Lollini, M.P. Pedferri and L. Bertolini, Building and Environment, 62 (2013) 174.
- [56] B. Ruot, A. Plassais, F. Olive, L. Guillot and L. Bonafous, Solar Energy, 83 (2009) 1794.
- [57] S.S. Lucas, V.M. Ferreira and J.L.B. de Aguiar, Cement and Concrete Research, 43 (2013) 112.
- [58] A. Rachel, M. Subrahmanyam and P. Boule, Applied Catalysis B: Environmental, 37 (2002) 301.
- [59] S. Guo, Z. Wu and W. Zhao, Chinese Science Bulletin, 54 (2009) 1137.
- [60] A. Mills, C. Hill and P.K. Robertson, Journal of Photochemistry and Photobiology A: Chemistry, 237 (2012) 7.
- [61] A. Mills, Applied Catalysis B: Environmental, 128 (2012) 144.
- [62] Information on contact angle. Contact angle goniometers and tensiometers [online]. <http://www.ramehart.com/contactangle.htm>, 2014.
- [63] P.C. Hiemenz and R. Rajagopalan, Principles of colloid and surface chemistry, CRC press, 1997.
- [64] E. Jimenez-Relinque and M. Castellote, Cement and Concrete Research, 74 (2015) 108.
- [65] N. Bengtsson and M. Castellote, Journal of Advanced Oxidation Technologies, 13 (2010) 341.
- [66] N. Sakai, A. Fujishima, T. Watanabe and K. Hashimoto, The Journal of Physical Chemistry B, 107 (2003) 1028.
- [67] M. Takeuchi, K. Sakamoto, G. Martra, S. Coluccia and M. Anpo, The Journal of Physical Chemistry B, 109 (2005) 15422.
- [68] S.-I. In, P.C.K. Vesborg, B.L. Abrams, Y. Hou and I. Chorkendorff, Journal of Photochemistry and Photobiology A: Chemistry, 222 (2011) 258.
- [69] J. Zita, J. Krýsa, U. Černigoj, U. Lavrenčič-Štangar, J. Jirkovský and J. Rathouský, Catalysis Today, 161 (2011) 29.
- [70] A.R. Jayapalan, B.Y. Lee, E.M. Land, M.H. Bergin and K.E. Kurtis, ACI Materials Journal, 112 (2015).
- [71] U. Černigoj, M. Kete and U.L. Štangar, Catalysis Today, 151 (2010) 46.
- [72] T. Wu, G. Liu, J. Zhao, H. Hidaka and N. Serpone, The Journal of Physical Chemistry B, 102 (1998) 5845.

- [73] Y.-L. Hu, Y. Lu, G.-J. Zhou and X.-H. Xia, *Talanta*, 74 (2008) 760.
- [74] A. Gomes, E. Fernandes and J.L. Lima, *Journal of biochemical and biophysical methods*, 65 (2005) 45.
- [75] N. Soh, *Analytical and bioanalytical chemistry*, 386 (2006) 532.
- [76] C. Lu, G. Song and J.-M. Lin, *TrAC Trends in Analytical Chemistry*, 25 (2006) 985.
- [77] D.M. Murphy and M. Chiesa, *Electron Paramagnetic Reson*, 19 (2004) 279.
- [78] P. Fernández-Castro, M. Vallejo, M. San Román and I. Ortiz, *Journal of Chemical Technology and Biotechnology*, 90 (2015) 796.
- [79] Z. Wang, W. Ma, C. Chen, H. Ji and J. Zhao, *Chemical Engineering Journal*, 170 (2011) 353.
- [80] G. Bartosz, *Clinica Chimica Acta*, 368 (2006) 53.
- [81] V. Roubaud, S. Sankarapandi, P. Kuppusamy, P. Tordo and J.L. Zweier, *Analytical biochemistry*, 247 (1997) 404.
- [82] W. He, Y. Liu, W.G. Wamer and J.-J. Yin, *Journal of Food and Drug Analysis*, 22 (2014) 49.
- [83] W.G. Wamer, J.-J. Yin and R.R. Wei, *Free Radical Biology and Medicine*, 23 (1997) 851.
- [84] K. Zhao, L. Zhang, J. Wang, Q. Li, W. He and J.J. Yin, *Journal of the American Chemical Society*, 135 (2013) 15750.
- [85] S.-C. Ke, T.-C. Wang, M.-S. Wong and N.O. Gopal, *The Journal of Physical Chemistry B*, 110 (2006) 11628.
- [86] O.I. Micic, Y. Zhang, K.R. Cromack, A.D. Trifunac and M.C. Thurnauer, *Journal of Physical Chemistry*, 97 (1993) 13284.
- [87] T. Rajh, O.G. Poluektov and M.C. Thurnauer, *Chemical Physics of Nanostructured Semiconductors*, (2003) 1.
- [88] J.R. Harbour and M.L. Hair, *The Journal of Physical Chemistry*, 81 (1977) 1791.
- [89] R.F. Howe and M. Gratzel, *The Journal of Physical Chemistry*, 89 (1985) 4495.
- [90] D.C. Hurum, A.G. Agrios, K.A. Gray, T. Rajh and M.C. Thurnauer, *The Journal of Physical Chemistry B*, 107 (2003) 4545.
- [91] D.C. Hurum, K.A. Gray, T. Rajh and M.C. Thurnauer, *The Journal of Physical Chemistry B*, 109 (2005) 977.
- [92] K. Komaguchi, H. Nakano, A. Araki and Y. Harima, *Chemical physics letters*, 428 (2006) 338.
- [93] K.-i. Setsukinai, Y. Urano, K. Kakinuma, H.J. Majima and T. Nagano, *Journal of Biological Chemistry*, 278 (2003) 3170.
- [94] K. Naito, T. Tachikawa, M. Fujitsuka and T. Majima, *The Journal of Physical Chemistry C*, 112 (2008) 1048.
- [95] K. Naito, T. Tachikawa, M. Fujitsuka and T. Majima, *Journal of the American Chemical Society*, 131 (2008) 934.
- [96] T. Tachikawa and T. Majima, *Chemical communications*, 48 (2012) 3300.
- [97] M. Price, J.J. Reiners, A.M. Santiago and D. Kessel, *Photochemistry and photobiology*, 85 (2009) 1177.

- [98] T. Hirakawa, K. Yawata and Y. Nosaka, *Applied Catalysis A: General*, 325 (2007) 105.
- [99] K.-i. Ishibashi, A. Fujishima, T. Watanabe and K. Hashimoto, *Electrochemistry Communications*, 2 (2000) 207.
- [100] J. Zhang and Y. Nosaka, *The Journal of Physical Chemistry C*, 118 (2014) 10824.
- [101] G.L. Newton and J.R. Milligan, *Radiation Physics and Chemistry*, 75 (2006) 473.
- [102] X. Fang, G. Mark and C. von Sonntag, *Ultrasonics Sonochemistry*, 3 (1996) 57.
- [103] S. Dominguez, P. Ribao, M.J. Rivero and I. Ortiz, *Applied Catalysis B: Environmental*, 178 (2015) 165.
- [104] Y. Lee, C. Lee and J. Yoon, *Water Research*, 38 (2004) 2579.
- [105] N.E. Polyakov, T.V. Leshina, E.S. Meteleva, A.V. Dushkin, T.A. Konovalova and L.D. Kispert, *The Journal of Physical Chemistry B*, 114 (2010) 14200.
- [106] METHOD 8315A determination of carbonyl compounds by high performance liquid chromatography (HPLC). US Environmental Protection Agency (1996).
- [107] A. Peter, A. Mihaly-Cozmuta, C. Nicula, L. Mihaly-Cozmuta, A. Jastrzębska, A. Olszyna and L. Baia, *Water, Air, & Soil Pollution*, 228 (2017) 41.
- [108] M.K. Arfanis, P. Adamou, N.G. Moustakas, T.M. Triantis, A.G. Kontos and P. Falaras, *Chemical Engineering Journal*, 310 (2017) 525.
- [109] C. Kim, H.-j. Park, S. Cha and J. Yoon, *Chemosphere*, 93 (2013) 2011.
- [110] C.-Y. Chen and C.T. Jafvert, *Environmental science & technology*, 44 (2010) 6674.
- [111] J. Zhao, B. Zhang, J. Li, Y. Liu and W. Wang, *Chemical communications*, 52 (2016) 11595.
- [112] A. Mills, J. Wang, S.-K. Lee and M. Simonsen, *Chemical communications*, (2005) 2721.
- [113] A. Mills and N. Wells, *Chemical Society Reviews*, 44 (2015) 2849.
- [114] A. Mills, C. O'Rourke, K. Lawrie and S. Elouali, *ACS Applied Materials & Interfaces*, 6 (2014) 545.
- [115] A. Mills and M. McGrady, *Journal of Photochemistry and Photobiology A: Chemistry*, 193 (2008) 228.
- [116] A. Kafizas, C. Crick and I.P. Parkin, *Journal of Photochemistry and Photobiology A: Chemistry*, 216 (2010) 156.
- [117] F. Piccinini, M. Levi and S. Turri, *Progress in Organic Coatings*, 76 (2013) 1265.
- [118] N. Farahani, P.J. Kelly, G. West, M. Ratova, C. Hill and V. Vishnyakov, *Thin Solid Films*, 520 (2011) 1464.
- [119] A. Mills, N. Wells and C. O'Rourke, *Catalysis Today*, 230 (2014) 245.
- [120] K.-i. Ishibashi, A. Fujishima, T. Watanabe and K. Hashimoto, *The Journal of Physical Chemistry B*, 104 (2000) 4934.
- [121] Y. Nosaka, Y. Yamashita and H. Fukuyama, *The Journal of Physical Chemistry B*, 101 (1997) 5822.
- [122] T. Hirakawa and Y. Nosaka, *The Journal of Physical Chemistry C*, 112 (2008) 15818.
- [123] X.Z. Wu, M. Lingyue and K. Akiyama, *Luminescence*, 20 (2005) 36.
- [124] O. Hirayama and M. Yida, *Analytical biochemistry*, 251 (1997) 297.

- [125] M.M. Oosthuizen and D. Greyling, *Redox Report*, 6 (2001) 105.
- [126] F.-C. Cheng, J.-F. Jen and T.-H. Tsai, *Journal of Chromatography B*, 781 (2002) 481.
- [127] Y. Kakuma, A.Y. Nosaka and Y. Nosaka, *Physical Chemistry Chemical Physics*, 17 (2015) 18691.
- [128] C.-H. Tsai, A. Stern, J.-F. Chiou, C.-L. Chern and T.-Z. Liu, *Journal of Agricultural and Food Chemistry*, 49 (2001) 2137.
- [129] G. Cui, Z. Ye, J. Chen, G. Wang and J. Yuan, *Talanta*, 84 (2011) 971.
- [130] F. Lisdat and F.W. Scheller, *Analytical Letters*, 33 (2000) 1.
- [131] F. Lisdat, B. Ge, E. Ehrentreich-Förster, R. Reszka and F. Scheller, *Analytical chemistry*, 71 (1999) 1359.
- [132] B. Ge and F. Lisdat, *Analytica Chimica Acta*, 454 (2002) 53.
- [133] P. Salvador, *The Journal of Physical Chemistry*, 89 (1985) 3863.
- [134] S. Borgmann, *Analytical and bioanalytical chemistry*, 394 (2009) 95.
- [135] A.V. Krylov, M. Beissenhirtz, H. Adamzig, F.W. Scheller and F. Lisdat, *Analytical and bioanalytical chemistry*, 378 (2004) 1327.
- [136] D. Monllor-Satoca and R. Gómez, *The Journal of Physical Chemistry C*, 112 (2008) 139.
- [137] V. Augugliaro, M. Litter, L. Palmisano and J. Soria, *Journal of Photochemistry and Photobiology C: Photochemistry Reviews*, 7 (2006) 127.
- [138] X. Chen, G. Chen, F. Gao and P.L. Yue, *Environmental science & technology*, 37 (2003) 5021.
- [139] D. Zigah, J. Rodríguez-López and A.J. Bard, *Physical Chemistry Chemical Physics*, 14 (2012) 12764.
- [140] Y. Koizumi and Y. Nosaka, *The Journal of Physical Chemistry A*, 117 (2013) 7705.
- [141] M.M. Richter, *Chemical Reviews*, 104 (2004) 3003.
- [142] A. Kafizas, X. Wang, S.R. Pendlebury, P. Barnes, M. Ling, C. Sotelo-Vazquez, R. Quesada-Cabrera, C. Li, I.P. Parkin and J.R. Durrant, *The Journal of Physical Chemistry A*, 120 (2016) 715.
- [143] T. Yoshihara, R. Katoh, A. Furube, Y. Tamaki, M. Murai, K. Hara, S. Murata, H. Arakawa and M. Tachiya, *The Journal of Physical Chemistry B*, 108 (2004) 3817.
- [144] M. Sachs, E. Pastor, A. Kafizas and J.R. Durrant, *The Journal of Physical Chemistry Letters*, 7 (2016) 3742.
- [145] S.T. Martin, H. Herrmann, W. Choi and M.R. Hoffmann, *Journal of the Chemical Society, Faraday Transactions*, 90 (1994) 3315.
- [146] S.T. Martin, H. Herrmann and M.R. Hoffmann, *Journal of the Chemical Society, Faraday Transactions*, 90 (1994) 3323.
- [147] Q. Tang, W. Jiang, Y. Cheng, S. Lin, T. Lim and J. Xiong, *Industrial & Engineering Chemistry Research*, 50 (2011) 9839.
- [148] Y. Nakabayashi and Y. Nosaka, *The Journal of Physical Chemistry C*, 117 (2013) 23832.
- [149] U. Černigoj, U.L. Štangaar, P. Trebše and M. Sarakha, *Journal of Photochemistry and Photobiology A: Chemistry*, 201 (2009) 142.

- [150] M. Sahni and B.R. Locke, *Industrial & Engineering Chemistry Research*, 45 (2006) 5819.
- [151] I. Gualandi and D. Tonelli, *Talanta*, 115 (2013) 779.
- [152] S.A. Coolen, F.A. Huf and J.C. Reijenga, *Journal of Chromatography B: Biomedical Sciences and Applications*, 717 (1998) 119.
- [153] R.A. Spurr and H. Myers, *Analytical chemistry*, 29 (1957) 760.
- [154] A. Murphy, *Solar Energy Materials and Solar Cells*, 91 (2007) 1326.
- [155] A.V.e. Shubnikov, *Principles of optical crystallography*, Consultants Bureau, 1960.
- [156] P. Kubelka and F. Munk, *Technical Physics*, 12 (1931) 593.
- [157] S. Judd, *Photoelectric sensors and controls: selection and application*, CRC Press, 1988.
- [158] E. Jimenez-Relinque, I. Llorente and M. Castellote, *Catalysis Today*, (2016).
- [159]
- [160] J.C. Barreto, G.S. Smith, N.H.P. Strobel, P.A. McQuillin and T.A. Miller, *Life Sciences*, 56 (1994) PL89.
- [161] S. Kohtani, K. Yoshida, T. Maekawa, A. Iwase, A. Kudo, H. Miyabe and R. Nakagaki, *Physical Chemistry Chemical Physics*, 10 (2008) 2986.
- [162] F. Xu, D. Guo, H. Han, H. Wang, Z. Gao, D. Wu and K. Jiang, *Res Chem Intermed*, 38 (2012) 1579.
- [163] D. Wang, Y. Duan, Q. Luo, X. Li, J. An, L. Bao and L. Shi, *Journal of Materials Chemistry*, 22 (2012) 4847.
- [164] M. Sahni and B.R. Locke, *Industrial & Engineering Chemistry Research*, 45 (2006).
- [165] X. Zheng, D. Li, X. Li, L. Yu, P. Wang, X. Zhang, J. Fang, Y. Shao and Y. Zheng, *Physical Chemistry Chemical Physics*, 16 (2014) 15299.
- [166] Z.-Y. Yang, G.-Y. Shen, Y.-P. He, X.-X. Liu and S.-J. Yang, *Journal of Porous Materials*, 23 (2016) 589.
- [167] H.M. Sung-Suh, J.R. Choi, H.J. Hah, S.M. Koo and Y.C. Bae, *Journal of Photochemistry and Photobiology A: Chemistry*, 163 (2004) 37.
- [168] K.R. Millington and L.J. Kirschenbaum, *Coloration Technology*, 118 (2002) 6.
- [169] M.E. Lindsey and M.A. Tarr, *Chemosphere*, 41 (2000) 409.
- [170] T. Maezono, M. Tokumura, M. Sekine and Y. Kawase, *Chemosphere*, 82 (2011) 1422.
- [171] E. Kowaska, M. Janczarek, J. Hupka and M. Gryniewicz, *Water Sci. Technol.*, 49 (2004) 261.
- [172] X.-Y. Yu and J.R. Barker, *J. Phys. Chem*, A107 (2003) 1325.
- [173] Y. Nosaka, S. Komori, K. Yawata, T. Hirakawa and A.Y. Nosaka, *Physical Chemistry Chemical Physics*, 5 (2003) 4731.
- [174] S. Goldstein, G. Czapski and J. Rabani, *The Journal of Physical Chemistry*, 98 (1994) 6586.
- [175] D. Lawless, N. Serpone and D. Meisel, *The Journal of Physical Chemistry*, 95 (1991) 5166.

- [176] S.-W. Lee, S. Obregón and V. Rodríguez-González, *RSC Advances*, 5 (2015) 44470.
- [177] N. Bengtsson and M. Castellote, *Materiales de Construcción*, 64 (2014) e013.
- [178] B. Choudhury and A. Choudhury, *International Nano Letters*, 3 (2013) 55.
- [179] B. Choudhury and A. Choudhury, *Physica E: Low-Dimensional Systems and Nanostructures*, 56 (2014) 364.
- [180] Y. Nakaoka and Y. Nosaka, *Journal of Photochemistry and Photobiology A: Chemistry*, 110 (1997) 299.
- [181] J.-G. Yu, H.-G. Yu, B. Cheng, X.-J. Zhao, J.C. Yu and W.-K. Ho, *The Journal of Physical Chemistry B*, 107 (2003) 13871.
- [182] A. Ibadon and P. Fitzpatrick, *Catalysts*, 3 (2013) 189.
- [183] Folli A., Jakobsen U. H., Guerrini G. L. and Macphee D. E., *Journal of advanced oxidation Technology* 12 (2009) 1.
- [184] Z. Zhang, C.-C. Wang, R. Zakaria and J.Y. Ying, *The Journal of Physical Chemistry B*, 102 (1998) 10871.
- [185] J.T. Carneiro, T.J. Savenije, J.A. Moulijn and G. Mul, *The Journal of Physical Chemistry C*, 115 (2011) 2211.
- [186] A. Yamakata, J.J.M. Vequizo and H. Matsunaga, *The Journal of Physical Chemistry C*, 119 (2015) 24538.
- [187] J. Wu, W. Walukiewicz, W. Shan, K. Yu, J. Ager III, E. Haller, H. Lu and W.J. Schaff, *Physical Review B*, 66 (2002) 201403.
- [188] R. López and R. Gómez, *Journal of sol-gel science and technology*, 61 (2012) 1.
- [189] E. Jimenez-Relinque, J. Rodriguez-Garcia, A. Castillo and M. Castellote, *Cement and Concrete Research*, 71 (2015) 124.
- [190] V. Nadochenko, N. Denisov, A. Gorenberg, Y. Kozlov, P. Chubukov, J. Rengifo, C. Pulgarin and J. Kiwi, *Applied Catalysis B: Environmental*, 91 (2009) 460.
- [191] P. Singla, O. Pandey and K. Singh, *International Journal of Environmental Science and Technology*, 13 (2016) 849.
- [192] M.M. Khan, S.A. Ansari, D. Pradhan, M.O. Ansari, J. Lee and M.H. Cho, *Journal of Materials Chemistry A*, 2 (2014) 637.
- [193] N. Bengtsson and M. Castellote, *Materiales de Construcción*, 64 (2014) 013.
- [194] E. Quagliarini, F. Bondioli, G.B. Goffredo, C. Cordoni and P. Munafò, *Construction and Building Materials*, 37 (2012) 51.
- [195] A. Folli, C. Pade, T.B. Hansen, T. De Marco and D.E. Macphee, *Cement and Concrete Research*, 42 (2012) 539.
- [196] Q.L. Yu and H.J.H. Brouwers, *Applied Catalysis B: Environmental*, 92 (2009) 454.
- [197] J.S. Dalton, P.A. Janes, N.G. Jones, J.A. Nicholson, K.R. Hallam and G.C. Allen, *Environmental Pollution*, 120 (2002) 415.
- [198] K. Hashimoto, K. Wasada, N. Toukai, H. Kominami and Y. Kera, *Journal of Photochemistry and Photobiology A: Chemistry*, 136 (2000) 103.
- [199] L. Shi, L. Liang, J. Ma, F. Wang and J. Sun, *Catalysis Science & Technology*, 4 (2014) 758.

- [200] L. Shi, L. Liang, J. Ma, Y. Meng, S. Zhong, F. Wang and J. Sun, *Ceramics International*, 40 (2014) 3495.
- [201] M. Sapiña, E. Jimenez-Relinque and M. Castellote, *Environmental Science and Pollution Research*, 21 (2014) 12091.
- [202] S. Wang, L. Zhao, L. Bai, J. Yan, Q. Jiang and J. Lian, *Journal of Materials Chemistry A*, 2 (2014) 7439.
- [203] J. Zhang and Y. Nosaka, *The Journal of Physical Chemistry C*, 117 (2012) 1383.
- [204] T. Watanabe, T. Takizawa and K. Honda, *The Journal of Physical Chemistry*, 81 (1977) 1845.
- [205] T.S. Natarajan, M. Thomas, K. Natarajan, H.C. Bajaj and R.J. Tayade, *Chemical Engineering Journal*, 169 (2011) 126.
- [206] Y. Fan, G. Chen, D. Li, Y. Luo, N. Lock, A.P. Jensen, A. Mamakhel, J. Mi, S.B. Iversen and Q. Meng, *International Journal of Photoenergy*, 2012 (2011).
- [207] K.N.d.S. Nascimento, M.C.A. de Oliveira, P.S. Oliveira, E.R. Macedo and H.P. de Oliveira, *Fibers and Polymers*, 16 (2015) 2177.
- [208] X. Li and J. Ye, *The Journal of Physical Chemistry C*, 111 (2007) 13109.
- [209] J. Zhuang, W. Dai, Q. Tian, Z. Li, L. Xie, J. Wang, P. Liu, X. Shi and D. Wang, *Langmuir*, 26 (2010) 9686.
- [210] M. Fulekar, A. Singh, D.P. Dutta, M. Roy, A. Ballal and A. Tyagi, *RSC Advances*, 4 (2014) 10097.
- [211] X. Zhang, S. Yu, Y. Liu, Q. Zhang and Y. Zhou, *Applied Surface Science*, 396 (2017) 652.
- [212] L. Xie, J. Ma and G. Xu, *Materials Chemistry and Physics*, 110 (2008) 197.
- [213] H. Fu, L. Zhang, W. Yao and Y. Zhu, *Applied Catalysis B: Environmental*, 66 (2006) 100.
- [214] T.A. Vu, C.D. Dao, T.T.T. Hoang, K.T. Nguyen, G.H. Le, P.T. Dang, H.T.K. Tran and T.V. Nguyen, *Materials Letters*, 92 (2013) 57.
- [215] S. Shamaila, A.K.L. Sajjad, F. Chen and J. Zhang, *Journal of Colloid and Interface Science*, 356 (2011) 465.
- [216] A. Laplaza, E. Jimenez-Relinque, J. Campos and M. Castellote, *Construction and Building Materials*, 144 (2017) 300.
- [217] M.-Z. Guo and C.-S. Poon, *Building and Environment*, 70 (2013) 102.
- [218] X. Xu, F. Ji, Z. Fan and L. He, *International journal of environmental research and public health*, 8 (2011) 1258.
- [219] Y. Xia and L. Yin, *Physical Chemistry Chemical Physics*, 15 (2013) 18627.
- [220] D. Barreca, G. Carraro, M.E. Warwick, K. Kaunisto, A. Gasparotto, V. Gombac, C. Sada, S. Turner, G. Van Tendeloo and C. Maccato, *CrystEngComm*, 17 (2015) 6219.
- [221] D. Chen, S.J. Hu and G.H. Li, *Advanced Materials Research* 2012.
- [222] P. Luan, M. Xie, D. Liu, X. Fu and L. Jing, *Scientific reports*, 4 (2014).
- [223] Y. Matsumoto, *Journal of Solid State Chemistry*, 126 (1996) 227.
- [224] X. Li, H. Lin, X. Chen, H. Niu, J. Liu, T. Zhang and F. Qu, *Physical Chemistry Chemical Physics*, 18 (2016) 9176.
- [225] A.-W. Xu, Y. Gao and H.-Q. Liu, *Journal of Catalysis*, 207 (2002) 151.

- [226] Q. Sun, W. Leng, Z. Li and Y. Xu, *Journal of hazardous materials*, 229 (2012) 224.